Application of Layered Double Hydroxides in Advanced Wastewater Remediation Processes for the Removal of Phenol, Efavirenz, and Nevirapine

By

Lehlogonolo Shane Tabana

Thesis submitted in fulfilment of the requirements for the degree of

Doctor of Philosophy

In

Chemical Engineering

In the Faculty of Engineering, Built Environment and Information Technology
University of Pretoria

Pretoria

12 December 2024

DECLARATION

I, **Lehlogonolo Shane Tabana, student No. 25154436,** do hereby declare that the thesis, which I submit for the degree Doctor of Philosophy in Chemical Engineering at the University of Pretoria, is my own work and has not previously been submitted by me for a degree at this or any other tertiary institution.

SIGNED on this 12 day of December 2024.

Lehlogonolo S. Tabana

Application of Layered Double Hydroxides in Advanced Wastewater Remediation Processes for the Removal of Phenol, Efavirenz, and Nevirapine

Student: Lehlogonolo Shane Tabana

Supervisor: Prof. Shepherd M. Tichapondwa

Department: Chemical Engineering

Faculty: Engineering, Built Environment and Information Technology

University: University of Pretoria

Degree: PhD (Chemical Engineering)

ABSTRACT

The global challenge of water contamination demands creative and sustainable methods for the effective treatment of wastewater. This study examined the use of modified layered double hydroxide (LDH)-based photocatalysts and adsorbents as potential solutions for removing persistent organic pollutants, primarily targeting antiretroviral drugs (ARVDs) such as efavirenz (EFV) and nevirapine (NVP). These drugs were selected because of their frequent occurrence in wastewater resulting from their extensive use in antiretroviral therapy for human immunodeficiency virus/acquired immunodeficiency syndrome (HIV/AIDS). Additionally, they are known to endure in the environment and resist conventional wastewater treatment methods, posing risks to both aquatic life and human health.

The investigation commenced with the synthesis and a comprehensive characterisation of a composite Ag-AgBr-LDH photocatalyst designed for visible light-induced photocatalysis. LDH and Ag-AgBr were selected for the synthesis of the photocatalyst based on their

complementary characteristics, offering the potential for improved photocatalytic performance through synergy. LDH materials are known for their durability and simplicity in synthesis, making them versatile materials that can be tailored to specific needs. However, their light absorption efficiencies, particularly in the visible light spectrum, are relatively limited. Conversely, Ag-AgBr is known for exceptional light absorption capabilities, especially in the visible light spectrum. However, its efficacy is often impeded by photo-corrosion, restricting its usefulness in photocatalytic processes. Through the combination of LDH and Ag-AgBr, the resultant photocatalyst can potentially capitalise on the advantages of both materials: the resilience and adaptability of LDH materials and the enhanced light absorption abilities of Ag-AgBr. The physicochemical characteristics of the photocatalyst, including crystalline structure, morphology, surface area, and chemical composition, were elucidated using techniques such as X-ray diffraction (XRD), scanning electron microscopy with energy-dispersive X-ray spectroscopy (SEM-EDS), Brunauer-Emmett-Teller (BET) surface area analysis, and X-ray photoelectron spectroscopy (XPS).

Subsequent evaluation of the photocatalyst's efficacy in degrading recalcitrant organic pollutants such as phenol, highlighted its potential in water treatment applications. Transitioning to the degradation of EFV and NVP, silver-halide-doped Mg-Zn-Al LDH emerged as a promising photocatalyst. For degradation of ARVDs, response surface modelling (RSM) was used to evaluate the interactions between the independent variables: initial pH of the solution, photocatalyst loading and initial concentration of the pollutants. The results showed that there were significant interactions between the initial concentration and photocatalyst loading for EFV degradation, while the interactions between photocatalyst loading and initial concentration, and the initial pH of the solution and photocatalyst loading were significant for NVP degradation. The highest degradation efficiencies were 84% and 100% for EFV and NVP, respectively. Scavenger tests revealed that the hydroxyl free radicals and photo-induced holes were the dominant active species that promoted the degradation of ARVDs.

The investigation delved deeper into the degradation of EFV and NVP in a continuous flow reactor, highlighting the complex relationship between light intensity, photocatalyst loading, and flow rate. The effect of light intensity was examined in batch experiments, while the impact of photocatalyst loading, flow rate, and initial concentration on the photodegradation efficiencies of the two ARVDs was evaluated using the continuous flow reactor. The results

indicated a clear correlation between light intensity and degradation efficiency, showing higher degradation rates at elevated light intensities. It was also determined that optimal conditions for achieving maximum degradation efficiency included a photocatalyst loading of 3 g L^{-1} and a flow rate of 10 mL min^{-1}. Elevated initial pollutant concentrations impeded degradation efficiency by reducing light penetration and increasing surface adsorption. Employing a membrane at the reactor outlet ensured retention of the photocatalyst within the reactor.

In a parallel endeavour, the study evaluated the adsorption potential of calcined layered double hydroxide (CLDH) for EFV and NVP removal from wastewater. Comprehensive characterisation analyses, including XRD, SEM-EDS, BET surface area analysis, and Fourier-transform infrared spectroscopy (FTIR), provided insights into the physicochemical properties and surface characteristics of the adsorbent. Computational analysis and adsorption isotherm studies revealed rapid kinetics, spontaneous and exothermic behaviour, and the dominance of physisorption interactions. The stable complexes formed between ARVDs and CLDH highlighted the efficacy of hydrogen bonding as a significant adsorption mechanism.

This comprehensive investigation highlighted the substantial promise of modified LDH-based photocatalysts and adsorbents in addressing the complex challenge of wastewater contaminated with pharmaceuticals specifically ARVDs. The insights gained provide a groundwork for ensuing research projects concentrating on the enhancement of photocatalytic systems and reactor designs, the investigation of alternative light sources, and ensuring the long-term stability and reusability of photocatalysts. Integrating adsorption and photocatalysis into hybrid systems, along with a deeper understanding of degradation mechanisms, could lead to more efficient and sustainable water treatment solutions.

Keywords: photocatalysis, surface plasmon resonance, antiretroviral therapy, adsorption, computational analysis.

ACKNOWLEDGEMENTS

I am appreciative of the Divine Guidance: Expressing thanks to the Almighty for directing me through my doctoral voyage!

I extend my deep appreciation to Prof. Shepherd M. Tichapondwa for his invaluable contribution, consistent guidance, unwavering assistance, and exceptional leadership throughout this endeavour.

The support extended by Prof. Johan Labuschagne regarding LDH materials and other resources is deeply valued.

I would like to express my sincere gratitude to Dr Joseph Adekoya for his assistance in the field of molecular modelling.

I am deeply thankful to Mrs. Alette Devenga, Mrs. Elmarie Otto, Ms. Olga Shokane, and Ms. Gymaisy Kenny for their unwavering patience and consistent availability to provide assistance throughout this journey.

The financial support received from the National Research Foundation (NRF), South Africa, is sincerely appreciated.

I am also thankful to the University of Pretoria for providing me with the Doctoral Bursary.

Wiebke Groete (XRD), Jeanette Dykstra (XRF), Charity Maepa and Erna van Wilpe (SEM), are thanked for their technical assistance.

I extend my heartfelt gratitude to Meisie Rasakanya, Mary Moja, Davy-Rayn Booysens, Dr. Job Tendenedzai, and my other esteemed colleagues at the Division of Water Utilisation and Environmental Engineering. Their generous sharing of time, ideas, unwavering support, and companionship have been invaluable throughout this journey.

To my parents, siblings, and extended family for all the love, support, and encouragement.

DEDICATION

Dedicated to

Ntakaneng, Makala, Ngaletjane, Mapula and Dineo.

TABLE OF CONTENTS

ABSTRACT i

ACKNOWLEDGEMENTS iv

DEDICATION v

LIST OF FIGURES xi

LIST OF TABLES xv

LIST OF ACRONYMS xvii

LIST OF SYMBOLS xix

PUBLICATIONS xx

CHAPTER 1: INTRODUCTION 1

1.1 Background 1

1.2 Problem Statement 3

1.3 Hypothesis 6

1.4 Aims and Objectives 7

1.5 Outline of the Thesis 7

1.6 Significance of the study 10

CHAPTER 2: LITERATURE REVIEW 12

2.1 Synopsis 12

2.2 Antiretroviral Drugs 12

2.2.1 Background 12

2.2.2 HIV/AIDS in sub-Saharan Region 17

2.2.3 Sources and Fate of Antiretroviral Drugs in Waterbodies 20

2.2.4 Determination of Antiretroviral Drugs in Aqueous Environment Matrices 26

2.2.5 Ecotoxicological studies for Antiretroviral Drugs 26

2.2.6 Processes for Remediation of Antiretroviral Drugs from Wastewater 30

2.2.7 Physicochemical Properties of Nevirapine and Efavirenz 34

2.3 Phenols in Waterbodies 35

2.3.1 Background 35
2.3.2 Sources and Fate of Phenols in Waterbodies 36
2.3.3 Challenges Associated with Phenols in Aqueous Solutions 36
2.3.4 Processes for removal of phenols from waterbodies 37
2.3.5 Physicochemical Properties of Phenol 40
2.4 Layered Double Hydroxide Materials 41
2.4.1 Background 41
2.4.2 Synthesis Methods 42
2.4.3 Applications of LDH Materials in Wastewater Treatment 44
2.5 Application of Silver Halides in Wastewater Treatment 48
2.5.1 Background 48
2.5.2 Mechanism in the Plasmonic Ag-based Metal@semiconductor Structure 49
2.5.3 Photoreactions in Z-scheme Hybrids with an Ag-based Metal@semiconductor@semiconductor Structure 50
2.5.4 Cases of Ag@AgX-based Plasmonic Photocatalysis 51
2.6 Conclusion 53
CHAPTER 3: EXPERIMENTAL 54
3.1 Synopsis 54
3.2 Materials 54
3.3 Synthesis of Layered Double Hydoxide and the Photocatalyst 54
3.3.1 Synthesis of Layered Double Hydroxide 54
3.3.2 Synthesis of Composite Photocatalyst 56
3.4 Calcination of Layered Double Hydroxide for Adsorption Process 56
3.5 Characterisation of the Photocatalysts and Adsorbents, and Analysis of Solution Samples 56
3.5.1 Characterisation of the Photocatalyst 56
3.5.2 Characterisation of the Adsorbent 57

3.5.3 Analysis of Solution Samples 59
3.6 Photocatalytic Degradation Processes 60
3.6.1 Photodegradation of Phenol 60
3.6.2 Photodegradation of ARVDs (batch studies) 60
3.6.3 Photodegradation of ARVDs (continuous flow process) 63
3.7 Adsorption studies 64
3.7.1 Experimental 64
3.7.2 Computational Analysis 67
3.8 Conclusion 69
CHAPTER 4: CHARACTERISATION OF THE PHOTOCATALYST COMPOSITE 70
4.1 Synopsis 70
4.2 X-Ray Diffraction Analysis of Photocatalysts 70
4.3 Scanning Electron Microscopy and Transmission Electron Microscope Analyses of Photocatalysts 71
4.4 X-ray Photoelectron Spectroscopy Analysis 74
4.5 Brunauer-Emmett-Teller Surface Area 76
4.6 Conclusion 76
CHAPTER 5: VISIBLE LIGHT ACTIVATED DEGRADATION OF PHENOL USING SILVER-SILVER BROMIDE-HYDROTALCITE NANOCOMPOSITE PHOTOCATALYST 78
5.1 Synopsis 78
5.2 Effect of Silver Content 78
5.3 Effect of Catalyst Loading 79
5.4 Effect of pH 80
5.5 Reaction Kinetics and the Effect of Phenol Concentration 81
5.6 Degradation Mechanism 83
5.7 Photo Stability and Reusability of the Catalyst 85
5.8 Conclusion 86

CHAPTER 6: PHOTOCATALYTIC DEGRADATION OF EFAVIRENZ AND NEVIRAPINE USING VISIBLE LIGHT-ACTIVATED AG-AGBR-LDH NANOCOMPOSITE CATALYST 87

6.1 Synopsis 87

6.2 Degradation of ARVDs using Various Photocatalysts 87

6.3 Statistical analysis of the ARVDs Photodegradation Process using ANOVA 88

6.4 Optimisation of Process Parameters using the Response Surface Method 91

6.5 Photodegradation Kinetics 93

6.6 Scavenger Tests and Photodegradation Mechanism 94

6.7 Photostability and Reusability of the Photocatalyst 96

6.8 Conclusion 97

CHAPTER 7: REMOVAL OF ANTIRETROVIRAL DRUGS FROM WASTEWATER USING CONTINUOUS FLOW PHOTOCATALYSIS 98

7.1 Synopsis 98

7.2 Effect of Light Intensity 98

7.3 Effect of Photocatalyst Loading 101

7.4 Effect of Flowrate 102

7.5 Effect of Initial Concentration and Degradation Kinetics 103

7.6 Conclusion 106

CHAPTER 8: INTEGRATED STUDY OF ANTIRETROVIRAL DRUGS ADSORPTION ONTO CALCINED LAYERED DOUBLE HYDROXIDE MATERIAL: EXPERIMENTAL AND COMPUTATIONAL ANALYSIS 107

8.1 Synopsis 107

8.2 Adsorbent Characterisation 107

8.2.1 X-ray Diffraction (XRD) Analysis 107

8.2.2 Thermogravimetric Analysis 108

8.2.3 Brunauer-Emmett-Teller (BET) Surface Area 109

8.2.4 Fourier Transform Infrared (FTIR) Analysis 110

8.2.5 Scanning electron microscopy (SEM) analysis 111

8.3 Adsorption Results 113
8.3.1 Statistical Analysis of the Adsorption Process Using Response Surface Methodology 113
8.3.2 Interpretation of 3-Dimensional (3D) and Contour Plots 115
8.3.3 Reaction Kinetics and the Effect of Pollutant Concentration 118
8.3.4 Adsorption Isotherms 122
8.3.5 Thermodynamics Studies 124
8.3.6 Recycling of the Adsorbent 126
8.3.7 Computational Modelling 128
8.4 Conclusion 131
CHAPTER 9: CONCLUSION AND RECOMMENDATIONS 133
9.1 Conclusion 133
9.2 Recommendations 134
REFERENCES 136
APPENDICES 163
Appendix A 163
Appendix B 164
Appendix C 168
Appendix D 170

LIST OF FIGURES

Figure 2.1: Structure of an LDH material (Richetta *et al*., 2017).....41

Figure 2.2: A schematic illustration of the charge transfer in an Ag-AgCl photocatalysts under the visible light irradiation (Cai *et al*., 2016).....50

Figure 2.3: Ag@AgCl@WO_3·H2O composite as an example for Ag-based metal@semiconductor@semiconductor (Fang *et al*., 2019).....51

Figure 3.1: Schematic diagram of the reactor configuration for LDH clay synthesis (Tabana, 2021).....55

Figure 3.2: Batch photocatalytic reactor setup (A: magnetic stirrer, B: magnetic stirrer bar, C: 350 mL reactor vessel, D: LED lamps).....63

Figure 3.3: Continuous flow photocatalytic reactor setup (A: feed tank, B: magnetic stirrer bar, C: magnetic stirrer, D: Watson Marlow peristaltic pump, E: 350 mL reactor vessel, F: frit membrane, G: LED lamps, H: ball valve).....64

Figure 3.4: 3D structure of the (a) (i) 3x3 CLDH (C4.5 O82.51 Mg8.67 Al9 Ca4.67 Zn4.67) showing the (ii) top, side, and isometric view of the modelled section of the CLDH, (b) EFV and, (c) NVP.....68

Figure 4.1: (a) X-ray diffraction spectra of neat LDH, Ag-AgBr and Ag-AgBr-LDH composite catalysts.....71

Figure 4.2:SEM and SEM-EDS analysis of LDH (a) & (b), Ag-AgBr (c) & (d) and Ag-AgBr-LDH (e) & (f) photocatalysts.....72

Figure 4.3: HAADF-STEM image of Ag-AgBr-LDH (a), EDS mapping, Mg (b), Al (c), Zn (d), Ag (e) & Br (f). TEM images, LDH (g), Ag-AgBr (h) & Ag-AgBr-LDH (i).....73

.Figure 4.4: XPS spectrum of LDH and Ag-AgBr-LDH photocatalysts (a) The survey spectrum peaks and the high resolution XPS spectra of (b) Mg 1S, (c)Br 3d5, (d) Zn 2p 3, (e) Ag 3d and (f) O 1s.....75

Figure 4.5: Nitrogen adsorption-desorption isotherms of LDH and Ag-AgBr-LDH.....76

Figure 5.1: Phenol degradation efficiencies with varying Ag content in the photocatalyst.....79

Figure 5.2: Phenol degradation efficiencies with varying photocatalyst loading.....80

Figure 5.3: Effect of pH on phenol degradation efficiencies.....81

Figure 5.4: Phenol degradation efficiencies at various initial concentrations. 82

Figure 5.5: First-order kinetics photodegradation of phenol at various initial concentrations. 83

Figure 5.6: Effect of different scavengers on the degradation of phenol by the composite photocatalyst. 84

Figure 5.7: Proposed phenol degradation pathway. 85

Figure 5.8: Stability and reusability tests of the photocatalyst. 86

Figure 6.1: Photodegradation efficiencies of ARVDs using various photocatalysts, (a) efavirenz and (b) nevirapine. 88

Figure 6.2: Comparison between the predicted and actual responses (c) efavirenz and (d) nevirapine. 89

Figure 6.3: (a) Response surface 3D plot for efavirenz, interactions between photocatalyst loading and pollutant concentration. Response surface 3D plot for nevirapine, (b) interactions between photocatalyst loading and pollutant concentration, (c) interaction between photocatalyst loading and initial pH of the solution. (d) PFO kinetics model fittings for efavirenz and nevirapine (10 mg L^{-1}). 92

Figure 6.4: Photodegradation efficiencies in the presence of various scavengers. 95

Figure 6.5: Formation of major active species during visible light irradiation of photocatalyst. 96

Figure 6.6: Photostability and reusability of the photocatalyst. 97

Figure 7.1: Degradation profiles of NVP with varying number of light sources (10 mg L^{-1} initial concentration, 2 g L^{-1} photocatalyst loading and neutral pH). 100

Figure 7.2: Photocatalytic degradation profiles with varying photocatalyst loading (initial concentration of 10 mg L^{-1}, neutral pH, and flow rate of 10 mL min^{-1}); (a) EFV and (b) NVP. 102

Figure 7.3: Photocatalytic degradation efficiencies of EFV and NVP at varying flow rate (initial concentration of 10 mg L^{-1}, photocatalyst loading of 3 g L^{-1} and neutral pH). 103

Figure 7.4: Photocatalytic degradation profiles at various initial concentration (flow rate 10 mL min^{-1}, neutral pH and photocatalyst loading of 3 g L^{-1}); (a) EFV and (b) NVP. 104

Figure 7.5: Photocatalytic degradation of EFV and NVP (initial concentration of 10 mg/L, photocatalyst loading of 3 g L^{-1}, flowrate of 10 mL min^{-1} and neutral pH).....105

Figure 8.1: X-ray diffraction spectra of neat and calcined LDH materials. 108

Figure 8.2: Thermogravimetric analysis of neat and calcined LDH material.....109

Figure 8.3: BET surface area analysis for neat LDH and CLDH. 110

Figure 8.4: FTIR analysis for neat LDH and CLDH. 111

Figure 8.5: SEM and SEM-EDS analysis for neat LDH (a) & (c) and CLDH (b) & (d). 112

Figure 8.6: HAADF-STEM image of neat LDH (a), EDS mapping (neat LDH), Mg (b), Al (c), Zn (d), HAADF-STEM image of CLDH (e), EDS mapping (CLDH), Mg (f), Al (g), Zn (h). 113

Figure 8.7: Predicted adsorption efficiency vs actual adsorption efficiency EFV (a) and NVP (b).....115

Figure 8.8: Response surface plots (3D and contour projection) showing variables' effects on adsorption of EFV (a) and (b) adsorbent loading (5 – 20 g L^{-1}) vs pH (5 – 20), (c) and (d) temperature (25 – 65 ℃) vs pollutant concentration (5 – 20 mg L^{-1}). 117

Figure 8.9: Response surface plots (3D and contour projection) showing variables' effects on adsorption of NVP (a) and b) adsorbent loading (5 – 20 g L^{-1}) vs pH (5 – 20), (c) and (d) temperature (25 – 65 ℃) vs pollutant concentration (5 – 20 mg L^{-1}). 118

Figure 8.10: Adsorbed amounts of EFV and NVP at an initial concentration of 10 mg L^{-1}, pH 5, T=25 ℃ and adsorbent loading of 10 g L^{-1}. 120

Figure 8.11: PSO kinetics model for EFV and NVP at an initial concentration of 10 mg L^{-1}, pH 5, T=25 ℃ and adsorbent loading of 10 g L^{-1}. 121

Figure 8.12: Intra-particle diffusion plots for EFV and NVP at an initial concentration of 10 mg L^{-1}, pH 5, T=25 ℃ and an adsorbent loading of 10 g L^{-1}. 122

Figure 8.13: Equilibrium adsorption isotherms (a) EFV and (b) NVP at various concentrations, pH 5 and T=25 ℃ and an adsorbent loading of 10 g L^{-1}.....123

Figure 8.14: (a) Recycling and reusability of CLDH for adsorption of EFV and NVP, (b) XRD plots of recalcined LDH material (initial concentration of 10 mg L^{-1}, pH 5 and T=25 ℃ and an adsorbent loading of 10 g L^{-1}). 128

Figure 8.15: Adsorption configuration of the (a) NVP and (b) EFV on the CLDH through classical simulation. 129

Figure 8.16: Non-covalent interaction analysis of (a) NVP and (b) EFV on the CLDH..... 131

LIST OF TABLES

Table 2.1: Approved antiretroviral drugs in the USA and Europe (De Clercq, 2009) 14

Table 2.2: Approved fixed dose combinations 16

Table 2.3: Global HIV Data (van Schalkwyk, *et al.*, 2024)..... 18

Table 2.4: Regional HIV Data (van Schalkwyk, *et al.*, 2024) 19

Table 2.5: Detected ARVDs and their concentrations in various waterbodies (Zitha *et al.*, 2022) 23

Table 2.6: Selected ARVDs and their Adverse Effects (Hawkins, 2010) 29

Table 2.7: Synthetic adsorbents that have been studied for removal of ARVDs 33

Table 2.8: Physical and chemical data for efavirenz and nevirapine..... 35

Table 2.9: Phenol's chemical and physical data 40

Table 3.1: Experimental runs and the corresponding degradation efficiencies for EFV and NVP 62

Table 3.2: Experimental runs and the corresponding adsorption efficiencies for EFV and NVP 66

Table 5.1: Apparent rate constant, half-life, and linearisation coefficient for the Langmuir-Hinshelwood model at various concentrations 83

Table 5.2**:** Quantitative XRD analysis of the photocatalyst composite used in each test run . 86

Table 6.1: Analysis of variance for the quadratic model (efavirenz) 90

Table 6.2: Analysis of variance for the quadratic model (nevirapine) 91

Table 6.3*:* Photocatalytic degradation kinetics parameters 93

Table 6.4*:* Comparison of nevirapine photocatalytic degradation kinetics parameters..... 94

Table 7.1: Mathematical modelling parameters for photocatalytic degradation of NVP with varying number of light sources 100

Table 7.2: Photocatalytic degradation kinetics parameters (flowrate 10 mL min^{-1}, photocatalyst loading of 3 g L^{-1} and neutral pH) 105

Table 8.1: Analysis of variance for the quadratic model (EFV)..... 114

Table 8.2: Analysis of variance for the quadratic model (NVP) 115

Table 8.3: PSO kinetic models' parameters (initial concentration of 10 mg L^{-1}, pH 5, T=25 °C and adsorbent loading of 10 g L^{-1}) 120

Table 8.4: Adsorption equilibrium isotherms parameters (pH 5, T=25 °C and an adsorbent loading of 10 g L^{-1})..... 124

Table 8.5: Thermodynamics parameters for EFV and NVP adsorption onto CLDH..... 126

Table 8.6: Phase quantification of regenerated CLDH..... 127

Table 8.7: Classical simulations for the adsorption of NVP and EFV on the CLDH showing the adsorption energies, total energies, and the average closest distance of the adsorbate from the substrate. 129

LIST OF ACRONYMS

AIDS:	Acquired Immunodeficiency Syndrome
ANOVA:	Analysis of Variance
AOP:	Advanced Oxidation Process
ART:	Antiretroviral Therapy
ARVD:	Antiretroviral Drug
AZT:	Azidothymidine
BET:	Brunauer-Emmet-Teller
CB:	Conduction Band
CLDH:	Calcined Layered Double Hydroxide
EFV:	Efavirenz
EIA:	Environmental Impact Assessment
EP:	Emerging Pollutants
FTIR:	Fourier transform infrared
GC-MS:	Gas Chromatography coupled with Mass Spectrometry
GP:	Gauteng Province
HAADG-STEM:	High Angle Annular Dark-Field Scanning Transmission Electron Microscopy
HAART:	Highly Active Antiretroviral Therapy
HIV:	Human Immuno Virus
HPLC:	High Performance Liquid Chromatography
KZN:	KwaZulu Natal
LC-MS:	Liquid Chromatography coupled with Mass Spectrometry
LDH:	Layered Double Hydroxide
MIP:	Molecularly Imprinted Polymers
MMO:	Mixed Metal Oxide
NBG:	Narrow Band Gap
NCI:	Non-Covalent Interactions
NNRTI:	Non- Nucleoside Reverse Transcriptase Inhibitor
NP:	Nano Particles
NRTI:	Nucleoside Reverse Transcriptase Inhibitor
NVP:	Nevirapine
PEC:	Predicted Environmental Concentration

PFO:	Pseudo-First Order
PI:	Protease Inhibitors
PNEC:	Predicted No Effect Concentration
PSO:	Pseudo-Second Order
RSM:	Response Surface Modelling
SEM:	Scanning electron microscopy
SPE:	Solid Phase Extraction
SPR:	Surface Plasmon Resonance
TEM:	Transmission Electron Microscope
TGA:	Thermogravimetric Analyser
US FDA:	United States Food and Drug Administration
USEPA:	United States Environmental Protection Agency
UV:	Ultraviolet
VB:	Valence Band
VMD:	Visual Molecular Dynamics
WHO:	World Health Organisation
WWTP:	Wastewater Treatment Plant
XPS:	X-Ray photoelectron spectroscopy
XRD:	X-Ray Diffraction

LIST OF SYMBOLS

λ	Wavelength (Å)
θ	Angle of incidence (°)
β	Line broadening at half maximum (FWHM) of the diffraction peak (°)
C_{cat}	Catalyst loading (g L^{-1})
C_e	Equilibrium concentration of adsorbate (mg L^{-1})
C_0	Equilibrium concentration of adsorbate (mg L^{-1})
C_t	Pollutant concentration at time t (mg L^{-1})
C	Layer thickness (Å)
d_{003}	Layer distance at plane (003) (Å)
$E_{sorbate}$	Isolate energy of sorbate (Kcal mol^{-1})
$E_{substrate}$	Isolated energy of the substrate (Kcal mol^{-1})
$\Delta G°$	Change in Gibbs free energy (kJ mol^{-1})
$\Delta H°$	Change in enthalpy (kJ mol^{-1})
K	Pseudo first order rate constant (h^{-1})
K_2	Pseudo second order rate constant (g mg^{-1} h^{-1}
K_F	Freundlich equilibrium constant (L mg^{-1})
K_L	Langmuir equilibrium constant (L mg^{-1})
L_{003}	Crystallite size in the direction parallel to plane (003) (Å)
MM_{ads}	Molar mass of adsorbate (g mol^{-1})
N	Order of the spectrum (dimensionless)
n	Adsorption intensity
q_e	Equilibrium adsorption capacity (mg g^{-1})
q_m	Maximum adsorption capacity (mg g^{-1})
q_t	Adsorption capacity at time t (mg g^{-1})
r	Rate of the reaction (mg L^{-1} h^{-1})
R	Universal gas constant (8.314 J mol^{-1} K^{-1})
$\Delta S°$	Change in entropy (kJ mol^{-1} K^{-1})
t	Time (min or h)
T	Temperature (°C or K)
V	Reaction vessel volume (L)
W	mass of catalyst

PUBLICATIONS

Peer Reviewed Articles from PhD Work

1. Tabana, L.S., Adekoya, G.J. and Tichapondwa, S.M., 2024. Integrated study of antiretroviral drug adsorption onto calcined layered double hydroxide clay: experimental and computational analysis. *Environmental Science and Pollution Research*, pp.1-19. https://doi.org/10.1007/s11356-024-33406-7.

2. Tabana, L., Booysens, D.R. and Tichapondwa, S., 2023. Photocatalytic Degradation of Efavirenz and Nevirapine using Visible Light-Activated Ag-AgBr-LDH Nanocomposite Catalyst. *Journal of Photochemistry and Photobiology A: Chemistry*, 444, p.114997, https://doi.org/10.1016/j.jphotochem.2023.114997.

3. Tabana, L.S. and Tichapondwa, S.M., 2023. Photocatalytic Degradation of Phenol using Visible light Activated Ag-AgBr-Hydrotalcite Composite. *Chemical Engineering Transactions*, 99, pp.259-264, DOI:10.3303/CET2399044.

4. Tabana L.S. and Tichapondwa S.M., Removal of Antiretroviral Drugs from Wastewater using Continuous flow Photocatalysis, *Brazilian Journal of Chemical Engineering, under review.*

Other Related Publications

5. Tabana, L.S., Kupa, A.R. and Tichapondwa, S.M., 2025. Adsorption of Hexavalent Chromium from Wastewater using Magnetic Biochar Derived from Peanut Hulls, *Physics and Chemistry of the Earth, Parts A/B/C*, 103815, doi.org/10.1016/j.pce.2024.103815.

Conference Presentations

1. Tabana, L.S. and Tichapondwa, S.M., Photocatalytic Degradation of Phenol using Visible light Activated Ag-AgBr-Hydrotalcite Composite, 16th International Conference on Chemical and Process Engineering (ICHEAP16), 21 – 24 May 2023, Naples, Italy, Oral presentation.

2. Tabana, L.S., Kupa, A.R. and Tichapondwa, S.M., *Adsorption of Hexavalent Chromium from Wastewater using Magnetic Biochar Derived from Peanut Hulls*, 24th WaterNet/WARFSA/GWP-SA Symposium, 25 – 27 October 2023, Zanzibar, United Republic of Tanzania, Oral presentation.

CHAPTER 1: INTRODUCTION

1.1 Background

Human Immunodeficiency Virus (HIV) infections represent the primary aetiology of Acquired Immune Deficiency Syndrome (AIDS), a condition of substantial global significance (Piot *et al*., 2001). The detection of AIDS traces back to the early 1980s, marking a pivotal milestone in medical history (Mahy *et al*., 2021). Initial observations indicated a dire prognosis, with all diagnosed individuals succumbing to the disease within a brief period of two years (Mahy *et al*., 2021). During this period, HIV/AIDS emerged as a leading cause of mortality in numerous nations, as supported by studies conducted by various authors (De Cock & Weiss, 2000). The approach to dealing with this potent disease saw a significant shift in the mid-1990s with the introduction of antiretroviral drugs (ARVDs) (Azu, 2012, Broder, 2010). The introduction of these medications signalled a new era in the field of HIV/AIDS treatment, instilling hope in those confronted with the grim future associated with the disease. Zidovudine, also known as azidothymidine (AZT), marked the beginning of antiretroviral treatment by gaining approval from the United States Food and Drug Administration (US FDA) in the year 1987, thus establishing the foundation for future progressions in HIV/AIDS pharmacotherapy (Broder, 2010). The subsequent approvals of didanosine in 1991 and zalcitabine in 1992 broadened the therapeutic armamentarium accessible to healthcare practitioners. These early approvals set the stage for a continuous progression of ARV development.

The study by Moyo *et al*. (2023) reported that, by 2022, more than two-thirds of the world's new HIV infections were from the Southern African region. This region is recognized as the epicenter of the HIV/AIDS pandemic, exhibiting the highest utilization of ARVDs. However, this widespread usage raises apprehensions regarding potential environmental contamination, particularly in water bodies, primarily attributable to deficient waste management practice. South Africa, Botswana, Eswatini, Namibia, Zambia, and Zimbabwe report prevalence rates ranging from 15% to 36% of the population (Adeola & Forbes, 2022). Recent estimates by Schoeman *et al*.(2017) indicate that a single patient requires approximately 990 mg per day of ARVD combination therapy which includes EFV and NVP. Since the rate of ARVD consumption, based on epidemiological statistics of various African countries, is relatively uncertain, it is difficult to precisely estimate the quantity of ARVDs consumed on the continent over time (aus der Beek, 2016). To put this into perspective, recent estimates in South Africa indicate that 7 million individuals may be HIV-positive. According to a report by the World

Health Organization, more than 70% of AIDS patients were receiving antiretroviral therapy; this suggests that the daily consumption of ARVDs is approximately 5.2 tons, or 1,898 tons annually. The excretion of ARVDs and their associated metabolites differs between compounds. Significant proportions of EFV and NVP are metabolised in the liver and eliminated via the kidneys, while small amounts are eliminated via urine and faeces (Thorp, 2008). EFV and NVP are excreted unchanged in urine at rates of 14 and 5%, respectively, in single doses (Cristofeletti *et al*., 2013). Assuming a typical excretion rate of 30% of ingested ARVDs reports to sewage via urine and faeces, it is estimated that 569 tons of drugs could reach South Africa's aquatic systems annually.

ARVD pollution in water bodies can also arise from the improper disposal of unused or expired medications (Zitha *et al*., 2022; Madikizela *et al*., 2020). Inadequate disposal methods, such as flushing unused drugs down toilets or drains, can instigate the introduction of ARVDs into wastewater systems, traversing into natural water bodies through sewage discharge. Furthermore, the leakage of septic tanks and underground sewage pipes poses a notable risk of ARVD contamination in water bodies, as leaks or ruptures in these systems can liberate ARVDs into the surrounding soil and groundwater, thereby contaminating proximate surface water sources. Additionally, runoff from landfills where pharmaceutical waste is ineffectively disposed-off can contribute to the proliferation of ARVDs in water bodies (Madikizela *et al*., 2022, Okoro *et al*., 2022). Rainwater can facilitate the transport of dissolved or suspended ARVD residues from landfill sites into nearby streams, rivers, or lakes, thereby jeopardising water quality and potentially endangering aquatic ecosystems and human health. Domestic and sewage waste disposal methods play a crucial role in contaminating of water bodies with ARVDs. When wastewater effluent is released into rivers or coastal areas without adequate treatment, it can become a reservoir for ARVD residues that persist in the environment and accumulate over time. Moreover, the manufacturing of ARVDs and the management of pharmaceutical manufacturing byproducts can intensify the pollution of aquatic environments with active pharmaceutical components.

In addition to ARVDs, phenolic compounds represent another class of pollutants that pose significant environmental risks. These compounds are extensively utilised across various industries, including paper production (Oshima *et al*., 2020), wood processing (Joseph *et al.*, 2024), coal gasification (Guo *et al*., 2019), textile (Afonso *et al*., 2023), resin manufacturing (Asim *et al*., 2018), and agro-industrial operations (Boher *et al*., 2023). Inadequate waste

disposal techniques and accidental leaks commonly result in their introduction into aquatic ecosystems, where they remain due to their hazardous and resilient nature. The environmental challenges posed by phenolic compounds, alongside ARVDs, highlight the pressing need for comprehensive and adaptable remediation strategies to address persistent organic pollutants and safeguard aquatic ecosystems and public health.

1.2 Problem Statement

Highly active antiretroviral therapy (HAART), commonly known as combination therapy or antiretroviral therapy (ART), is a therapeutic regimen for HIV/AIDS that involves the simultaneous administration of multiple antiretroviral medications. Its main goal is to prevent the spread of HIV in the body, reducing the viral load to undetectable levels and slowing down the progression of the disease (Yen *et al*., 2004, Brechtl *et al*., 2001). Despite its effectiveness in bolstering the immune systems of individuals with HIV/AIDS and preventing physical symptoms, HAART is linked to several adverse effects. These adverse effects may impede treatment adherence and increase the risk of drug resistance. ARVDs toxicity reviews have identified a spectrum of adverse effects, with certain ARVDs demonstrating particularly severe cases. Protease inhibitors (PIs) such as ritonavir, lopinavir and atazanavir are commonly linked to gastrointestinal side effects and insulin resistance. Furthermore, certain ARVDs such as ritonavir and amprenavir are associated with sensory neurotoxic effects and skin rashes, respectively (Hawkins, 2010). Nucleoside reverse transcriptase inhibitors (NRTIs) that include zidovudine, lamivudine and tenofovir, and non-nucleoside reverse transcriptase inhibitors (NNRTIs) such as efavirenz (EFV) and nevirapine (NVP) typically cause side effects in the peripheral and central nervous systems, respectively, with mitochondrial toxicity and renal dysfunction being notable adverse effects. Additionally, cardiovascular hazards have been associated with certain PIs and NRTIs (Hatleberg *et al*., 2021). Aquatic species are increasingly at risk due to the prevalence of ARVDs in the environment, posing significant threats to aquatic ecosystems and food sources. Studies conducted by Akenga *et al*. (2021) have revealed that these ARVDs can be absorbed by plants, especially lettuce, suggesting potential unintentional exposure of animals and humans to ARVDs through contaminated crops. Furthermore, studies performed by Fernández *et al.* (2022) and Kowlaser *et al*. (2022) have demonstrated the adverse consequences of EFV and NVP on aquatic organisms such as *Rhinella arenarum* tadpoles and *Oreochromis*, respectively. The bioactivity of emerging pollutants (EPs) at minimal concentrations, coupled with the risk of unintended exposure to non-target species

from inadequate pharmaceutical disposal and prospective contamination of potable water sources, mandates prompt intervention to mitigate these issues.

The presence of phenol in aquatic ecosystems represents a significant health hazard, as the consumption of water polluted with phenolic compounds has been correlated with protein degradation, tissue death, paralysis of the central nervous system, and damage to critical organs like the kidneys, liver, and pancreas (Geyikci & Coruh, 2013). To address these threats, the World Health Organization (WHO) prescribes a maximum allowable level of 1 mg/L for phenolic chemicals in potable water (WHO, 1996). Moreover, the United States Environmental Protection Agency (USEPA) enforces strict guidelines, demanding that phenol levels in effluent be curtailed to below 1 mg/L to safeguard both public health and the ecological environment (Anku, Mamo & Govender, 2017).

Various methods can be utilised to tackle the presence of ARVDs and other organic pollutants in aquatic environments, such as degradation, adsorption, phytoremediation, and biological processes. The importance of wastewater treatment plants (WWTPs) in collecting and remediating pollutants is well known; however, incomplete pollutant removal may result in the discharge of organics and pharmaceuticals into the ecosystem. The increased detection of ARVDs and other pharmaceuticals in aquatic systems has led to their classification as EPs. EFV and NVP were discovered to be among the ARVDs that are persistent in waterbodies (Adeola & Forbes, 2022, Zitha et al., 2022, Abafe et al., 2018). Studies by multiple researchers have reported influent WWTP concentrations of up to 34,000 ng/L and effluent concentrations as high as 33,000 ng/L. These values indicate that conventional WWTPs that typically rely on technologies such as activated sludge treatment, are ineffective in removing ARVDs. Even at low concentrations, ecotoxicological and human assessment studies have revealed the potential long-term toxicity of these compounds. The dangers posed by ARVDs to non-target species have prompted the monitoring and remediation of their presence in waterbodies (Mahaye & Musee, 2022, Souza *et al*., 2022, Abafe *et al*., 2018), particularly in nations with a substantial population on ART. Advanced oxidation processes (AOPs) are preferred for the removal of recalcitrant pollutants in wastewater due to their ability to generate highly reactive and non-selective free radicals, which are capable of completely mineralizing organic pollutants. Although several AOPs exist, heterogeneous photocatalysis is regarded as one of the most viable processes due to its capacity to achieve greater degradation efficiencies, eco-friendliness, and ease of operation. Adsorption-based processes are also favoured in the

treatment of ARVDs in wastewater due to their simplicity, low energy requirements, cost-effectiveness, reduced sludge formation, and the feasibility of regenerating and reusing adsorbents (Capra *et al*., 2018, Yin *et al*., 2016).

Layered double hydroxides (LDHs) are some of the materials that have attracted attention as photocatalysts and adsorbents for the remediation of various organic pollutants (Jothivenkatachalam & Pandikumar, 2019). This is due to their attractive physicochemical properties including flexible compositions and structures, as well as higher specific areas (Naseem *et al*., 2019). As photocatalysts, ternary LDHs have been reported to perform better than binary LDHs when applied in water remediation processes. This is due to the additional metal constituent which enhances the material's physical and chemical features, and ultimately its efficacy in water remediation processes. Valente *et al*. (2009) reported that a Mg-Zn-Al LDH was 10 times more effective than Mg-Al LDH in degrading phenol and 2,4- dichlorophenoxyacetic acid under ultraviolet (UV) light irradiation. They attributed this to the presence of photoactive Zn metal in the photocatalyst's composition. The amount of Zn in LDH was controlled at a molar concentration of 5% as it presented a higher specific area than photocatalysts with elevated Zn content. A separate study by Kim *et al*. (2017) revealed that adding cobalt to a Zn- Al LDH doubled the performance of the photocatalyst in degrading methyl orange from wastewater.

Although extensive research has been conducted on the photocatalytic properties of LDHs, their effectiveness is usually confined to the UV region of the electromagnetic spectrum, which comprises only a small portion (4% – 5%) of the solar spectrum (Diffey, 2002). This limitation is due to their large bandgap energy, that inhibits their ability to absorb visible light, which has a lower energy than UV light. Sherryna and Tahir (2022) and Ng *et al*. (2021) reported that LDHs possess bandgap energies ranging from 4 – 5 eV. This property restricts their light absorption capabilities to shorter wavelengths than 300 nm, that is in the UV region. As a result, their efficiency as photocatalysts for visible light-induced reactions is compromised, as they are unable to absorb visible light with wavelengths between 400 and 700 nm. Numerous studies have been conducted to improve the photocatalytic activity of LDHs under visible light irradiation, including doping them with transition metal ions (Kim *et al*., 2017; Valente *et al*., 2009) and modifying the interlayer anions of LDHs to alter their electronic structure and bandgap energy (Liu *et al*., 2019). In addition, LDHs can be paired with materials that possess narrower bandgaps, such as carbon nitride (Luo *et al*., 2017), to create hybrid materials that

can efficiently absorb visible light and facilitate photocatalytic reactions (Wu *et al*., 2018). Another approach involves doping LDHs with materials that are effective in absorbing visible light, such as silver halides, to enhance their photocatalytic activity under visible light irradiation (Zheng *et al*., 2022).

Nano-photocatalysts comprising of silver-silver halide (Ag-AgX) have garnered significant attention owing to their exceptional photocatalytic properties. This attention can be attributed to the silver nanoparticles' enhanced light absorption efficiency, making them an essential component in various photocatalytic nanocomposite materials. However, these halides have limitations such as susceptibility to high rates of electron-hole pair recombination and photo-corrosion. Huang *et al*. (2022) and Weng *et al*. (2019) reported that coupling Ag-AgX with robust materials can make these shortfalls less significant. LDHs, when combined with Ag-AgX, can significantly improve photocatalytic performance by tackling stability issues and preventing electron-hole pair recombination. This is accomplished by providing a robust structural support that prevents the aggregation of nanoparticles and acts as a protective barrier against photo corrosion. Furthermore, LDHs can capture and immobilise silver ions, thereby decreasing AgX dissolution and boosting overall stability of the photo-composite. Additionally, the heterojunction formed between Ag-AgX and LDH can facilitates efficient charge separation, extending charge carrier lifetimes and reducing recombination rates.

In addition to their photocatalytic capabilities, LDHs can also exhibit multidimensional adsorption mechanisms that include anion exchange, surface adsorption, memory effect, and adsolubilisation (Tabana *et al*., 2020). Studies by Jie *et al*. (2022), Kazeem *et al*. (2019), and Li *et al.* (2017) have shown that the performance of ternary LDHs surpasses that of binary LDHs when employed in adsorption processes. This is due to their improved physicochemical properties, such as enhanced thermal stability, presence of basic sites, and increased surface area resulting from the synergistic effect between the two metals.

1.3 Hypothesis

The versatility of LDHs makes them suitable for modification to be used in water remediation applications, serving a dual purpose as photocatalysts and adsorbents. When utilised as a photocatalyst, LDHs collaborative integration with less robust materials that exhibit significant absorption of visible light results in composite catalysts that are characterised by increased effectiveness and improved stability compared to the individual components. Furthermore,

LDHs ability to transform into mixed metal oxides (MMOs) through thermal treatment, along with their capability to undergo reconstruction when in contact with aqueous solutions, enhances their effectiveness as an adsorbent for water remediation purposes.

1.4 Aims and Objectives

The primary aim of this research was to assess the effectiveness of a modified LDH as a photocatalyst in removing phenol and ARVDs under visible light exposure, and to evaluate its adsorption capacity for ARVDs. Specific objectives were to develop and characterise a composite photocatalyst consisting of LDH, silver (Ag) and silver bromide (AgBr), while determining the optimal Ag composition in the photocatalyst. The investigation was carried out to investigate the effects of pH, photocatalyst loading, and initial pollutant concentration on the photodegradation of phenol, including the examination of reaction kinetics, scavenger effects, degradation mechanisms, and the recyclability of the photocatalyst. The interactions between pH, photocatalyst loading, and initial pollutant concentration in removing of ARVDs (EFV and NVP) were evaluated using experimental design software. Subsequently, the degradation kinetics and mechanisms were elucidated based on the experimental findings. Moreover, the investigation explored the application of continuous flow in the photodegradation of ARVDs, examining the impact of flow rate, initial concentration, and photocatalyst loading. Additionally, the research involved the synthesis and calcination of LDH material for the purpose of adsorption applications, including an assessment of the physicochemical properties of the adsorbent. Besides, it utilised experimental design software to scrutinise the interrelationships among pH, adsorbent dosage, operating temperature, and initial contaminant levels in the adsorption of ARVDs, utilising experimental design software. Computational analysis was utilised to predict the adsorption mechanism.

1.5 Outline of the Thesis

Chapter 1

Chapter 1 introduces the study by providing background information on the global impact of HIV/AIDS, with a particular focus on the increasing use of highly active antiretroviral therapy (HAART) in Southern Africa. It highlights the environmental concerns surrounding the persistence of ARVDs in aquatic ecosystems, emphasising their contamination of water resources and the limitations of traditional water treatment methods. The problem statement discusses the challenges of ARVDs in water bodies, their resistance to conventional treatments, and their ecological and health risks. The hypothesis suggests that advanced oxidation

processes and adsorption techniques could be effective in degrading and removing ARVDs from water. The chapter also outlines the aims and objectives of the research, which focus on evaluating various degradation methods, including photocatalysis, and optimising their application. Finally, the chapter highlights the significance of the study, which lies in its potential to advance sustainable and efficient water treatment technologies, addressing a critical environmental issue while contributing to the broader efforts of safeguarding aquatic ecosystems and public health.

Chapter 2

Literature review conducted for this study is outlined, comprising two segments, each focusing on distinct themes. The first segment examines pollutants, with phenol presented as a model pollutant due to its persistence as an organic contaminant. Additionally, the segment explores emerging pollutants, specifically ARVDs such as EFV and NVP. The second segment focuses on LDH, the material under examination, which is suggested for modification using various techniques to enhance its properties as a photocatalyst and adsorbent. The objective of this chapter is to provide a comprehensive overview of the pollutants under investigation and the material being explored for their removal, supporting the rationale for the study's approach.

Chapter 3

Chapter 3 offers an in-depth overview of the materials and experimental procedures used in the study. This includes detailed descriptions of the methods employed for synthesising and modifying the materials, specifically focusing on LDH material. The chapter also outlines the characterisation techniques used to analyse the physical and chemical properties of the materials, such as X-ray diffraction (XRD), scanning electron microscopy (SEM), and other relevant methods. Additionally, it discusses the analytical techniques employed to assess the effectiveness of the materials in photocatalytic degradation and adsorption processes, with a focus on High-Performance Liquid Chromatography (HPLC) for quantifying pollutant degradation and adsorption efficiency. The objective of this chapter is to ensure a clear understanding of the experimental setup and analytical methods used to validate the study's hypotheses.

Chapter 4

The characterisation results of the composite photocatalyst are presented, including findings from various analytical techniques. These include XRD for identifying the crystal structure,

SEM-EDS for surface morphology and elemental composition analysis, and transmission electron microscopy (TEM) for examining the nanostructure. Additionally, X-ray photoelectron spectroscopy (XPS) is used to analyse surface chemistry, while Brunauer-Emmett-Teller (BET) surface area analysis provides insights into the material's surface properties and porosity. The objective of this section is to offer a comprehensive understanding of the structural and surface characteristics of the composite photocatalyst.

Chapter 5

This section discusses the results and findings related to the visible light-activated degradation of phenol using the silver-silver bromide-LDH nanocomposite photocatalyst under batch reactor conditions. It presents the effectiveness of the photocatalyst in breaking down phenol, highlighting the impact of various experimental parameters such as reaction time, photocatalyst concentration, and initial pH of the solution. The findings also include a discussion on the degradation efficiency, the potential mechanisms involved in the photocatalytic process, and how the presence of silver-silver bromide enhances the photocatalytic activity of LDH. The objective is to demonstrate the potential of this composite material in environmental applications, particularly for the treatment of organic pollutants under visible light irradiation.

Chapter 6

Results and discussion focus on the photocatalytic degradation of EFV and NVP using a visible light-activated Ag-AgBr-LDH nanocomposite catalyst under batch reactor conditions. The efficiency of the photocatalyst in degrading these ARVDs is explored, considering factors such as reaction time, catalyst dosage, and initial pH of the solution. The degradation rates of EFV and NVP are compared, offering insights into the photocatalytic process mechanisms. The objective of this section is to present and discuss the results related to the photocatalytic degradation of EFV and NVP using a visible light-activated Ag-AgBr-LDH nanocomposite catalyst under batch reactor conditions.

Chapter 7

The findings and discussion regarding the removal of ARVDs from wastewater through continuous flow photocatalysis are presented. The analysis focuses on the effectiveness of the Ag-AgBr-LDH nanocomposite catalyst under continuous flow conditions, examining the degradation efficiency of ARVDs and the optimisation of operational parameters. The objective is to assess the performance of the photocatalytic process in removing ARVDs from

wastewater, exploring its feasibility for large-scale applications and the influence of various operational factors on degradation efficiency.

Chapter 8

The results and discussion present an integrated study combining both experimental and computational analyses, focusing on the adsorption of ARVDs onto calcined LDH (CLDH). The study evaluates the efficiency of CLDH as an adsorbent for ARVDs and explores the adsorption mechanisms through experimental data and computational modelling. The objective is to assess the adsorption capacity and mechanisms of ARVD removal using CLDH, highlighting its potential as an effective adsorbent for the treatment of wastewater contaminated with ARVDs.

Chapter 9

The conclusions and recommendations are derived from the collective results presented in Chapters 4 through 8. These chapters collectively cover the photocatalytic degradation of pollutants, including phenol and ARVDs, as well as the adsorption studies using CLDH. Based on the findings, the chapter synthesises key insights into the effectiveness of the silver-silver bromide-hydrotalcite nanocomposite as a photocatalyst, the application of continuous flow photocatalysis for ARVD removal, and the potential of CLDH for adsorbing ARVDs.
The objective is to provide final conclusions on the overall efficacy of the materials and processes explored in the study, while offering recommendations for future research and practical applications in wastewater treatment.

1.6 Significance of the study

This research is of great significance in advancing sustainable water remediation technologies by addressing critical challenges associated with the removal of persistent organic pollutants, such as phenol and ARVDs, from wastewater environments. By capitalising on the exceptional adaptability of LDHs and their modified derivatives as photocatalysts and adsorbents, this study promotes the innovation of advanced composite materials defined by increased stability, performance, and multifunctional features. The integration of LDHs with silver and silver bromide not only improves visible-light absorption but also demonstrates the potential for scalable application through batch and continuous flow systems. Furthermore, the comprehensive investigation into degradation kinetics, adsorption mechanisms, and the role of key parameters such as pH, pollutant concentration, and material loading offer critical insights

for optimising pollutant removal processes. Beyond experimental findings, the incorporation of computational analyses enriches the understanding of adsorption mechanisms at the molecular level, paving the way for targeted material design. Overall, the study provides a scientific foundation for advancing environmental engineering practices and contributes to global efforts to mitigate water pollution through sustainable and efficient remediation solutions.

CHAPTER 2: LITERATURE REVIEW

2.1 Synopsis

This chapter reviews literature to establish the study's foundation. It highlights the prevalence of ARVDs in sub-Saharan Africa, their significance in HIV/AIDS management, and associated environmental issues from water system accumulation. The discussion addresses the fate, transport, and occurrence of ARVDs in wastewater, surface water, and groundwater, focusing on their ecotoxicological risks to humans and aquatic ecosystems. The physicochemical properties of the target ARVDs, EFV and NVP, are examined through parameters like solubility, stability, and hydrophobicity, which influence their environmental behaviour. Similarly, phenol is evaluated as a model pollutant due to its recalcitrant properties and relevance to water contamination studies. Remediation strategies are detailed, including oxidative degradation, adsorption using materials such as activated carbon and biochar, and phytoremediation techniques involving aquatic plants. LDHs are introduced as promising materials for water treatment. Their synthesis methods, including co-precipitation and hydrothermal techniques, are discussed alongside their structural properties, thermal stability, and surface reactivity. The chapter concludes by presenting the integration of LDHs with silver halides, which enhances photocatalytic efficiency under visible light through improved charge separation and extended light absorption, offering a viable solution for ARVD degradation in water systems.

2.2 Antiretroviral Drugs

2.2.1 Background

The emergence of acquired immune deficiency syndrome (AIDS), predominantly instigated by human immunodeficiency virus (HIV) infections, has had a long-lasting effect on the international arena, with implications that extend beyond geographical and cultural confines. The detection of AIDS can be pinpointed to the early 1980s, highlighting a crucial moment in the annals of medicine (Mahy *et al.*, 2021). During its initial manifestation, AIDS raised significant alarm, as those impacted were faced with a sombre outlook, frequently succumbing to death within a limited period of two years (De Cock & Weiss, 2000). Throughout this period, AIDS became increasingly prominent as the leading cause of death in many countries. At a pivotal moment in the fight against this formidable illness, a significant turning point occurred in the mid-1990s with the introduction of ARVDs (Azu, 2012, Broder, 2010). These therapeutic medications signified a substantial transformation in the treatment of AIDS, offering a glimmer

of hope amidst the prevailing darkness. The introduction of zidovudine, more commonly known as azidothymidine (AZT), was approved by the United States Food and Drug Administration (US FDA) in 1987, establishing the foundation for subsequent progress in HIV/AIDS treatment (De Clercq, 2009). Subsequent to this milestone, US FDA endorsements for didanosine in 1991 and zalcitabine a year later broadened the range of treatment choices accessible to healthcare professionals. These initial advancements set the stage for a continuous series of innovations in developing ARVDs. The groundbreaking discoveries of ARVDs played a pivotal role in shaping the development of highly active antiretroviral treatment (HAART) regimens, marking the beginning of a new phase in the treatment of HIV/AIDS. A thorough review of the ARVDs authorised by the US FDA for the treatment of HIV infection, as displayed in Table 2.1, highlights the progressive improvement of pharmaceutical interventions in combating this global health crisis. The approved fixed dose combinations are shown in Table 2.2.

Table 2.1: Approved antiretroviral drugs in the USA and Europe (De Clercq, 2009)

Generic name	**Brand name**	**Manufacturer**	**Year of approval**
Zidovudine	Retrovir	GlaxoSmithkline	1987
Didanosine	Videx (Tablet)	Bristol-Myers Squibb	1991
	Videx EC (Capsule)	Bristol-Myers Squibb	2000
Zalcitabine	Hivid	Hoffmann-La Roche	1992
Stavudine	Zerit	Merck	1994
Lamivudine	Epivir	GlaxoSmithkline	1995
Saquinavir	Invirase (hard gel capsule)	Hoffmann-La Roche	1995
	Fortovase (soft gel capsule)	Hoffmann-La Roche	1997
Ritonavir	Norvir	Abbott Laboratories	1996
Indinavir	Crixivan	Merck	1996
Nevirapine	Viramune	Boehrtinger Ingelheim	1996
Nelfinavir	Viracept	Agouron Pharmaceuticals	1997
Delavirdine	Rescriptor	Pfizer	1998
Efavirenz	Sustiva (USA)	Bristol-Myers Squibb	1998
	Stocrin (Europe)	Merck	1998
Abacavir	Ziagen	GlaxoSmithkline	1999
Amprenavir	Agenerase	GlaxoSmithkline	2000
Lopinavir + ritonavir	Kaletra	Abbott Laboratories	2000

Table 2.1: Approved antiretroviral drugs in the USA and Europe (Continues)

Generic name	**Brand name**	**Manufacturer**	**Year of approval**
Tenofovir disoproxil fumarate	Viread	Gilead Sciences	2003
Enfuvirtide	Fuzeon	Hoffmann-La Roche & Trimeris	2003
Atazanavir	Reyataz	Bristol-Myers Squibb	2003
Emtricitabine	Emtriva	Gilead Sciences	2003
Fosamprenavir	Lexiva (USA)	GlaxoSmithkline	2003
	Telzir (Europe)	GlaxoSmithkline	2003
Tipranavir	Aptivus	Boehringer Ingelheim	2005
Maraviroc	Celsentri	Pfizer	2007
	Selzentry (USA)	Pfizer	2007
Raltegravir	Isentress	Merck & Co., Inc.	2007
Etravirine	Intelence	Tipotec Therapeutics	2008

Table 2.2: Approved fixed dose combinations

Generic name	**Brand name**	**Manufacturer**	**Year of approval**
Lamivudine/Zidovudine	Combivir	GlaxoSmithKline	1997
Abacavir/Lamivudine/Zidovudine	Trizivir	GlaxoSmithKline	2000
Abacavir/Lamivudine	Epzicom (USA)	GlaxoSmithKline	2004
	Kivexa (Europe)	GlaxoSmithKline	2004
Tenofovir/Emtricitabine	Truvuda	Gilead Sciences	2004
Efavirenz/Emtricitabine/Tenofovir	Atripla	Gilead Sciences	2006
Rilpivirine/Emtricitabine/Tenofovir	Complera	Gilead Sciences	2011
Elvitegravir/Cobicistat/Emtricitabine/Tenofovir	Stribild	Gilead Sciences	2012
Abacavir/Dolutegravir/Lamivudine	Triumeq	ViiV Healthcare	2014
Elvitegravir/Cobicistat/Emtricitabine/Tenofovir	Genvoya	Gilead Sciences	2015
Rilpivirine/Emtricitabine/Tenofovir	Odefsey	Gilead Sciences	2016
Bictegravir/Emtricitabine/Tenofovir	Biktarvy	Gilead Sciences	2018

2.2.2 HIV/AIDS in sub-Saharan Region

2.2.2.1 Prevalence of HIV/AIDS in sub-Saharan region

The sub-Saharan region has become the focal point of the global HIV/AIDS pandemic, contending with an unequal share of the disease. Recent data indicates that by 2022, this region represented more than two-thirds of the world's new infections and observed over 70% of AIDS-related fatalities (Moyo *et al*., 2023). The intricate web of elements influencing the prevalence of HIV/AIDS in sub-Saharan Africa highlights the region's susceptibility to the outbreak. One crucial element is the genetic variation of HIV strains prevalent in the region (Perrin *et al*., 2003). The existence of diverse viral subtypes creates obstacles to devising effective prevention measures and therapies customised to the particular genetic composition of the virus. Furthermore, the economic landscape characterised by financial inequality and widespread poverty worsens the spread of HIV/AIDS (Masanjala, 2007; Mbirimtengerenji, 2007). Individuals living in marginalised societies encounter increased vulnerability due to restricted access to vital healthcare, education, and economic prospects (Deuchert & Brody, 2006, Coovadia & Hadingham, 2005).

The elevated prevalence of sexually transmitted infections (STIs) worsens the HIV/AIDS crisis in the region (Quilter *et al*., 2017, Katz *et al*., 2016). Co-infections with other STIs not only heighten the risk of HIV transmission but also complicate efforts related to diagnosis and treatment. Moreover, complex sexual networks and behaviours that are common in sub-Saharan Africa, such as engaging in multiple concurrent sexual partnerships and transactional sex, facilitate the rapid dissemination of the virus within communities (Ramjee & Daniels, 2013, Kenyon *et al*., 2009, Boerma *et al*., 2003). Additionally, the overcrowding observed in prisons acts as a catalyst for the transmission of HIV/AIDS in the region (Jürgens *et al*., 2011). Inadequate healthcare, sanitation, and prevention strategies within correctional facilities contribute to increased transmission rates among incarcerated individuals, thus sustaining the epidemic beyond the prison environment. Despite considerable advancements in HIV/AIDS prevention and treatment, stigma and discrimination continue to pose significant challenges throughout Africa (Kimera *et al*., 2020; Land & Linsk, 2013). The fear of encountering stigma deters individuals from accessing testing, treatment, and support services, perpetuating the cycle of transmission, and hindering advancements in combating the disease.

According to the Joint United Nations Programme on HIV/AIDS (UNAIDS) data presented in Table 2.3 and 2.4, approximately 39 million individuals were living with AIDS globally in

2022, with 25.6 million (66%) of them located in sub-Saharan Africa. By the end of 2022, over 29.8 million (76%) (globally) had access to antiretroviral therapy (ART), a figure more than double the 2010 count of 7.7 million. Notably, the sub-Saharan region accounted for a significant portion of individuals on ART, with over 82% of the affected population receiving treatment. Despite a decrease in new infections, the overall number of people living with HIV has continued to rise. This trend may be attributed to increased testing rates and awareness of HIV statuses, as well as the life-saving effects of ART.

Table 2.3: Global HIV Data (van Schalkwyk, *et al.*, 2024)

Year	**People living with HIV**	**New infections (aged 15 +)**	**AIDS related deaths**
2000	22.6 million	2.8 million	1.7 million
2005	24.5 million	2.5 million	2.0 million
2010	26.7 million	2.1 million	1.3 million
2021	38.7 million	1.4 million	660 000
2022	39.0 million	1.3 million	630 000

Table 2.4: Regional HIV Data (van Schalkwyk, *et al*., 2024)

Location	People Living with HIV	New infections (aged 15 +)	AIDS related deaths	People on ART (%)
Global	39 million	1.2 million	630 000	76
Asia and the Pacific	6.5 million	300 000	150 000	65
Caribbean	330 000	16 000	5 600	68
Eastern and Southern Africa	20.8 million	500 000	260 000	83
Eastern Europe and central Asia	2 million	160 000	48 000	51
Latin America	2.2 million	110 000	27 000	72
Middle East and North Africa	190 000	17 000	53 000	50
Western and central Africa	4.8 million	160 000	120 000	78
Western and central Europe and North America	2.3 million	58 000	13	76

2.2.2.2 ARVDs as a Therapeutic Measure

Efforts aimed at addressing the HIV/AIDS epidemic have prompted various stakeholders such as national governments, non-governmental organisations (NGOs), and global entities to initiate multiple campaigns focused on the dissemination of knowledge and prevention strategies. These endeavours have played a crucial role in enhancing awareness levels and controlling the spread of the disease. Notably, educational initiatives, community engagement schemes, and the provision of accessible healthcare services have been instrumental in enabling individuals to embrace safer behaviours and access timely medical care (Obeagu & Obeagu, 2024, Davis *et al*., 2018, Schwartländer *et al*., 2011). A significant advancement in the fight against HIV/AIDS has been the emergence and widespread availability of ARVDs. These pharmaceuticals serve as a fundamental component in disease management, presenting patients with the possibility of prolonged survival and enhanced quality of life (Yen *et al*., 2004, Brechtl

et al., 2001). Although ARVDs do not eliminate the virus, they effectively inhibit its replication in the body, thereby alleviating symptoms and lowering the likelihood of opportunistic infections.

UNAIDS has established ambitious objectives, such as the 95-95-95 target, to facilitate significant advancements in global endeavours to contain HIV/AIDS (Granich *et al*., 2018). The 95-95-95 goal is designed to guarantee that 95% of individuals with HIV are cognisant of their status, 95% of those with an HIV diagnosis receive consistent ART, and 95% of patients undergoing treatment achieve viral suppression. These initiatives, commonly referred to as ART, involve a variety of antiretroviral medications customised to the distinct requirements and viral load profiles of individual patients (Damulak *et al*., 2021, Hendrickson *et al*., 2018, Granich *et al*., 2012). The efficacy of ARVDs in managing the transmission of HIV/AIDS highlights the crucial significance of accessible and comprehensive healthcare services in enhancing health outcomes and alleviating the disease burden among affected populations.

2.2.3 Sources and Fate of Antiretroviral Drugs in Waterbodies

The Southern African region is being regarded as the focal point of the HIV/AIDS pandemic. This further translates to the region being witnessing the highest consumption of ARVDs. The widespread utilisation of ARVDs brings forth concerns regarding potential environmental pollution, particularly in waterbodies. Over 7 million individuals in South Africa have been diagnosed with HIV/AIDS (Johnson *et al*., 2017). Each patient is anticipated to require approximately 990 mg/day of ARVDs in combination therapy (Schoeman *et al*., 2017). This translates to an estimated daily consumption of over 5.2 tons of ARVDs, amounting to approximately 1,898 tons annually, if 70% of the infected population is on ART. The excretion pathways for ARVDs and their metabolites vary depending on the specific compound. For instance, significant portions of EFV and nevirapine NVP undergo hepatic metabolism and are subsequently excreted via the kidneys, with smaller quantities being eliminated through urine and faeces (Thorp, 2008). EFV and NVP are excreted unchanged in urine at rates of 14% and 5%, respectively, following single doses (Cristofeletti *et al*., 2013). Assuming an average excretion rate of 30% for ARVDs through urine and faeces, it is estimated that approximately 569 tons of these drugs could enter South Africa's aquatic ecosystems annually. Other factors that can cause contamination of waterbodies with ARVDs include improper disposal of unused or expired medications (Madikizela *et al*., 2022; Schoeman *et al*., 2017). Methods such as flushing unused drugs down toilets or drains can introduce ARVDs into wastewater systems,

eventually reaching natural waterbodies through sewage discharge. Furthermore, leaks or ruptures in septic tanks and underground sewage pipes pose a significant risk of ARVD contamination in waterbodies (Adeola & Forbes, 2022). This could potentially release these drugs into the surrounding soil and groundwater, thus compromising nearby surface water sources. Moreover, runoffs from landfills where pharmaceutical waste is ineffectively disposed can contribute to the pollution of waterbodies with ARVDs (Madikizela *et al.*, 2022; Okoro *et al.*, 2022). Rainwater may wash dissolved or suspended ARVD residues from landfill sites into nearby streams, rivers, or lakes, compromising water quality and posing potential risks to aquatic ecosystems and human health. Domestic and sewage waste disposal practises also play a crucial role in ARVD contamination of waterbodies (Kunene & Mahlambi, 2023, Kairigo *et al.*, 2020). Untreated or inadequately treated sewage effluent discharged into rivers or coastal areas may contain residues of ARVDs, which can persist in the environment and accumulate over time.

2.2.3.1 Fate of ARVDs in Wastewater Treatment Plants

Wastewater treatment facilities (WWTPs) play a crucial role in the management of a wide range of pollutants, such as pharmaceutical compounds, prior to their release into the ecosystem. These establishments employ a variety of remediation techniques that can be categorised into three primary classifications: physical, chemical, and biological processes. Physical methods for treating wastewater harness physical processes to eliminate impurities, without incorporating biological or chemical alterations, which include methods like sedimentation and filtration (Bahuguna *et al.*, 2021, Saleh *et al.*, 2020). Chemical approaches are implemented to control the release of pollutants into aquatic environments, frequently in conjunction with physical or biological processes. These processes entail the alteration or elimination of contaminants via chemical processes, such as flocculation and coagulation, oxidation, chemical precipitation, adsorption, and ion exchange (Saleh *et al.*, 2020, Crini and Lichtfouse, 2019)

Biological processes include the elimination of dissolved and suspended organic chemical components *via* biodegradation. In these processes, microorganisms are intentionally introduced in optimal amounts to replicate the natural self-cleaning mechanism (Jain *et al.*, 2022). Microorganisms are responsible for degrading organic substances in wastewater through two primary biological mechanisms: biological oxidation and biosynthesis. During biological oxidation, microorganisms decompose the organic substances, yielding by-products

such as minerals, carbon dioxide, and ammonia (Jain *et al*., 2022, Paillat *et al*., 2005). Recalcitrant compounds that persist in wastewater are discharged with the effluent. Conversely, in biosynthesis, microorganisms use the organic matter to generate fresh microbial cells with substantial biomass, which is subsequently eliminated through sedimentation (Lee & Stuckey, 2022, Zheng *et al*., 2021).

While conventional remediation processes in WWTPs primarily focus on removing carbon-based substances such as carbohydrates, proteins, and lipids; emerging pollutants like ARVDs often escape treatment due to incomplete processes or the ineffectiveness of bioremediation. The limitations of bioremediation can be attributed to several factors, including organic overload or underload, which can disrupt the balance of microbial activity (Patel *et al*., 2022, Sipma *et al*., 2010). The presence of toxic chemicals in the wastewater can inhibit or kill the microorganisms essential for biodegradation (Saeed *et al*., 2022, Subramaniam *et al*., 2020). Additionally, environmental factors such as temperature fluctuations, pH imbalances, and aeration issues can negatively impact microbial performance, further reducing the efficiency of bioremediation (Ojha *et al*., 2021, Luka *et al*., 2018). Moreover, complex organic compounds often resist degradation, making it challenging for the biological treatment processes to fully eliminate these pollutants from the wastewater (Chan *et al*., 2022, Maurya & Raj, 2020).

A study conducted in the KwaZulu Natal province by Mtolo *et al*.(2019) reported the highest concentration of 114 µg L^{-1} for EFV in a WWTP influent. Similarly, the study by Akawa et. al. (2021) reported the highest concentrations of NVP in influent and effluent to be 2.1 µg L^{-1} and 1.72 µg L^{-1}, respectively. Details of concentrations of other ARVDs in various regions are outlined in Table 2.5. It is important to note that due to a scarcity of data from other countries, the presented information is based on South African water bodies (mostly from Gauteng (GP) and KwaZulu Natal (KZN)).

Table 2.5: Detected ARVDs and their concentrations in various waterbodies (Zitha *et al*., 2022)

ARVD	Region	Detected concentration (µg L^{-1})					References
		Influent	Effluent	Surface water	Tap	Groundwater	
Atazanavir	KZN	0.064 – 14	0.074 – 0.3				(Abafe *et al*., 2018)
	KZN	3.1	3				(Späth *et al*., 2021)
Didanosine	GP			0.054			(Wood *et al*., 2015)
	GP				0. 0.0061		(Swanepoel *et al*.)
Efavirenz	GP	17.4	7.1				(Schoeman *et al*., 2015)
	GP	0.550 – 14					(Schoeman *et al*., 2017)
	GP			0.7			(Wooding *et al*., 2017)
	KZN	24 – 34	20 – 33				(Abafe *et al*., 2018)
	KZN	89.8 – 114.4	78.8 – 93.1				(Mtolo *et al*., 2019)
	KZN	0.5	0.3	0.14		0.005	(Rimayi *et al*., 2018)
	GP	0.303	0.213	0.13		0.002	(Rimayi *et al*., 2018)
Emtricitabine	GP			0.36			(Wooding *et al*., 2017)
	KZN	0.3 – 3.1	0.025 – 0.042				(Mlunguza *et al*., 2020)
Lamivudine	KZN			00.242			(Abafe *et al*., 2018)
	KZN	74	130				(Späth *et al*., 2021)
	KZN	0.13	0.84 – 2.2				(Abafe *et al*., 2018)
Lopinavir	GP	1.2 – 2.5	1.9 – 3.8				(Wood *et al*., 2015)
	KZN		0.13	0.283 – 0.305			(Abafe *et al*., 2018)

Table 2.5: Detected ARVDs and their concentrations in various waterbodies (continues)

ARVD	**Region**	**Detected concentration (µg L^{-1})**					**References**
		influent	Effluent	Surface water	Tap	Groundwater	
Nevirapine	GP		0.236	0.13 – 0.294			(Wood *et al*., 2015)
	KZN	0.35	0.35				(Späth *et al*., 2021)
	GP	2.1	0.35				(Schoeman *et al*., 2015)
	GP		0.43	0.0068	0.0035	0.0053	(Swanepoel *et al*., 2015)
	GP	2.1	1.72	5.62			(Akawa *et al*., 2021)
Ritonavir	KZN	1.6 – 3.2	0.46 – 1.5				(Abafe *et al*., 2018)
	GP	0.004 – 0.393	0.0144 – 0.675				(Mhuka *et al*., 2020)
Tenofovir	GP			0.145 – 0.243			(Wood *et al*., 2015)
	KZN	0.1 – 0.25		0.11			(Mlunguza *et al*., 2020)
	GP		0.0016			0.0024	(Swanepoel *et al*., 2015)
Zidovudine	GP		0.453 – 0.627	0.0517 – 0.35	0.0727		(Wood *et al*., 2015)
	KZN	6.9 – 53	0.087 – 0.5				(Abafe *et al*., 2018)
	GP		0.0003	0.0012	0.0019		(Swanepoel *et al*., 2015)

2.2.3.2 Occurrence of ARVDs in Surface Waters

ARVDs are commonly ingested orally and undergo complex metabolic pathways within the human body. After consumption, these substances undergo partial metabolic changes before being excreted through urine or faeces (Jain *et al*., 2013; Lawal *et al*., 2022), and eventually are transported through sanitary sewer systems to wastewater treatment plants. The investigation by Nannou *et al*. (2020) highlighted that ARVDs are primarily excreted in the bioactive state of the initial compound. The role of human metabolism is crucial in determining the overall impact of ARVDs released into the environment. This metabolic process includes specific biotransformation pathways such as sulfoxidation, sulfate conjugation, N-dimethylation, and glucuronidation (Deng *et al*., 2013; Farrukh *et al*., 2024). Sulfoxidation, facilitated by cytochrome P450 oxidases, involves the oxidation of sulfur atoms to sulfoxide functional groups, enhancing solubility for subsequent excretion through urine or bile. Sulfate conjugation, mediated by sulfotransferases, attaches sulfate groups to substrates, increasing their water solubility and facilitating elimination. N-Dimethylation, catalysed by methyltransferases, adds methyl groups to nitrogen atoms within molecules, altering their pharmacological properties and influencing metabolism or excretion. Lastly, glucuronidation, facilitated by UDP-glucuronosyltransferases, involves the attachment of glucuronic acid molecules to substrates, enhancing water solubility and aiding elimination through urine or bile. These metabolic pathways collectively contribute to detoxification and maintain physiological homeostasis by efficiently removing various endogenous and exogenous compounds from the body.

2.2.3.3 The Presence of Antiretroviral Drugs in Groundwater

Groundwater contamination by ARVDs presents a complex challenge influenced by various sources, including landfills, improper disposal practises, and the excretion of these pharmaceuticals. Additionally, pit latrines, which are commonly used in Sub-Saharan Africa, also contribute significantly to this contamination (Gwenzi *et al*., 2023). Despite the acknowledged significance of ARVDs in groundwater, a notable observation arises from the insufficiency of data compared to their extensively documented prevalence in surface waters and WWTPs. The investigations carried out by Rimayi *et al*.(2018) and Wood *et al*.(2015) yielded crucial insights by uncovering the presence of ARVDs, like abacavir, didanosine, efavirenz (EFV), lamivudine, nevirapine (NVP), nelfinavir, saquinavir, stavudine, tenofovir, zalcitabine, and zidovudine, in groundwater.

Significant findings from these investigations revealed that certain ARVDs, like EFV and NVP, are present in groundwater at levels of concern. Notably, the highest documented concentration of EFV in groundwater was 0.005 µg L^{-1} (Rimayi *et al*., 2018), highlighting the necessity for thorough monitoring and assessment of these levels to determine potential risks. Similarly, a concentration of 0.0053 µg L^{-1} (Swanepoel *et al*., 2015) was detected for NVP, highlighting the persistent need for further research and vigilance concerning the presence of ARVDs in groundwater. Comprehensive details regarding the concentrations of various ARVDs in groundwater are displayed in Table 2.5.

2.2.4 Determination of Antiretroviral Drugs in Aqueous Environment Matrices

The quantification of ARVDs in environmental matrices presents challenges due to the intricate composition of the matrices and the complexities associated with detecting them at remarkably low levels. The existence of additional trace pollutants further complicates the quantification process. Methodologies commonly employed in this context include the utilisation of solid-phase extraction (SPE) for sample separation, in conjunction with liquid chromatography-tandem mass spectrometry (LC-MS/MS) for quantification (Mosekiemang *et al*., 2019; Schoeman *et al*., 2017). The utilisation of OASIS HLB cartridges in solid-phase extraction (SPE) has become prominent due to their adaptability and efficacy in accommodating a diverse array of compounds with varying physicochemical properties. Moreover, other solid-phase extraction (SPE) cartridges, such as ENVI-C18, are deemed suitable to fulfil this objective (Semreen *et al*., 2019; Togola & Budzinski, 2007). Although direct injection into liquid chromatography-mass spectrometry (LC-MS) systems enhances efficiency, the absence of preconcentration may pose challenges, especially in scenarios involving pollutants with concentrations below the detection limit, which is typically 0.1 – 1.5 ng L^{-1} for LC. Gas chromatography-mass spectrometry (GC-MS) methodologies are not extensively utilized in examining ARVDs. Kahilu *et al*. (2022) and Schoeman *et al*. (2015) have contributed to this field by utilising gas chromatography with time-of-flight mass spectrometry (GC-GC-TOFMS) as their selected analytical technique.

2.2.5 Ecotoxicological studies for Antiretroviral Drugs

ARVDs have been studied for their implications on aquatic environments, employing an array of ecotoxicological and human health risk evaluations. These evaluations incorporate parameters such as predicted environmental concentration (PEC) and predicted no effect concentration (PNEC). PEC evaluates the concentration of a substance in the environment by

considering its release, behaviour, transformation, and elimination through biological or chemical mechanisms (Zhang *et al*., 2017). The fate and modification procedures are influenced by physicochemical traits like pKa and Kow values, with the initial discharge being tied to data on consumption and excretion. PNEC represents the level at which the substance is anticipated to pose no harm to organisms, based on ecotoxicity details (Zhang *et al*., 2017). Predicted critical environmental concentration (CEC) is occasionally employed instead of PNEC. The Risk Quotient (RQ), derived from the ratio of PEC to PNEC, serves as a tool for forecasting pharmaceutical environmental hazards (Mheidli *et al*., 2022). RQ values below 0.1 suggest minimal risk, RQ values ranging from 0.1 to 10 indicate moderate risk, and RQ values exceeding 10 signify high risk. However, these ratios are specific to the site and reliant on dosage levels, limiting their ability to forecast the overall toxicity of a particular ARVD at a global scale.

The prediction accuracy depends on the data related to prescription and consumption, where prescription data is biased by presuming all prescribed medications are consumed. The inflexibility of this approach overlooks the possibility of degradation products, which could pose more significant risks than the original compounds (Rogowska *et al*., 2020, Jain *et al*., 2013). Moreover, the methodology is based on average annual consumption figures, disregarding variations stemming from migration-related demographic shifts. Monitoring strategies can benefit from utilising PEC/PNEC values tailored to an ARVD sink on an institutional level. Although predictive screening offers advantages like focused detection, decreased workload, and cost efficiency, it is advisable to complement it with regular monitoring. This is due to empirical findings indicating that certain ARVDs might elude random scrutiny. Predictive models are fundamental in examining of ARVDs presence, specifically in the effluents of WWTPs and medical facilities.

2.2.5.1 Human Risk Effects

Despite its efficacy in enhancing the immune systems of individuals living with HIV/AIDS and preventing the physical symptoms of the infection, HAART has a variety of adverse effects that could impede adherence to treatment, possibly resulting in drug resistance (Hawkins, 2010; Spire *et al*., 2002). ARVDs toxicity reviews have identified a range of adverse effects, with certain ARVDs demonstrating particularly severe cases. Table 2.6 shows some of the Protease inhibitors (PIs) that are frequently associated with gastrointestinal tract side effects such as diarrhoea, nausea, and vomiting. Ritonavir, which is used as a booster in ART, has been related

to sensory neurotoxic effects like paraesthesia and altered taste sensations. Nucleoside reverse transcriptase inhibitors (NRTIs) and non-nucleoside reverse transcriptase inhibitors (NNRTIs) generally cause side effects in the peripheral and central nervous systems, respectively. Peripheral neuropathy is prevalent with NRTIs due to the suppression of mitochondrial DNA polymerase, which results in mitochondrial toxicity. Zidovudine and stavudine, among other NRTIs, have been associated with mitochondrial myopathy and lactic acidosis. Tenofovir is associated with renal dysfunction while didanosine is said to be causing pancreatitis and emtricitabine frequently cause renal dysfunction. NNRTIs, such as EFV and NVP, have been linked to hepatotoxicity and rash, with EFV being particularly hazardous to the central nervous system, producing dizziness, drowsiness, odd dreams, hallucinations, suicidality, anxiety, and reduced attention.

Table 2.6: Selected ARVDs and their Adverse Effects (Hawkins, 2010)

ARVD	Abbrevation	Most common adverse effects
Nucleoside reverse transcriptase inhibitors (NRTIs)		
Zidovudine	AZT	Nausea, headache, rash, anemia, leukopenia, elevation of liver enzyme levels, elevation of lactic acid level, lactic acidosis, mitochondrial myopathy
Lamivudine	3TC	Neutropenia (rare), lactic acidosis, mitochondrial myopathy
Didanosine	ddl	Gastrointestinal intolerance, pancreatitis, gout, reversible peripheral neuropathy
Tenofovir	TDF	Gastrointestinal upset, low phosphate
Non-nucleoside reverse transcriptase inhibitors (NRTIs		
Nevirapine	NVP	Rash, elevation of liver enzyme levels
Efavirenz	EFV	Central nervous system toxicity (“hangover,” drowsiness), rash
Protease inhibitors		
Ritonavir	RTV	Gastrointestinal upset, diarrhoea, circumoral paraesthesia, elevation of liver enzyme levels, hypertriglyceridemia
Lopinavir	LPV	Gastrointestinal upset

2.2.5.2 Aquatic Species Risk Effects

ARVDs are becoming increasingly prevalent in the environment, posing a substantial risk to aquatic ecosystems and food sources. Akenga *et al*. (2021) reported that ARVDs such as EFV, lamivudine, and NVP can be absorbed by vegetation, particularly lettuce. This suggests that the cultivating of vegetables in contaminated regions may result in animals and humans unintentionally consuming ARVDs. The study established that concentrations of the three ARVDs above 100 µg L^{-1} were harmful to lettuce, resulting in lower root and leaf biomass. The studies by Almeida *et al*. (2021) and Cid *et al*. (2021) provide further details concerning the toxicity of various ARVDs to aquatic species. For example, EFV was shown to be toxic to two aquatic species, with an EC50 value of 26 µg L^{-1} for *Ceriodaphnia dubia* and an IC50 value of 34 µg L^{-1} for *Raphidocelis supcapitata*. The observed concentration levels are consistent with the documented ranges in the effluents of South African WWTPs (Mtolo *et. al.*, 2019). Lamivudine demonstrated a significant ecological hazard with respect to *Cerodaphnia dubia*. Cid *et al*. (2021) investigated the acute and chronic toxicity of atazanavir, NVP, and EFV on embryo-larval development and sea urchin fertilisation (IC50; 42 h; range: 0.52 – 0.97 mg L^{-1}; 1 h; 84.61 mg L^{-1}). However, these concentrations surpass those that are commonly observed in a variety of aquatic environments. Studies by Fernadez et. al. (2020) also shown the adverse effects of abacavir, EFV, and NVP on aquatic species such as *Rhinella arenarum* tadpoles. The morphological development of juvenile Oreochromis was evidently affected when exposed to an EFV concentration of about 2 ng L^{-1}.

2.2.6 Processes for Remediation of Antiretroviral Drugs from Wastewater

ARVDs and other organic pollutants can be removed from water bodies through various remediation methods, including degradation, adsorption, plant absorption, and biological processes. WWTPs provide a critical function in collecting and treating pollutants. However, insufficient removal can lead to the release of pharmaceuticals into the environment. Additionally, the treatment operations may result in the formation of secondary compounds (Wood *et al*., 2016). The persistent presence of pharmaceuticals and their metabolites in the effluents of WWTPs indicates that conventional processes like activated sludge treatment are ineffective at removing these contaminants. Therefore, they require advanced processes such as advanced oxidation processes (AOPs) including photocatalysis, membrane filtration, and adsorption techniques to effectively remove these recalcitrant pollutants.

2.2.6.1 Degradation

The degradation of ARVDs in aquatic environments has predominantly been examined through the utilisation of AOPs, with a specific focus on photocatalytic techniques. Bhembe *et al*. (2020) conducted a study on the photocatalytic decomposition of NVP using a heterostructure comprising few-layer black phosphorus combined with niobium (V) oxide nanoflowers (FL-BP@Nb_2O_5). Their research assessed the degradation efficiency of 3% FL-BP@Nb_2O_5 and Nb_2O_5 under varying pH levels, concentrations, and catalyst loadings. Results demonstrated a significant decrease in degradation efficiency at alkaline pH levels, with maximum degradations of 68.5% and 30.3% achieved by 3% FL-BP@Nb2O5 and Nb_2O_5, respectively, in acidic conditions (pH 1 and 3). The study identified seven degradation by-products, including the less harmful compound butanol. Furthermore, the post-treatment of lamivudine, NVP, and zidovudine in municipal wastewater was explored through UV/Cl_2, UV/H_2O_2, and direct UV photolysis methods (Ngumba *et al*., 2020). Zidovudine exhibited a high removal efficiency (>90%) via direct photolysis, while NVP and lamivudine displayed lower efficiencies of 13.4% and 48.1%, respectively. The incorporation of Cl_2 and H_2O_2 augmented the removal efficiency for all substances, with UV/Cl_2 and UV/H_2O_2 processes yielding total removal rates of 20.8% and 52.9% for NVP, and 77.4% and 72.2% for lamivudine, respectively.

A study by Zhou *et al*. (2015) investigated the photodegradation of acyclovir, zidovudine, and lamivudine in various water matrices when subjected to simulated solar irradiation. The rate of zidovudine degradation was found to be higher in neutral and alkaline environments. The photodegradation process of all compounds was enhanced by the presence of nitrate ions, while the photolysis of acyclovir and lamivudine was accelerated by dissolved organic matter. Electrochemical methods built into Fenton's reaction chemistry have also been utilised to degrade organic compounds and pharmaceuticals in water samples (Emeji *et al*., 2021; Hayleeyesus, 2021). These environmentally friendly methods produce hydroxyl (OH•) radicals to breakdown organic molecules. While these technologies have been widely used in European countries, their applicability to ARVD degradation in African contexts is restricted, with possible limitations posed by matrix components that can affect the degradation process.

2.2.6.2 Adsorption

Adsorption is a physically predominant method utilised for removing of contaminants from waterbodies. Several research studies have investigated a variety of adsorbents for removing

pharmaceuticals from water. Both synthetic and natural adsorbents have been investigated for this purpose.

Synthetic Adsorbents

Molecularly imprinted polymers (MIPs) have garnered attention in scientific studies for their ability to remove ARVDs from aquatic environments selectively (Xolo & Mahlambi, 2024; Qwane *et. al*., 2020). These synthetic polymers were synthesised by polymerising monomers to achieve specific recognition of target molecules in diverse aqueous environments (Terzopoulou *et. al*., 2016). Their interactions with a pollutant are determined by covalent or non-covalent binding, as well as the size, shape, and functional group imprints present on the monomer (Mlunguza *et. al*., 2019). A recent application involved using a novel MIP in solid - phase microextraction fibre to extract abacavir from aqueous solutions efficiently (Terzopoulou *et. al*., 2016). The identification capabilities of MIP were notably affected by the pH of the solution, leading to removal rates ranging from 88% to 99% at pH 8. The maximum adsorption capacities recorded were 149 and 167 mg g^{-1} at temperatures of 25 and 45 °C, respectively. In a separate study, an abacavir MIP was formulated to treat of surface water and wastewater, demonstrating a maximum adsorption capacity of 5.98 mg g^{-1} at pH 5 (Qwane *et. al*., 2020). Both investigations indicated that the adsorption processes followed the Freundlich isotherm, suggesting the presence of multiple layers of adsorbate coverage. The limited exploration of MIPs in adsorption studies can be attributed to the challenges associated with large-scale production.

Graphene wool has also been assessed for its effectiveness in selectively removing specific ARVDs from water, such as EFV and NVP (Adeola *et. al*., 2021). Graphene, an allotrope of carbon, is a versatile material utilised in developing adsorbents for organic compound removal from water (Adeola *et. al*., 2021). The removal efficiencies reported for 1 – 20 mg L^{-1} of EFV (80%) and NVP (84%) with graphene-based adsorbents produced through chemical vapor deposition were remarkable. The adsorption process was significantly affected by the pH of the solution with pH 5 being regarded as the optimum. The presence of electron pairs on the nitrogen atom in the pyridine aromatic structure of NVP suggested potential interactions with the adsorbent, leading to higher adsorption efficiency compared to EFV. The involvement of van der Waals forces in the adsorption of ARVDs with graphene-based adsorbents was also proposed. Table 2.7 shows some of the synthetic adsorbents that have been used for removing of EFV and NVP from wastewater.

Table 2.7: Synthetic adsorbents that have been studied for removal of ARVDs

Adsorbent	**Pollutant**	**Adsorption capacity ($mg\ g^{-1}$)**	**Reference**
Activated Macadamia Nutshells	EFV	38.17	(Simelane *et al*., 2024)
	NVP	10.79	
Molecular imprinted Polymer	EFV	1.10	(Xolo & Mahlambi, 2024)
	NVP	2.16	
Graphene wool	EFV	4.41	(Adeola *et al*., 2021)
	NVP	48.31	

Natural Adsorbents

Nanofibers derived from the Mondia whitei root have been utilised to eliminate ARVDs and other pharmaceuticals from both the influents and effluent of WWTPs (Kebede *et al*., 2020). Kedebe *et al*. (2020) study's main aim was to optimise the temperature conditions favourable for the elimination of pharmaceutical substances by utilising a nanofiber adsorbent. The findings suggested that raising the temperature from 25 to 35℃ enhanced the efficacy of elimination. The observed trend revealed that adsorbates displayed minimal kinetic energy at lower temperatures, leading to restricted occupancy of the adsorbent surface, while higher temperatures enabled better adsorption. This approach exhibited comparable tendencies to those recorded with MIPs in the examination of wastewater specimens, with effluent samples displaying increased removal efficiency in comparison to influent samples. The maximum adsorption capacities for the specified drugs were determined in the wastewater effluents: 189.1 mg g^{-1} for NVP, 72.5 mg g^{-1} for didanosine, 72.8 mg g^{-1} for ritonavir, 138.4 mg g^{-1} for EFV, and 150.2 mg g^{-1} for stavudine. Conversely, biochar derived from residues of olives, tomatoes, rice husks, and the African palm tree *Raphia farinifera* displayed decreased efficiencies in the elimination of abacavir, atazanavir, darunavir, lamivudine, nevirapine, and ritonavir (Spath *et. al*., 2021).

2.2.6.3 Phytoremediation

Numerous studies have explored the uptake of pharmaceuticals by plants, with a primary focus on pharmaceuticals across various therapeutic classes rather than ARVDs (Madikizela *et. al*., 2022, Akenga *et. al*., 2021, Rimayi *et. al*., 2018, Bartha *et. al*., 2014). Most of these

investigations utilised hydroponic trials, exposing plant species to specified drug concentrations in solution for a defined duration. These investigations aimed to evaluate human exposure to pharmaceuticals excreted through the ingestion of contaminated plants. Akenga *et al*. (2021) conducted research to assess the absorption of three ARVDs EFV, lamivudine, and NVP by lettuce cultivated in hydroponic settings. The preference for lettuce as the model vegetable was informed by past research that pointed out the substantial absorptive capacity of leafy greens for organic substances (Christou *et. al*., 2019). The findings indicated removal efficiencies of 75% for EFV, 88% for NVP, and 42% for lamivudine for initial concentrations of 100 µg L^{-1} by lettuce. Additionally, studies by Reddy *et. al*. (2021) and Mlunguza *et. al*. (2020) have highlighted the potential application of algae and hyacinth plants in water remediation, respectively.

2.2.7 Physicochemical Properties of Nevirapine and Efavirenz

EFV and NVP, two NNRTIs employed in the treatment of HIV/AIDS, exhibit resemblances in their physicochemical attributes. EFV, usually in solid form, appears as a white to slightly yellow crystalline powder. In contrast, NVP is seen as a white to off-white crystalline powder with a distinctive aroma and a bitter taste. EFV is characterised by its lack of odour and taste. Both medications demonstrate low solubility in water and have melting points ranging around 161 – 196 °C, with a slightly acidic nature. Other physical and chemical attributes of the drugs are displayed in Table 2.8. The detection and quantification of these substances commonly utilise high-performance liquid chromatography (HPLC) in conjunction with UV detection or mass spectrometry (MS) owing to these shared properties.

Table 2.8: Physical and chemical data for efavirenz and nevirapine

Name	Efavirenz	Nevirapine
Molecular formula	$C_{14}H_9ClF_3NO_2$	$C_{15}H_{14}N_4O$
Molecular weight (g mol^{-1})	315.7	266.3
Structure	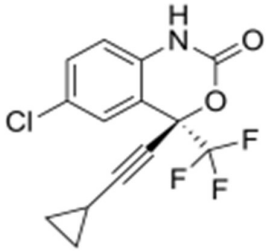	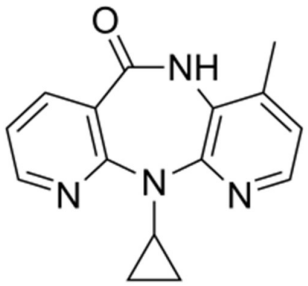
Density (g L^{-1}) at 25 °C	1 500	1 400
Melting point (°C)	161	196 °C
pKa	10.2	2.8
$LogK_{ow}$	4.15	3.89

2.3 Phenols in Waterbodies

2.3.1 Background

Phenol and its derivatives, including Bisphenol A (BPA) and phenolic resins, are substances that can exist in aquatic environments due to a range of factors. A pivotal point to consider is the extensive use of these substances in industrial operations across various sectors, leading to the potential release into the environment. Notably, facilities involved in the producing of plastics (Oshima *et al*., 2020), resins (Asim *et al*., 2018), adhesives (Yang & Rosentrater, 2020), and coatings (Sabarinathan *et al*., 2022) may release phenolic compounds into wastewater streams during manufacturing or as part of waste management. Additionally, improper practices in the handling, storage, or disposal of items containing phenolic compounds may result in their runoff or seepage into adjacent water bodies. Furthermore, phenolic compounds might find their way into water systems through atmospheric deposition or runoff from agricultural lands where phenol-based pesticides or herbicides are utilised (Boher *et al*., 2023). Once introduced into aquatic environments, phenolic compounds can

endure for prolonged periods and may undergo alterations or breakdown processes, potentially causing harmful impacts on aquatic ecosystems and organisms.

2.3.2 Sources and Fate of Phenols in Waterbodies

Phenolic compounds are widespread in water sources, originating from natural phenomena and anthropogenic activities. The breakdown of organic material from flora and fauna is a crucial contributor to the existence of phenolic compounds, while the metabolic processes in both humans and animals produce phenol, which is subsequently released into the environment. Industries extensively employ phenol in various chemical processes, including alkyl phenols (Afreen & Upadhyayula, 2021), cresols (Weber & Weber, 2010), aniline (Bugosen *et al*., 2020), as well as in the manufacturing of textiles (Afonso *et al*., 2023), explosives (Chikhradze *et al*., 2017), and dyes (Hanafi & Sapawe, 2020). The release of industrial effluents containing phenol into aquatic environments results in pollution, and vehicular discharges can introduce phenolic compounds into the air, eventually leading to water contamination through precipitation.

In the agricultural domain, the application of insecticides, herbicides, and pesticides introduces phenolic compounds into water systems, which subsequently degrade to produce phenol (Boher *et al*., 2023). The runoff from agricultural practices during irrigation contributes to water pollution. Household activities also play a role in the presence of phenolic compounds, as everyday household items like disinfectants, ointments, antiseptics, and personal care products contain phenols. The drainage of wastewater containing these products results in water contamination. Municipal waste, especially originating from landfill sites and incineration residues, intensifies water pollution with phenolic compounds via leachates. Compounds such as p-cresols, trichlorophenol, tetra butyl phenol, and BPA can leach into water bodies from these sources.

2.3.3 Challenges Associated with Phenols in Aqueous Solutions

Phenol, known for its detrimental characteristics, poses notable health risks by inducing chemical damage upon contact and systemic intoxication through various exposure pathways (Michałowicz & Duda, 2007). The human epidermis has the capacity to assimilate phenolic compounds, thereby facilitating their passage into the gastrointestinal system where they undergo biotransformation, resulting in the generation of active intermediates capable of forming covalent bonds with proteins, consequently eliciting deleterious effects (Naguib &

Badawy, 2020, Schweigert *et al*., 2001). Chemical substances such as BPA and alkylphenols have been identified as endocrine disruptors in animals (Muñoz-de-Toro *et al*., 2005).

The ingestion of water contaminated with phenol has been associated with protein decomposition, tissue erosion, impairment of the central nervous system, and harm to vital organs such as the liver, kidney, and pancreas in human beings (Geyikci & Coruh, 2013). Entities responsible for regulation, such as the World Health Organization (WHO), advocate for a maximum permissible concentration of 1 mg/L of phenolic compounds in drinkable water (World Health Organisation, 1996). Correspondingly, guidelines established by the United States Environmental Protection Agency (USEPA) dictate the necessity of reducing phenol concentrations in wastewater to levels below 1 mg L^{-1}.

2.3.4 Processes for removal of phenols from waterbodies

2.3.4.1 Biological Processes:

Phenol toxicity presents a significant challenge to the elimination of this compound in wastewater treatment processes from a biological perspective. Phenol's reputation stems from its potent harmful effects on a diverse array of microorganisms, pivotal in the degradation of organic contaminants (Subramaniam *et al*., 2020). Elevated concentrations of phenol in wastewater can significantly hinder the growth and metabolic functions of microbial communities. This hindrance is a result of phenol's interference with multiple cellular mechanisms, such as membrane stability, enzymatic functions, and energy generation, all critical for the maintenance and operation of microorganisms (Xu *et al*., 2021). The penetration of microbial cell membranes' lipid bilayer by phenol results in increased membrane permeability. Consequently, this disruption leads to the leakage of cellular contents, loss of essential ions, and ultimately, cell death. The detrimental impact of phenol on cell membranes is significant due to its broad-spectrum effect on various microorganisms, such as bacteria, fungi, and protozoa, all of which have significant roles in processes related to wastewater treatment.

Furthermore, phenol has the capability to disrupt the functioning of enzymes within microorganisms (Singh *et al*., 2021, Subramaniam *et al*., 2020). Enzymes play a vital role in facilitating biochemical reactions that support the breakdown of organic pollutants. Nevertheless, phenol can hinder enzyme functionality by attaching to active sites or modifying the conformation of enzymes, thereby diminishing their efficacy, or rendering them

nonfunctional. This hindrance results in a decrease in the effectiveness of microbial degradation pathways, ultimately causing phenol and other organic compounds to undergo incomplete or delayed biodegradation. Due to the toxic nature of phenol, only specific strains of microorganisms with specialised adaptation mechanisms are capable of surviving and efficiently breaking down phenol in wastewater. These microorganisms often need a period of acclimatisation to develop resistance to phenol and sustain their metabolic functions. The necessity of this acclimatisation process, coupled with the potential danger of toxic shock resulting from sudden spikes in phenol levels, adds complexity to the biological treatment process. Consequently, the treatment of phenol-contaminated wastewater *via* biological processes requires precise regulation of operational parameters and may involve the utilisation of AOPs to support microbial populations and enhance phenol decomposition.

2.3.4.2 Chemical Processes

Chemical oxidation processes, such as the use of chlorine dioxide, chlorine, chloramines, ozone, ferrate, and permanganate, can fully degrade phenols in wastewater under mild conditions of pH and temperature. The utilisation of ferrate and permanganate is prevalent due to their elevated reduction potentials, with ferrate facilitating proficient phenol elimination through reduction to ferric hydroxide and functioning as a coagulant (Villegas *et al*., 2016). Permanganate demonstrates cost-effectiveness and avoids the formation of halogenated by-products, whereas hypochlorite has the potential to generate chlorophenolic by-products (Peings *et al*., 2015). These oxidising agents exhibit effectiveness in breaking down phenolic compounds, and the degradation rate is impacted by the surplus of oxidant applied (Peings *et al*., 2015; Zhang *et al*., 2013).

Electrochemical oxidation, whether direct or indirect, entails lower reagent expenses but higher costs associated with equipment and energy usage. Direct oxidation involves the adsorption of contaminants onto the anode surface prior to degradation via electron transfer reactions, whereas indirect oxidation employs redox agents to prevent electrode fouling. Various factors such as pH, types of anode materials, electrolytes, and current density play a role in determining the efficacy of electrochemical oxidation, whereby chloride ions enhance phenol breakdown by producing chlorine gas and hypochlorite (Rabaaoui *et al*., 2013; Pillai and Gupta, 2015).

2.3.4.3 Advanced Oxidation Processes

Advanced oxidation processes are renowned for their aptitude to generate active radicals *in situ*, which exhibit the capacity to decompose organic substances (Bartolomeu *et al*., 2018; Belghit *et al*., 2022). These methods, which involve UV/H_2O_2, Fenton reactions, ozonation, and photocatalytic degradation, provide benefits such as their high effectiveness in eliminating microorganisms and their self-sustaining quality using atmospheric oxygen (Ribeiro *et al*., 2015). Ozone, which can be naturally formed due to UV radiation or artificially produced using UV-type ozone generators, demonstrates superior oxidative properties in comparison to other common oxidising agents and can eliminate a wide range of pollutants without generating chemical byproducts (Epelle *et al*., 2022; Kim *et al*., 2024). The photocatalytic degradation process entails the utilisation of catalysts to break down pollutants by initiating electrons under light exposure, resulting in creating highly reactive radicals capable of transforming contaminants into less harmful substances (Laoufi *et al*., 2008). The efficacy of photocatalytic degradation is influenced by various factors including the type and amount of catalyst utilised, residence time, solution pH, as well as the properties of the light source and its intensity.

2.3.4.4 Physical Processes

Adsorption is a phenomenon distinguished by the accumulation of a substance on the surface of another substance, leading to an increased concentration of the substance in question. This phenomenon arises due to the intermolecular forces of attraction between gas or liquid molecules and the porous surface structure of the solid material (Rashed, 2013). Adsorption processes can be conducted using various configurations such as batch systems, column flow, or fixed bed setups. In batch configurations, an adsorbent is uniformly blended with a solution containing the adsorbate until the desired concentration is reached or equilibrium is achieved. Column operations involve the continuous interaction of the adsorbent with a fresh solution, offering benefits such as the rate's dependence on the adsorbate concentration in the solution (Villegas *et al*., 2016). The utilisation of activated carbon, particularly commercial activated carbon (CAC), has been prevalent in the remediation of diverse phenols from wastewater owing to its extensive surface area and porous structure (Ahmaruzzaman & Sharma, 2005). However, the regeneration of spent carbon often presents complex and costly challenges, leading to its usage being less favourable amongst other adsorbents.

2.3.5 Physicochemical Properties of Phenol

Phenol, in its solid form at standard room temperature and pressure, manifests as crystalline structures that shift from white to pink or red upon contact with air and light (Swearingen, 2002). Characterised by a specific scent and acrid taste, its solubility in water is restricted to 6.7 g/100 mL, although it readily dissolves in various organic solvents (Gross & Seybold, 2001). The compound's initial melting point of 43 °C reduces upon interaction with water, causing it to transition into a liquid state even at ambient temperature in a 90% phenol-water blend. Considering its chemical properties, phenol functions as a weak acid, resulting in a nearly neutral pH in water. Other properties of phenol are shown in Table 2.9. Phenol's existence may originate from both natural sources and synthetic production on an industrial scale, usually upholding a purity threshold of no less than 98%. GC and HPLC equipped with a UV detector are commonly employed techniques for the identifying and quantifying of phenol.

Table 2.9: Phenol's chemical and physical data

Name	Phenol
Molecular formula	C_6H_6O
Molecular weight	94.1
Structure	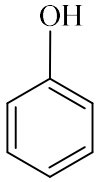
Density (25 ºC)	1072.2 g L^{-1}
Boiling point	181.7ºC
Melting point	40.5ºC
pKa	9.9
$LogK_{ow}$	1.5

2.4 Layered Double Hydroxide Materials

2.4.1 Background

LDH materials, commonly referred to as hydrotalcites-like materials, display a dual existence in both natural environments and synthetically produced substances by combining metal salts with a suitable base (Forano *et al*., 2013). The preparation of LDHs involves partially substituting of divalent cations in brucite-like ($Mg(OH)_2$) compounds with trivalent metals. This exchange results in a deficit of negative charge, which is compensated for by anions situated in the interlayer space. The interlayer region, recognised for its easy accessibility, offers promising opportunities for the adsorption and displacement of anions. A typical structure of an LDH material is shown in Figure 2.1.

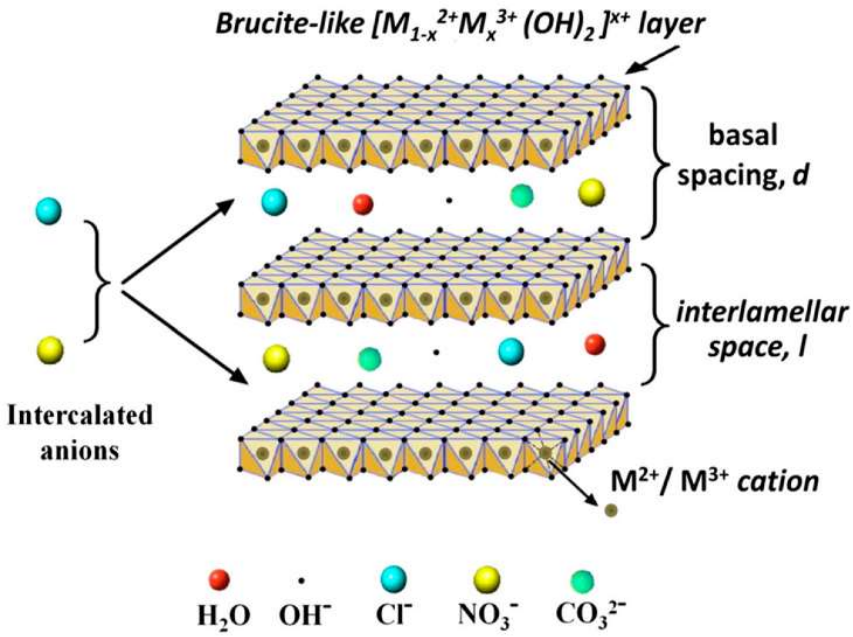

Figure 2.1: Structure of an LDH material (Richetta *et al*., 2017)

The multifaceted attributes of LDHs, stemming from their distinctive structural characteristics and capacity to interchange anions within the interlayer space, have spurred their application across various domains. These involve catalytic processes, delivery of pharmaceutical agents, remediation of environmental pollutants, and integration into nanocomposite structures. The persistent exploration of LDHs and the optimisation of their synthesis methodologies are essential in moulding their gradual engagement in tackling current issues in the domain of materials sciences.

2.4.2 Synthesis Methods

The synthesis methods used for LDHs present a wide range of processes, chosen based on criteria for the intended product, that include characteristics such as heightened crystallinity, reduced energy and material consumption, precise time control, and increased purity. Notable among the commonly employed processes for LDH preparation are co-precipitation (Theiss *et al*., 2016), hydrothermal synthesis (Ezeh *et al*., 2018), and the sol-gel method (Smalenskaite *et al*., 2019). Co-precipitation entails the simultaneous precipitation of bivalent (M^{2+}) and trivalent (M^{3+}) metal ions in an alkaline environment, appreciated for its straightforwardness and scalability. Hydrothermal synthesis, conducted under elevated temperature and pressure circumstances, aids in enhancing crystallinity and controlling particle size. The sol-gel method transforms a precursor solution into a gel and offers meticulous control over LDH composition and structure. Additionally, LDHs may undergo changes like thermal treatment, acid activation, and anion exchange to generate modified products with distinct characteristics. Improving crystallinity by thermal treatment, introduction of imperfections through acid activation, and replacing interlayer anions *via* anion exchange are crucial processes in this context. These versatile strategies for creating and modifying of LDHs play a crucial role in customising LDH properties to meet various application requirements in an environmentally conscious and regulated manner.

2.4.2.1 Co-precipitation

The method commonly used for synthesising of LDH involves dissolving metallic salts in a basic solution at a consistent or varying pH, allowing for the control of morphology and particle size based on the level of solution supersaturation. The resulting structure of the precipitate can be enhanced through the management of factors such as the M^{2+}/M^{3+} molar ratio, the type of interlayer anion, reaction duration, pH, and temperature (Sharma *et al*., 2007, Cormenzana *et al*., 2001). This technique can be executed under low or high supersaturation conditions, with the initial concentration of reactants maintained above the saturation point and pH carefully controlled to avoid incomplete precipitation or the loss of metallic ions through leaching (Chaillot *et al*., 2020).

During the process of low supersaturation co-precipitation, solutions containing predetermined ratios of metal ions are combined, followed by the addition of an aqueous solution containing the desired interlayer anion. Consequently, an alkaline solution is employed to adjust the pH level and promote the co-precipitation of metals, allowing for the manipulation of charge

density under conditions of low supersaturation, while maintaining a consistent pH level. The manipulation of high supersaturation is achieved through introducing of dissolved metal salts into a solution containing a slight excess of alkali carbonates, resulting in the formation of a less crystalline precipitate as opposed to the conditions of low supersaturation. Despite the effectiveness of this method in producing crystalline precipitates, the particles generated often demonstrate lower specific surface areas, ranging from 50 to 100 m^2 g^{-1}, in comparison to those synthesised using the sol-gel technique, which typically exhibit specific surface areas of 150-200 m^2 g^{-1} (Zhao *et al*., 2002). A study conducted by Gevers *et al*. (2019) investigated the impact of partially substituting Mg with transition metals on altering the crystal lattice parameters and thermal stability of hydrotalcite through the utilisation of this method. Additionally, post-synthesis procedures such as hydrothermal treatment, sonication, or microwave irradiation can be employed to enhance the crystallinity of precipitates obtained via this method (Pérez-Barrado, 2015).

2.4.2.2 Sol-gel Method

The sol-gel method is renowned for its effectiveness in terms of energy, expenditure, and time, offering the advantage of producing pure materials with diverse compositions (Paredes *et al*., 2011; Sharma *et al*., 2007). This method permits the exact modification of the structural attributes of materials by managing the chemical properties of the reactants and altering the residence time. The process of preparing LDH using the sol-gel approach consists of dissolving the targeted metal sources in water at room temperature, and then introducing a base during hydrolysis for condensation. The solution blend is permitted to mature for several hours, resulting in precipitates distinguished for their outstanding reproducibility, uniformity, purity, nanoscale particles, and significant surface area (Prince *et al*., 2009). However, a drawback of this technique is the formation of less crystalline precipitates. To address this issue, additional post-synthesis treatments like sonication (Hu *et al*., 2007), microwave irradiation (Benito *et al*., 2006), or hydrothermal treatment (Gu *et al*., 2014; Kovanda *et al*., 2005) can be utilised to enhance crystallinity.

2.4.2.3 Hydrothermal Treatment

Primarily utilised for optimisation purposes or as a subsequent treatment after other LDH synthesis methods, hydrothermal treatment is employed to enhance the crystallinity and size of crystallites (Sharma *et al*., 2007). Commonly carried out under moderate conditions at roughly 200°C with internal pressure, this process can extend from a few hours to several days. The

process involves dissolving metallic salts in water, transferring the resultant solution to a stainless-steel reactor, and heating it under hydrothermal circumstances (Chaillot *et al*., 2020). The range of hydrothermal conditions includes temperatures from 30 to 300 °C with steam pressure (Jang *et al*., 2014; Zhu *et al*., 2006). Metal sources used in hydrothermal treatment may consist of metal hydroxides, oxides (Jang *et al*., 2014; Labuschagne *et al*., 2018), nitrates (Roelofs *et al*., 2001), or naturally occurring minerals like brucite and gibbsite (Ogawa & Asai, 2000). The primary limitation of this synthesis method is its high energy consumption, making it less practical for large-scale industrial applications (Chaillot *et al*., 2020).

2.4.3 Applications of LDH Materials in Wastewater Treatment

2.4.3.1 Use of LDH Materials as Adsorbents for Organic Compounds

LDH materials possess favourable physical and chemical properties, including high specific surface area, adjustable compositions, and structures, making them attractive for various applications in water treatment. The potential of LDHs as efficient water treatment agents has been emphasised by their cost-effective production (Foruzin *et al*., 2020), exceptional catalytic performance (Bodhankar *et al*., 2021), significant adsorption capabilities (Daud *et al*., 2019), non-toxic nature (Alexa *et al*., 2011), durability, and easy regeneration. The utilisation of LDHs in water treatment can be categorised into four main areas: (i) use as adsorbents through anion exchange and surface adsorption, (ii) exploitation of calcined LDHs (CLDHs) regeneration capabilities, (iii) use of LDHs intercalated with organic compounds to improve the efficiency of pollutant uptake, and (iv) employ as photocatalysts for the conversion of pollutants into less detrimental substances. Anion exchange involves the displacement or exchange of anions with one or more different anions. LDH layers possess positive charges, facilitating the adsorption of anions through electrostatic interactions. LDHs with nitrate as an interlayer anion demonstrate increased exchange capacities, whereas carbonate is more difficult to displace due to its stronger affinity for LDHs (Chakraborty *et al*., 2012; Olfs *et al*., 2009). The difficulty of substituting interlayer anions follows a specific order, from most to least challenging: carbonate (CO_3^{2-}) > sulfate (SO_4^{2-}) > hydroxide (OH^-) > fluoride (F^-) > hydrogen phosphate (HPO_4^{2-}) > chloride (Cl^-) > bromide (Br^-) > nitrate (NO_3^-) > iodide (I^-) (Forano *et al*., 2013).

Neat LDHs generally demonstrate specific surface areas in the range of 15 to 120 m^2 g. The materials' surface area can be enhanced through thermal treatment at moderate temperatures, leading to the formation of mixed metal oxides (MMO) with enhanced anion uptake capacity. Thermally treated or CLDHs demonstrate a notable memory effect upon exposure to an

aqueous solution. Following the absorption of anions and water, CLDHs have the potential to be reconstructed into a layered structure (Tabana *et al*., 2020, Chen *et al*., 2017, Tzompantzi *et al*., 2014). The interlayer anion within the reconstructed LDH is contingent upon the concentration of the anion in the solution and the LDH's inclination towards that anion. LDH , being inorganic materials, exhibit inherent hydrophilic characteristics, resulting in a diminished affinity towards non-ionic hydrophobic organic compounds. To address this concern, the hydrophilicity can be modified by introducing hydrophobic anions, like surfactants, into the layers, resulting in the development of organo-LDHs. These altered LDH materials then become promising choices for the absorption of organic substances from water through a process known as adsolubilisation.

2.4.3.2 Use of Layered Double Hydroxides in Photocatalytic Degradation of Organic Compounds

Materials derived from LDHs are typically categorised into several distinct groups, including calcined LDHs (CLDHs), LDHs used as substrates, intercalated LDHs, and modified LDHs. CLDHs are frequently referred to as MMOs or layered double oxides (LDOs). These substances exhibit a memory effect, returning to the original LDH structure when dispersed in water (Tabana *et al*., 2020, Chen *et al*., 2017). LDHs used as supports materials involve dispersing metal, metal oxide, or non-metal materials onto the layered structure of LDHs (Zhang *et al*., 2017). This approach facilitates synergistic interactions between the components, allowing LDHs to function as both supports and co-catalysts. Furthermore, intercalating LDHs are achieved by modifying the chemical composition, size, and charge of the interlayer anions, resulting in LDHs with varied interlayer distances that can impact their characteristics (Meng *et al*., 2017, Xia *et al*., 2017). Lastly, modified LDHs are synthesised by introducing metal atoms or organic compounds onto the surface or between the interlayers of LDHs, enhancing the optical responsiveness or efficiency in separating electron-hole pairs within the original LDHs (Li *et al*., 2018, Tao *et al*., 2018).

Layered Double Hydroxides-derived Mixed Metal Oxides

LDHs-derived MMOs, also referred to as semiconducting metal oxides, constitute a noteworthy class of photocatalysts. Although mono-metal oxides are frequently employed, their practical use faces limitations such as wide and fixed band gaps as well as limited surface areas. MMOs provide a remedy by combining the positive attributes of individual components to produce superior photocatalytic characteristics (Zhu *et al*., 2016). Among the MMO groups,

LDOs form a subgroup derived from the medium-temperature (*ca* 500 °C) calcination of precursor LDHs. Variations in the chemical composition of metal ions enable the synthesis of LDO with different structures and compositions. Typically, LDOs display a broader spectral response to photons in comparison to their LDH precursors, featuring band gaps that generally span from 2.0 eV to 3.0 eV, thereby enhancing the efficacy of visible light absorption (Asghar *et al*., 2024, Chivu *et al*., 2020).

A demonstration of LDO as a photocatalyst is exemplified in a study conducted by Ju *et al*. (2018), wherein ZnAlTi-LDHs were subjected to calcination at 500°C to produce ZnAlTi-LDO nanoparticles. The photocatalytic efficacy of the LDO was observed to be influenced by the pH of the reaction medium. In a slightly acidic environment (pH 5), the excitation of dissolved oxygen by electrons generated free radicals, whereas basic conditions obstruct photocatalytic performance due to the cathodic shift of the valence band. Various free radical scavengers were utilised to investigate the reaction mechanism, including sodium oxalate (h^+ scavenger), NaF (•OH scavenger), methanol (•OH scavengers), and 1,4-benzoquinone ($\bullet O_2^-$ scavenger). The influence of calcination temperature on the structural recoverability of LDOs is substantial. With increasing temperature, characteristics derived from LDHs diminish, eventually leading to the disappearance of the LDHs structure, making it irrecoverable when the temperature surpasses a certain threshold (typically above 550 °C) (Ye *et al*., 2022, Antoniak-Jurak *et al*., 2021).

Layered Double Hydroxides as Support Materials for Photocatalysis

LDHs used as supports have been extensively studied as photocatalysts to address the limitations associated with semiconducting mono-metal oxides, such as ZnO, TiO_2, and Cu_2O. These oxides are known for their cost-effectiveness and documented photocatalytic capabilities but are hindered by wide band gaps and inefficient photocarrier transportation (Wang *et al*., 2020, Xie *et al*., 2019). To enhance the performance of these materials, researchers have explored various metals, metal alloys, and carbon-based materials with high electron storage capacity and transportation efficiency. Incorporating these materials into LDHs has been shown to significantly widen the absorption range of visible light and improve hot carrier transportation efficiency. For example, Tao *et al*.(2023) synthesised a CdS/CoAl-LDH nanocomposite through hydrothermal methods and ionic exchange, resulting in a reduced band gap and enhanced visible light absorption efficiency. The photocatalytic activity of this nanocomposite, tested through tetracycline degradation, exhibited markedly improved

reactivity and stability compared to individual CdS or CoAl-LDHs. Despite its wide band gap, cerium oxide has energised electrons and holes with longer lifetimes compared to common semiconductors like TiO_2. Valente *et al*. (2009) improved the optical properties of cerium oxide by creating CeO_2/MgAl-LDH through calcination. The proposed reaction mechanism involved the formation of intermediate complexes at the interface between LDH and CeO_2, supported by the movement of energised electrons and holes. Moreover, Au/LDH-based photocatalysts exhibited potential in visible light-driven selective hydrogenation of crotonaldehyde and gaseous toluene photodegradation. AuNi and AuCo alloy nanoparticles supported on LDH were synthesised for crotonaldehyde hydrogenation, showing high catalytic activity due to a synergistic effect of localised surface plasmon resonance and electronic structure modification of Au atoms by Co or Ni (Xia *et al*., 2020). Additionally, Lewis's acid-base pairs on material surfaces enhanced catalytic activity by promoting H_2 dissociation and initiating hydrogenation reactions.

Intercalated Layered Double Hydroxides

Intercalated LDHs, distinguished by the presence of electrostatic interactions between interlayer anions and distributed positive charges, play a crucial role in maintaining the overall charge neutrality and structural integrity of LDHs. The fluidity and exchangeability of intercalated anions are often high due to the relatively weak interlayer interactions, allowing for a significant degree of tunability in the intercalation properties of LDHs. This tunability includes factors such as interlayer spacings, which are influenced by parameters like the size, chemical composition, and charge of the intercalated anions (Pan *et al*., 2021; Samuei *et al*., 2020). The physicochemical attributes of LDHs are significantly influenced by various factors, including the size and valence of the anions. Additionally, the strength of the interlayer hydrogen bond network plays a crucial role in controlling properties such as interlayer spacing, volume, electron density, and band structures. These properties, in turn, dictate the photocatalytic activity of LDHs.

X-ray Diffraction (XRD) analysis is commonly utilised to investigate the crystalline structures and diffraction patterns of intercalated LDHs, providing valuable insights into features such as interlayer spacing and the outcomes of the intercalation process. It is important to note that there is no universally applicable method for the optimal preparation of intercalated LDHs with diverse types of anions. Tailored synthetic methods specific to individual anions are essential to achieve intercalated LDHs with desired structures while retaining the characteristic

properties necessary for targeted photocatalytic applications. For example, a study by Chen *et al*.(2023) demonstrated the incorporation of Pt-containing organic ligands into LDHs, resulting in a Pt/ZnTi-LDHs complex with enhanced specific surface area and pore volume, leading to improved charge separation and transport efficiencies and superior photocatalytic performance, as evidenced by accelerated Rhodamine B photodegradation compared to untreated LDHs.

Modified Layered Double Hydroxides

Modified LDHs constitute a significant area of research focusing on altering the structural, morphological, and electronic characteristics of semiconducting materials by introducing dopants. Incorporating of metallic dopants like Mn and Pt into LDHs-based photocatalysts results in the modification of LDHs' atomistic structure, leading to the formation of new energy bands within the band gap and reducing electron-hole recombination probabilities. For example, Contreras-Ruiz *et al*. (2019) conducted a study on various metal ion doped TiO_2 catalysts for chloroform reduction reactions, observing improved surface charge transportation and decreased recombination probabilities in LDHs doped with Fe^{3+}, Re^{5+}, Ru^{3+}, V^{3+}, and Rh^{3+}. They highlighted the minimal impact of metal ions with closed-shell electronic configurations on the activity of TiO_2 photocatalysts. In contrast, open-shell metal ions significantly influenced the photocatalytic performance of LDHs-based catalysts. Additionally, Li *et al*. (2004) discovered that La^{3+} doping inhibited crystal transformation, enhanced thermal stability, and reduced the particle size of TiO_2. Carja *et al*.(2017) developed ZnMe-LDHs (Me=Al, Ga) as a precursor, which was then combined with Ga_2O_3 or In_2O_3 using SO_4^{2-} and $CH3COO^-$ as interlayer anions, followed by calcination in a reducing environment. The resulting mixed spinel metal oxide, ZnMe-LDO, displayed visible light absorption and exceptional photocatalytic activity towards the degradation of phenol and 4-nitrophenol. The exploration of incorporating rare-earth elements and nonmetal elements like N and S into LDHs has also been undertaken.

2.5 Application of Silver Halides in Wastewater Treatment

2.5.1 Background

Nano-photocatalysts composed of Ag-AgX (where X represent Cl, Br, F or I) have gained significant attention due to their exceptional photocatalytic properties, driven by silver nanoparticles' enhanced light absorption efficiency. This has resulted in their extensive utilisation in diverse photocatalytic nanocomposite materials. The energy and environmental

sustainability sector have been dedicated to enhancing sustainable energy resources and developing efficient approaches for harnessing solar energy (Hasan *et al*., 2023; Ibrahim & Waziri, 2020; Tanvir *et al*., 2021). Photocatalysis has emerged as a viable technology for water purification (Prakruthi *et al*., 2022, Belver *et al*., 2019), with the ability to convert carbon dioxide (CO_2) into chemical fuels (Verma *et al*., 2021), break down pollutants, and disinfect bacteria (Dai *et al*., 2022; Wang *et al*., 2015) using solar energy. Anatase/rutile-phase TiO_2 nanoparticles are among the most extensively studied photocatalytic materials due to their cost-effectiveness and structural durability (Žerjav *et al*., 2022, Luttrell *et al*., 2014). However, the wide band gap of TiO_2 limits its utilisation, especially as it solely reacts to UV radiation, which constitutes a minor segment of the solar spectrum.

Efforts have been directed towards the advancing photocatalysts that can capture visible light, a crucial segment of the solar spectrum. Silver-containing photocatalysts have become a subject of interest due to their remarkable light absorption efficiencies in the visible range, which is linked to the plasmonic effect (Wang *et al*., 2024, Shi *et al*., 2022). Ag-AgX composites have become favoured choices for solar-driven photocatalysis, enabling reactions like organic dye degradation, pathogenic organism inactivation, heavy metal reduction, and water splitting. Hybrid Ag@AgX photocatalysts operate by absorbing visible light through the surface plasmon resonance (SPR) of Ag nanoparticles (Pius *et al*., 2023; Xu *et al*., 2022), deviating from conventional semiconductor photocatalysts. The mechanisms governing photochemical processes involve plasmonic metal@semiconductor structures and Z-scheme hybrids with a metal@semiconductor@semiconductor configuration.

2.5.2 Mechanism in the Plasmonic Ag-based Metal@semiconductor Structure

The Ag-based plasmonic metal@semiconductor structure operates through a synergistic interaction between excitons deriving from semiconductors and plasmons emerging from metallic silver (Ag^0) nano-species under photo-irradiation (Fu *et al*., 2019, Wu, 2018, Cai *et al*., 2016). This cooperative effect enhances the SPR effect, resulting in increased light absorption. The coherent electronic configuration of the photocatalysts, alongside the reduced effective masses of the photoexcited electrons (e^-) and holes (h^+), enables the movement of charge carriers from the bulk photocatalysts to their surface-active zones. Subsequently, the energised electrons engage in reactions with dissolved O_2 to yield highly reactive species such as $\bullet O_2^-$ and hydrogen peroxide (H_2O_2) as shown in Figure 2.2. Concurrently, the residual positive charges (h^+) present within the Ag nanoparticles (NPs) interact with X^- ions at the

Ag@AgX interfaces, resulting in the production of highly reactive halogen X• radicals (X(0) atoms) with the ability to directly oxidise molecules of organic pollutants. Simultaneously, the X• radicals are reduced to yield X^- ions, thus completing the catalytic sequence.

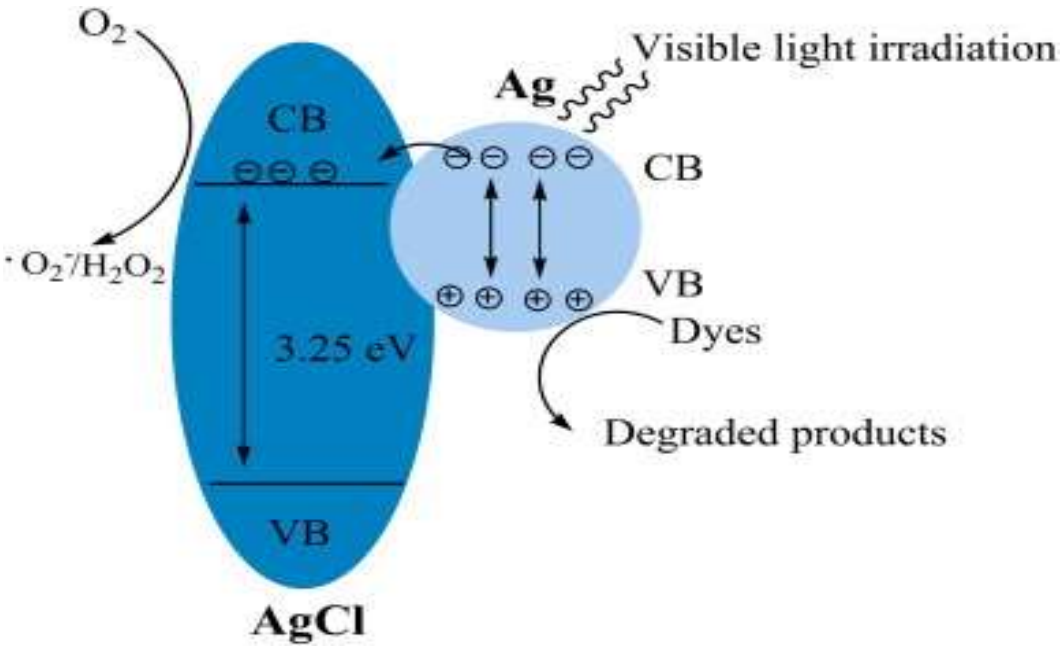

Figure 2.2: A schematic illustration of the charge transfer in an Ag-AgCl photocatalysts under the visible light irradiation (Cai *et al*., 2016).

2.5.3 Photoreactions in Z-scheme Hybrids with an Ag-based Metal@semiconductor@semiconductor Structure

In Z-scheme hybrids consisting of an Ag-based metal@semiconductor@semiconductor configuration, the adjustment of band gaps and redox potentials of photocatalysts can be realised through the combination of appropriate semiconductors (Saber *et al*., 2020, Wang *et al*., 2018). This deliberate manipulation is intended to satisfy the energy needs of the catalytic mechanism. Typically, the system consists of Ag@AgX and a semiconductor characterised by a narrower band gap (NBG), enabling efficient interfacial transfer of photo-excited carriers and optimising photocatalytic efficacy. Upon light exposure, the conduction band (CB) of one semiconductor yields e^- that exhibit remarkable photo-reduction capability. In contrast, the valence band (VB) of the other semiconductor generates h^+ with robust oxidation potential, as demonstrated by the Ag@AgCl@WO_3·H_2O composite (Figure 2.3). This configuration enables dual-step absorption of visible light, propelled by both the SPR of Ag nanoparticles (NPs) and the photoexcitation of the NBG semiconductor. The modified plasmonic behaviour

initiated by Ag nanoparticles plays a crucial role in enhancing the photoactivity of the semiconductor with a sub-band gap by traversing to its conduction band. The activated Ag-NPs transition into positively charged Ag-NPs$^{n+,}$ which facilitate oxidation reactions or electron transfer from the VB of AgX. The photo-induced electrons are subsequently captured by oxygen molecules, leading to the initiation of reactive oxygen species production, which enhances the efficacy and robustness of the hybridised photocatalyst. Simultaneously, the photo-induced gaps in the semiconductor promote the oxidation of X^- ions, generating reactive X• radicals that directly act on contaminants or electron donors. Furthermore, the photo-generated electrons possess the capability to convert X• radicals back into X^-ions.

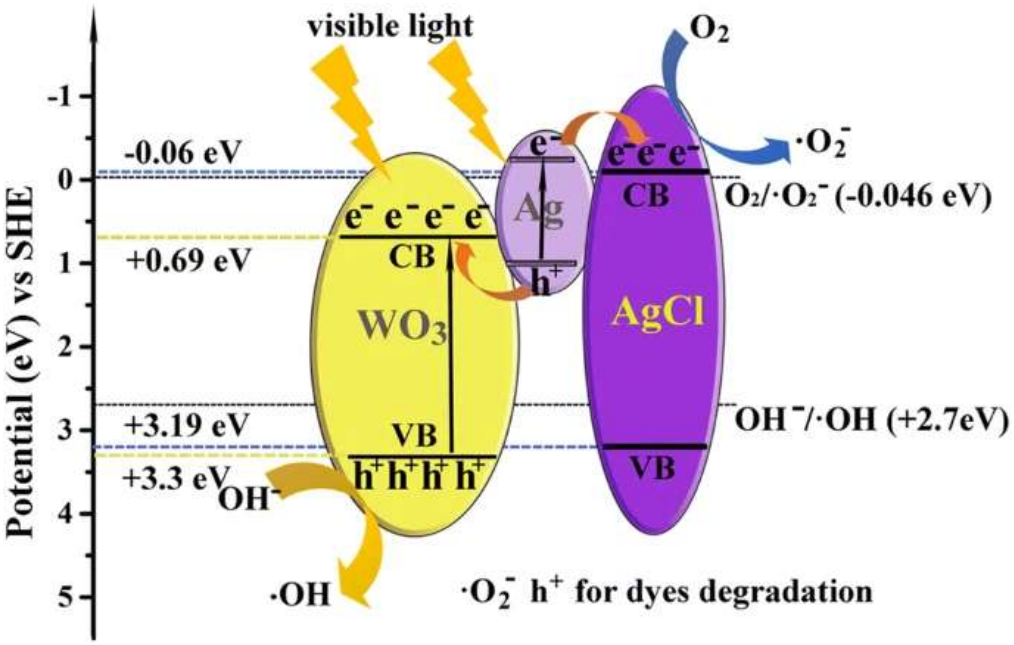

Figure 2.3: Ag@AgCl@WO_3·H2O composite as an example for Ag-based metal@semiconductor@semiconductor (Fang *et al*., 2019).

2.5.4 Cases of Ag@AgX-based Plasmonic Photocatalysis

2.5.4.1 Self-sensitised AgBr Nano-photocatalysts.

The photocatalytic performance of AgBr particles is significantly influenced by their shape and crystal arrangement (Pang *et al*., 2017, Liang *et al*., 2013). Wang *et al*. (2012) demonstrated that Ag@AgBr nanorods exhibit superior photocatalytic activity under visible light due to their increased number of active sites and enhanced charge separation and transfer compared to irregularly structured Ag@AgBr nanoparticles. The morphology of AgBr particles, particularly the customisation of facets such as [111], [100], and [110], has been a focal point in optimising

their performance (Liang *et al*., 2013; Wang *et al*., 2012). Among these, [111]-facet-terminated AgBr nanoparticles, which feature unsaturated Ag atoms, show higher surface energy and improved efficiency in degrading model contaminants like Methyl Orange (MO) compared to other facets (Liang *et al*., 2013). Various synthesis methods, including a modified ion-exchange strategy with polyvinylpyrrolidone (PVP) as a stabiliser, have been employed to produce [111]-dominant Ag@AgBr nanoparticles (Fan *et al*., 2018; Tang *et al*., 2016). Despite these advances, Ag@AgBr photocatalysts exhibit low surface areas and are vulnerable to the recombination of plasmon-induced electron-hole pairs (Xu *et al*., 2013). Additionally, they are prone to photocorrosion, leading to a gradual loss of photoactivity over time (Moja *et al*., 2024). To achieve effective and sustained photocatalytic activity, Ag@AgBr typically requires support from other materials.

2.5.4.2 Hybridised Nano-Photocatalysts of AgBr with Photoactive Semiconductors

Efforts have been directed towards enhancing the use of the visible spectrum in the conventional TiO_2 photocatalyst by integrating Ag@AgBr NPs. These NPs have been anchored on various substrates, including porous anatase TiO_2 nanotubes (Zhang *et al*., 2016), porous nickel (An *et al*., 2016), apatite (Ahmadvand *et al*., 2019), and zeolite (Sohrabnezhad & Rezaei, 2013), resulting in enhanced photocatalytic efficiency. Moreover, using various methods, ZnO-based nanostructures have been designed to absorb visible light by incorporating AgBr NPs (Jandaghian *et al*., 2023). Photocatalysts have been created by mixing AgBr with varying tungstates, such as AgBr@WO_3 and AgBr@H_2WO_4 (Puga *et al*., 2021, Fan *et al*., 2013). The former was prepared by depositing AgBr NPs onto a WO_3 support, while the latter involved loading H_2WO_4 NPs onto an AgBr substrate. Both catalysts contained minimal levels of Ag, which were reduced through photo-illumination, and showed efficiency in decomposing dyes such as methyl orange (MO) and rhodamine B (RhB) under visible light exposure.

2.5.4.3 Hybridised Nano-photocatalysts of AgBr with Photoinactive Substrates

Deposition of AgBr and Ag@AgBr NPs on non-photosensitive substrates can enhances photocatalytic performance significantly. Combining stratified materials such as Co-Ni-NO_3 LDH with Ag@AgBr NPs resulted in improved catalytic activities by utilising the high surface area of LDH (Fan *et al*., 2013; Miao *et al*., 2015). Similarly, due to their significant surface area, mesoporous materials like Al-MCM-41 exhibit effectiveness when paired with Ag@AgBr NPs (Pica, 2019; Pourahmad *et al*., 2010). Catalysts composed of carbon nanotubes

(CNTs) doped with Ag@AgBr displayed improved catalytic activity for degrading methyl orange (MO) under visible light exposure (Pica, 2019; Xu *et al*., 2013). Additionally, mesoporous substrates like AgBr@Y–zeolite and AgBr@SiO2 demonstrate efficacy in various applications, including MO degradation under halogen light or direct sunlight exposure, as well as hydrogen generation from methanol photolysis in distilled water (Jinfeng & Tao, 2013). Mesoporous alumina (MA) and titanium-doped MA (MA-Ti) combined with Ag@AgBr NPs effectively catalyze the breakdown of persistent toxic organic contaminants in water under visible light (Zhou *et al*., 2012). Integrating Ag@AgBr NPs with superparamagnetic Fe_3O_4 NPs simplified catalyst separation post-reactions, facilitating recovery and reusability, thereby enhancing overall efficiency and sustainability in the realm of photocatalytic processes (You *et al*., 2019).

2.6 Conclusion

This chapter highlighted the environmental risks of ARVDs and phenol due to their persistence in water and their harmful effects on human health and aquatic ecosystems. It stressed the need for effective remediation strategies. LDHs, modified with silver halides, were identified as effective materials for photocatalytic degradation. Their synthesis methods, properties, and applications were reviewed, demonstrating their potential as sustainable solutions for water treatment.

CHAPTER 3: EXPERIMENTAL

3.1 Synopsis

This chapter details the experimental methods and materials used in the study. LDHs were synthesised via the co-precipitation method, and Ag-AgBr-LDH nanocomposites were prepared using a photo-assisted doping technique. Thermal treatment of LDHs in a furnace produced CLDH to enhance adsorption performance. Material characterisation was conducted using various techniques, including XRD, BET surface area, SEM-EDS, XPS, FTIR, and TGA. Solution samples containing the pollutants were analysed using HPLC. Phenol and ARVD removal processes were studied through photocatalytic degradation experiments, including continuous flow tests for ARVDs. Adsorption experiments utilised CLDH as the adsorbent, and computational modelling provided molecular-level insights into adsorption mechanisms.

3.2 Materials

Precursor chloride salts, aluminium chloride hexahydrate ($AlCl_3 \cdot 6H_2O$), magnesium chloride hexahydrate ($MgCl_2 \cdot 6H_2O$), and zinc chloride ($ZnCl_2$) were obtained from Glassworld in South Africa. Sodium hydroxide (NaOH), sodium bromide (NaBr), and silver nitrate ($AgNO_3$) were purchased as solid compounds from Merck (Pty) Ltd. The ARVDs, EFV and NVP, were sourced as solid powders from Adcock Ingram while phenol crystals were procured from Glassworld. Solvents used in the experiments were methanol (99%) and acetonitrile (99.9%), which were supplied as solutions by Sigma Aldrich. Hydrochloric acid (HCl) (32%) was also supplied as a solution by Sigma Aldrich, while acetic acid (99%) was obtained as a liquid from Glassworld. All the materials were utilised as received without further processing except for NaOH and HCl which were diluted prior to usage in pH adjustment. Furthermore, all the chemicals used in the study were obtained in analytical grade quality. Deionised water dispensed by an Elga Purelab Flex 3 water purifier was used for all the experiments.

3.3 Synthesis of Layered Double Hydoxide and the Photocatalyst

3.3.1 Synthesis of Layered Double Hydroxide

LDHs was synthesised using co-precipitation at a constant pH of 10 (± 0.25) to prevent the formation of metal hydroxides (Wang & O'Hare, 2012). Co-precipitation synthesis method was selected because it provides a convenient and versatile approach for the preparation of LDHs with controlled composition, uniform structure, high purity, and scalability (Jiang *et al*., 2022). The required amounts of metal salts were dissolved in deionised water to produce a 1

M solution based on cations with molar ratios of 75%, 5%, and 20% for Mg, Zn, and Al, respectively. This was made in a total volume of 250 mL. The composition of LDH was carefully selected to optimise its physicochemical properties (Tabana *et al*., 2020). The salt solutions were added gradually to a 60 °C pre-heated 1 L glass reactor containing 250 mL of 1 M Na_2CO_3 solution. The pH of the slurry was maintained at 10 by adding the required amount of 2 M NaOH solution. The resulting slurry was stirred at 500 rpm for 24 h. A Daihan Scientific magnetic stirrer (MSH-20D) with a hot plate and temperature controller was used to mix and regulate the temperature of the reactor's contents. The schematic diagram of the reactor setup for LDH clay synthesis is presented in Figure 3.1. After the reaction was complete, the suspensions were allowed to cool to room temperature before being centrifuged at 9000 rpm for 10 min. The precipitate was washed three times with excess deionised water before being dried in an oven set at 50 °C for 12 h. The dried precipitate was then pulverised before being used for characterisation, synthesis of photocatalyst composite, photodegradation and adsorption studies.

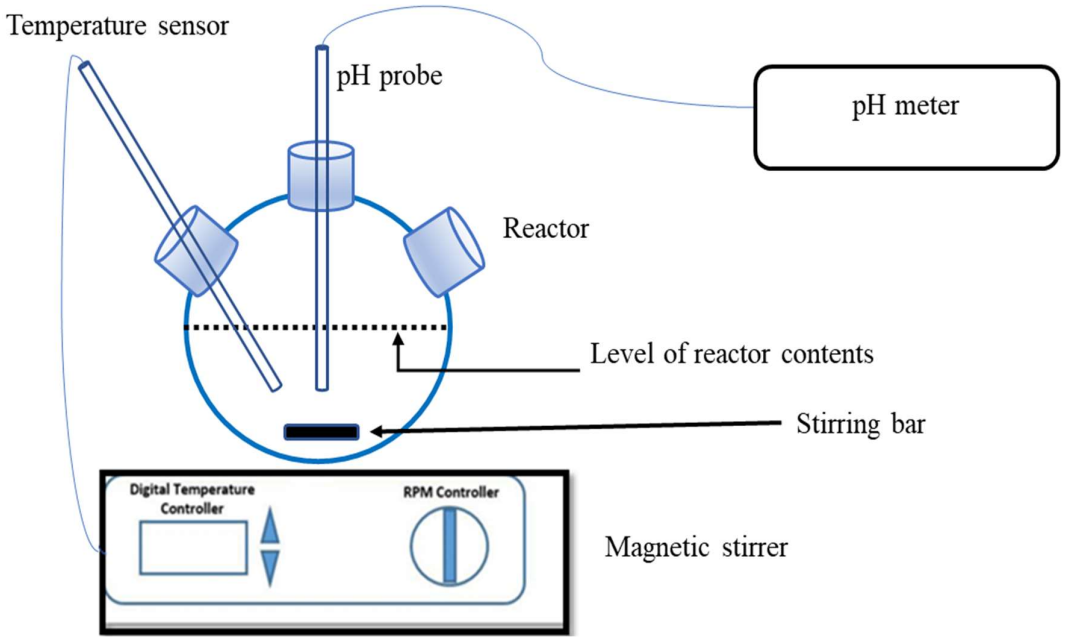

Figure 3.1: Schematic diagram of the reactor configuration for LDH clay synthesis (Tabana, 2021).

3.3.2 Synthesis of Composite Photocatalyst

The photocatalyst composite was produced by doping LDH with AgBr using a photo-assisted technique adapted from Chen *et al*.(2020a). LDH material amounting to 1 g was added to 200 mL of deionised water and dispersed through ultrasonication for 45 min. Subsequently, 0.46 g of $AgNO_3$ dissolved in 5 mL of deionised water was added to the LDH suspension. After mixing for 2 h, 20 mL of a 2 M NaBr solution was added to the suspension and stirred in the dark to prevent photoionisation of the produced AgBr (Svanstrom *et al*., 2020). This process resulted in the production of LDH-doped 30 photocatalyst. Additionally, LDH-doped 15 and LDH-doped 7.5 photocatalysts were produced by reducing the silver content by half and by a quarter, respectively. Thereafter, 20 mL of methanol was added as a hole scavenger before subjecting the mixture to visible light irradiation. This was to reduce silver ions to metallic silver, preventing them from reacting with other species and producing unwanted by-products. Centrifugation was used to collect the precipitate, which was then washed three times with deionised water and once with methanol.

3.4 Calcination of Layered Double Hydroxide for Adsorption Process

Calcination process was conducted using an Aluminium Electric Muffle furnace set at 500°C. At this temperature, it was expected that the LDH material would undergo a transition, leading to the formation of MMOs (Tabana *et al*., 2020). The furnace was initially preheated to 500°C, and a sample of LDH was then placed in a porcelain crucible before being charged into the furnace. The temperature was maintained at 500°C for a period of 4 h. Following the completion of the calcination process, the porcelain crucible was withdrawn from the furnace, and the residues were retrieved for subsequent analysis and adsorption experiments.

3.5 Characterisation of the Photocatalysts and Adsorbents, and Analysis of Solution Samples

3.5.1 Characterisation of the Photocatalyst

3.5.1.1 X-ray Diffraction Analysis

X-ray powder diffraction (XRD) spectra were determined using a PANalytical X'Pert Pro powder diffractometer in θ-θ configuration fitted with an X'Celerator detector and variable divergence with Fe-filtered Co-Kα radiation (λ = 1.789 Å) fixed slits. o The mineral phases present were confirmed using X'Pert Highscore plus software, which indexed the spectra against the ICSD database.

3.5.1.2 Scanning Electron Microscopy and Transmission Electron Microscope

A Zeiss Ultra Plus field emission scanning electron microscope (FEG-SEM) was used to capture the SEM/EDS images. SEM samples were prepared by distributing the samples on carbon tape stuck to a microscopy stub; the samples were then sputter coated with carbon under argon gas. A Jeol-2100 F Field Emission Electron Microscope was used for Transmission Electron Microscope (TEM) analysis. A few milligrams of the photocatalysts were placed in well-marked vials before adding 3 mL of ethanol. The suspensions were sonicated for 15 minutes to dissolve the photocatalysts. Small droplets of the dispersed samples were placed onto a TEM grid and allowed to dry in air. The dried grids were individually mounted onto a specimen holder for TEM analysis.

3.5.1.3 X-ray Photoelectron Spectroscopy (XPS) Analysis

The surface elemental compositions and electrochemical states of the photocatalysts were established through X-ray photoelectron spectroscopy (XPS) analysis. The analysis was conducted using a Thermo Fisher Scientific ESCALAB 250Xi coupled with a monochromatic Al Kα X-ray source (1486.7 eV) operated at 300 W.

3.5.1.4 Brunauer-Emmet-Teller Surface Area

A Micrometrics Tristar 3000 BET analyser was used to determine the BET surface area through nitrogen adsorption-desorption method. The instrument was operated at -196 °C (77 K) which is boiling point for nitrogen. All samples were degassed for 24 hours at 150 °C under a 10^{-5} Torr vacuum to remove any moisture or dissolved gases prior to analysis.

3.5.2 Characterisation of the Adsorbent

3.5.2.1 X-ray diffraction analysis

The XRD analysis was conducted as described in Section 3.4.1.1. Furthermore, the crystal lattice parameters were estimated using Equations (3.1) to (3.4).

$$d_{003} = \frac{N\lambda}{2\mathrm{Sin}\theta} \quad (3\text{-}1)$$

$$c = \frac{1}{3}(3d_{003} + 6d_{006} + 9d_{009}) \quad (3\text{-}2)$$

$$a = 2d_{110} \quad (3\text{-}3)$$

$$L_{003} = \frac{K\lambda}{\beta\mathrm{Cos}\theta} \quad (3\text{-}4)$$

Where:

d_{003} = layer distance at plane (003) (Å)

c= layer thickness (Å)

a = density of metal-ion stacking (Å)

L_{003} = crystallite size in the direction parallel to plane (003) (Å)

λ = wavelength (Å)

θ = angle of incidence (°)

N=order of the spectrum (dimensionless)

β = line broadening at half maximum (FWHM) of the diffraction peak (°)

3.5.2.2 SEM analysis

As conducted in Section 3.4.1.2.

3.5.2.3 BET surface area

As demonstrated in Section 3.4.1.4.

3.5.2.4 Thermal Stability Analysis

To monitor the thermal phase transitions of LDH, approximately 10 mg of the sample was weighed into alumina crucibles. The crucible containing the sample was then analysed using the Q5000 Thermogravimetric Analyser (TGA). The TG analysis involved subjecting the sample to a temperature scan from 25 to 950 °C, with a heating rate of 10 °C min^{-1}. The analysis was carried out under a nitrogen flow rate of 50 ml min^{-1}, which served to create an inert atmosphere during the experiment.

3.5.2.5 Fourier transform infrared spectroscopy

Identification of the main functional groups and anions in LDH was done on a Perkin Elmer 100 Spectrophotometer. The instrument was equipped with a MIRacle attenuated total reflection (ATR) attachment which had a zinc-selenide (ZnSe) crystal plate. A powdered sample weighing ca. 20 mg was placed onto the crystal plate and pressed by lowering down the pressure arm until the force gauge was ca. 80 before data could be collected. The spectra were recorded between 550 to 4000 cm^{-1} at a resolution of 2 cm^{-1} with data collected over 32 scans.

3.5.3 Analysis of Solution Samples

3.5.3.1 Analysis of Phenol solution

A Waters 2695 HPLC coupled with a Waters 2489 UV-vis detector was used to analyse the concentration of the phenol solutions before and after exposure to the photocatalytic process. Separation was done in a Waters PAH C18 column while Empower Software was used for data analysis. Elution was done with a mobile phase consisting of 70% acetonitrile and 30% deionised water with each solvent containing 1% (v/v) acetic acid. The flowrate was kept constant at 1 mL min^{-1} with an injection volume of 10 µL while maintaining a temperature of 30 °C at a wavelength of 280 nm.

GC-MS analysis were carried out on a Perkin Elmer Clarus 600 (GC) and Clarus 600 T (MS) with Turbomass software being used for data analysis. The supernatant from a photocatalytic degradation process was prepared according to the method as elaborated by Klen and Vodopivec (2012). Separation was done on an Elite 5 MS column (30 m x 0,25 mm x 0,25 µm) in a scan mode between 30 to 300 m z^{-1}. The temperature profile started at 60 to 245 °C at a heating rate of 15 °C min^{-1}. The carrier gas (helium) was kept constant at a flowrate of 1 mL min^{-1}.

3.5.3.2 Analysis of ARVDs

EVF and NVP stock solutions of 100 mg L^{-1} were made by dissolving 1 mg of each pollutant in a 10 mL solution containing equal parts methanol and deionised water. The suspensions were sonicated for 30 min to dissolve all solids. The stock solutions were diluted with deionised water to create other desired concentrations. The same instrument as stated in Section 3.4.3.1. was used for this purpose. However, in this case elution was accomplished through a gradient flow of a mobile phase composed of acetonitrile, methanol, and a pH 4.5 buffer solution. The mobile phase used to analyse the pollutants was separated into 2 distinct fractions. Mobile phase (1) contained acetonitrile, methanol, and a pH 4.5 buffer solution in the ratios of 60:15:25, whereas mobile phase (2) contained the same components in the proportions of 50:15:35. The two mobile phases were delivered using a gradient elution method as follows: 0 – 4 min with 100% mobile phase (1), 4.01 – 8 min with 100% mobile phase (2), and 8.01 – 12 min with 100% mobile phase (1).

3.6 Photocatalytic Degradation Processes

3.6.1 Photodegradation of Phenol

The degradation tests were conducted in a closed compartment lined with a reflective material. Three magnetic stirrers were kept in the compartment for mixing with the sources of irradiation placed directly above the stirrers. A 72 W LED lamp with a peak wavelength range of 380 – 800 nm and a total current density of 53.5 mW cm^{-2} was used as the source of visible light irradiation. Reaction vessels with a nominal capacity of 250 mL were employed as reactors; 100 mL of phenol solution was used in all the experiments. Phenol-photocatalyst suspensions were allowed to mix and equilibrate in the dark for 30 min prior to turning on the light source. Aliquots were withdrawn at predetermined periods, filtered, and analysed with high performance liquid chromatography (HPLC). The initial conditions were set as follows: phenol concentration of 10 mg L^{-1}, LDH-doped 30 as the photocatalyst with a loading of 1 g L^{-1}, the initial pH of the solution was not adjusted and measured to be 6.68 $\pm$ 0.2 at an ambient temperature of 22 °C under visible light irradiation. Thereafter, the experiments were conducted using the same procedure as detailed above with adjustments made to various parameters to establish their effect on phenol degradation efficiency. The effect of silver (Ag) content (dopant) was tested by varying Ag amount from 0 to 0.3 g per 1 g of LDH. The effect of photocatalyst loading was evaluated in a range of 0 to 4 g L^{-1}. Additionally, the effect of pH was investigated at pH values of 5, 6.68, 9 and 12. Acidic pH solution was achieved by adding 0.1 M HCl while alkaline pH solutions were achieved by adding the required amount of 0.1 M NaOH solution. Upon establishing of the optimum conditions, phenol concentration was varied to evaluate the effect of the initial concentration (5, 10 and 20 mg L^{-1}) on the performance of the catalyst. The dominant reaction mechanism was established by conducting scavenger tests and analyses of residual phenol solutions on the gas chromatography coupled with mass spectrometry (GC-MS). The photostability and reusability tests were conducted by recovering the spent photocatalyst from the solution, washing it with deionised water, and drying it at 60 °C for 24 h before reuse.

3.6.2 Photodegradation of ARVDs (batch studies)

A similar setup of reactor vessels and sources of light as detailed in Section 3.5.1. were used for this purpose. 100 mL of predetermined concentrations of EFV or NVP solution were used in each experiment, and the amount of photocatalyst loaded varied based on the experimental design. Before switching on the light source, pollutant-catalyst suspensions were allowed to mix and equilibrate in the dark for 30 min. The initial pH of the solutions was adjusted by

adding 0.1 M HCl for acidic solutions and the required amount of 0.1 M NaOH solution for alkaline solutions.

The experimental plan was divided into two sections. In the first section, photodegradation tests were carried out using different photocatalysts, namely Ag-AgBr, LDH, and Ag-AgBr-LDH, to determine the most effective one. The Ag-AgBr-LDH photocatalyst utilised in this investigation was specifically selected for its demonstrated ability to enhance phenol degradation as detailed in the preceding section. Experiments were conducted under neutral pH conditions, with an initial concentration of 10 mg L^{-1}, and a photocatalyst loading of 2 g L^{-1}. The photocatalyst that demonstrated the highest performance was subsequently used in the second section for parameter optimisation tests. Design Expert software (version 13.0, Stat-Ease, Minneapolis, United States) was utilised to design a series of experiments and optimise the levels of the process parameters, A: photocatalyst loading (0.5 – 4 g L^{-1}), B: initial solution pH (5 – 12), and C: initial pollutant concentration (5 – 20 mg L^{-1}). A total of 22 experimental runs were simulated using an optimal design with four levels for each parameter as shown in Table 3.1. The three parameters were identified as independent variables, while degradation efficiency was chosen as the response output variable. The optimal values for the process variables were determined using a three-dimensional response surface modelling (RSM). Analysis of variance (ANOVA) was used to analyse the data, with $p < 0.05$ indicating a significant difference between the means. The experimental data were fitted to the quadratic equation shown in Equation (3.1) for statistical analysis. Equation (3.2) was used to determine the experimental response (photodegradation efficiency (%)).

$$Y = P_0 + \sum_{i=1} P_i x_i + \sum_{i=1}^{k} \sum_{j=1}^{k} P_{ij} x_i x_j \sum_{i=1}^{k} P_{ii} x_{ii} + \varepsilon \quad (3.1)$$

$$Y = \left(1 - \frac{C_t}{C_0}\right) \times 100 \quad (3.2)$$

Where Y represents the response; P_0 is the intercept; P_i, P_{ij} and P_{ii} are coefficients of the linear effect and double interactions; x_i and x_j are independent variables; ε is error; C_t and C_0 are pollutant concentration at time t and initial concentration in mg L^{-1}.

Table 3.1: Experimental runs and the corresponding degradation efficiencies for EFV and NVP

Run	A: Photocatalyst loading (g L^{-1})	B: pH	C: Pollutant concentration (mg L^{-1})	Efavirenz degradation efficiency (%)	Nevirapine degradation efficiency (%)
1	0.5	5	15	16.2	18.9
2	0.5	9	10	44.7	49.5
3	2	9	5	40.2	43.2
4	4	5	5	18.6	20.2
5	4	5	5	22.8	18.7
6	2	7	15	42.3	46.3
7	4	12	20	68.6	73.6
8	4	12	20	32.9	27.9
9	0.5	5	5	74.3	71.4
10	2	5	10	42.4	37.3
11	4	5	20	29.9	32.9
12	2	12	15	42.5	45.7
13	4	12	5	34.6	27.6
14	4	5	20	35.8	33.7
15	0.5	9	20	24.8	19.3
16	4	12	5	38.6	42.7
17	0.5	5	5	45.8	41.7
18	4	7	10	24.9	18.3
19	2	5	20	27.7	33.3
20	4	9	15	12.5	6.9
21	1	12	20	75.4	72.9
22	0.5	12	5	75.4	72.9

After optimising the process parameters, kinetics studies were conducted at initial concentrations of 5, 10, and 20 mg L^{-1}. The primary radicals responsible for degradation were identified using scavenger tests. The photostability and reusability tests were conducted as demonstrated in Section 3.5.1.

3.6.3 Photodegradation of ARVDs (continuous flow process)

The study began with batch experiments to establish the effect of light intensity on the efficiency of ARVDs photodegradation. The experiments were conducted in a controlled environment with reflective surfaces to optimise light distribution. A reaction vessel with a capacity of 350 mL was used, containing 200 mL of a 10 mg L^{-1} NVP solution for each test. The experiments utilised 1 to 3 LED lamps as light sources, each emitting a current density of 17.83 mW cm^{-2}, with a combined total power output of 72 W and a wavelength range of 380 – 800 nm. The lamps were positioned 50 mm away from the reactor axis, as illustrated in Figure 3.2. The amount of photocatalyst loading remained consistent at 2 g L^{-1} for all tests. Before exposure to light, the mixtures of pollutant and catalyst were left to reach equilibrium in darkness for 30 min. Hourly samples were taken post-light activation, filtered, and analysed.

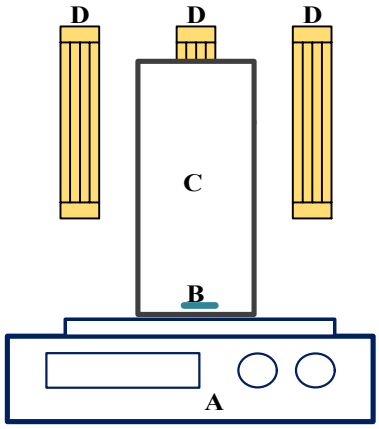

Figure 3.2: Batch photocatalytic reactor setup (A: magnetic stirrer, B: magnetic stirrer bar, C: 350 mL reactor vessel, D: LED lamps).

Continuous flow photodegradation experiments were carried out using the reactor configuration depicted in Figure 3.3, which included a cylindrical Perspex photoreactor with dimensions of 58.5 mm inner diameter and 130 mm height. A solution containing the targeted concentration of either EFV or NVP pollutants was introduced into the photoreactor through a peristaltic pump at a controlled flow rate ranging from 10 to 20 mL min^{-1}. Flow rates below 10 mL/min proved inadequate for membrane penetration, resulting in a batch-like system. Before initiating the pollutant solution flow, a predetermined amount of the photocatalyst was introduced into the reactor to achieve the desired photocatalyst loading for the duration of the experiment. The photocatalyst loading was adjusted between 1 to 3 g L^{-1} with increments of

0.5 g L^{-1}. Photocatalyst loadings exceeding 3 g L^{-1} presented operational difficulties by blocking the lines, necessitating a return to a batch system. Mixing within the reactor was sustained through a magnetic stirrer. Irradiation was initiated once the solution began passing through the membrane, indicating overflow, with this specific moment denoted as zero hour. Subsequent to this, samples were collected hourly, filtered to eliminate any breakthrough particles, and analysed.

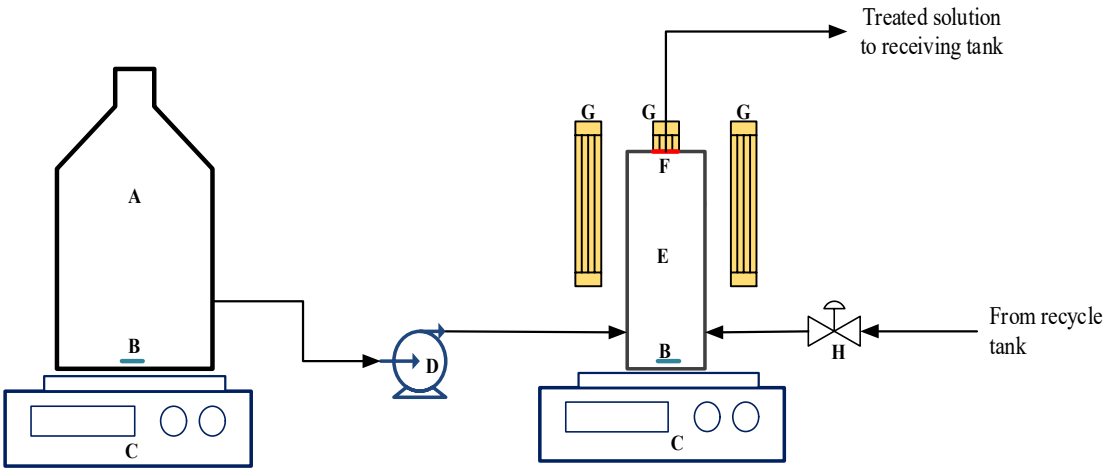

Figure 3.3: Continuous flow photocatalytic reactor setup (A: feed tank, B: magnetic stirrer bar, C: magnetic stirrer, D: Watson Marlow peristaltic pump, E: 350 mL reactor vessel, F: frit membrane, G: LED lamps, H: ball valve).

3.7 Adsorption studies

3.7.1 Experimental

3.7.1.1 Design of Experiments

The experimental design and statistical data analysis were performed using Design Expert software (version 13.0, Stat-Ease Minneapolis, USA). Response surface methodology (RSM) with an optimal (custom) design was employed to investigate the effects of four independent variables on the system. These variables included adsorbent loading (A), operational temperature (B), initial pH of the solution (C), and initial concentration of the pollutant (D). Separate experiments were conducted for EFV and NVP. The optimal design approach was chosen because it allows for any type of input (numeric, discrete, or categorical) and accommodates any constraints while minimising the number of experimental runs required for the specified polynomial model. In this study, a total of 21 experimental runs were conducted to optimise the levels of the design factors as shown in Table 3.2. The ranges for the variables

were as follows: adsorbent loading (A) ranged from 5 to 20 g L^{-1}, operational temperature (B) ranged from 25 to 60 ℃, initial pH of the solution (C) ranged from 5 to 12, and initial pollutant concentration (D) ranged from 5 to 20 mg L^{-1}. The experimental data were fitted to a quadratic model for the statistical analysis, as represented by Equation (3.1). The response variable of interest was the adsorption efficiency (%), determined according to Equation (3.2). The residence time for all 21 runs was kept constant at 24 h.

Table 3.2: Experimental runs and the corresponding adsorption efficiencies for EFV and NVP

Run	A: Adsorbent loading (g L^{-1})	B: Temperature (°C)	C: pH	D: Pollutant concentration (mg L^{-1})	Efavirenz adsorption efficiency (%)	Nevirapine adsorption efficiency (%)
1	20	25	5	20	16.2	18.9
2	10	65	9	5	44.7	49.5
3	5	25	9	10	40.2	43.2
4	12.5	45	7	12.5	18.6	20.2
5	5	65	12	20	22.8	18.7
6	5	45	12	5	42.3	46.3
7	10	25	5	5	68.6	73.6
8	10	25	12	15	32.9	27.9
9	20	25	12	5	74.3	71.4
10	20	65	5	5	42.4	37.3
11	15	55	12	20	29.9	32.9
12	12.5	45	5	10	42.5	45.7
13	5	35	5	20	34.6	27.6
14	20	25	12	20	35.8	33.7
15	20	55	9	20	24.8	19.3
16	5	65	5	10	38.6	42.7
17	20	45	7	5	45.8	41.7
18	12.5	65	5	20	24.9	18.3
19	20	65	12	12.5	27.7	33.3
20	20	45	9	12.5	12.5	6.9
21	20	35	9	5	75.4	72.9

3.7.1.2 Adsorption Studies

Batch experiments were carried out to investigate the adsorption of ARVDs using CLDH as an adsorbent. A volume of 100 mL of simulated wastewater containing the desired concentration of either EFV or NVP was brought into contact with a known mass of CLDH to achieve the desired adsorbent loading. Prior to contact, the initial pH of the solution was adjusted using 0.1 M HCl (acidic) or NaOH (basic). The resulting suspensions were placed on the magnetic

stirrers with temperature control, and continuous stirring was maintained for 24 h at the targeted operational temperature to ensure maximum adsorption. After the 24 h runs, the suspensions were filtered through a 0.45 µm Millipore filter. The solution samples that were obtained from the above-mentioned experiments were analysed as detailed in Section 3.4.3.2. Statistical analysis was performed on the data obtained from the 21 runs to determine the optimum operational conditions. Additional tests were conducted to investigate the adsorption kinetics, isotherms, thermodynamics studies, and reusability of the adsorbent.

3.7.2 Computational Analysis

Materials Studio 2020 software was used for computational analysis of the adsorption and non-covalent interactions (NCI) of EFV and NVP on CLDH. Figure 3.4 shows the modeled structures of the adsorbates and adsorbents, generated using the builder module within the software. The lattice parameters of the 3x3 supercell of CLDH were a = 9.13 Å and b = 9.13 Å with a vacuum of c = 20 Å for the adsorption of the ARVDs. The Adsorption Locator module was used for geometry optimisation and adsorption annealing simulation (Adekoya *et al.*, 2022). This module employs COMPASSIII forcefield for geometry relaxation and the Monte Carlo method to explore various configurational spaces and predict the most stable binding locations of the drugs on the CLDH.

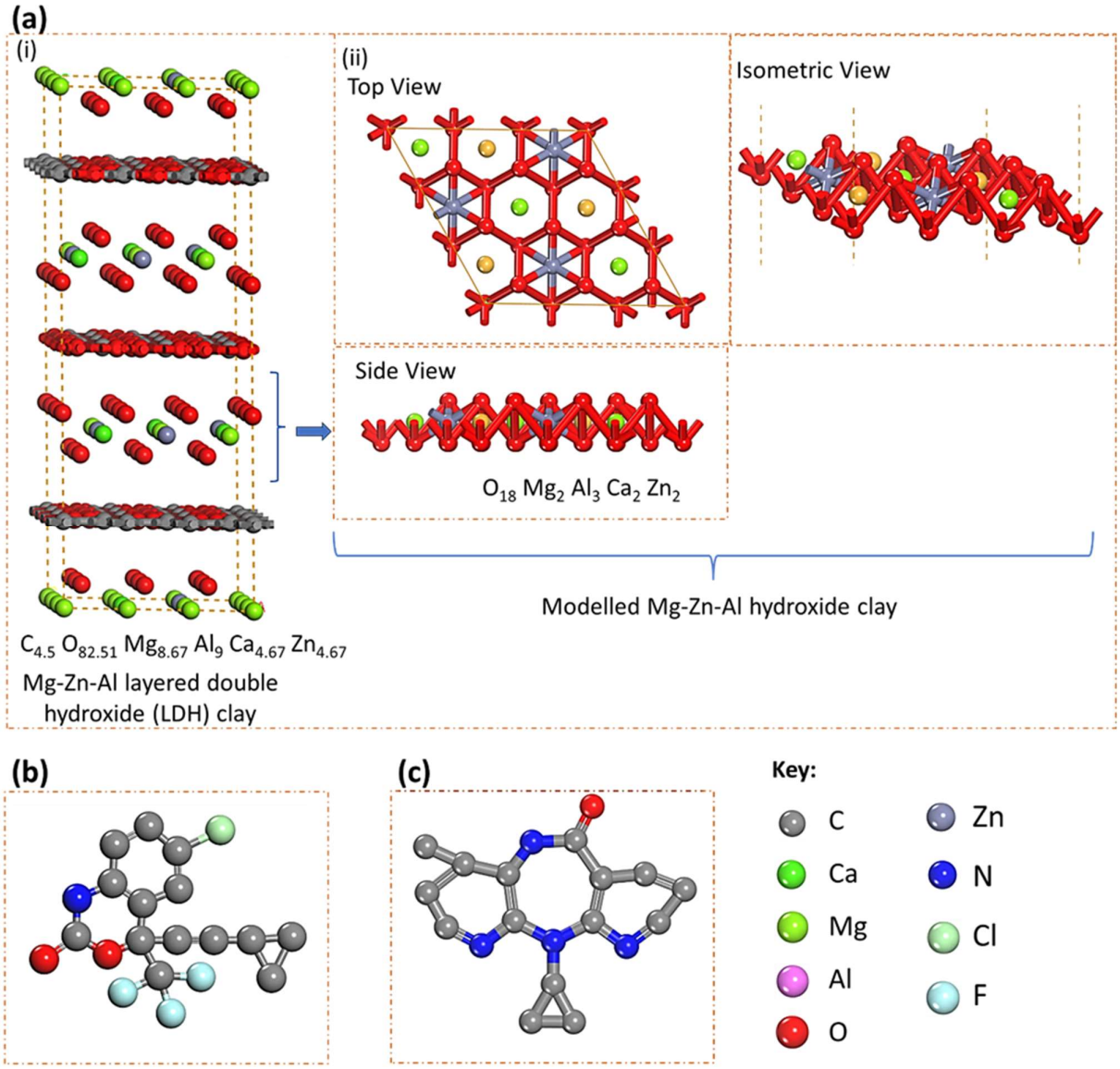

Figure 3.4: 3D structure of the (a) (i) 3x3 CLDH (C4.5 O82.51 Mg8.67 Al9 Ca4.67 Zn4.67) showing the (ii) top, side, and isometric view of the modelled section of the CLDH, (b) EFV and, (c) NVP.

The procedure involved gradually lowering the system's temperature as the drug molecules adsorbed onto CLDH. This allowed for the determination of local energy minima, indicating the most thermodynamically favourable configurations. The probability of accepting a selected configuration was determined using Equation (3.3) while the adsorption energy was estimated by the Adsorption Locator using Equation (3.4) (Adekoya *et al*., 2023).

$$P_{\mathrm{mn}} = min\left(1, \frac{\rho_n}{\rho_m}\right) \quad (3.3)$$

$$\Delta E = E_{\mathrm{sorbate/substrate}} - (E_{sorbate} + E_{substrate}) \quad (3.4)$$

where ρ_m represents the frequency of sampled m configurations, ρ_n represents the frequency of suggested n configurations, and P_{mn} denotes the likelihood of a configuration transition from m to n, ΔE represents the binding energy of the adsorbed atom to CLDH (kcal/mol), $E_{sorbate/substrate}$ is the energy of the system per cell (kcal/mol). In contrast, $E_{sorbate}$ and $E_{substrate}$ represent the isolated energies for the sorbate and adsorbate in the supercell (kcal/mol), respectively.

Non-covalent interactions (NCIs) were computed using the Multiwfn software. Scatter plots were generated using gnuplot, and the visual representation of the plots was facilitated by visual molecular dynamics (VMD) software. Various types and strengths of interactions, including steric repulsion and strong attraction, can be identified through the analysis of isosurfaces and the reduced density gradient (RDG). RDG was calculated using Equation (3.5) (Adekoya *et al.*, 2022).

$$RDGs = \frac{1}{2(3\pi^2)^{\frac{1}{3}}} \frac{|\overline{\Delta\rho}(r)|}{\overline{\rho(r)^{\frac{4}{3}}}} \quad (3.5)$$

Here, ρ(r) is the electron density, and Δρ(r) is gradient norm of electron density.

3.8 Conclusion

The experimental framework combined the synthesis, characterization, and performance evaluation of LDH-based materials for efficient water treatment. LDHs were synthesised, modified with AgBr, and calcined to enhance photocatalytic and adsorption properties. Various characterisation techniques, including XRD, BET, SEM-EDS, XPS, FTIR, and TGA, provided detailed insights into the structural and surface properties of the materials. Computational modelling further clarified the adsorption mechanisms at a molecular level. Pollutant removal was systematically investigated through photocatalytic degradation and adsorption experiments, demonstrating the dual functionality of the materials.

CHAPTER 4: CHARACTERISATION OF THE PHOTOCATALYST COMPOSITE

4.1 Synopsis

This study aimed to characterise a novel composite photocatalyst that consists of Ag-AgBr NPs incorporated in an LDH matrix. The integration of Ag and AgBr within the LDH structure was predicted to enhance the effectiveness of photocatalysis by facilitating the charge separation and expanding the range of light absorption. Various characterisation techniques that include XRD, SEM, TEM, and XPS were utilised to elucidate the structural, morphological, and elemental properties of the photocatalyst. This comprehensive analysis aimed to confirm the successful synthesis of the Ag-AgBr-LDH composite and to provide insights into its photocatalytic performance.

4.2 X-Ray Diffraction Analysis of Photocatalysts

The XRD patterns of the neat LDH, Ag-AgBr and doped LDH were determined through XRD analysis (Figure 4.1). The characteristic peaks of LDH (ICSD 6296) were identified at the following angles: 13.2°, 26.6°, 40.2°, 45.1°, 54.8°, 72.1° and 73.2°. These peaks were assigned the following planes: (003), (006), (012), (015), (018), (110) and (113), respectively. These results confirmed the formation of LDH with carbonate ions (CO_3^{2-}) in the interlayer region (Chen *et al*., 2020a). The positions of the basal planes, d-spacing, crystal parameters (c and a) and the crystallite size (L) for LDH and Ag-AgBr-LDH are shown in Table A1 in the Appendix A. The XRD patterns of the composite catalyst Ag-AgBr-LDH revealed the presence of both LDH and AgBr (ICSD 65061) in the material. A feint peak in the composite at 2θ of 45° was designated to Ag^0 (ICSD 64706) (Feng *et al*., 2020) (an XRD report of the Ag-AgBr-LDH spectra is shown in Figure A1 in the Appendix). This confirmed the successful synthesis of the desired photocatalyst and coexistence of Ag^0, AgBr and LDH in the composite.

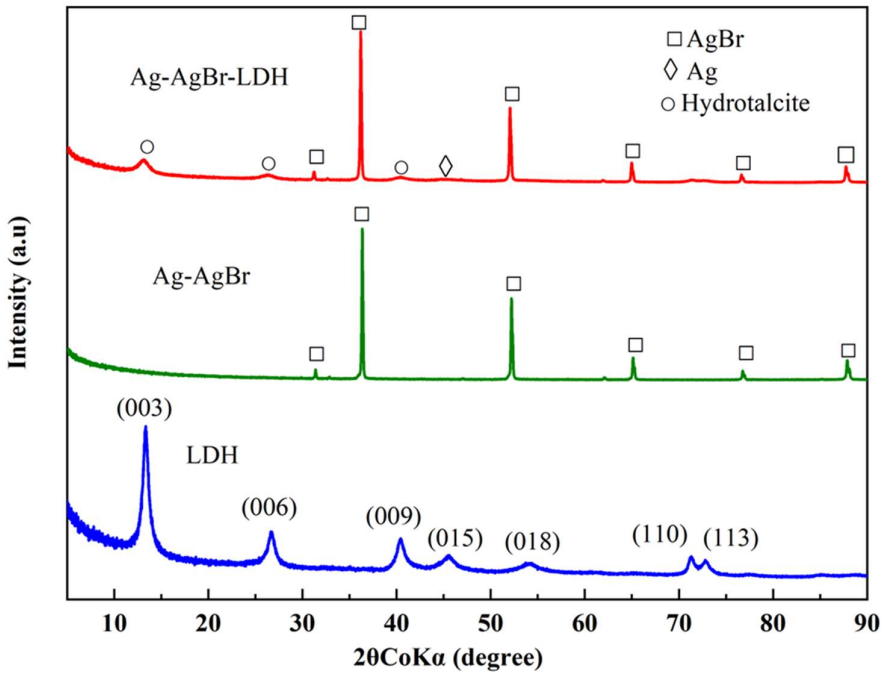

Figure 4.1: (a) X-ray diffraction spectra of neat LDH, Ag-AgBr and Ag-AgBr-LDH composite catalysts.

4.3 Scanning Electron Microscopy and Transmission Electron Microscope Analyses of Photocatalysts

The morphologies of LDH, Ag-AgBr and Ag-AgBr-LDH photocatalysts are shown in Figure 4.2. LDH was characterised by platelet-like structures that are synonymous with hydrotalcites (Figure 4.2 (a)). Ag-AgBr photocatalyst exhibits irregular spherical-like shapes, as demonstrated in Figure 4.2 (c) (Moja *et al*., 2021), with the presence of mesopores observed on the surface of these particles. The presence of minute particles in Figure 4.2(c) could plausibly be attributed to the partial reduction of Ag^{+} ions within the AgBr compound. Figure 4.2(e) displays the morphology of the composite catalyst, which shows the LDH platelet-like structures covered by near-spherical Ag-AgBr nanoparticles. The elemental compositions of LDH, Ag-AgBr and Ag-AgBr-LDH photocatalysts were examined using energy dispersive X-ray spectroscopy (EDS) and the results are presented in Figure 4.2(b), (d) and (f), respectively. The elemental analysis conducted on both LDH and the Ag-AgBr-LDH composite confirmed the presence of Mg, Zn, and Al in both materials. Additionally, the molar ratios of Ag to Br were determined to be 1.43 and 1.48 in Ag-AgBr and Ag-AgBr-LDH composite photocatalysts, respectively. These ratios indicated an excess of Ag relative to Br, providing further evidence of the successful formation of Ag^{0} in the photocatalyst composite.

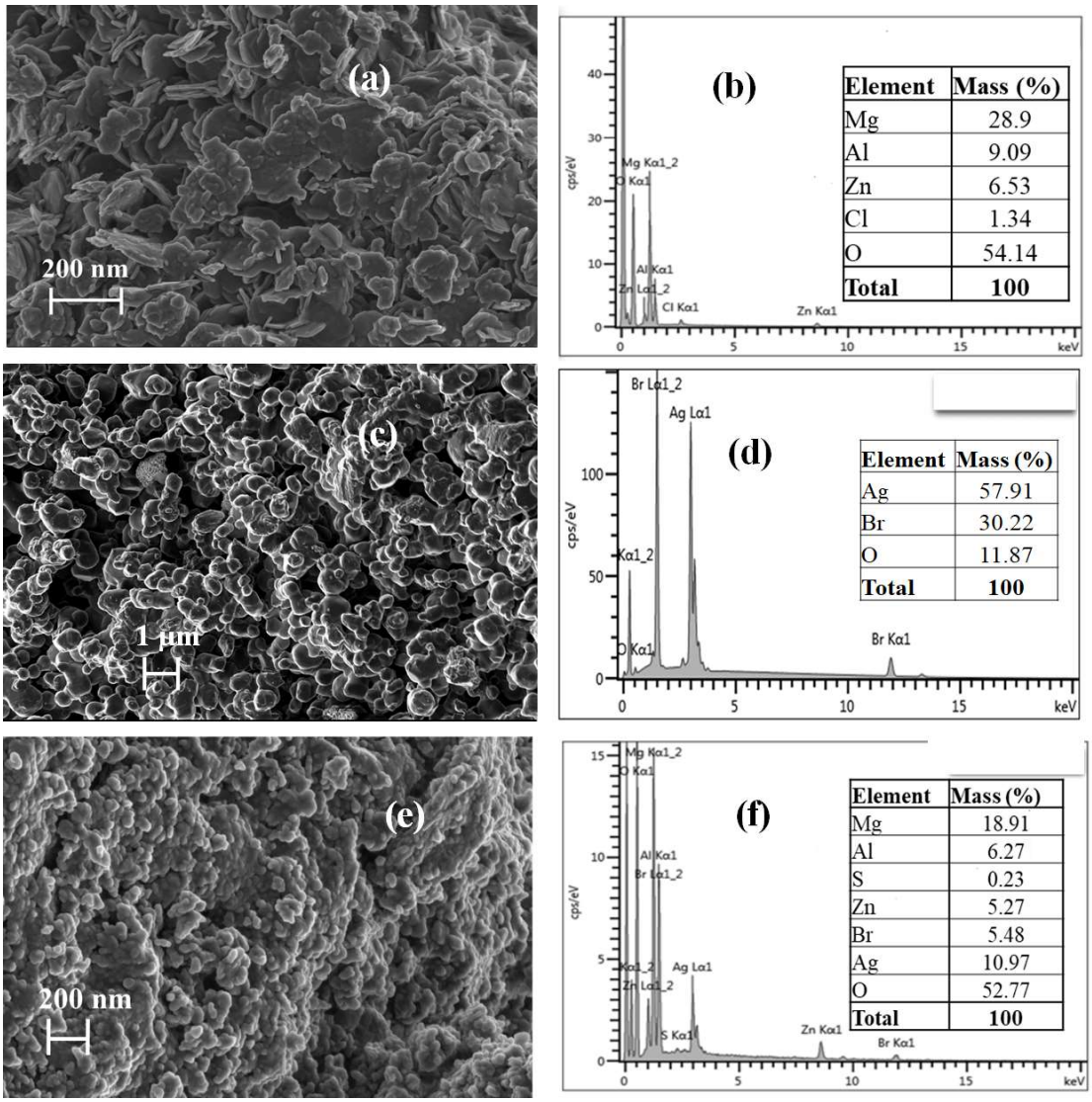

Figure 4.2:SEM and SEM-EDS analysis of LDH (a) & (b), Ag-AgBr (c) & (d) and Ag-AgBr-LDH (e) & (f) photocatalysts.

Figures 4.3 (a) – (f) depict the High-Angle Annular Dark-Field Scanning Transmission Electron Microscopy (HAADF-STEM) image and EDS elemental mapping images of the Ag-AgBr-LDH composite photocatalyst. The HAADF-STEM (Figure 4.3(a)) represents the composite photocatalyst, revealing the spatial distribution and arrangement of different elements. The elemental maps (Figures 4.3 (b) – (f)) indicate the presence and distribution of Mg, Al, Zn, Ag, and Br. Notably, the well-distributed elements in their respective regions confirm the successful loading of Ag-AgBr particles onto LDH substrate. Figures 4.3(g) – (i) show the results obtained from TEM analysis of LDH, Ag-AgBr, and Ag-AgBr-LDH photocatalyst. The TEM image of LDH (Figure 4.3(g)) exhibits a well-structured morphology,

suggesting a high level of crystallinity in the material. This observation is consistent with the findings from XRD analysis, further supporting the crystalline nature of LDH. In Figure 4.3(h), distinct near-spherical Ag-AgBr particles are clearly visible. Notably, Figure 4.3(i) highlights the encircled area where Ag-AgBr particles are observed near the LDH substrate. These findings confirm the successful embedding of Ag-AgBr particles onto LDH.

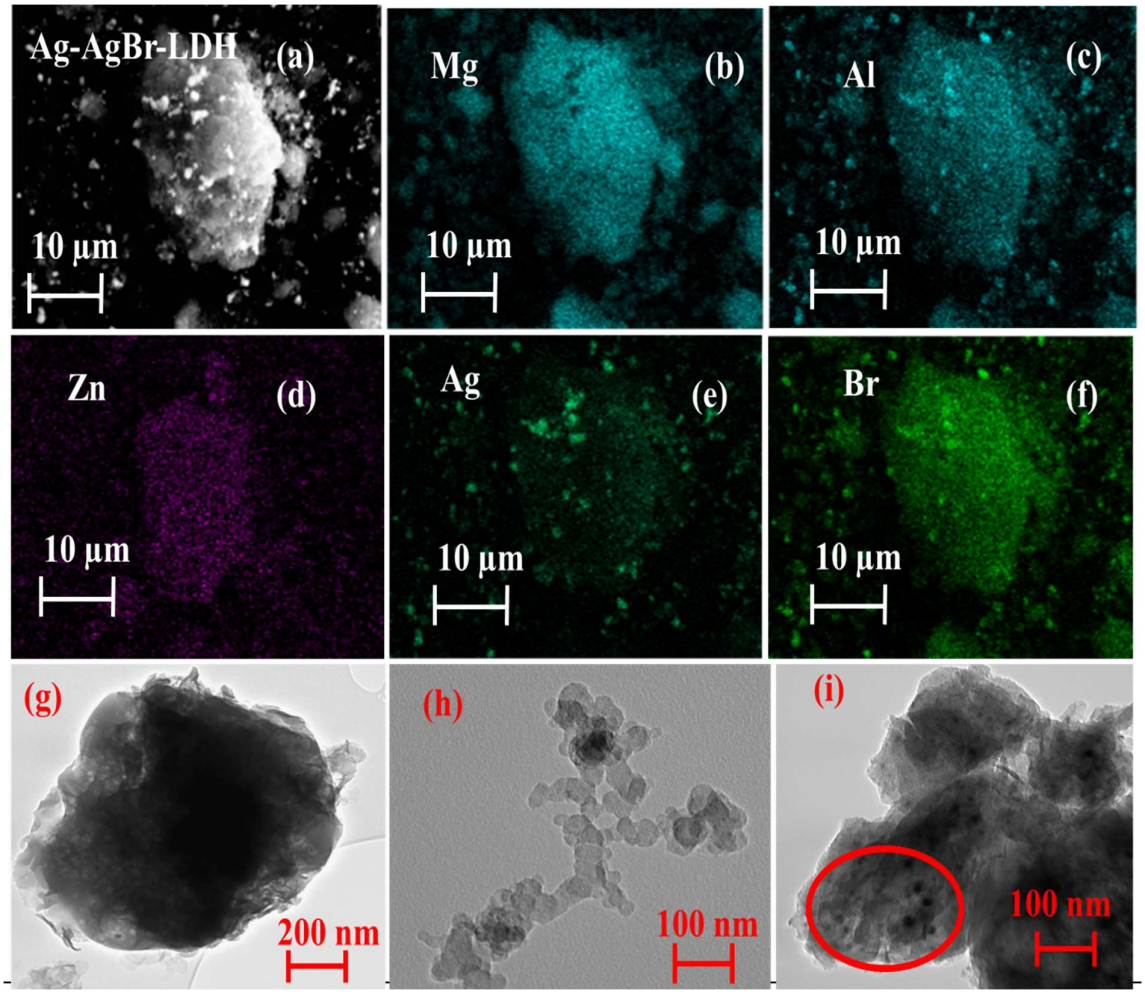

Figure 4.3: HAADF-STEM image of Ag-AgBr-LDH (a), EDS mapping, Mg (b), Al (c), Zn (d), Ag (e) & Br (f). TEM images, LDH (g), Ag-AgBr (h) & Ag-AgBr-LDH (i).

4.4 X-ray Photoelectron Spectroscopy Analysis

Figure 4.4 shows the X-ray photoelectron spectroscopy (XPS) spectra for LDH and Ag-AgBr-LDH photocatalysts. The Mg 1s spectra (Figure 4.4(b)) at the binding energies of 1304.4 and 1305.6 for LDH and Ag-AgBr-LDH photocatalyst respectively were attributed to the magnesium containing hydroxides (Zhu *et al*., 2021). The Al 2p spectra (Figure 4.4(c)) at 74.6 eV displayed only one peak that showed the presence of aluminium containing hydroxides (Wang *et. al*., 2016). In Figure 4.4 (d), Zn enriched hydroxides are represented by the Zn $2p_{3/2}$ and Zn $2p_{1/2}$ peaks located at 1022.2 and 1045.4 eV respectively (Zhu *et al*., 2021). The Ag3d spectra (Figure 4.4(e) displayed two individual peaks at 368 and 374 eV which were ascribed to Ag $3d_{5/2}$ and $3d_{3/2}$ of Ag^0 and Ag^+. The Ag 3d spectra in this study are similar to those reported by Zhang *et al*. (2020), Liu *et al*. (2013), and Wang *et al*. (2009) who stated that the peak at 368 eV was due to Ag^0 while Ag^+ was represented at 374 eV. These results are in agreement with XRD spectra for the composite catalyst which also revealed the presence of Ag^0. The peak at 68 eV in the Br 3d spectrum (Figure 4.4(d)) was attributed to the crystal lattice of Br^- in AgBr (Parvizi *et al*., 2022). The O 1s spectra showed three peaks at 532.2, 532 and 530 eV, representing O in adsorbed water, metal hydroxides and lattice oxygen respectively (Nayak & Parida, 2018).

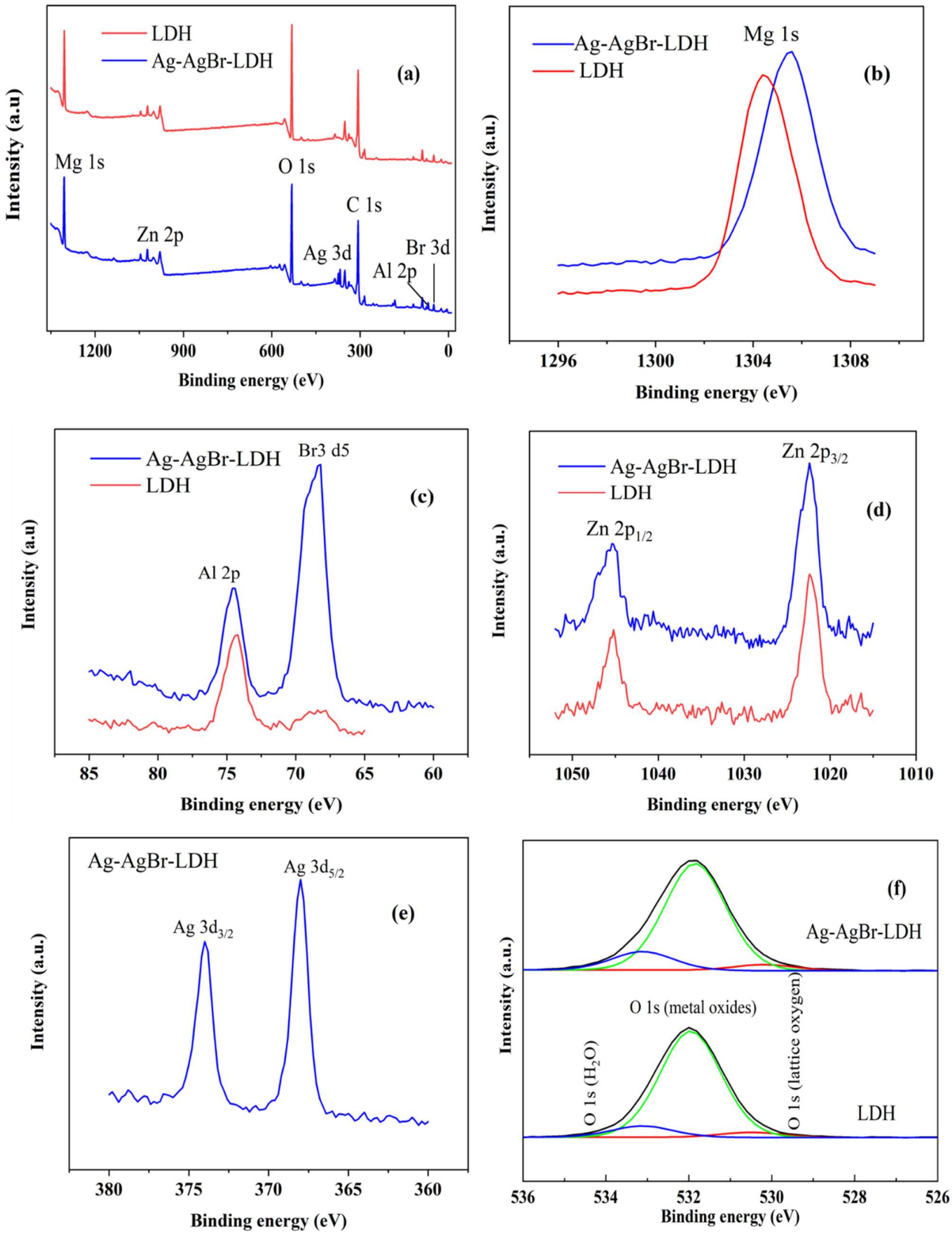

Figure 4.4: XPS spectrum of LDH and Ag-AgBr-LDH photocatalysts (a) The survey spectrum peaks and the high resolution XPS spectra of (b) Mg 1S, (c)Br 3d5, (d) Zn 2p 3, (e) Ag 3d and (f) O 1s.

4.5 Brunauer-Emmett-Teller Surface Area

Figure 4.5 depicts the nitrogen gas adsorption and desorption isotherms of LDH and Ag-AgBr-LDH. The isotherm curves correspond to Type IV isotherms in accordance with IUPAC classification (Muttakin et. al., 2018). This showed that the photocatalysts had mesopores with a diameter range of 2-50 nm (Tun et. al., 2019). This finding aligns with the mesoporous structure observed in the SEM analysis. Doping the LDH with Ag-AgBr NPs resulted in decreased pore volume (0.075 cm^3 g^{-1} to 0.022 cm^3 g^{-1}) and specific surface area (28.5 m^2 g^{-1} to 10.6 m^2 g^{-1}) compared to neat LDH.

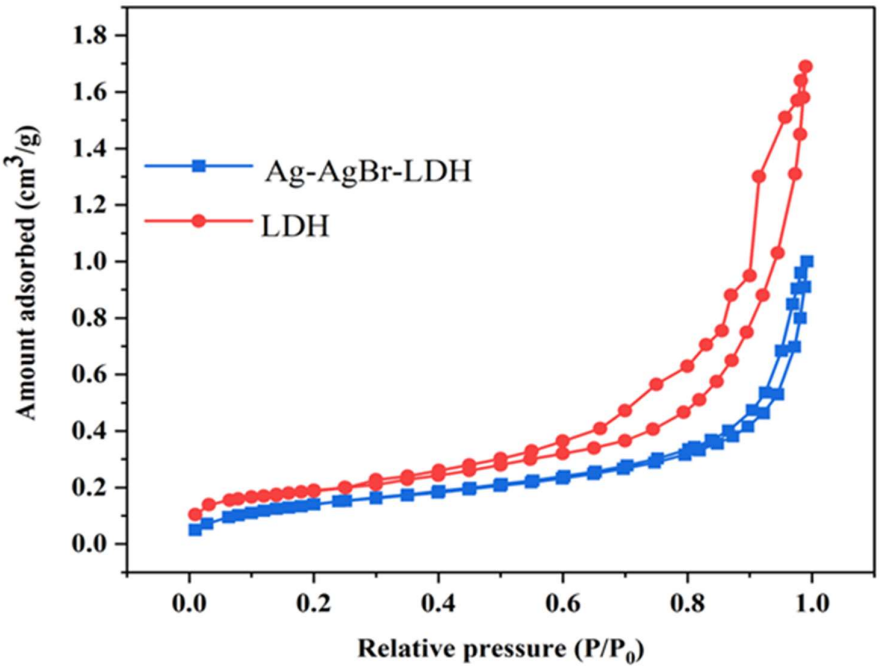

Figure 4.5: Nitrogen adsorption-desorption isotherms of LDH and Ag-AgBr-LDH.

4.6 Conclusion

The detailed characterisation of the Ag-AgBr-LDH composite photocatalyst have been demonstrated through various analytical techniques. XRD analysis confirmed the formation of LDH with carbonate ions in the interlayer region and the incorporation of Ag0 and AgBr in the composite. SEM and TEM analyses revealed the platelet-like structure of the LDH and the well-distributed Ag-AgBr particles, confirming the effective embedding of Ag-AgBr onto the LDH substrate. XPS provided further evidence of the presence of key elements such as Mg, Zn, Al, Ag, and Br, supporting the findings from the structural analyses. Additionally, nitrogen adsorption-desorption isotherms indicated a reduction in pore volume and specific surface area

upon doping with Ag-AgBr NPs. These findings collectively confirm the successful synthesis of the Ag-AgBr-LDH composite.

CHAPTER 5: VISIBLE LIGHT ACTIVATED DEGRADATION OF PHENOL USING SILVER-SILVER BROMIDE-HYDROTALCITE NANOCOMPOSITE PHOTOCATALYST

5.1 Synopsis

This section focuses on evaluating the performance of the Ag-AgBr-LDH composite material as a photocatalyst, with phenol serving as the model pollutant. Phenol was selected due to its properties, which are similar to those of recalcitrant organic pollutants, such as the ARVDs under investigation. By investigating the effects of varying silver content, catalyst loading, and pH on the photocatalytic degradation of phenol, the study aimed to determine the optimal conditions for achieving the highest degradation efficiency. Additionally, this research explored the kinetics of the reaction, the mechanisms underlying phenol degradation, and the stability and reusability of the composite catalyst.

5.2 Effect of Silver Content

Figure 5.1 shows the degradation efficiencies of phenol with varied compositions of Ag in the photocatalysts. The pristine LDH adsorbed 4% phenol in the dark while the photodegradation control experiment resulted in 19% degradation efficiency under visible light irradiation. Previous studies show similar findings under adsorption conditions (Tabana *et al*., 2020) and photolysis (Gevers *et al*., 2022). Tabana *et al*. (2020) demonstrated that neat LDH, comprising MgAlZn, exhibited an adsorption efficiency of only 6% in a system with an initial phenol concentration of 40 mg/L and an adsorbent loading of 10 g/L. This highlights the limited adsorption capacity of neat LDH, which aligns with my findings where the inclusion of Ag and AgBr enhances the functional performance of the composite. Gevers *et al*. (2022) reported that LDH materials exhibit limited light absorption under visible light irradiation. This suggests that, in photocatalytic degradation systems using LDH as the photocatalyst, phenol removal is primarily due to adsorption and photolysis rather than photocatalytic degradation. The photocatalyst containing only Ag and AgBr was able to reach 8 and 45% phenol degradation in the dark and under visible light irradiation respectively. Doped LDH materials showed an improvement in phenol degradation efficiencies compared to neat LDH. There was a slight increase in degradation efficiency (52% to 57%) when the Ag content in the photocatalyst composite was increased from 0.075 to 0.15 g per 1 g of LDH after 8 h of visible light irradiation. Phenol removal of 76% was observed when 0.3 g Ag per 1 g LDH was used in the photocatalyst. The increase in Ag content in the photocatalyst composite meant that there was

an increase in Ag NPs on the surface of AgBr (which is bound to LDH). The Ag NPs can improve photocatalytic activity by enhancing light harvesting capacity of the photocatalyst through SPR (Chen *et al*., 2020a), and Ag^0 can be active as an electron mediator to form the z-scheme heterojunction (Sharma *et al*., 2021). The enhanced degradation efficiency at higher Ag content can be attributed to these two phenomena, particularly when considering that the bandgaps of the photocatalysts exceed 3 eV, implying limited light absorption within the visible spectrum. The Tauc diagrams illustrating the optical properties of LDH, Ag-AgBr, and Ag-AgBr-LDH photocatalysts are presented in Figure B1 (Appendix B).

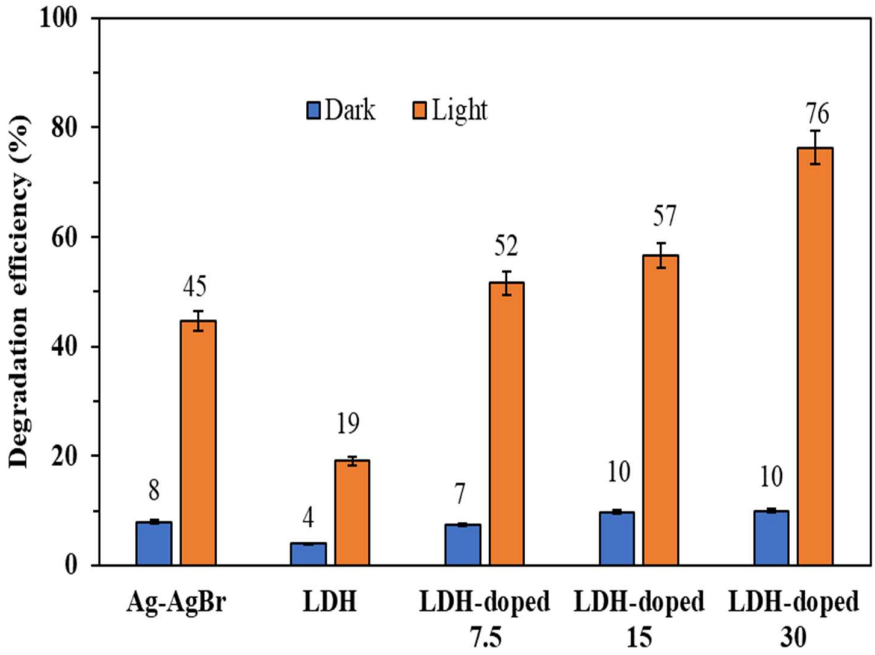

Figure 5.1: Phenol degradation efficiencies with varying Ag content in the photocatalyst.

5.3 Effect of Catalyst Loading

Figure 5.2 shows how the degradation efficiency varied with catalyst dosage from photolysis (0 g L^{-1}) to 4 g L^{-1}. Phenol degradation efficiency increased with catalyst loading up to 2 g L^{-1}, with the highest removal of 92% observed after 8 h. An increase in photocatalyst loading beyond 2 g L^{-1} (at 4 g L^{-1}) resulted in an increase in solution turbidity and subsequently a decrease in photocatalytic degradation of phenol. An increase in the amount of photocatalyst is expected to increase the photocatalytic efficiency, as more active sites become available. However, an excess number of nanoparticles in a photocatalytic reactor can create a light screening effect that can reduce the surface area of the nanoparticles being exposed to light;

subsequently affect the photocatalytic efficiency (Chong *et al.*, 2010). The photocatalyst loading of 2 g/L was identified as the optimal loading and was subsequently used for the proceeding tests.

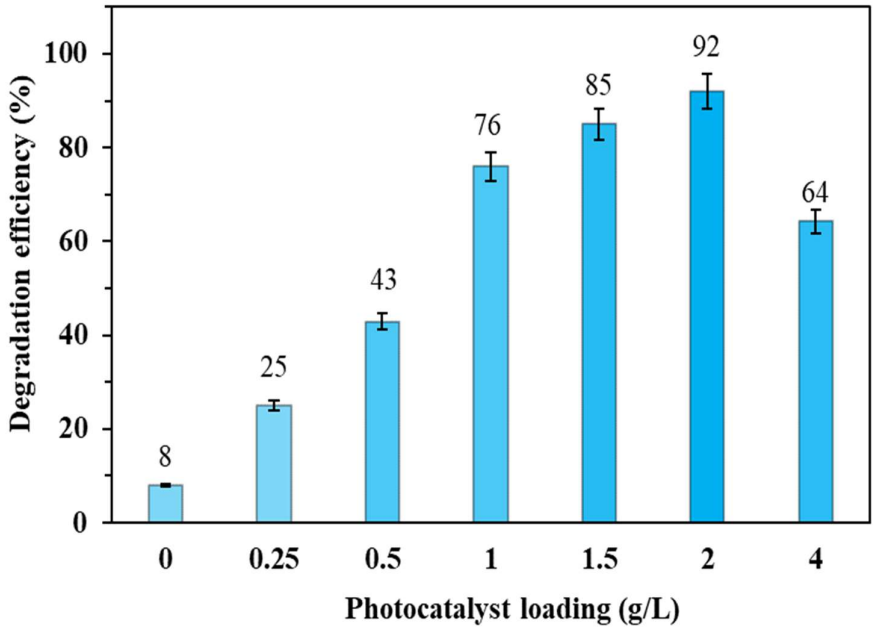

Figure 5.2: Phenol degradation efficiencies with varying photocatalyst loading.

5.4 Effect of pH

Figure 5.3 shows the effect of pH on the extent of phenol degradation. The highest phenol degradation efficiency occurred when the initial pH of the solution was kept at 6.68 (unadjusted pH). Phenol adsorption capacities using LDH materials have been reported to be at their highest at neutral pH (Tabana *et al.*, 2020, Lupa *et al.*, 2018). This is due to the hydrogen bonds between the surface of the photocatalyst and the hydroxyl groups in phenol (Tsukanov & Psakhie, 2016). The degradation efficiencies of phenol in acidic and basic conditions were lower than in neutral conditions for the following reasons. In an acidic medium, phenol does not dissociate, meaning that the solution would contain phenol, protons, and chloride ions. Chloride ions can inhibit photocatalysis degradation of phenol by acting as scavengers for photo-induced holes and hydroxyl radicals, as shown in Equations (5.1) and (5.2). Chlorine radicals (Cl•) have been reported to be ineffective in abstracting hydrogen atoms from saturated compounds, hence a lower phenol degradation efficiency (Kashif & Ouyang, 2009). In basic solutions, sodium phenolate becomes the dominant phenol species; the displacement of

hydroxyl ions by sodium can result in reduced hydrogen bonding between phenolate and the surface of the photocatalyst. This causes a drop in adsorption capacities and, subsequently lower degradation efficiencies. Neutral pH (approximately 7) was determined to be the optimal pH for the system and was used for the subsequent tests.

$$Cl^- + \bullet OH \rightarrow Cl + OH^- \quad (5.1)$$

$$Cl^- + h_{vb}^+ \rightarrow Cl\bullet \quad (5.2)$$

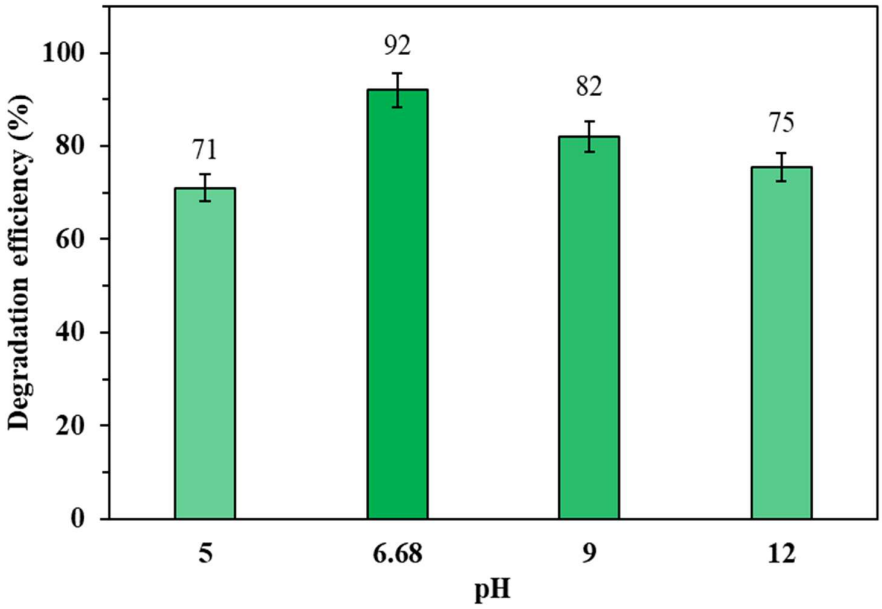

Figure 5.3: Effect of pH on phenol degradation efficiencies.

5.5 Reaction Kinetics and the Effect of Phenol Concentration

An increase in phenol concentration from 5 mg L^{-1} to 10 mg L^{-1} led to a reduction in the extent of phenol degradation from 100% to 73% in 4 h (Figure 5.4). A further decline in phenol degradation efficiency from 73% to 44% was observed when the initial concentration was increased from 10 mg L^{-1} to 20 mg L^{-1} within the same period. The three possible reasons for the decline in degradation efficiency at elevated concentrations, as elaborated by Li *et al.* (2019) were: firstly, the formation of intermediate products results in competition with the primary pollutant for active sites, leading to poor contact between the pollutant and photocatalyst. Secondly, the generation of radicals on the surface is reduced in the presence of high pollutant concentration since pollutant molecules cover the active sites. Lastly, a significant amount of light can be absorbed by pollutants leading to a drop in the generation of active radicals. As a comparison of the photocatalyst in this study with previous work reported

by other authors: a 71% degradation efficiency of 5 mg L^{-1} phenol was achieved in 2 h with Zn-Al LDH photocatalyst (Patzkó, 2005), and 70% of 40 mg L^{-1} phenol was degraded after 6 h with Mg-Zn-Al LDH photocatalyst (Valente *et al*., 2009); both studies were conducted under UV light irradiation. Therefore, the photocatalyst composite presented in this study presents a feasible alternative for degradation of phenolic contaminants from wastewater under visible light irradiation.

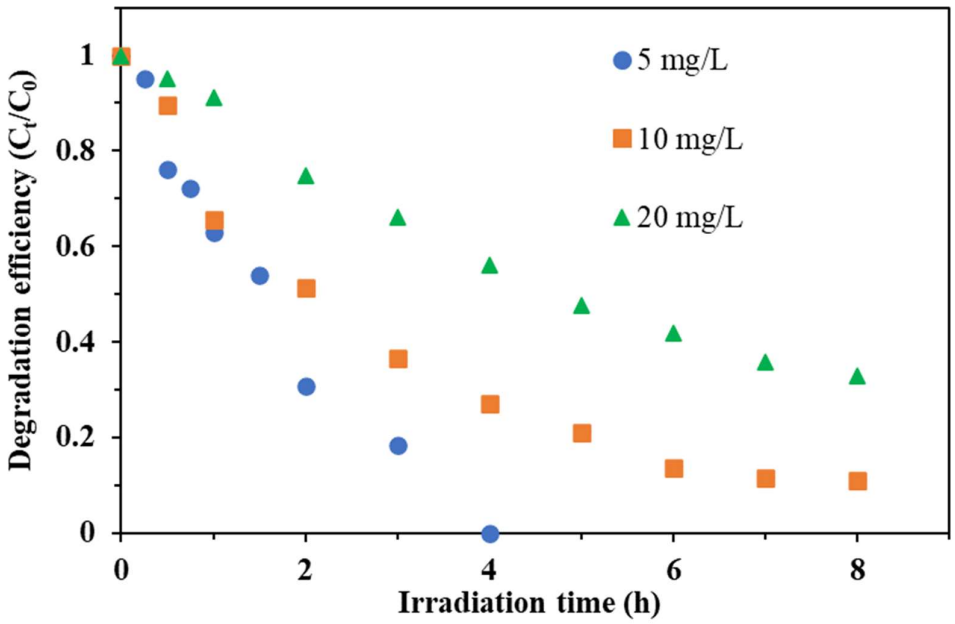

Figure 5.4: Phenol degradation efficiencies at various initial concentrations.

The kinetics of photocatalytic reactions of organic contaminants are usually described by the Langmuir-Hinshelwood (L-H) model (Valente *et al*., 2009, Li *et al*., 2019, Mantilla *et al*., 2010). The model relates the degradation rate r and the concentration of the pollutant C as shown in Equation 5.3.

$$r = \frac{-dC}{dt} = \frac{k_r K_{ad} C}{1 + K_{ad} C} \qquad (5.3)$$

Where k_r is the rate constant, and K_{ad} is the adsorption equilibrium constant. At lower concentrations of the pollutant and adsorption capacities, the term $K_{ad}C$ becomes negligible, and the equation can be simplified to be first-order kinetics with an apparent rate constant ($k_{app} = k_r K_{ad}$). After simplification and integration of the L-H model over the interval [C_0, C_t] the new expression becomes as shown in Equation 5 4.

$$\ln\left(\frac{C_0}{C_t}\right) = k_{app} t \qquad (5.4)$$

The plot of $\ln(C_0/C_t)$ against irradiation time t is linear where k_{app} is the slope. Figure 5.5 shows the lineal plot of phenol degradation at various initial concentrations with k_{app}, half-life $(t_{1/2})$ and the linearisation coefficient R^2 listed in Table 5.1.

Table 5.1: Apparent rate constant, half-life, and linearisation coefficient for the Langmuir-Hinshelwood model at various concentrations

Concentration (mg L^{-1})	**k_{app} (h^{-1})**	**$(t_{1/2})$ (h)**	**R^2**
5	0.578	1.32	0.978
10	0.294	2.12	0.985
20	0.146	4.86	0.997

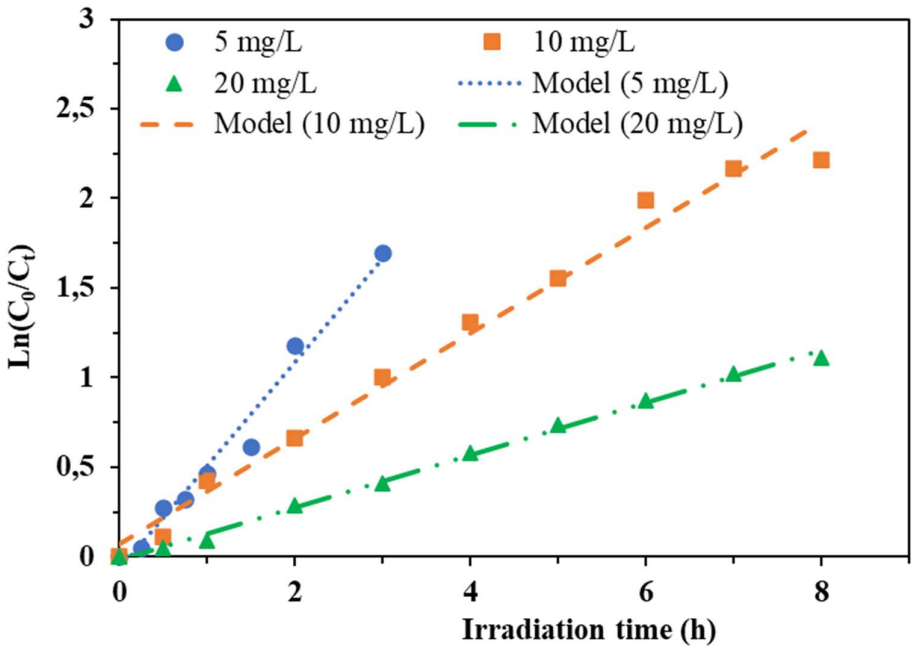

Figure 5.5: First-order kinetics photodegradation of phenol at various initial concentrations.

5.6 Degradation Mechanism

Figure 5.6 shows phenol degradation efficiencies in the presence of various radical scavengers. Isopropanol (IPA), p-benzoquinone (PBQ), copper (II) nitrate (CN) and sodium oxalate (SO) were used as scavengers for hydroxyl radical ($^{\bullet}OH$), superoxide radical $^{\bullet}O_2^-$, electrons (e^-) and photo-induced holes (h^+) respectively. Figure 5.6 shows that phenol degradation efficiency

decreased from 92% to 32% when IPA was added into the system, indicating that (•OH) plays a critical role in the degradation process. The addition of PBQ and SO showed a moderate reduction in phenol degradation efficiencies of 63% and 55%, which suggests that superoxide radicals and the photo-induced holes were not the major drivers of the phenol degradation mechanism. A 12% reduction in phenol concentration was observed upon the addition of CN as an electron scavenger. Several researchers who studied photocatalytic degradation of pollutants using LDH-based materials have reported similar results (Zheng *et al*., 2022, Wang *et al*., 2021, Pica, 2019).

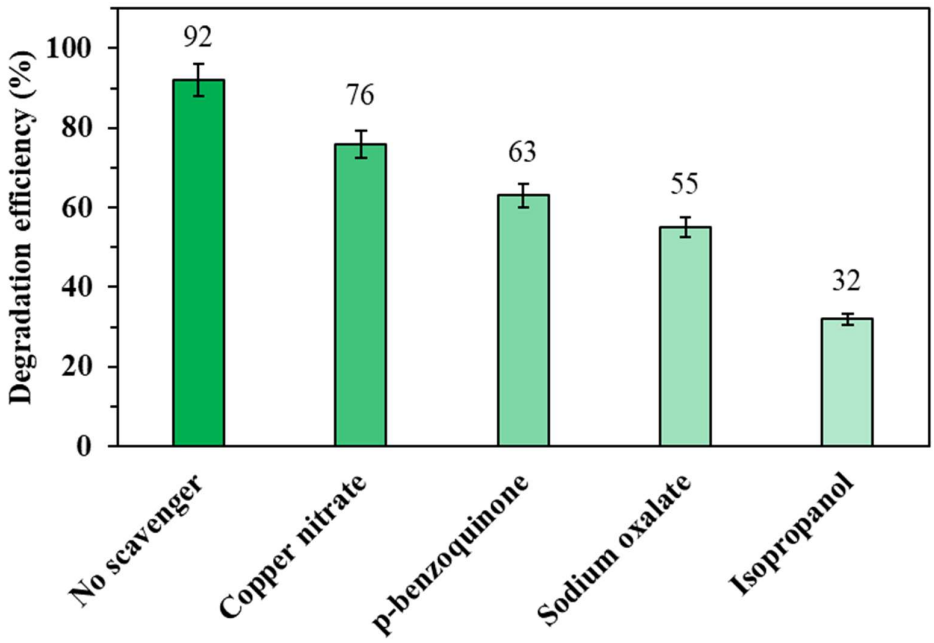

Figure 5.6: Effect of different scavengers on the degradation of phenol by the composite photocatalyst.

The reaction of phenol with •OH radicals produce catechol, resorcinol and hydroquinone as intermediates (Wu *et al*., 2001). The breaking of the phenyl rings follows to produce short-chain organic acids, such as oxalic, formic, maleic, and acetic acid before carbon dioxide (CO_2) can be formed. It is hypothesised that a similar degradation pathway (Figure 5.7) took place in this study. GC-MS analysis on the residual phenol solutions after the photocatalytic process revealed that catechol, glycerol, and hydroxy acetic acid were some of the intermediates formed (Figure B2 to B6 (Appendix B)). Maleic, oxalic, malonic acid and benzoquinone were not detected.

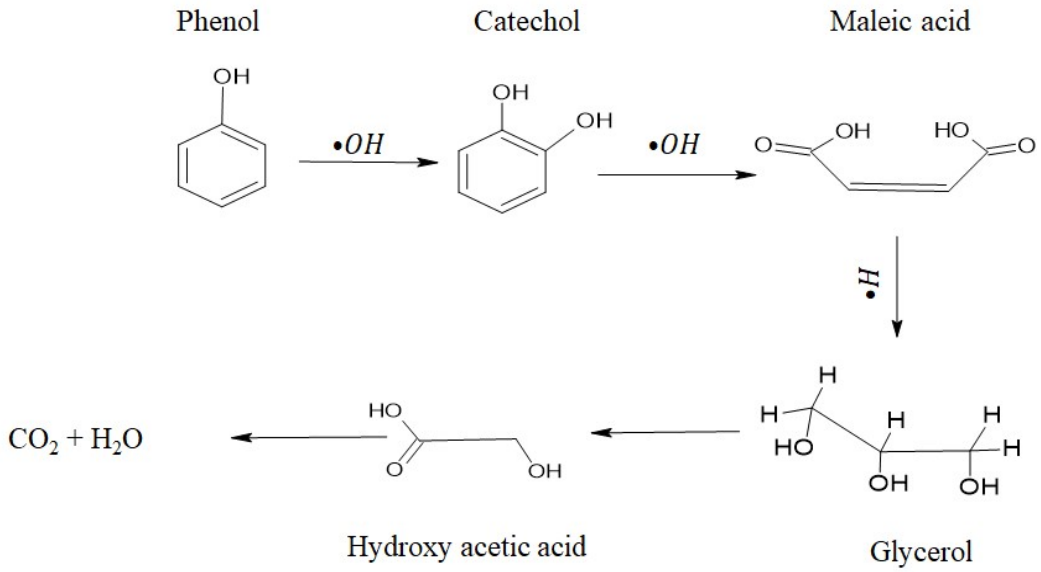

Figure 5.7: Proposed phenol degradation pathway.

5.7 Photo Stability and Reusability of the Catalyst

The composite catalyst was recycled in a series of tests to evaluate its stability and reusability. Figure 5.8 shows a gradual decrease in the degradation efficiency after the first two cycles from 92% to 80% degradation. Thereafter, there was a 27% decrease in efficiency between Run 3 and 4. XRD analysis on the photocatalyst composition used for each run showed that the amount of Ag^0 increased after each run (Table 5.2 and Figure B7). While Ag^0 plays a role in SPR phenomenon, it has a potential to cause photo-corrosion of the catalyst when present in elevated quantities (Sharma *et al*., 2021). Therefore, it can be postulated that the increased amounts of Ag^0 caused photo-corrosion of the photocatalyst, which resulted in a decline in degradation efficiency.

Table 5.2**:** Quantitative XRD analysis of the photocatalyst composite used in each test run

Run number	Phase composition (%)		
	Ag	AgBr	Hydrotalcite
Run 1	0.92	29.58	69.5
Run 2	1.4	26.8	71.8
Run 3	2.2	24.3	73.5
Run 4	3.8	20.5	75.7

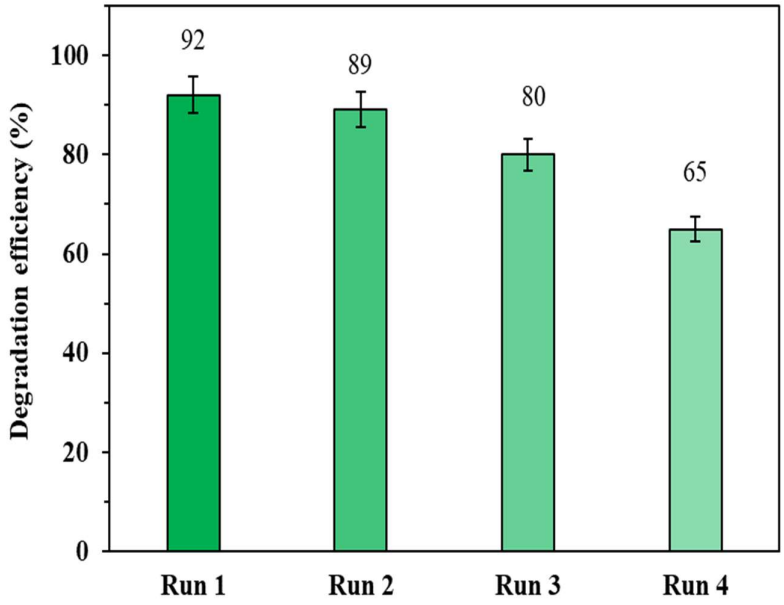

Figure 5.8: Stability and reusability tests of the photocatalyst.

5.8 Conclusion

This composite photocatalyst containing Ag-AgBr and LDH proved to be more effective in degrading phenol than Ag-AgBr and LDH separately. The presence of Zn in the photocatalyst was vital in enhancing the photocatalytic activity of the material and subsequently led to a higher phenol degradation efficiency. More than 92% of phenol was degraded over 8 h at neutral pH, under visible light irradiation. Catechol, glycerol, and hydroxy acetic acid were detected as the main intermediates produced during the phenol degradation pathway which was primarily driven by the hydroxy free radicals' present followed a process mechanism that has hydroxyl radical as the dominant species.

CHAPTER 6: PHOTOCATALYTIC DEGRADATION OF EFAVIRENZ AND NEVIRAPINE USING VISIBLE LIGHT-ACTIVATED AG-AGBR-LDH NANOCOMPOSITE CATALYST

6.1 Synopsis

This study investigated the degradation of EFV and NVP using an Ag-AgBr-LDH composite photocatalyst. The research explored the performance of a composite photocatalyst and its constituents under different conditions that include adsorption and visible light irradiation. Statistical analysis using ANOVA was employed to optimise the degradation parameters, and the kinetics of the photodegradation process were examined. Additionally, the study evaluated the photostability and reusability of the photocatalyst, providing insights into the mechanisms driving the degradation process.

6.2 Degradation of ARVDs using Various Photocatalysts

Figure 6.1 shows the removal efficiencies of EFV (Figure 6.1(a)) and NVP (Figure 6.1(b)) for the composite photocatalyst and its constituents under control conditions, adsorption, photolysis, and visible light irradiation. LDH materials are well-known for their ability to remove pollutants through various mechanisms such as surface adsorption, intercalation (Tabana *et al*., 2020, Lei *et al*., 2014), and adsolubilisation (Ruan *et al*., 2013). It is noteworthy that the LDH material in this study was neither calcined nor did its interlayer anions undergo modification, so surface adsorption was most likely to occur. However, since the bonding forces involved in the physical adsorption of pollutants onto LDH are weak (Cornejo *et al*., 2008), the adsorption efficiencies of neat LDH were limited to 5%. The Ag-AgBr photocatalyst could only degrade 41% of EFV and 55% of NVP under visible light irradiation, with adsorption efficiencies for both pollutants falling below 10%. However, the Ag-AgBr-LDH nanocomposite photocatalyst demonstrated up to 13% adsorption efficiencies and significantly improved photodegradation efficiencies of 84% and 100% for EFV and NVP, respectively. This enhancement can be attributed to surface plasmon resonance and/or z-scheme heterojunction formation (Zheng *et al*., 2022). The Ag NPs in the photocatalyst can improve the photocatalyst's light-harvesting capacity through SPR and act as electron mediators in the formation of a Z-scheme heterojunction (Zheng *et al*., 2023). LDH and AgBr play essential roles as photo-induced electron and hole sinks, respectively. After establishing that Ag-AgBr-LDH was the most effective photocatalyst, parameter optimisation tests with this photocatalyst were performed.

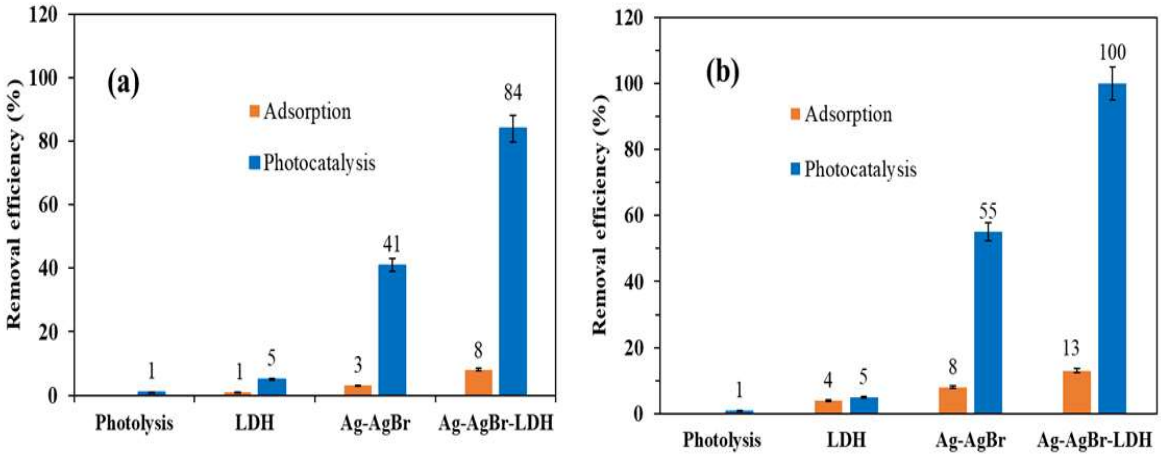

Figure 6.1: Photodegradation efficiencies of ARVDs using various photocatalysts, (a) efavirenz and (b) nevirapine.

6.3 Statistical analysis of the ARVDs Photodegradation Process using ANOVA

Table 3.1 showed the experimental design results for the degradation efficiencies of EFV and NVP. Tables 6.1 and 6.2 show the ANOVA results for EFV and NVP, respectively. The quadratic polynomial equations (Equations (6.1) and (6.2)) were derived using relative parameters to optimise the conditions for maximising the degradation efficiencies of the ARVDs. ANOVA was utilised to assess the significance and adequacy of the quadratic models in describing the experimental data. The statistical significance of each variable and its effect on the response were determined using p-values and F-values at a 95% confidence level. Variables with p-values less than 0.05 were considered to be statistically significant. F-values of 30.13 for EFV and 35.45 for NVP indicated that the second-order polynomial models were highly significant. The probability that these F-values resulted from random noise was estimated to be 0.01%.

$$Y_{EP} = 86.69 + 16.87A - 1.98B - 7.75C + 6.69AC - 14.50A^2 + 7.16C^2 \quad (6.1)$$

$$Y_{NP} = 91.48 + 17.07A - 2.62B - 7.70C + 2.28AB + 6.84AC - 15A^2 + 5.12C^2 \quad (6.2)$$

Where Y_{EP} and Y_{NP} represent the responses for EFV and NVP respectively.

Figure 6.2 depicts the actual and predicted response values for EFV (Figure 6.2(a)) and NVP (Figure 6.2(b)), respectively. The close proximities of the actual and predicted experimental values to the straight lines in Figure 6.2 indicate a good correlation between these values.

Photocatalyst loading (A), initial pH of the solution (B), and pollutant concentration (C), second-order effects of photocatalyst loading (A^2) and pollutant concentration (C^2), and interactions between catalyst loading (A) and pollutant concentration (C) were statistically significant for EFV degradation. For NVP degradation, photocatalyst loading (A), initial pH of the solution (B), and pollutant concentration (C), second-order effects of photocatalyst loading (A^2) and pollutant concentration (C^2), and interactions between photocatalyst loading (A) and initial pH of the solution (B) and photocatalyst loading (A) and pollutant concentration (C) were statistically significant.

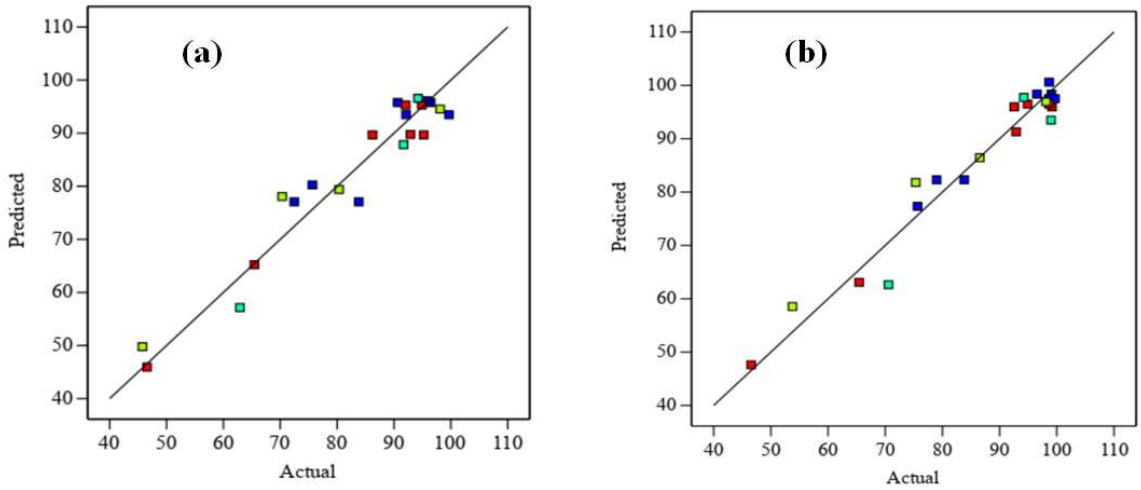

Figure 6.2: Comparison between the predicted and actual responses (c) efavirenz and (d) nevirapine.

Table 6.1: Analysis of variance for the quadratic model (efavirenz)

Source	**Sum of Squares**	**Degrees of freedom**	**Mean Square**	**F-value**	**p-value**
Model	5031.45	6	838.57	30.13	< 0.0001
A-Photocatalyst loading	4159.04	1	4159.04	149.42	< 0.0001
B-pH	60.86	1	60.86	2.19	0.0163
C-pollutant concentration	837.42	1	837.42	30.08	0.0001
AC	520.1	1	520.1	18.68	0.0008
A^2	663.83	1	663.83	23.85	0.0003
C^2	168.05	1	168.05	6.04	0.0288
Residual	361.86	13	27.84		
Lack of Fit	207.33	8	25.92	0.8386	0.6081
Pure Error	154.52	5	30.9		
Cor Total	5434.23	21			

Table 6.2: Analysis of variance for the quadratic model (nevirapine)

Source	Sum of Squares	Degrees of freedom	Mean Square	F-value	P-value
Model	4949.94	7	707.13	35.45	< 0.0001
A-Photocatalyst loading	4174.68	1	4174.68	209.28	< 0.0001
B-pH	95.76	1	95.76	4.8	0.0489
C-pollutant concentration	821.6	1	821.6	41.19	< 0.0001
AB	52.44	1	52.44	2.63	0.0131
AC	535.21	1	535.21	26.83	0.0002
A^2	707.42	1	707.42	35.46	< 0.0001
C^2	84.31	1	84.31	4.23	0.0622
Residual	239.37	12	19.95		
Lack of Fit	195.17	7	27.88	3.15	0.1122
Pure Error	44.2	5	8.84		
Cor Total	5200.01	21			

6.4 Optimisation of Process Parameters using the Response Surface Method

Figure 6.3 (a) shows the degradation efficiency of EFV as a function of photocatalyst loading and pollutant concentration. For NVP, Figure 6.3 (b) and (c) show the degradation efficiency as functions of photocatalyst loading and pollutant concentration, and photocatalyst loading and pH respectively. The responses from Figure 6.3 (a) and (b) are similar with the degradation efficiency being directly proportional to photocatalyst loading and inversely proportional to pollutant concentration. An increase in the amount of photocatalyst results in an increase in the active sites and a subsequent increase in degradation efficiency. However, when the pollutant concentration is increased, the ratio of active sites to pollutant molecules is reduced leading to decreased degradation efficiency. From Figure 6.3(c), the photodegradation of NVP increased with an increase in photocatalyst loading irrespective of the change in pH. The effect of pH on the photodegradation of NVP can be explained as follows: firstly, the point of zero charge for

the photocatalyst was established to be 9.5, as shown in Figure C1 in Appendix C. This implied that the surface of the photocatalyst was positively charged at pH < 9.5 and negatively charged at pH > 9.5. Secondly, NVP has a pKa of 2.8 (Kim *et al*., 2021) indicating that it is positively charged at pH < 2.8 and neutral at higher pH values. The operational pH of neutral fell within the region where the photocatalyst's surface was predicted to be positively charged while the NVP molecules were neutral. This enhanced the intermolecular interactions between the two components and enhanced the adsorption capacity, resulting in enhanced photocatalytic NVP degradation.

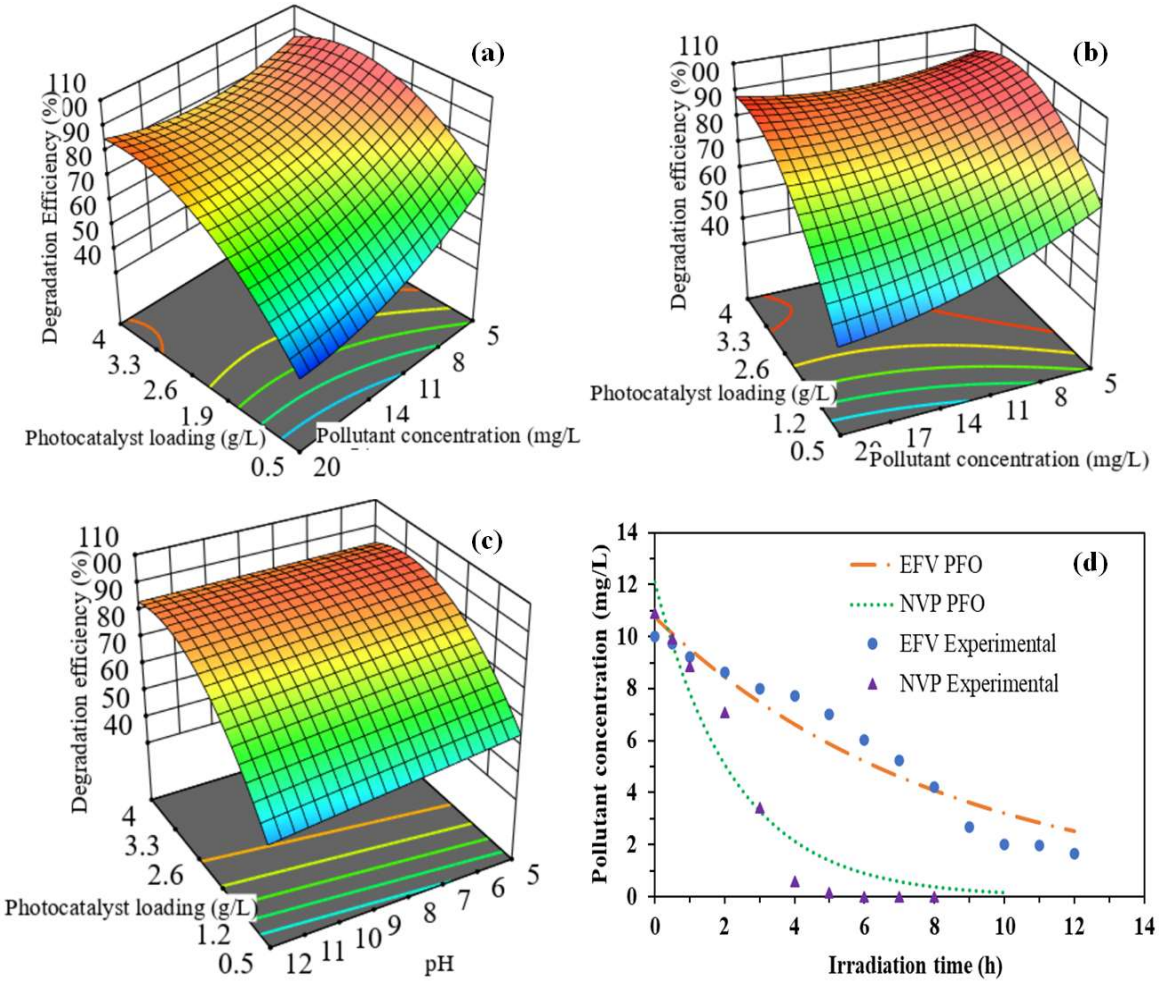

Figure 6.3: (a) Response surface 3D plot for efavirenz, interactions between photocatalyst loading and pollutant concentration. Response surface 3D plot for nevirapine, (b) interactions between photocatalyst loading and pollutant concentration, (c) interaction between photocatalyst loading and initial pH of the solution. (d) PFO kinetics model fittings for efavirenz and nevirapine (10 mg L^{-1}).

6.5 Photodegradation Kinetics

The photocatalytic degradation kinetics of EFV and NVP were investigated by fitting a simple pseudo-first order (PFO) model (Equation (6.3)) to experimental data. Figure 6.3(d) shows the fitted model for EFV and NVP at 10 mg L^{-1} (model fittings at 5 and 20 mg L^{-1} are shown in Figure C2 and C3 in Appendix C). The corresponding kinetics parameters are shown in Table 6.3. The results show that the degradation rate constants were inversely proportional to the initial concentration for the two pollutants, which can be attributed to numerous factors, including competition for active sites between intermediate products and primary pollutants (Hequet *et al*., 2017), a decrease in radical generation on the surface due to high pollutant concentrations (Khaki *et al*., 2017), and light absorption by the pollutant, which leads to a reduction in active radical generation (Ahmed *et al*., 2021). Furthermore, the photodegradation rate constants of NVP were compared to those reported in previous studies (Table 6.4), and it was determined that the rate constant at 5 mg L^{-1} (0.585 h^{-1}) is comparable to that reported by Bhembe et. al. (2020) (0.912 h^{-1}) for a similar concentration. However, their overall degradation efficiency was higher than the total degradation in this study. Ncube et. al. (2022) and Ngumba et. al. (2015) reported higher degradation constants of 2.2 and 4.8 h^{-1}, respectively, but their pollutant concentrations were lower. It is also worth noting that previous studies were conducted under UV irradiation, whereas the current study used visible light irradiation. This demonstrates that Ag-AgBr-LDH is a viable photocatalyst for the degradation of EFV and NVP under visible light irradiation.

$$C = C_0 e^{-kt} \tag{6.5}$$

Table 6.3*:* Photocatalytic degradation kinetics parameters

Pollutant	Parameter	Concentration (mg L^{-1})		
		5	10	20
Efavirenz	k	0.151	0.121	0.117
	R^2	0.97	0.93	0.96
Nevirapine	k	0.585	0.433	0.322
	R^2	0.985	0.941	0.965

Table 6.4*:* Comparison of nevirapine photocatalytic degradation kinetics parameters

Photocatalyst	Initial concentration	Degradation efficiency (%)	Rate constant (h^{-1})	Reference
Ag-AgBr-LDH	5 mg L^{-1}	100	0.585	this study
UV/TiO2/H2O2	40 µg L^{-1}	89	2.2	(Ncube *et al*., 2022)
UV/H2O2	20 µg L^{-1}	53	4.8	(Ngumba *et al*., 2016)
UV/(FL-BP@Nb2O5)	5 mg L^{-1}	69	0.91	(Bhembe *et al*., 2020)

6.6 Scavenger Tests and Photodegradation Mechanism

Figure 6.4 shows the degradation efficiencies of the two ARVDs in the presence of various radical scavengers. Isopropanol (IPA), p-benzoquinone (PBQ), copper (II) nitrate (CN) and formic acid (FA) were used as scavengers for hydroxyl radical ($^{\bullet}OH$), superoxide radical $^{\bullet}O_2^-$, electrons (e^-) and photo-induced holes (h^+), respectively. The degradation efficiency of both EFV and NVP decreased by 46% and 60% when IPA was added. Significant reduction in degradation efficiency was also noted upon FA addition. These observations indicated that both $^{\bullet}OH$ and h^+ played an important role in the degradation process. This accession was also reported by Ncube *et al*. (2022) and. Tafreshi et. al. (2019). The addition of PBQ and CN showed a moderate reduction in degradation efficiencies of 14% and 22% for EFV, 32% and 22% for NVP. This implied that the superoxide radicals and the electrons were not the major drivers of the photodegradation process.

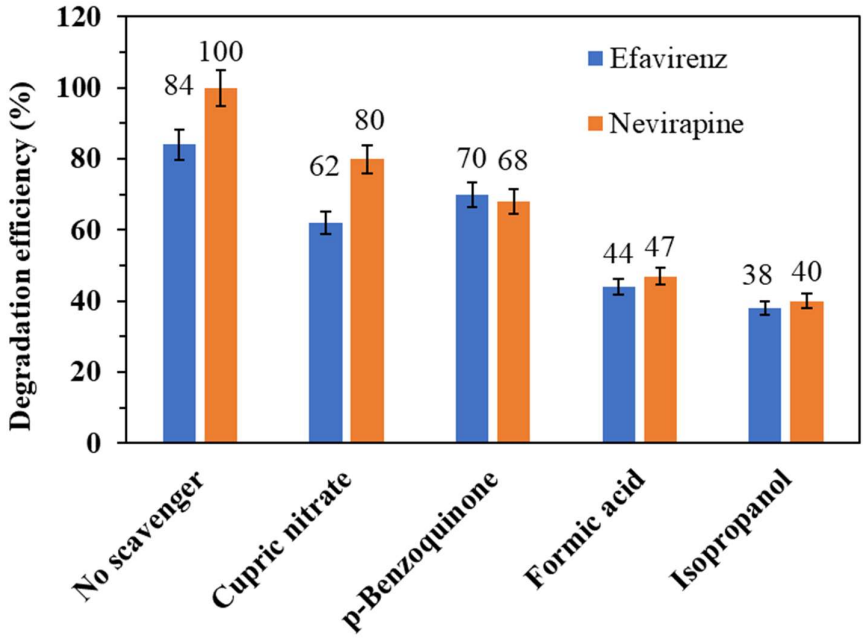

Figure 6.4: Photodegradation efficiencies in the presence of various scavengers.

The proposed mechanism for the photocatalytic degradation of ARVDs involves the generation of electron-hole pairs on the surface of silver nanoparticles through SPR when exposed to light, as shown in Figure 6.5. The photo-excited silver nanoparticles then transfer electrons to the conduction band of AgBr, leading to the formation of $^{\bullet}O_2^-$ and other oxidants. The resulting silver nanoparticles can shift to a more positive potential, allowing them to either oxidise contaminants or capture electrons to revert to non-charged Ag nanoparticles. The surface of LDH materials is covered with OH^-, which can accept the photo-induced holes from the valence band of AgBr to produce $^{\bullet}OH$. The binding of Ag-AgBr particles to LDH increases the probability of the occurrence of this process. The scavenger tests further supported this, which demonstrated that when $^{\bullet}OH$ and h^+ were scavenged, the photodegradation efficiencies decreased substantially.

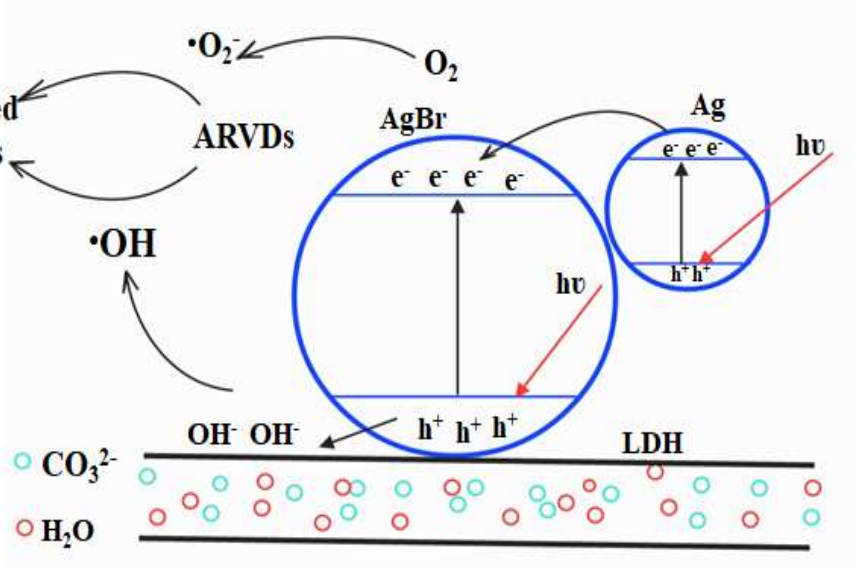

Figure 6.5: Formation of major active species during visible light irradiation of photocatalyst.

6.7 Photostability and Reusability of the Photocatalyst

The composite photocatalyst was recycled in a series of tests to evaluate its stability and reusability. Figure 6.6 shows a gradual decrease in the degradation efficiency after the first two runs from 84% to 80% (EFV) and 100% to 95% (NVP). Thereafter, there were 24% and 21% decrease in efficiencies for EFV and NVP after Run 4. The decline in photodegradation efficiencies was due to the inevitable deactivation of the photosensitive AgBr which is unstable under visible light irradiation (Xue *et al*., 2016, Yang *et al*., 2014). This deactivation can cause aggregation of Ag^0 followed by a disfigured heterojunction structure. Ultimately the SPR property of silver nanoparticles becomes compromised, giving rise to poor stability of the photocatalyst. Therefore, it can be postulated that the increased amounts of Ag^0 caused photo-corrosion of the photocatalyst, resulting in a decline in degradation efficiency.

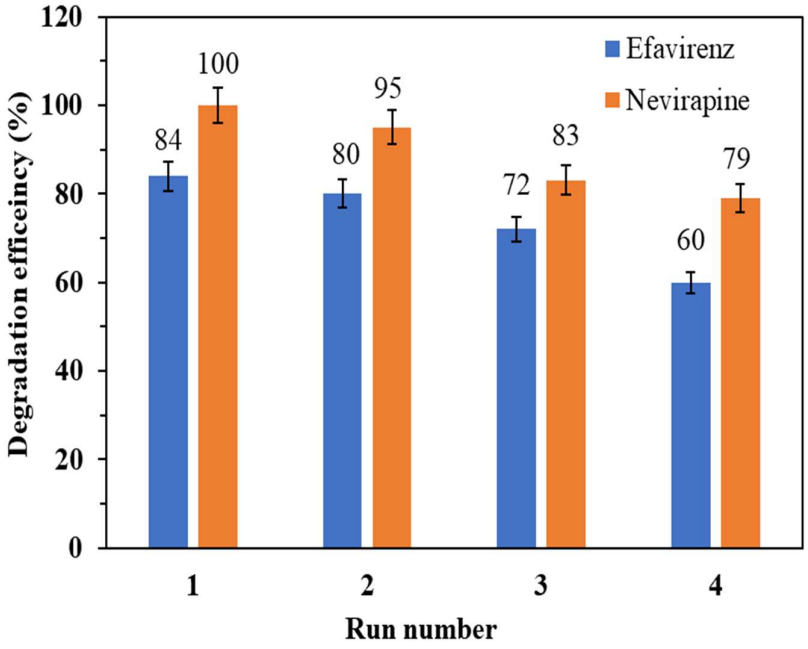

Figure 6.6: Photostability and reusability of the photocatalyst.

6.8 Conclusion

The photocatalyst composite containing Ag-AgBr and LDH proved to be more effective in degrading the ARVDs (efavirenz and nevirapine) than Ag-AgBr and LDH separately. The response surface modelling showed the interaction between photocatalyst loading and initial concentration was significant for EFV while the interactions between pH and photocatalyst loading, and photocatalyst loading and initial concentration were significant for NVP. More than 80% and 100% of EFV and NVP were degraded over 12 and 8 h under visible light irradiation. The hydroxy free radicals and photo-induced holes were established to be the active species responsible for the degradation of ARVDs.

CHAPTER 7: REMOVAL OF ANTIRETROVIRAL DRUGS FROM WASTEWATER USING CONTINUOUS FLOW PHOTOCATALYSIS

7.1 Synopsis

This study investigated the degradation of EFV and NVP, two commonly employed ARVDs, utilising heterogeneous photocatalysis in a continuous flow reactor. The impact of light intensity was examined through batch experiments, while the effect of photocatalyst loading, flow rate, and initial concentration on photodegradation efficiencies of the two ARVDs was evaluated using the continuous flow reactor. The findings demonstrated a direct relationship between light intensity and degradation efficiency, with higher degradation rates observed at increased light intensities.

7.2 Effect of Light Intensity

Figure 7.1 shows the concentration profiles of NVP under varying numbers of light sources during visible light irradiation. Predictably, a higher rate of NVP degradation was observed to coincide with an increase in the quantity of light sources, which signified greater light intensity. The estimation of process parameters was performed by employing mathematical modelling, which comprised a sequence of equations. Equation (7.1) describes the mass balance of NVP within a batch reactor.

$$V\frac{dC(t)}{dt} = r(C,I)\cdot W \tag{7.1}$$

Where V is the solution volume (L), $C(t)$ is the NVP concentration (mg L^{-1}), r is the reaction rate (mg g^{-1} h^{-1}), I is the light intensity reaching the photocatalyst surface (mW cm^{-2}), and W is the mass of the photocatalyst (g). The initial conditions were $t = 0$ and $C = C_0$.

The kinetic expressions used in the model are as shown in Equation (7.2) to (7.4).

$$-r = K_1 r_C r_I \tag{7.2}$$

$$r_C = \frac{bC(t)}{1+bC(t)} \tag{7.3}$$

$$r_I = \frac{\alpha I}{1+\alpha I} \tag{7.4}$$

Where K_1 is the kinetic constant (mg $g^{-1}h^{-1}$), r_C is the contribution of NVP concentration to the degradation rate, r_I is the effect of light intensity adsorbed by the photocatalyst, and α is the light absorption coefficient (cm^2 mW^{-1}).

Equation (7.3) assumes that the adsorption equilibrium of NVP onto the catalyst follows the Langmuir adsorption isotherm. The reaction rate dependency on photonic flux was developed to propose a simple method for designing photocatalytic reactors. This consideration derives from the idea that photons can be thought of as simulated reactants, as reported by Palma *et al.* (2010) and Camera-Roda *et al.* (2005). This conceptual framework makes it more convenient to recognise that only a portion of the incident light intensity that reaches the photocatalyst particle is efficiently absorbed. Furthermore, the availability of active sites on the catalyst surface is directly proportional to the catalyst concentration in the suspension (Sannino *et al.*, 2013). Concurrently, the light penetration may decrease as catalyst concentration increases due to the screening effect. To overcome this issue, a first-order correlation similar to the Lambert-Beer law was used to determine the effective light intensity received by photocatalyst particles, as shown in Equation (7.5) (Sannino *et al.*, 2013). A PFO kinetic model was used to determine the change in time of the NVP concentration, as shown in Equation (7.6). Using Equation (7.2) to (7.6), mass balance can be written as in Equation (7.7).

$$I = I_0 e^{-K_I C_{cat}} \tag{7.5}$$

$$C(t) = C_0 e^{-K_r t} \tag{7.6}$$

$$\frac{dC(t)}{dt} = K_1 \frac{bC_0 e^{-K_r t}}{1+bC_0 e^{-K_r t}} \cdot \frac{\alpha I_0 e^{-K_I C_{cat}}}{1+\alpha I_0 e^{-K_I C_{cat}}} \cdot 1000 \cdot C_{cat} \tag{7.7}$$

Where K_I is the specific extinction coefficient per unit mass of catalyst (L mg^{-1}), I_0 is the light intensity incident on the reactor surface (mW cm^{-2}) and C_{cat} is the photocatalyst dosage in (mg L^{-1}).

The Euler iterative method was used to compute the mass balance parameters for various light sources. Table 7.1 shows the parameters determined by fitting the model to the experimental data. The overall kinetic constant (K_I) increased with light intensity, ranging from 0.003 mg g h^{-1} at 17.83 mW cm^{-2} to 0.099 mg g^{-1} h^{-1} at 53.5 mW cm^{-2}. Similarly, the degradation rate constant increased from 4.23 to 6.75 h^{-1}. The specific extinction coefficient per unit mass remained constant at 0.008 L mg^{-1} across the intensity range of 35.66 mW cm^{-2} to 53.5 mW cm^{-2}. This observation suggests that the influence of light intensity was marginal beyond 35.66 mW cm^{-2}, implying that factors such as mass transfer limitations might have governed the degradation of NVP.

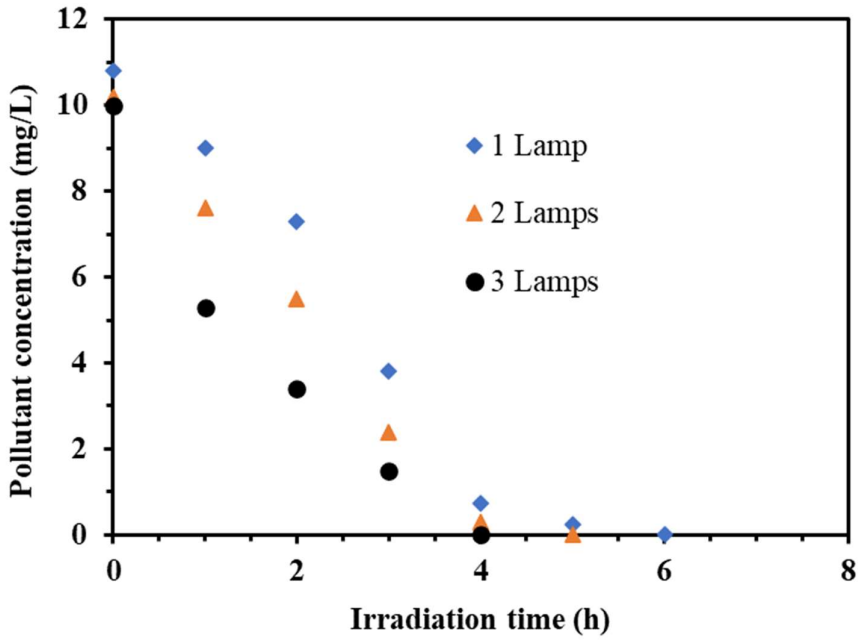

Figure 7.1: Degradation profiles of NVP with varying number of light sources (10 mg L^{-1} initial concentration, 2 g L^{-1} photocatalyst loading and neutral pH).

Table 7.1: Mathematical modelling parameters for photocatalytic degradation of NVP with varying number of light sources

Parameter	**1 Lamp**	**2 Lamps**	**3 Lamps**
I_0 (mW cm^{-2})	17.83	35.66	53.5
K_1 (mg g^{-1} h^{-1})	3.448 X 10^{-3}	7.377 X 10^{-2}	9.912 X 10^{-2}
K_I (L mg^{-1})	5.051 X 10^{-3}	7.8 X 10^{-3}	7.667 X 10^{-3}
K_r (h^{-1})	4.232	4.4	6.754
C_{cat} (mg L^{-1})	2000	2000	2000
α (cm^2 mW^{-1})	0.485	2.901	1.535
b (L mg^{-1})	1.139 X 10^8	2.88 X 10^7	8.94 X 10^7

7.3 Effect of Photocatalyst Loading

Figures 7.2(a) and (b) show the photodegradation profiles of EFV and NVP at various photocatalyst loadings, respectively. The highest degradation efficiencies were 56% for EFV and 69% for NVP with a catalyst loading of 3 g L^{-1}. For photocatalyst loadings up to 2.5 g L^{-1}, the degradation kinetics showed a peak after 4 h, while a peak for a loading of 3 g/L was observed after 5 h. The phenomenon of photo-corrosion, which impacts the photocatalyst, could account for the observed decrease in activity beyond the optimal loading. This can be attributed to extended exposure to intense visible light irradiation (Huang *et al.*, 2022, Weng *et al.*, 2019). Furthermore, the vulnerability to photo-corrosion is clearly related to silver-containing photocatalysts, as reported by Huang *et al.* (2022).

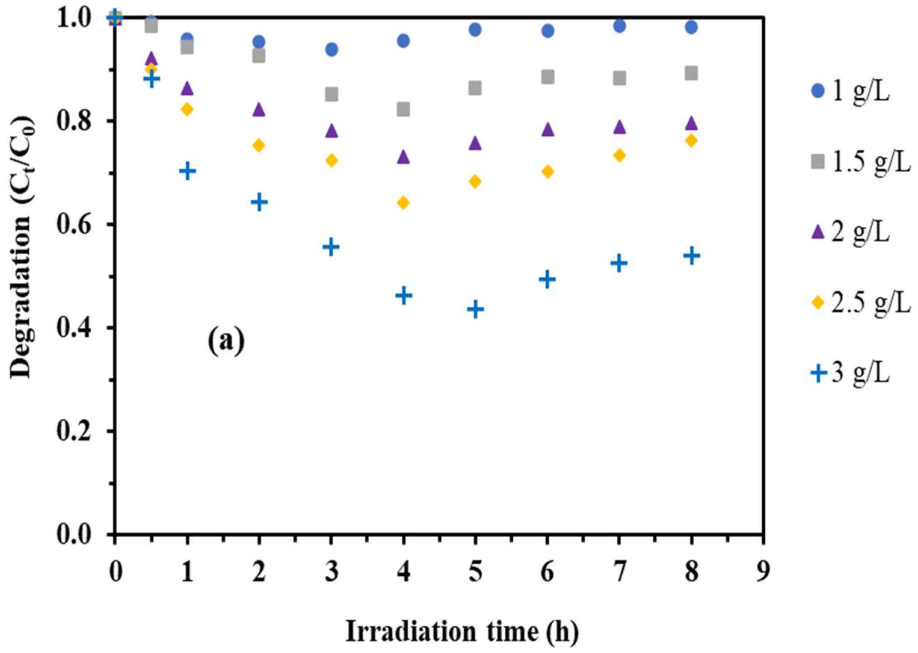

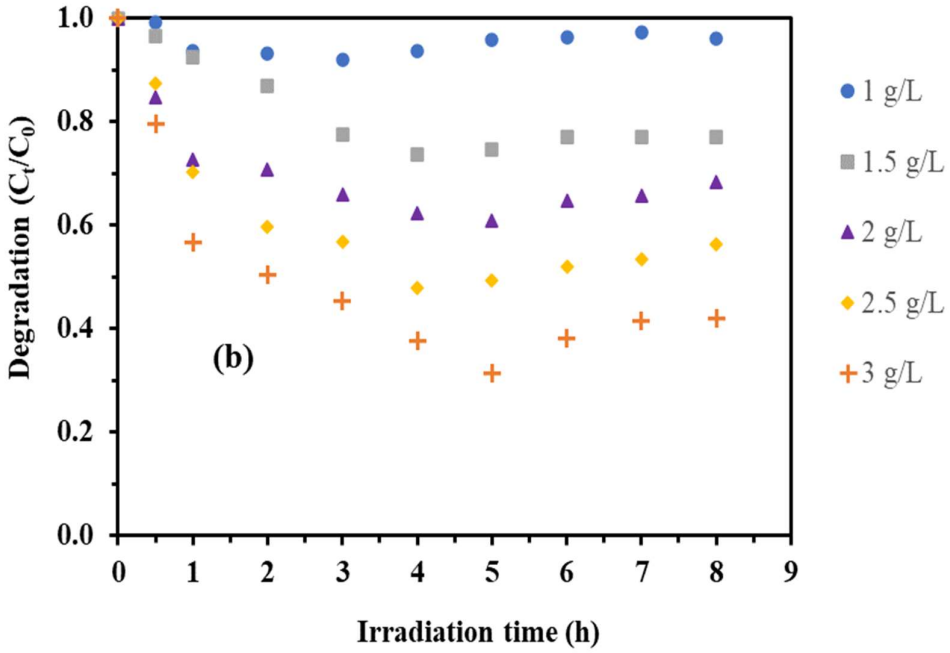

Figure 7.2: Photocatalytic degradation profiles with varying photocatalyst loading (initial concentration of 10 mg L^{-1}, neutral pH, and flow rate of 10 mL min^{-1}); (a) EFV and (b) NVP.

7.4 Effect of Flowrate

Figure 7.3 shows the degradation efficiencies of EFV and NVP at varying flow rates. The highest degradation efficiencies of 56% (EFV) and 69% (NVP) were achieved at a flowrate of 10 mL min^{-1}, corresponding to a residence time of 35 min. Increasing the flowrate to 20 mL min^{-1} reduced degradation efficiencies by more than 30%. This decrease in degradation efficiencies can be attributed to incomplete reactions caused by a shortened residence time brought about by increased flow rates. Although larger flow rates can improve mass transfer and ensure more effective usage of the photocatalyst, they may interfere with irradiation homogeneity, resulting in unequal exposure of the photocatalyst to light and a decline in degradation efficiencies (Binjhade *et al.*, 2022, Sundar &Kanmani, 2020).

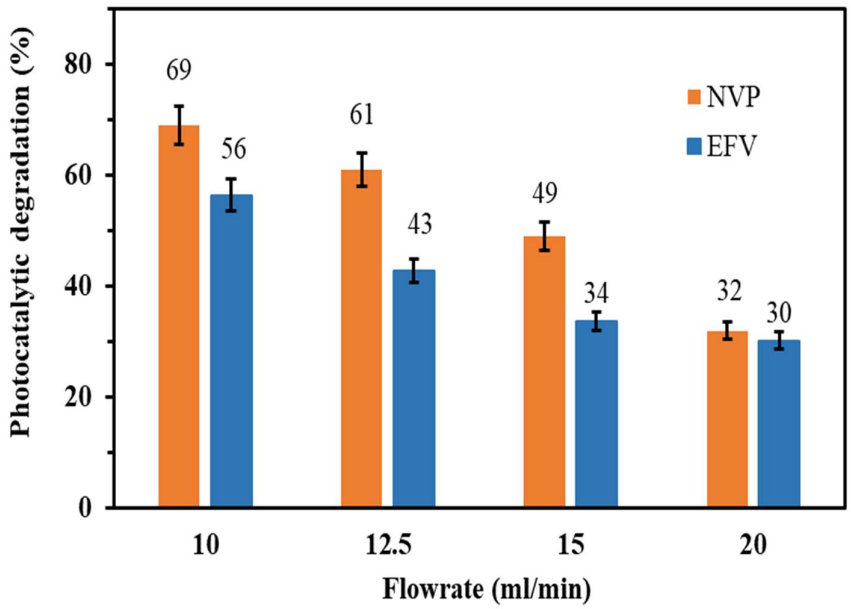

Figure 7.3: Photocatalytic degradation efficiencies of EFV and NVP at varying flow rate (initial concentration of 10 mg L^{-1}, photocatalyst loading of 3 g L^{-1} and neutral pH).

7.5 Effect of Initial Concentration and Degradation Kinetics

Figures 7.4(a) and (b) present EFV and NVP degradation profiles with varying initial concentrations. The observed trends indicate that degradation efficiencies peaked after 5 h possibly due to a decline activity of the photocatalyst, as outlined in the previous sections (Section 7.1 – 7.3). The maximum achieved degradation efficiencies at an initial concentration of 20 mg L^{-1} were 15% and 25% for EFV and NVP, respectively. Correspondingly, the highest degradation efficiencies at an initial concentration of 5 mg L^{-1} were 59% and 73% for EFV and NVP, respectively. While higher concentration systems are less susceptible to mass transport dynamics, their main challenge lies in light intensity dispersion. With increasing pollutant concentrations, the rate of surface adsorption on the photocatalyst intensifies, covering the monolayer active sites (Natarajan *et al.*, 2018, Wang *et al.*, 2016). Moreover, the pollutants rather than the photocatalyst absorb a substantial amount of light intensity. This hinders light penetration to the photocatalyst surface, resulting in a diminished generation of photo-induced holes and hydroxyl radicals, thereby reducing degradation efficiencies.

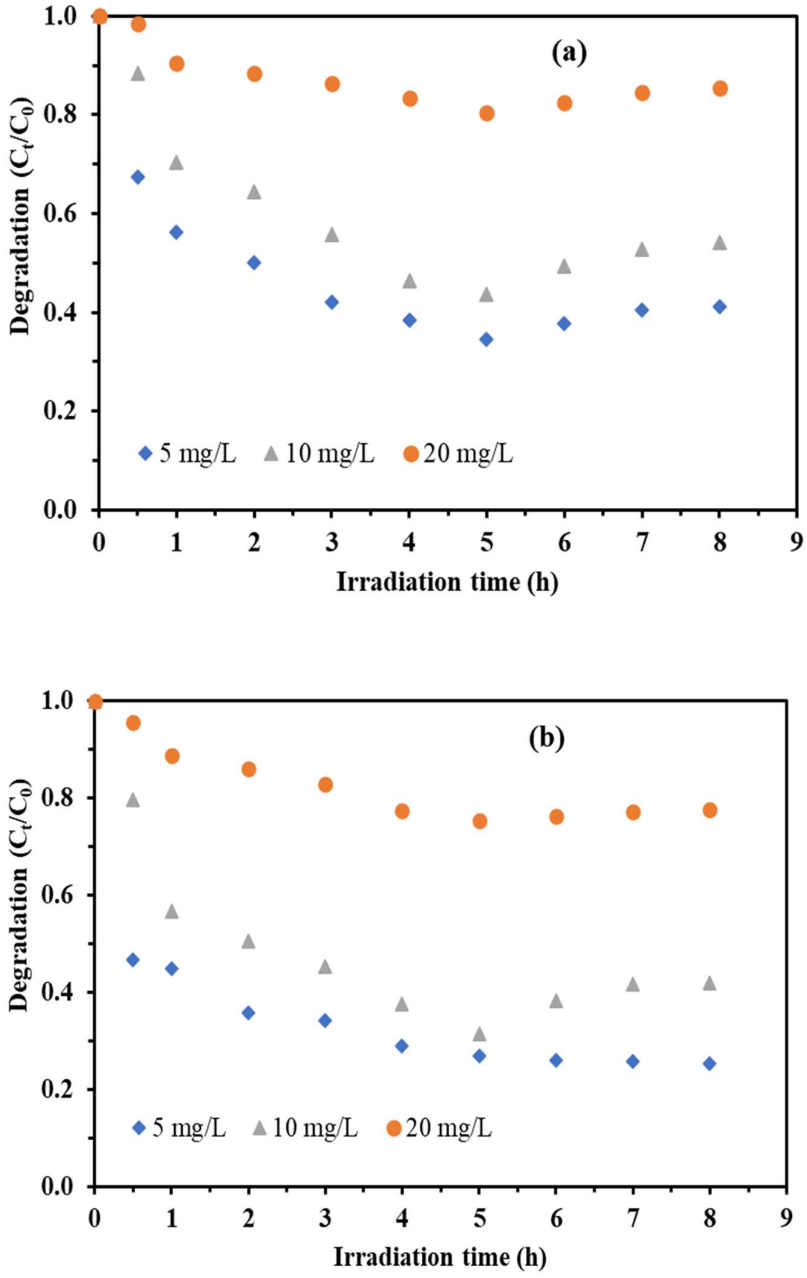

Figure 7.4: Photocatalytic degradation profiles at various initial concentration (flow rate 10 mL min^{-1}, neutral pH and photocatalyst loading of 3 g L^{-1}); (a) EFV and (b) NVP.

The degradation kinetics of EFV and NVP were examined through the application of a PFO model (Equation (7.6)), utilising experimental data, without accounting for the influence of light intensity. The fitted model for EFV and NVP at an initial concentration of 10 mg L^{-1} is presented in Figure 7.5. The corresponding kinetics parameters are summarised in Table 7.2.

The findings revealed that the degradation rate constants exhibited an inverse relationship with the initial concentration for both pollutants. This observation can be attributed to various factors, including competition for active sites among intermediate products and the primary pollutant (Yu *et al.*, 2021), a decrease in radical generation on the surface due to high pollutant concentrations (Yang *et al.*, 2018), and light absorption by the pollutant, resulting in diminished active radical generation (Chen *et al.*, 2020b).

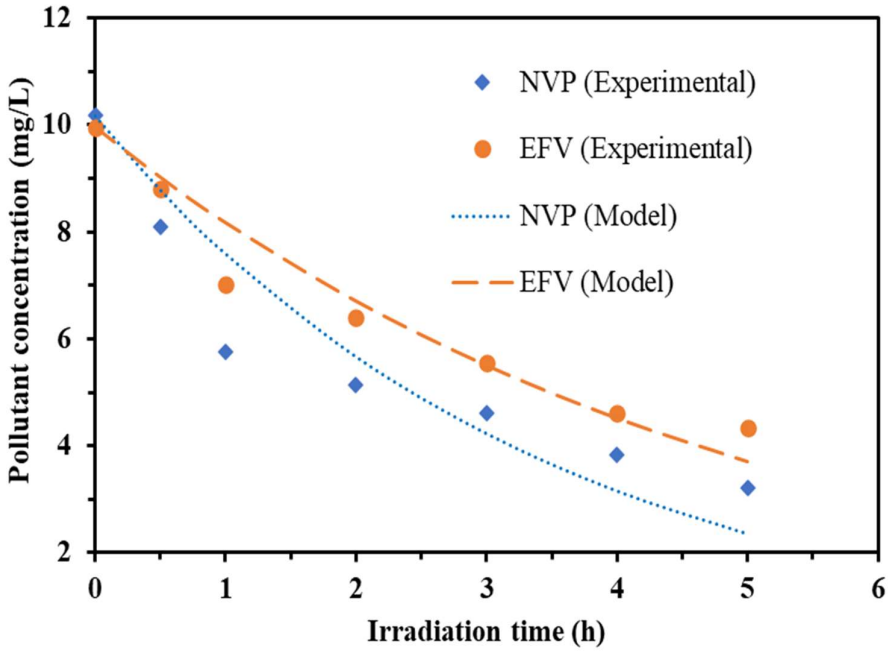

Figure 7.5: Photocatalytic degradation of EFV and NVP (initial concentration of 10 mg L^{-1}, photocatalyst loading of 3 g L^{-1}, flowrate of 10 mL min^{-1} and neutral pH).

Table 7.2: Photocatalytic degradation kinetics parameters (flowrate 10 mL min^{-1}, photocatalyst loading of 3 g L^{-1} and neutral pH)

Pollutant	**Parameter**	**Concentration (mg L^{-1})**		
		5	10	20
Efavirenz	k	0.302	0.198	0.048
	R^2	0.98	0.98	0.95
Nevirapine	k	0.486	0.292	0.064
	R^2	0.95	0.95	0.98

7.6 Conclusion

This study successfully established the efficacy of continuous-flow photocatalytic reactors in degrading ARVDs in wastewater. The effect of light intensity, initial pollutant concentration, photocatalyst loading and flow rate on photodegradation efficiencies of EFV and NVP were established through systematic experiments. Light intensity was found to have a direct relationship with degradation efficiency, with higher degradation rates observed at increased light intensities. However, the catalyst was susceptible to photo corrosion when exposed to intense light irradiation for extended periods. While higher initial pollutant concentration and flow rate were not affected by mass transfer limitations, low photodegradation efficiencies were achieved under these conditions due to a lack of irradiation homogeneity.

CHAPTER 8: INTEGRATED STUDY OF ANTIRETROVIRAL DRUGS ADSORPTION ONTO CALCINED LAYERED DOUBLE HYDROXIDE MATERIAL: EXPERIMENTAL AND COMPUTATIONAL ANALYSIS

8.1 Synopsis

This study focused on the efficacy of a calcined layered double hydroxide (CLDH) material in adsorbing EFV and NVP from wastewater. The neat and calcined LDH materials were subjected to various characterisation techniques to elucidate their physical and chemical properties. Response surface modelling (RSM) was used to evaluate the interactions between the solution's initial pH, adsorbent loading, reaction temperature, and initial pollutant concentration. Additionally, the adsorption kinetics, thermodynamics, and reusability of the adsorbent were evaluated.

8.2 Adsorbent Characterisation

8.2.1 X-ray Diffraction (XRD) Analysis

The XRD spectra of the neat LDH and CLDH materials are shown in Figure 8.1. The neat LDH material exhibited characteristic peaks that were clearly identified and assigned to specific crystal planes. The amorphous-dominated CLDH displayed two phases that were identified as periclase (MgO) (ICSD 9863) and spinel ($MgAl_2O_4$) (ICSD 79000). The quantitative analysis of CLDH indicated that it contained 55% periclase and 45% spinel. The periclase peaks were observed at 2θ values of 42°, 50°, and 74°, while the spinel peaks appeared at 2θ values of 37°, 66°, 71°, and 77°. The results are consistent with those reported by Samandari *et al.* (2021) and Leon'teva *et al.* (2020). Samandari *et al.* (2021) studied Mg-Al LDH and calcined LDH for wet peroxide oxidation of phenol in wastewater, while Leon'teva *et al.* (2020) examined the structural analysis of defects in LDHs and related mixed oxides. In both studies, the LDH was calcined at 500 ℃. Dos Santos *et al*. (2017) and Gao *et al*. (2013) revealed that of the two phases, the periclase phase played a key role in the adsorption process. A substantial amount of this phase holds promising potential for the adsorption of ARVDs from wastewater.

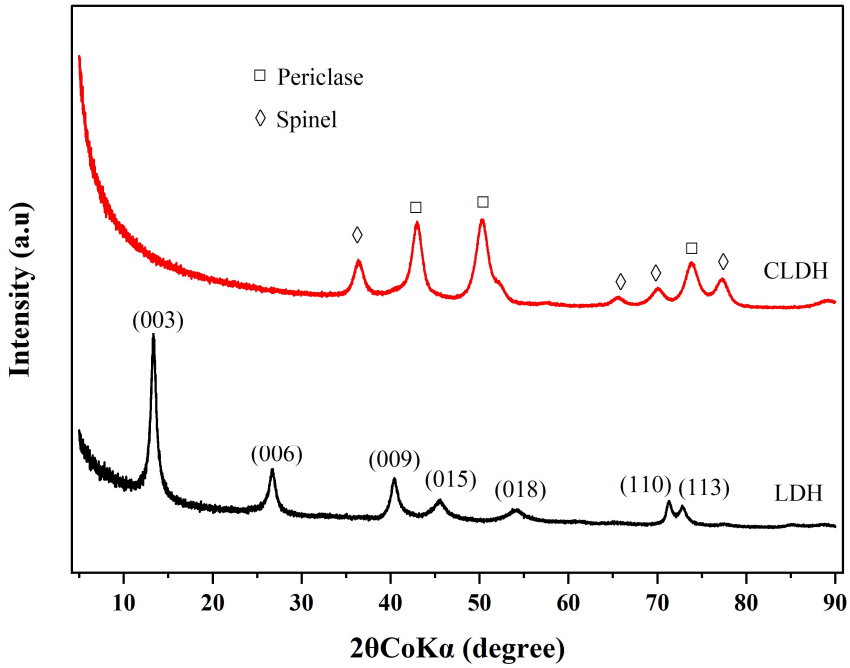

Figure 8.1: X-ray diffraction spectra of neat and calcined LDH materials.

8.2.2 Thermogravimetric Analysis

Figure 8.2 shows the thermal analysis of the neat LDH and CLDH materials. Thermal analysis of the neat LDH displayed two distinct decomposition stages, a characteristic synonymous with LDH materials with an M^{2+}/M^{3+} ratio of 2. The first decomposition stage occurred at 210 °C and was accompanied by a mass loss of 18%. This weight loss can be attributed to the loss of physiosorbed water and a partial loss of hydroxyl ions (OH^-), which are an integral part of the LDH structure. The second decomposition stage took place at 385 °C, resulting in a mass loss of 25%. This stage is associated with the interlayer ions' complete decomposition in the LDH structure. These decompositions transformed a highly crystalline LDH into an amorphous-dominated mixed metal oxide (MMO). The thermal analysis of CLDH indicated a minimal loss of 3% throughout the evaluated temperature range. This negligible loss can be attributed to the removal of surface moisture, as the material was anticipated to completely transform into MMO during the calcination process.

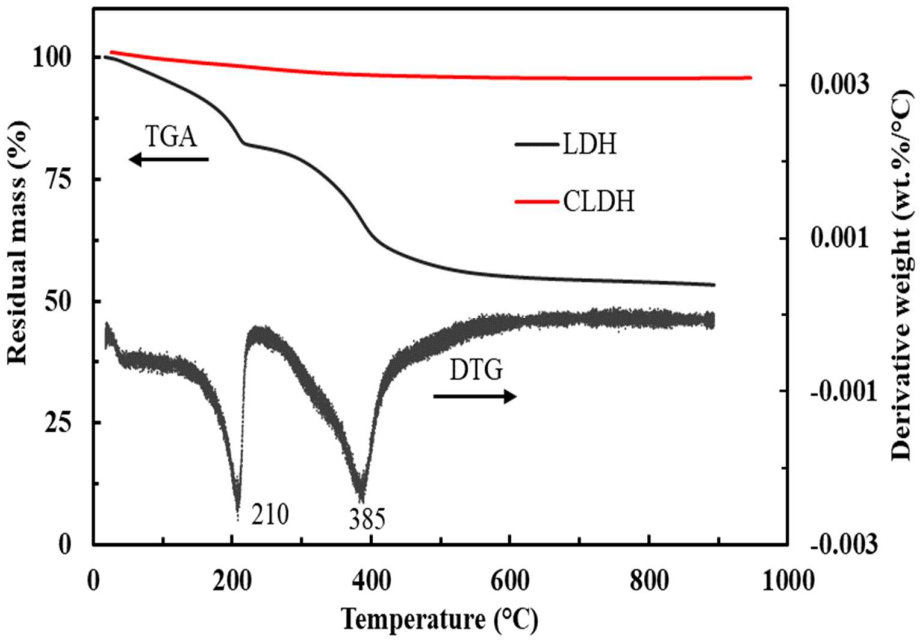

Figure 8.2: Thermogravimetric analysis of neat and calcined LDH materials.

8.2.3 Brunauer-Emmett-Teller (BET) Surface Area

Figure 8.3 illustrates the nitrogen gas adsorption and desorption isotherms for both neat LDH and CLDH. The isotherms demonstrated a distinct sorption behaviour of Type IV, characterised by a hysteresis loop of Type H3, as per the IUPAC (Li *et al*., 2016). The estimated parameters for the BET surface area, pore volume, and average pore diameter from the neat LDH were 28.5 $m^2 g^{-1}$ for the BET surface area, 80.6 Å for the average pore diameter and a pore volume of 0.155 $cm^3 g^{-1}$. The pore size distribution curve showed a broad peak between 2 and 100 nm, with a maximum at 5 nm, indicating the presence of mesopores/macropores in the product, possibly related to pores created between hexagonal plates. CLDH had a BET surface area of 90.4 $m^2 g^{-1}$, an average pore diameter of 44.3 Å and a pore volume of 0.344 $cm^3 g^{-1}$. The pore size distribution curve, like that of neat LDH, showed a noticeable peak within the 2 to 100 nm range, peaking at 10 nm, indicating the presence of mesopores/macropores, presumably due to the pores generated between hexagonal plates.

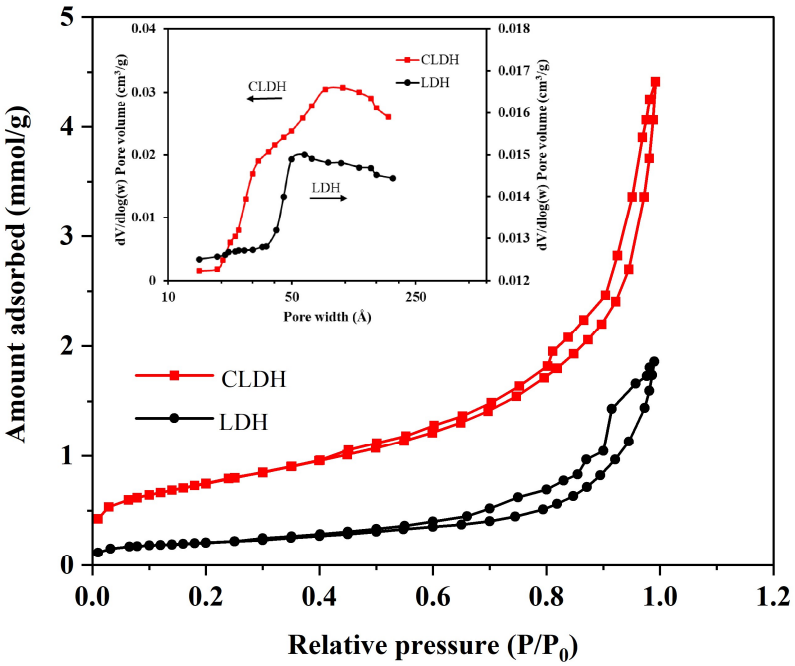

Figure 8.3: BET surface area analysis for neat LDH and CLDH.

8.2.4 Fourier Transform Infrared (FTIR) Analysis

Figure 8.4 presents the infrared spectra obtained for the neat LDH and CLDH materials. The neat LDH spectra revealed distinct bands associated with specific vibrational modes and molecular interactions within the material. The band observed at 840 cm^{-1} can be attributed to the ν1 vibrational modes of carbonate ions (CO_3^{2-}), while the peak at 880 can be related to ν2 of the same ions. The band at 960 cm^{-1} corresponded to the vibrational modes of metal-O-metal linkages, signifying the presence of bonds between the metal cations within the layered structure of LDH. Furthermore, the ν1 vibrational mode of CO_3^{2-} is represented by a weaker band at 1100 cm^{-1}, indicating the asymmetric stretching of CO_3^{2-} ions.

Additionally, a band at 1390 cm^{-1} indicated the presence of CO_3^{2-} ions in the interlayer region of the LDH structure. The bands observed within the range of 1515 and 1455 cm^{-1} were attributed to the vibration of OH^-, confirming their presence in the LDH material. The peak at 3500 cm^{-1} was ascribed to stretching the O–H bond associated with water molecules in the interlayers and metal hydroxide layers (Naseem *et al.,* 2019, Li *et al*., 2016). Calcination of LDH resulted in the disappearance of the main spectra, which corresponded with XRD results indicating structural changes and the transformation of LDH to MMO.

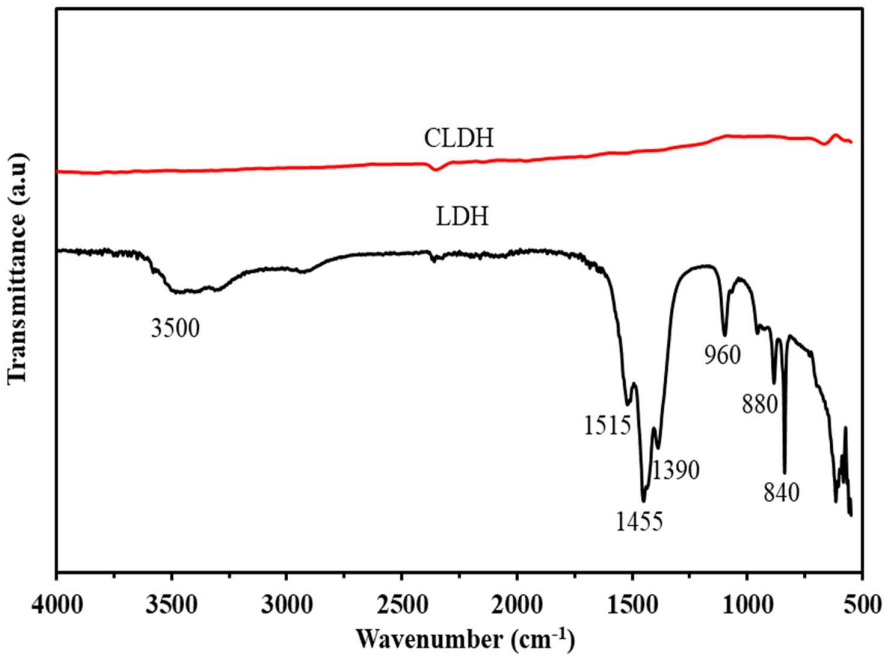

Figure 8.4: FTIR analysis for neat LDH and CLDH materials.

8.2.5 Scanning electron microscopy (SEM) analysis

Figures 8.5 (a) and (b) present the morphological analysis of the neat and CLDH materials using SEM. For the neat LDH, the SEM images exhibit a hexagonal plate-like morphology of the particles. This particular structure aligns with previous reports in the literature concerning LDH materials based on magnesium and aluminium (Naseem *et al*., 2019). The observed hexagonal platelets reflected the well-ordered arrangement of layers within the LDH structure. Additionally, the SEM analysis reveals mesoporosity in the neat LDH particles, which correlates with the findings from BET analysis, where a mesopore diameter range of 2-50 nm was quantified. Conversely, upon subjecting LDH to calcination at 500 ℃, noticeable changes in morphology occurred. SEM images for CLDH displayed the absence of ordered hexagonal platelets observed in the neat LDH. Instead, the particles demonstrated an irregular and less defined morphology, indicating the structural transformation during the calcination process. This transformation led to the formation of irregular particles composed of MMO. Despite these changes, the calcined LDH (CLDH) material still retains some mesoporosity, which is consistent with the BET analysis results that also identified mesopores in the range of 2-50 nm. The platelet assemblies displayed in Figure 8.5(a) had an estimated size of 200 nm, as demonstrated by the scanning electron micrographs. Scherrer's equation was used to estimate particle sizes, with two orientations considered: one parallel to the LDH layers and another

perpendicular to the LDH layers, as explained by Gevers *et al*. (2019). The estimated crystallite sizes in perpendicular and parallel dimensions were 12 and 20 nm, respectively. This substantiates the presence of nano-sized particles in the material, further validating the material's nanoscale properties. The elemental compositions of both the neat and CLDH materials were analysed utilising energy dispersive X-ray spectroscopy (EDS), with the findings depicted in Figures 8.5(c) and (d), respectively. The conducted elemental analysis affirmed the existence of Mg, Zn, and Al within both materials.

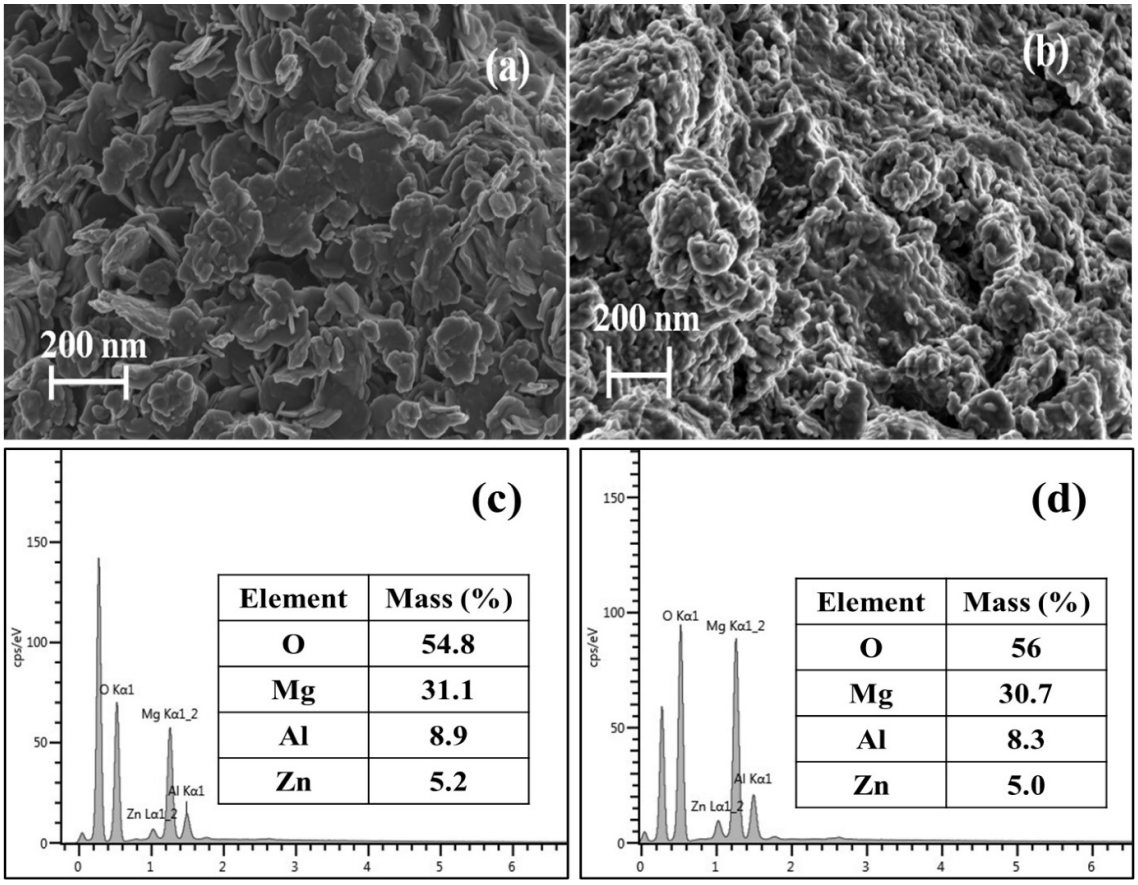

Figure 8.5: SEM and SEM-EDS analysis for neat LDH (a) & (c) and CLDH (b) & (d).

Figure 8.6 shows the High-Angle Annular Dark-Field Scanning Transmission Electron Microscopy (HAADF-STEM) image as well as the Energy Dispersive X-ray Spectroscopy (EDS) elemental mapping images for both the neat LDH (Figures 8.6(a) – (d)) and the CLDH (Figures 8.6(e) – (h)). The HAADF-STEM images (Figures 8.6(a) and (e)) provide visual representations of the neat LDH and CLDH, respectively, revealing the spatial distribution and arrangement of various elements within the materials. The elemental maps (Figures 8.6(b)–(d)

and 8.6(f)–(h)) depict the presence and distribution of Mg, Al, and Zn. The spatial distribution observed in the mapping images aligns with the peaks detected in the EDS spectra, further validating the presence of these elements in both neat and calcined LDH samples.

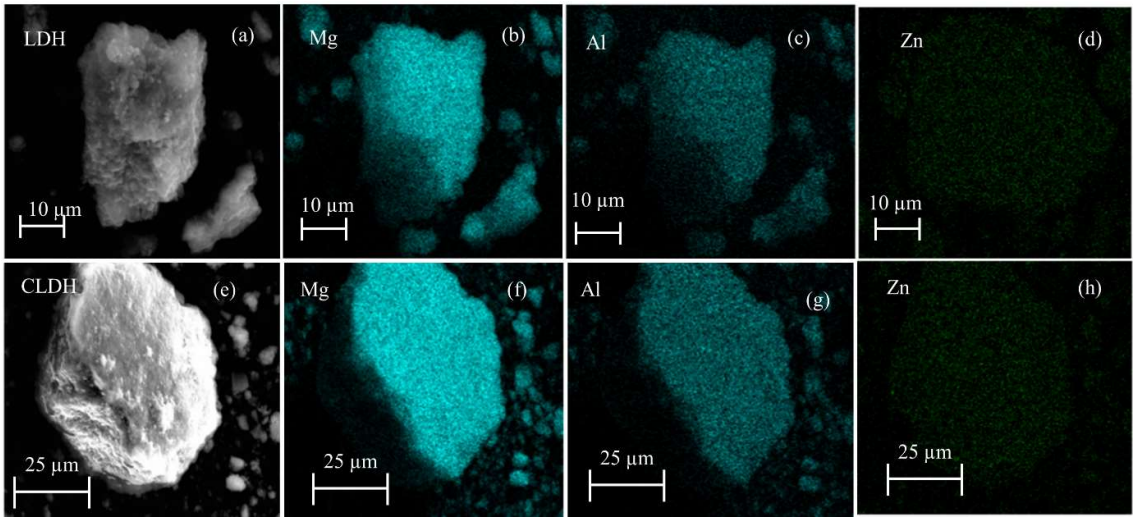

Figure 8.6: HAADF-STEM image of neat LDH (a), EDS mapping (neat LDH), Mg (b), Al (c), Zn (d), HAADF-STEM image of CLDH (e), EDS mapping (CLDH), Mg (f), Al (g), Zn (h).

8.3 **Adsorption Results**

8.3.1 Statistical Analysis of the Adsorption Process Using Response Surface Methodology

RSM was employed to assess the comparative importance of the experimental parameters, utilising a combination of mathematical and statistical analysis techniques. A quadratic equation was adjusted to the experimental responses obtained from the designed experiments, and an analysis of variance (ANOVA) was performed. Table 3.2 presented the different combinations of independent variables and their corresponding responses (adsorption efficiency) for both EFV and NVP from the 21 experimental runs. The significance of the model equation was evaluated using the F-test for ANOVA. The ANOVA statistics for EFV and NVP adsorption efficiencies are displayed in Tables 8.1 and 8.2, respectively. The p-values for the adsorption efficiency in both tables were found to be lower than 0.05, indicating that the model was statistically significant. The minimal values of the standard deviations (4.62 and 5.61 for EFV and NVP, respectively) between the predicted and experimental results indicated that the model equations (Equations (8.1) and (8.2)) accurately represented the realistic relationship between the significant variables and the responses. Higher values of R^2 (0.877 and 0.898 for EFV and NVP, respectively) and predicted R^2 (0.811 and 0.854 for EFV and

NVP, respectively) further confirmed a strong dependence and correlation between the predicted and observed values. These observations are also visually depicted in Figure 8.7 (a) and (b), which compare the predicted values from the respective models with the experimental ones. Given the linear trend demonstrated by the data points on the plots, it can be deduced that the residuals follow a normal distribution, hence negating the need for data transformation (Alimohammady *et al.*, 2017). Therefore, it can be concluded that the prediction of the experimental data acquired from the quadratic model for the adsorption of EFV and NVP by CLDH is reasonably satisfactory.

$$Y = 25.64 - 3.99A - 5.07B + 0.13C - 15.35D + 11.14AC + 4.87BD + 16.45D^2 \quad (8.1)$$

$$Y = 26.36 - 5.49A - 5.54B - 17.05D + 11.97AC + 4.02BD + 14.74D^2 \quad (8.2)$$

Table 8.1: Analysis of variance for the quadratic model (EFV)

Source	**Sum of squares**	**DF**	**Mean square**	**F-value**	**P-Value**
Model	5375.75	7	767.96	13.25	< 0.0001
A-Adsorbent loading	168.01	1	168.01	2.9	0.1124
B-Temperature	410.67	1	410.67	7.09	0.0196
C-pH	0.1389	1	0.1389	0.0024	0.9617
D-pollutant concentration	3298.93	1	3298.93	56.92	< 0.0001
AC	646.05	1	646.05	11.15	0.0053
BD	203.68	1	203.68	3.51	0.0084
D^2	1011.59	1	1011.59	17.45	0.0011
Residual	753.45	13	57.96		
Lack of fit	17.05	5	3.41	0.7056	0.6587
Pure error	14.5	3	4.83		
Cor Total	6129.2	20			

Table 8.2: Analysis of variance for the quadratic model (NVP)

Source	Sum of squares	DF	Mean square	F-value	P-Value
Model	5900.99	6	983.5	13.24	< 0.0001
A-Adsorbent loading	320.53	1	320.53	4.32	0.0567
B-Temperature	390.51	1	390.51	5.26	0.0379
D-pollutant concentration	4105.01	1	4105.01	55.26	< 0.0001
AC	746.89	1	746.89	10.06	0.0068
BD	144.22	1	144.22	1.94	0.0019
D^2	813.16	1	813.16	10.95	0.0052
Residual	1039.9	14	74.28		
Lack of fit	305.47	6	50.91	8.13	0.569
Pure error	18.8	3	6.27		
Cor Total	6940.89	20			

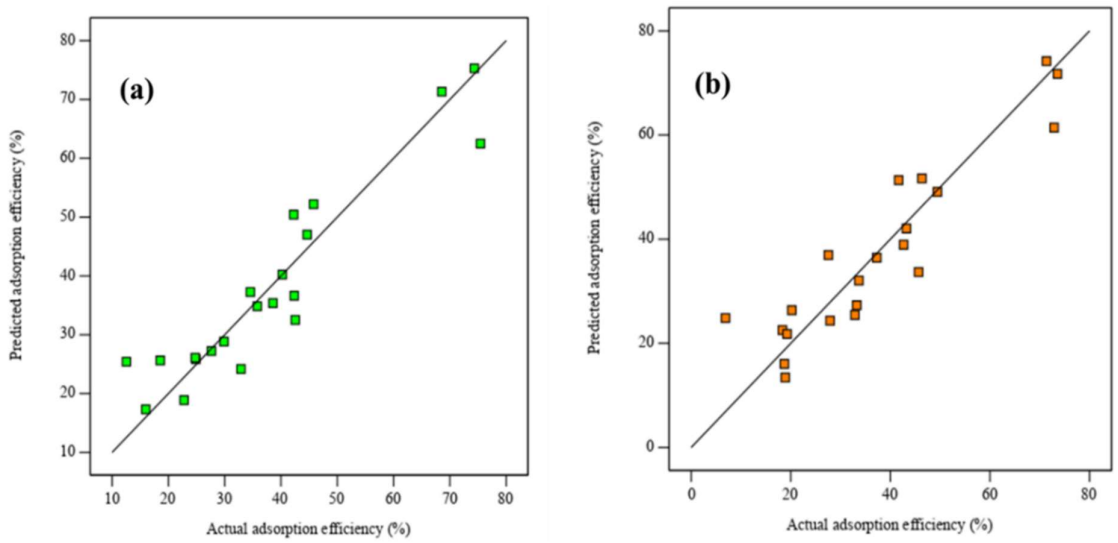

Figure 8.7: Predicted adsorption efficiency vs actual adsorption efficiency EFV (a) and NVP (b).

8.3.2 Interpretation of 3-Dimensional (3D) and Contour Plots

Figures 8.8 and 8.9 depict the 3D plots and contour projections for the interactions between pH and adsorbent loading, along with pollutant concentration, and temperature, for both EFV and NVP. The temperature versus pollutant concentration projections were similar for both

pollutants, indicating a consistent trend. However, there was a slight variation in the projections for pH versus adsorbent loading, particularly in the contour plot for EFV, where the 40% adsorption efficiency percentile was not clearly defined.

The temperature versus pollutant concentration projections demonstrated that higher adsorption efficiencies can be achieved at lower pollutant concentrations and temperatures. The explanation of this occurrence can be attributed to two primary factors. Firstly, as pollutant concentrations decrease, the number of active sites accessible for interaction increases. This enhanced availability of active sites allows for more effective pollutant adsorption. Secondly, at lower temperatures, molecular species have less mobility, making them more susceptible to being captured by adsorbent particles (Chabi *et al*., 2020; Oliveira *et al*., 2008).

The interactions between pH and adsorbent loading revealed that high adsorption efficiencies can be obtained under two conditions: low pH and low adsorbent loading, as well as high pH and high adsorbent loading. The pKa value of NVP is 2.8, indicating that the molecule has a positive charge at pH levels below 2.8 and becomes neutral at pH values over 2.8. Similarly, the point of zero charge for CLDH is 8.9, as shown in Figure D1 in Appendix D. Consequently, conducting the adsorption process at a pH range of 2.8 to 8.9 was expected to promote NVP removal due to electrostatic interactions with CLDH. EFV has a pKa value of 10.2, suggesting that the molecule is positively charged at pH values lower than 10.2. This means that electrostatic interactions between EFV and CLDH will be influenced by the material's pH-neutralising capacity, which is regulated by adsorbent loading. At pH greater than 12, the reconstruction of CLDH may be accelerated due to the increased concentration of OH^- (Clark *et al*., 2019; Eiby *et al*., 2016). Both molecules (EFV and NVP) would be neutral under these conditions, whereas the adsobernt would be negatively charged. As a result, weak electrostatic interactions would occur, leading to reduced removal efficiencies.

Moderate adsorbent loadings are favoured as they provide an adequate number of active sites while minimising the risk of reduced dispersion efficiency and agglomeration of the adsorbent, which can block active sites (Tabana *et al*., 2020). Acidic pH conditions are not recommended for processes involving LDH materials, as they can potentially damage the material structure (Dos Santos *et al*., 2013). However, this negative impact can be mitigated by operating at optimum adsorbent loadings, as the LDH can neutralise the solution due to its natural pH being between 8 to 10 (Elhachemi *et al*., 2022, Amamra *et al*., 2021). Based on these results, the

optimal conditions were determined to be a pH of 5, an adsorbent loading of 10 g/L, and an ambient temperature of approximately 25 °C.

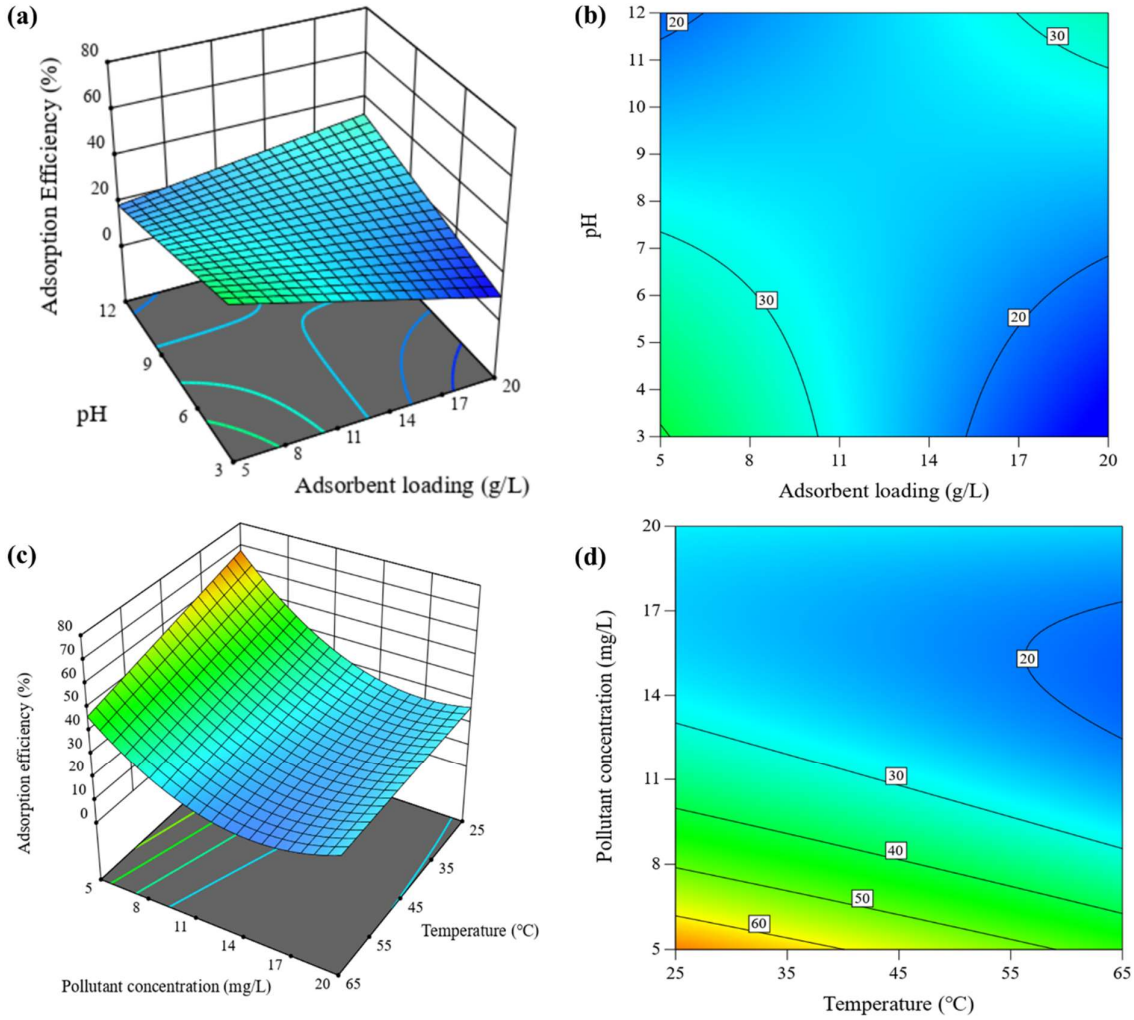

Figure 8.8: Response surface plots (3D and contour projection) showing variables' effects on adsorption of EFV (a) and (b) adsorbent loading (5 – 20 g L^{-1}) vs pH (5 – 20), (c) and (d) temperature (25 – 65 °C) vs pollutant concentration (5 – 20 mg L^{-1}).

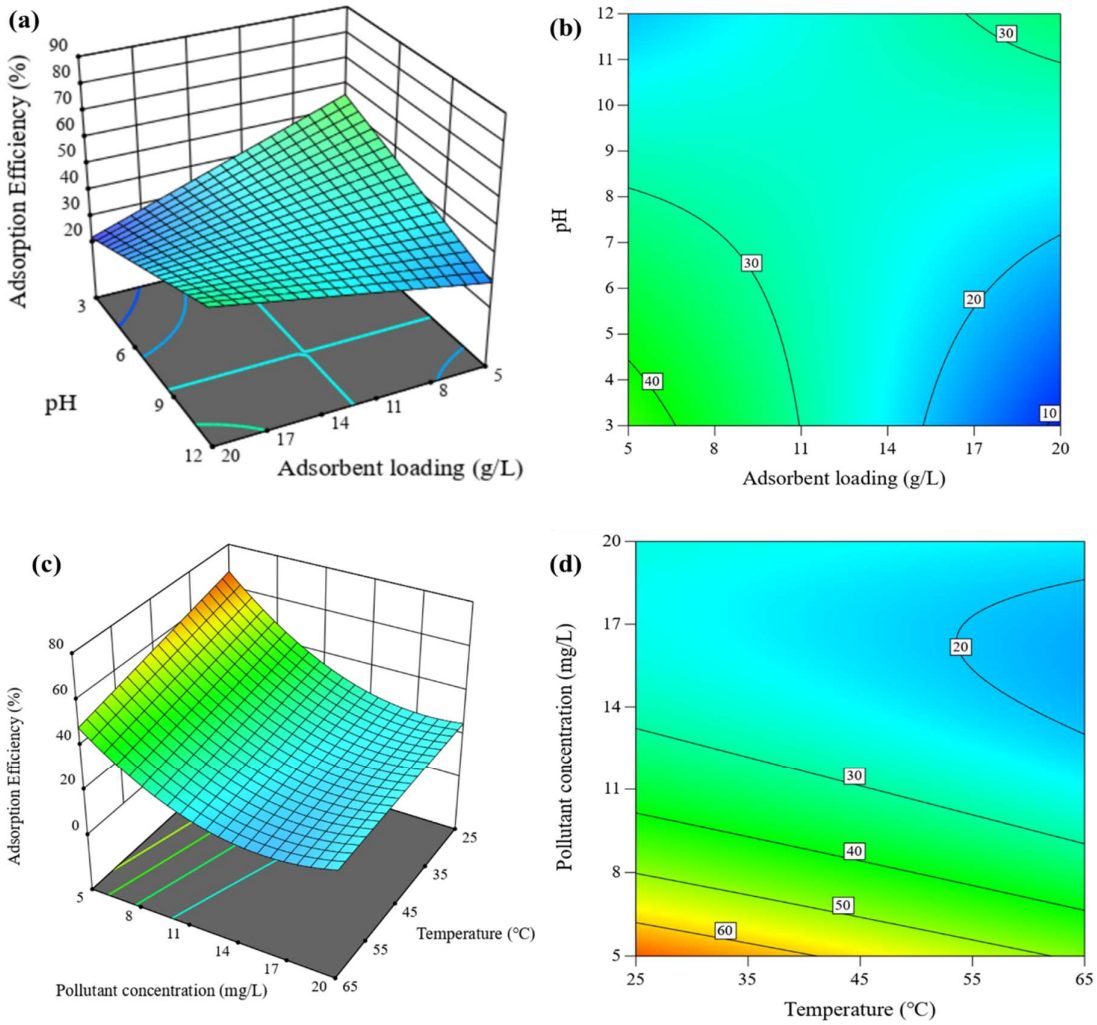

Figure 8.9: Response surface plots (3D and contour projection) showing variables' effects on adsorption of NVP (a) and b) adsorbent loading (5 – 20 g L^{-1}) vs pH (5 – 20), (c) and (d) temperature (25 – 65 °C) vs pollutant concentration (5 – 20 mg L^{-1}).

8.3.3 Reaction Kinetics and the Effect of Pollutant Concentration

Figure 8.10 displays the amounts of EFV and NVP adsorbed by a CLDH as determined through Equation (8.3). The results indicated that NVP exhibited a faster adsorption rate compared to EFV, reaching equilibrium after 20 h, whereas EFV required 24 h to reach equilibrium. The kinetic data was fitted to the pseudo-first order (PFO) and pseudo-second order (PSO) kinetics models, as represented by Equations (8.4) and (8.5). The kinetics data was found to be fitting onto the PSO model as depicted in Figure 8.11 for both pollutants with an initial concentration of 10 mg L^{-1} (the fitted kinetics at 5 mg L^{-1} and 20 mg L^{-1} for EFV and NVP are shown in

Figure D2 and D3 in Appendix D). Detailed kinetics parameters for EFV and NVP adsorption are displayed in Table 8.3 (PFO parameters are shown in Table D1 in Appendix D).

$$q_t = \frac{V}{m}(C_0 - C_t) \quad (8.3)$$

$$q_t = q_e(1 - e^{-k_1 t}) \quad (8.4)$$

$$q_t = \frac{q_e^2 k_2 t}{q_e k_2 t + 1} \quad (8.5)$$

Where V is the volume of wastewater solution (L); m is the mass of adsorbent (g); qe is the mass adsorbed at equilibrium (mg g^{-1}); k_1 is the PFO rate constant (h^{-1}); k_2 is the PSO rate constant (g mg^{-1} h^{-1}).

The rate constants for both EFV and NVP showed a decrease with an increase in initial concentration, indicating a complex reaction governed by numerous factors, including initial concentration, molecular collisions, or reaction mechanisms (Soustelle, 2011). The calculated equilibrium capacities were established to be consistently higher than the experimental values. These disparities demonstrated the model's inadequacies in fully describing the system's actual adsorption kinetics. The consistent increase in calculated adsorption capacities indicated a divergence from the PSO kinetic model's assumptions, particularly those relating to monolayer adsorption and uniform adsorption sites (Guo &Wang, 2019; Zhang, 2019). These variations indicated that the adsorption mechanisms driving the interaction of EFV and NVP with CLDH were more complex than a monolayer adsorption process and involved non-uniform adsorption sites. Based on these findings, it is evident that the adsorption process is a multidimensional mechanism.

Table 8.3: PSO kinetic models' parameters (initial concentration of 10 mg/L, pH 5, T=25 ℃ and adsorbent loading of 10 g L^{-1})

Concentration	Parameter	Efavirenz	Nevirapine
5 mg/L	k_2 (g mg^{-1} h^{-1})	0.073	0.016
	q_e (calculated)(mg g^{-1})	0.647	1.23
	q_e (experimental)(mg g^{-1})	0.362	0.42
	R^2	0.998	0.997
10 mg/L	k_2 (g mg^{-1} h^{-1})	0.034	0.028
	q_e (calculated)(mg g^{-1})	1.19	1.32
	q_e (experimental)(mg g^{-1})	0.629	0.748
	R^2	0.996	0.995
20 mg/L	k_2 (g mg^{-1} h^{-1})	0.017	0.006
	q_e (calculated)(mg g^{-1})	1.62	2.81
	q_e (experimental)(mg g^{-1})	0.64	0.824
	R^2	0.997	0.997

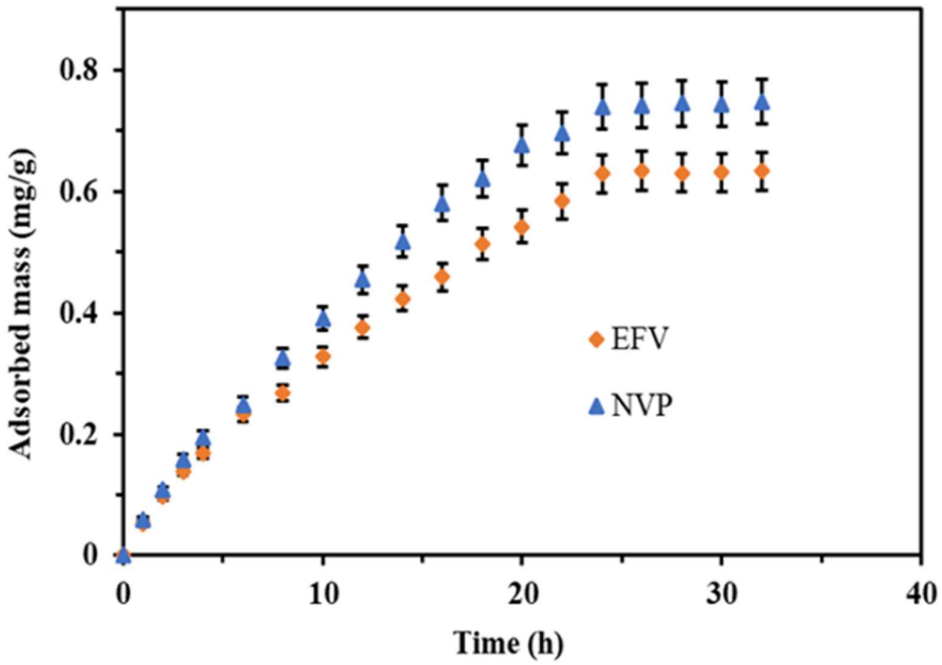

Figure 8.10: Adsorbed amounts of EFV and NVP at an initial concentration of 10 mg L^{-1}, pH 5, T=25 ℃ and adsorbent loading of 10 g L^{-1}.

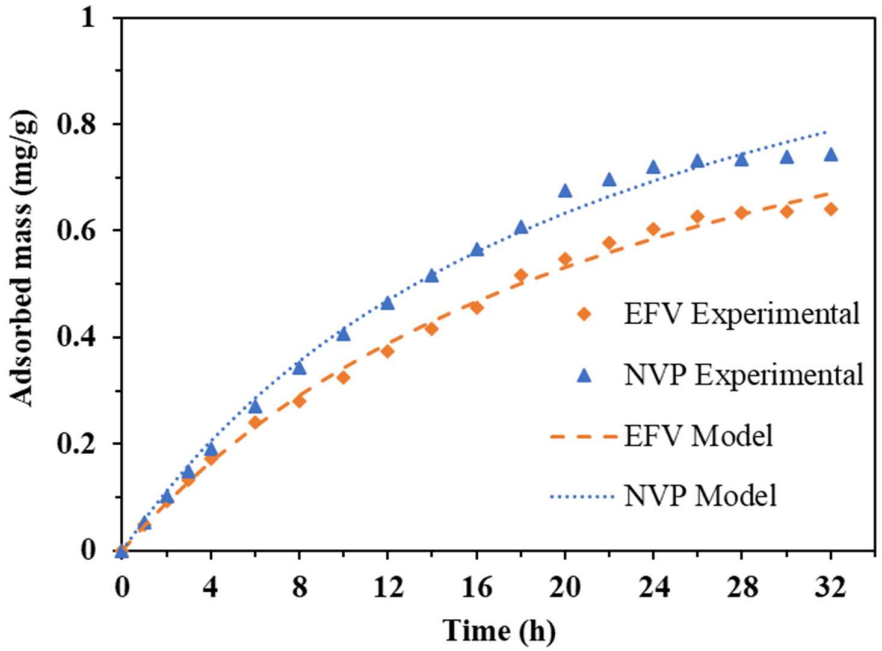

Figure 8.11: PSO kinetics model for EFV and NVP at an initial concentration of 10 mg L^{-1}, pH 5, T=25 ℃ and adsorbent loading of 10 g L^{-1}.

The investigation of the intra-particle behaviour in the adsorption processes was carried out using Equation (8.6), and the corresponding results are presented in Figure 8.12. Since the linearised trendlines deviated from passing through the origin, it indicated that intra-particle diffusion alone was not the sole rate-limiting step in the adsorption mechanism (Santi, 2012). Therefore, it can be deduced that both surface adsorption and intra-particle diffusion processes operate concurrently during the interaction between ARVDs and CLDH.

$$q_t = K_{ip} t^{0.5} + C \qquad (8.6)$$

Where K_{ip} is the rate constant of intra-particle diffusion; C is the vertical axis intercept.

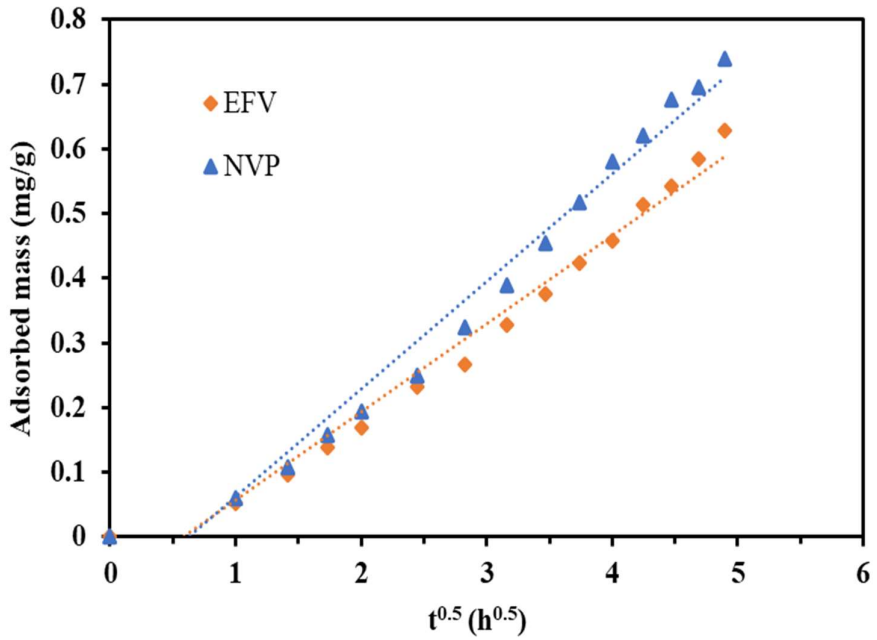

Figure 8.12: Intra-particle diffusion plots for EFV and NVP at an initial concentration of 10 mg L^{-1}, pH 5, T=25 °C and an adsorbent loading of 10 g L^{-1}.

8.3.4 Adsorption Isotherms

Figures 8.13 (a) and (b) show the adsorption isotherms for both EFV and NVP, respectively, with the adsorption isotherm parameters presented in Table 8.4. The data was fitted onto the Langmuir and Freundlich isotherms (as shown in Equations (8.7) and (8.8), respectively), with the latter providing the best fit for both pollutants. Notably, the heterogeneity factor (n) exceeds 1 under the tested conditions, indicating favourable adsorption characteristics. The maximum adsorption capacities obtained for EFV and NVP were estimated to be 2.73 mg/g and 2.93 mg/g, respectively. These values are relatively low compared to the results reported by Adeola *et al.* (2021), who achieved maximum adsorption capacities of 4.41 mg g^{-1} and 48.31 mg g^{-1} for EFV and NVP, respectively, using graphene wool as the adsorbent.

$$q_e = \frac{q_m K_L C_e}{1+K_L C_e} \quad (8.7)$$

$$q_e = K_F C_e^n \quad (8.8)$$

Where K_F is the Freundlich equilibrium constant (L g^{-1}); K_L is the Langmuir constant (L mg^{-1}); C_e is the pollutant concentration at equilibrium (mg L^{-1}); n is the heterogeneity constant (dimensionless); q_m is the maximum adsorption capacity (mg/g).

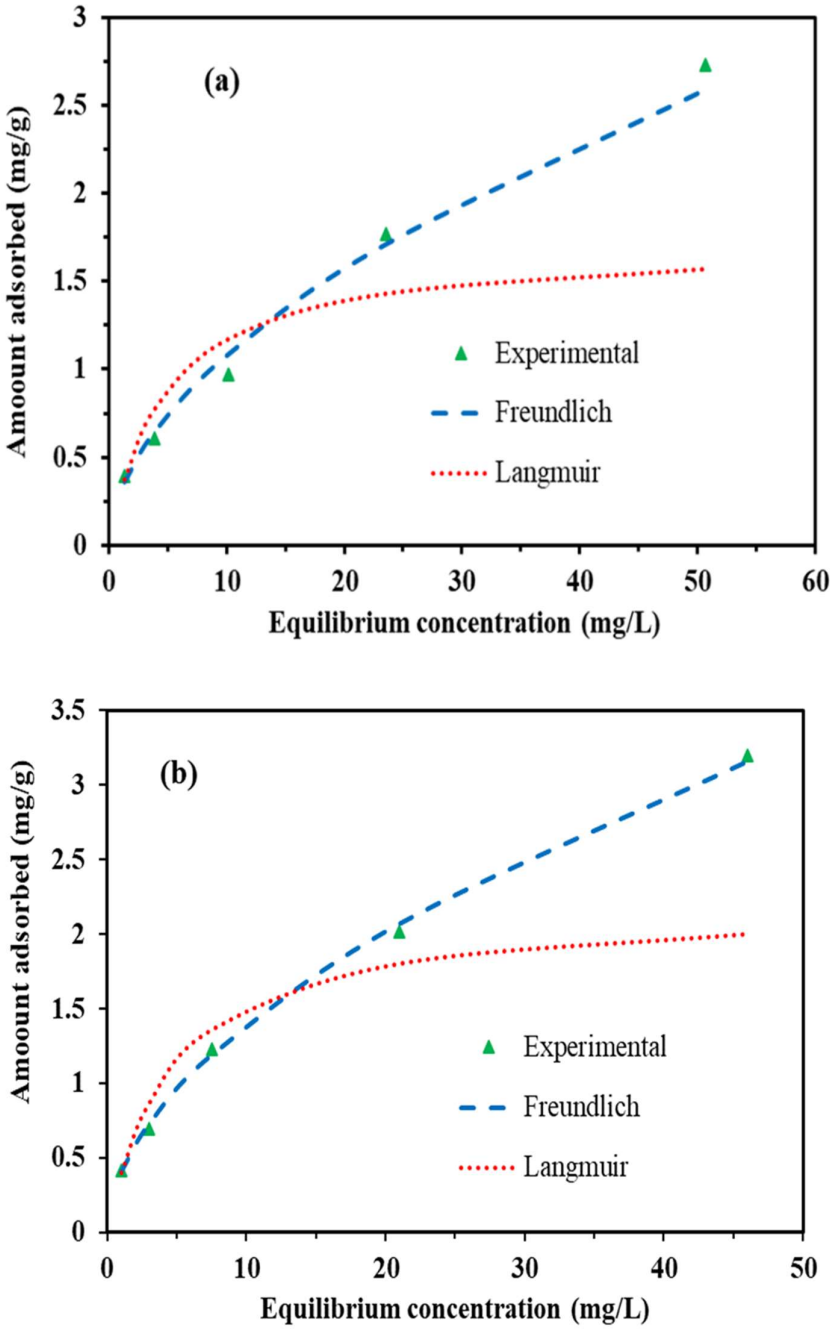

Figure 8.13: Equilibrium adsorption isotherms (a) EFV and (b) NVP at various concentrations, pH 5 and T=25 ℃ and an adsorbent loading of 10 g L^{-1}.

Table 8.4: Adsorption equilibrium isotherms parameters (pH 5, T=25 °C and an adsorbent loading of 10 g L^{-1})

Isotherm	Parameters	Efavirenz	Nevirapine
Langmuir	K_L (L mg^{-1})	0.21	0.48
	q_m (mg g^{-1})	1.71	1.52
	R^2	0.79	0.80
Freundlich	K_F (L g^{-1})	0.31	0.44
	n	1.85	2.07
	R^2	0.99	0.95

8.3.5 Thermodynamics Studies

The adsorption isotherm results were further analysed to investigate the thermodynamics of the adsorption process. The thermodynamics equilibrium constant (K_c) and the change in Gibbs free energy (ΔG°) were determined using Equations (8.9) and (8.10), respectively. The other parameters were estimated using a linear plot of ln K_c vs 1/T, as shown in Equation (8.11). The corresponding parameters obtained from the thermodynamic studies are presented in Table 8.5. The negative values of ΔG° indicated a spontaneous adsorption process.

Additionally, the negative values of the change in enthalpy (ΔH°) suggested that the adsorption process was exothermic, aligning with the findings presented in Section 3.2.2. Notably, the values of the change in enthalpy (ΔH°) were determined to be –9.67 kJ mol^{-1} for EFV and – 11.19 kJ mol^{-1} for NVP, indicating that the adsorption process was predominantly governed by physisorption interactions rather than chemisorption (Alimohammady & Ghaemi, 2020). It can be deduced that the adsorption of EFV and NVP onto CLDH involved relatively weaker physical interactions rather than strong chemical bonding. The positive value of ΔS° signified the affinity of the adsorbent for the adsorbate species. Additionally, it indicated an augmented level of randomness at the solid/solution interface, accompanied by structural modifications in both the adsorbate and the adsorbent. This phenomenon was particularly relevant to CLDH, given the structural alterations occurring during the reformation of the material upon contact with aqueous solutions.

$$K_{\mathrm{c}} = \frac{1000 \times K_{\mathrm{I}} \times MM_{\mathrm{ads}} \times C^{\circ}_{\mathrm{ads}}}{\gamma} \tag{8.9}$$

$$\Delta G^{\circ} = -\mathrm{R}T \ln K_{\mathrm{c}} \tag{8.10}$$

$$\ln K_c = \frac{\Delta S^\circ}{\mathrm{R}} - \frac{\Delta H^\circ}{\mathrm{R}T} \qquad (8.11)$$

Where T is the reaction temperature (K); R is the universal gas constant (8.314 J mol^{-1}K^{-1}); C°_{ads} is the standard adsorbate concentration (1 mol L^{-1}); K_c is the thermodynamic equilibrium constant (dimensionless); K_I is the equilibrium constant depending on the best isotherm model fitted (L mg^{-1}); MM_{ads} is the molar mass of adsorbate (g mol^{-1}); $\Delta G°$ is the change in Gibbs free energy (kJ mol^{-1}); $\Delta H°$ is the change in enthalpy (kJ mol^{-1}); $\Delta S°$ is the change in entropy (kJ mol^{-1}K^{-1}); γ is the activity coefficient (dimensionless).

Table 8.5: Thermodynamics parameters for EFV and NVP adsorption onto CLDH

Pollutant	**T (K)**	***Ln* (K_c)**	**$\Delta G°$ (kJ mol^{-1})**	**$\Delta H°$ (kJ mol^{-1})**	**$\Delta S°$ (J mol^{-1}K^{-1})**
Efavirenz	298	11.5	–28.49	–9.67	62.98
	308	11.35	–29.06		
	318	11.19	–29.58		
	338	11.04	–31.02		
Nevirapine	298	11.67	–28.91	–11.9	56.31
	308	11.37	–29.12		
	318	11.19	–29.58		
	338	11.08	–31.14		

8.3.6 Recycling of the Adsorbent

The spent adsorbent suspensions (from both EFV and NVP adsorption) were recovered and subsequently subjected to recalcination at 500 °C for 4 h. Figure 8.14 (a) shows the adsorption efficiencies of EFV and NVP using the regenerated materials after recalcination of their respective spent CLDH. The results indicated that the decrease in EFV and NVP adsorption over the first three runs was relatively minor, amounting to approximately 11% and 7%, respectively. However, a notable decline in adsorption efficiency was observed after the fourth run, with EFV and NVP experiencing reductions of 20% and 23%, respectively. These findings suggested that the thermal regeneration of CLDH for reuse was only feasible for up to three runs, after which the material lost its sorption capacity. This observation aligned with a study by Mourid *et al*. (2019), who reported that LDH material could experience a loss in its adsorption capacity upon repeated calcinations due to increased crystallinity.

Furthermore, the quantification of XRD analysis conducted on the residues from NVP adsorption experiments revealed that the proportion of the periclase phase decreased from 55% in the first run to 32% in the fourth run, as presented in Table 8.6. Figure 8.14 (b) further supports this finding, as the diffraction peaks corresponding to the first run were characterised

by broad peaks, indicative of the amorphous periclase phase. In contrast, subsequent runs exhibited sharper peaks, suggesting an increase in crystallinity and the dominance of the spinel content. It can be inferred that the same phenomenon occurred on the material's reusability for EFV adsorption.

Table 8.6: Phase quantification of regenerated CLDH

Run number	Periclase	Spinel
1	55.34	44.66
2	52.89	47.11
3	48.57	51.43
4	32.46	67.54

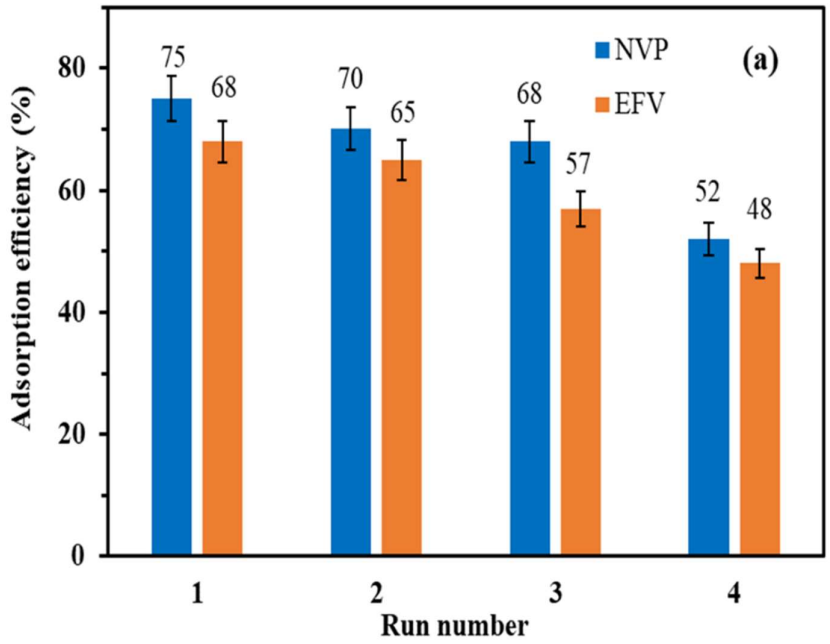

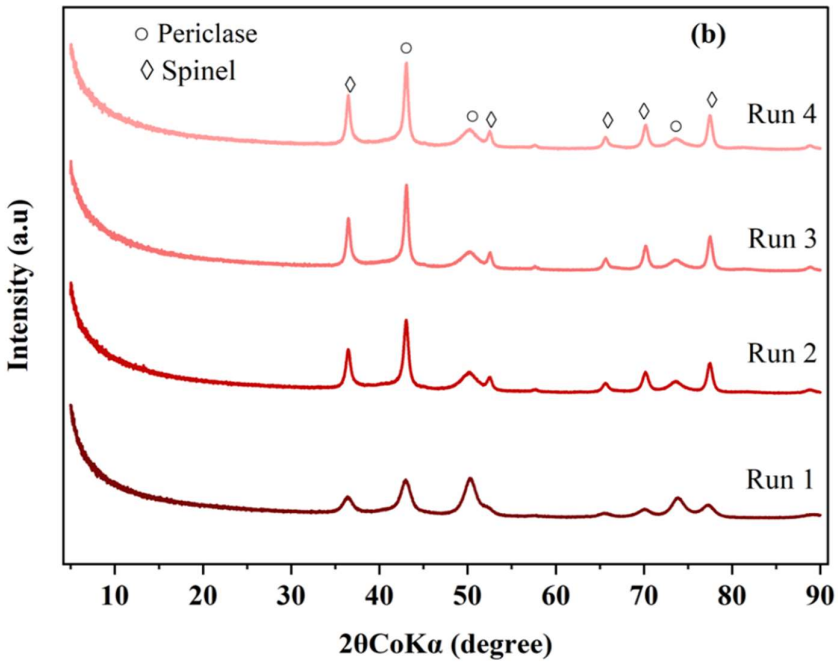

Figure 8.14: (a) Recycling and reusability of CLDH for adsorption of EFV and NVP, (b) XRD plots of recalcined LDH (initial concentration of 10 mg L^{-1}, pH 5 and T=25 °C and an adsorbent loading of 10 g L^{-1}).

8.3.7 Computational Modelling

Both classical and quantum simulations were employed to examine the adsorption behaviour of NVP and EFV on the CLDH. Figure 8.15 shows the resulting configuration of the optimised complex of NVP-CLDH and EFV-CLDH, respectively. Table 8.7 details the adsorption energies, total energies, and the average distances of the adsorbates from the substrate. The adsorption energy refers to the energy exchange upon adsorption of the relaxed species onto the substrate surface, a fundamental mechanism well-acknowledged in pollutant-LDH interactions (Thiebault *et al*., 2015).

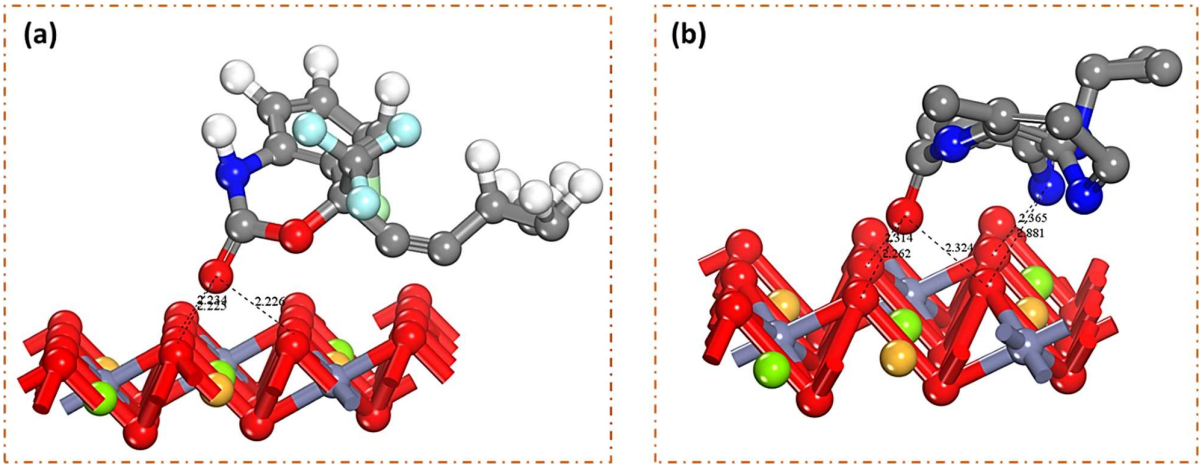

Figure 8.15: Adsorption configuration of the (a) NVP and (b) EFV on the CLDH through classical simulation.

Table 8.7: Classical simulations for the adsorption of NVP and EFV on the CLDH showing the adsorption energies, total energies, and the average closest distance of the adsorbate from the substrate.

Structure of complex	**Adsorption energy (kcal mol^{-1})**	**Total energy (kcal mol^{-1})**	**Average distance (Å)**
NVP -CLDH	-731.78	-223.17	2.30
EFV -CLDH	-512.60	-500.22	2.23

Both NVP and EFV displayed robust interactions with CLDH, as reflected in their highly negative adsorption energies. This highlighted the spontaneity of the adsorption process, which aligned with the findings from the thermodynamics studies. Furthermore, the close proximity of the adsorbates to the substrate (2.3 Å for NVP and 2.23 Å for EFV) reinforced the notion of robust adsorptive interactions. The computed adsorption energies indicated a notably stronger interaction between NVP and CLDH than EFV, with NVP exhibiting an adsorption energy of –731.78 kcal mol^{-1} compared to EFV's –512.60 kcal mol^{-1}. This discrepancy indicated that NVP forms a more stable complex with CLDH in compared to EFV. This aligned with the reaction kinetics studies, as presented in Section 8.2.3.

Furthermore, the in-depth analysis involved applying the RDG and Sign(λ_2)*ρ function to examine weak interaction zones. RDG isosurfaces, representing electron density and its gradient, were color-coded to denote the intensity and nature of the interactions. Blue

isosurfaces indicated strong non-covalent interactions, while green represented Van der Waals interactions, and red signified strong repulsive interactions, such as steric hindrance. Identifying regions with low electron density provided valuable insights (Adekoya *et al*., 2022). Hence, the NCI plots (Figure 8.16) visually represent the interactions between NVP, EFV, and CLDH. These plots highlighted the presence of hydrogen bonding, reiterating its role in the adsorption process. The analysis suggested he presence of dipole-dipole interactions in both NVP and EFV adsorption processes. Specifically, in NVP, the closest oxygen atom to the surface of the material, carrying a partial negative charge (δ-), exhibited attraction towards the electropositive hydrogen atoms of the three neighboring hydroxides in CLDH, indicating the formation of a hydrogen bond.

Additionally, there was a strong attraction between the oxygen of NVP and the Mg atom in CLDH, suggesting the potential formation of an ionic bond resulting in MgO. Similarly, in EFV, the oxygen atom with a partial negative charge (δ-) experienced attraction towards the electropositive hydrogen atoms of the neighboring oxygen atoms in CLDH, forming a hydrogen bond. Furthermore, a strong attraction was observed between the oxygen of EFV and the Mg atom in CLDH, implying the potential formation of an ionic bond leading to MgO. Additionally, a hydrogen bond was observed between the nitrogen atom of EFV and one of the neighboring hydroxides in the material structure. Therefore, the study established that both NVP and EFV formed stable complexes with CLDH, with NVP displaying a higher affinity. These interactions were predominantly driven by hydrogen bonding, as supported by the NCI plots.

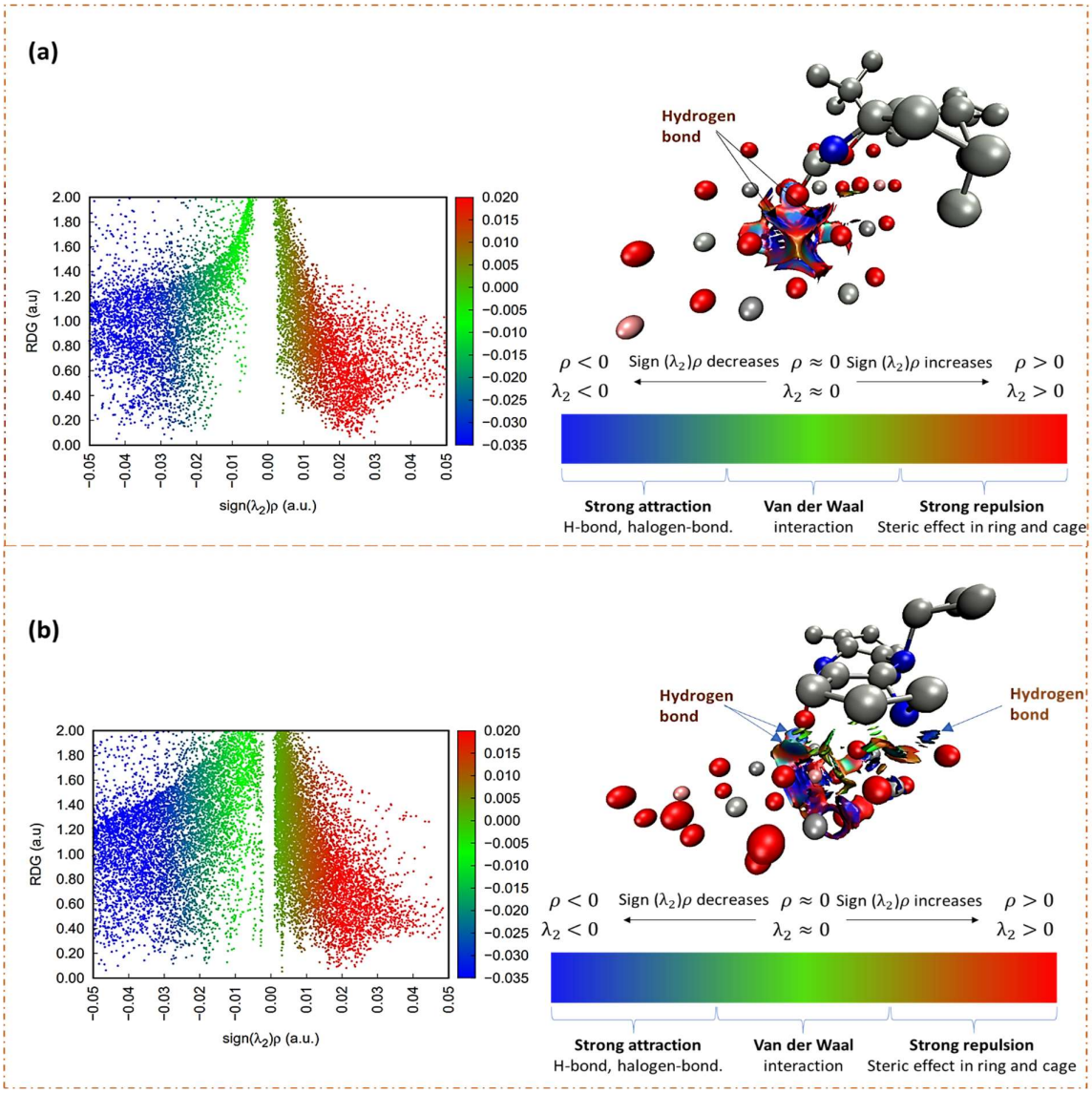

Figure 8.16: Non-covalent interaction analysis of (a) NVP and (b) EFV on the CLDH.

8.4 Conclusion

This study provided insightful knowledge about the adsorption of EFV and NVP on CLDH. These two ARVDs have been identified as persistent pollutants in waterbodies, posing potential risks to human health and the environment. The characterisation of CLDH through XRD analysis revealed that it predominantly consisted of the periclase phase, which is known to be favourable for adsorption processes. This finding supported the suitability of CLDH as an effective adsorbent for the removal of EFV and NVP. Additionally, the investigation of the interactions between the independent adsorption variables revealed significant interactions between the solution's initial pH and adsorbent loading, along with the interaction between the

reaction temperature and the initial concentration of the pollutants. Subsequent investigations into the adsorption kinetics, isotherms, and thermodynamics revealed that the physical interactions primarily governed the adsorption process.

Additionally, the feasibility of regenerating LDH material for reuse through thermal recalcination was highlighted. However, the recycling capability was limited to three runs, as the adsorption efficiency decreased significantly after that point. This decline resulted from a rise in crystallinity and a shift in phase proportions. The computational analysis reiterated that physisorption was the predominant mechanism driving the adsorption of ARVDs onto CLDH, primarily facilitated by hydrogen bonding. Furthermore, it was revealed that NVP demonstrated a higher affinity for the adsorbent than EFV.

CHAPTER 9: CONCLUSION AND RECOMMENDATIONS

9.1 Conclusion

The comprehensive characterisation of LDH and Ag-AgBr-LDH photocatalysts through various analytical techniques has provided valuable insights into their structural, morphological, compositional, and textural properties. X-ray diffraction (XRD) analysis confirmed the formation of LDH material with carbonate ions in the interlayer region, while also identifying the presence of LDH, AgBr, and metallic silver (Ag^0) in the composite catalyst. Scanning electron microscopy (SEM) and transmission electron microscope (TEM) images elucidated the platelet-like structures of LDH and the spherical-like shapes of Ag-AgBr nanoparticles within the composite. Energy dispersive X-ray spectroscopy (EDS) confirmed the elemental compositions of both materials and revealed an excess of Ag relative to Br in the composite, indicating successful silver formation. Further characterisation through X-ray photoelectron spectroscopy (XPS) unveiled the chemical states of the elements present, with distinct peaks corresponding to magnesium, aluminum, zinc, silver, bromine, and oxygen species. Additionally, nitrogen gas adsorption-desorption isotherms unveiled mesoporous structures with pore diameters ranging from 2 to 50 nm. The incorporation of Ag-AgBr nanoparticles into LDH led to a notable reduction in pore volume and specific surface area, indicating structural alterations induced by nanoparticle introduction.

The synthesised photocatalyst containing Ag-AgBr and LDH exhibited enhanced efficacy in degrading phenol compared to Ag-AgBr and LDH separately. The presence of zinc in the photocatalyst was found to be crucial in enhancing its photocatalytic activity, leading to higher phenol degradation efficiencies. Over 92% of phenol was degraded over 8 hours at neutral pH under visible light irradiation. The degradation pathway of phenol involved the formation of catechol, glycerol, and hydroxy acetic acid intermediates, primarily driven by hydroxyl free radicals as the dominant reactive species. Furthermore, the synthesised photocatalyst demonstrated superior performance in degrading ARVDs (efavirenz and nevirapine) compared to Ag-AgBr and LDH individually. Response surface modelling revealed significant interactions between photocatalyst loading and initial concentration for efavirenz, and between pH and photocatalyst loading, as well as photocatalyst loading and initial concentration for nevirapine. Over 80% and 100% of efavirenz and nevirapine were degraded over 12 and 8 h, respectively, under neutral pH and visible light irradiation. The degradation mechanism

involved the generation of hydroxy free radicals and photo-induced holes as the active species responsible for ARVD degradation.

Additionally, the study established the efficacy of continuous flow photocatalytic reactors in degrading ARVDs in wastewater. Systematic experiments revealed the influence of light intensity, initial pollutant concentration, photocatalyst loading, and flow rate on photodegradation efficiencies of EFV and NVP. While light intensity correlated positively with degradation efficiency, prolonged exposure led to photo corrosion of the catalyst. Higher initial pollutant concentration and flow rate were not limited by mass transfer yet achieved lower photodegradation efficiencies due to irradiation homogeneity issues.

Moreover, the investigation into the adsorption of EFV and NVP on CLDH provided insightful knowledge for their removal from water. XRD analysis confirmed the predominance of the periclase phase in CLDH, favouring adsorption processes. Significant interactions between the initial pH of the solution and adsorbent loading, and between the reaction temperature and initial concentration of the pollutants, were observed. Adsorption kinetics, isotherms, and thermodynamics revealed physical interactions governing the adsorption process, with regeneration potential through thermal recalcination highlighted. Computational analysis reaffirmed physisorption as the primary mechanism, primarily facilitated by hydrogen bonding, with NVP exhibiting higher affinity for the adsorbent compared to EFV.

9.2 Recommendations

To enhance the efficacy of photocatalytic systems for ARVD degradation, several key areas warrant further investigation. First, optimising the design of photocatalytic reactors is crucial. The study highlights the effectiveness of continuous flow reactors, but fine-tuning parameters such as light intensity, flow rate, and photocatalyst loading could lead to significant improvements in degradation efficiency. Advanced reactor configurations that ensure uniform light distribution and efficient mass transfer should be explored to maximise treatment performance. Integrating adsorption and photocatalysis into a hybrid system presents another promising avenue for research. The study's findings suggest that combining these processes could enhance pollutant removal. Future work should focus on optimising the parameters for both adsorption and photocatalysis within a single treatment system, potentially leading to more efficient and effective water treatment solutions.

Exploring alternative light sources, such as LEDs or natural sunlight, could offer practical advantages in photocatalytic applications. Evaluating the performance of Ag-AgBr-LDH photocatalysts under these light sources may provide insights into their effectiveness and cost benefits, further broadening the applicability of photocatalytic systems. Long-term stability and reusability of photocatalysts are critical for practical applications. Extending stability tests and assessing photocatalyst performance over multiple cycles under various operational conditions will provide valuable data on their durability and viability. Implementing regeneration strategies, such as thermal or chemical treatments, could also enhance the reusability of photocatalysts.

A deeper understanding of the degradation mechanisms and intermediate products formed during the photocatalytic process is essential. Investigating these mechanisms will shed light on the roles of reactive species, such as hydroxyl radicals and photo-induced holes, in pollutant removal. This knowledge could guide the development of more efficient photocatalysts and treatment processes. Finally, combining computational models with experimental data can also offer a comprehensive understanding of photocatalyst performance and pollutant interactions. Advanced computational techniques should be employed to predict behaviour and optimise materials and processes, providing a robust framework for future research and development in photocatalytic systems.

REFERENCES

Abafe O.A., Späth J., Fick J., Jansson S., Buckley C., Stark A., Pietruschka B., and Martincigh B.S. (2018), Lc-Ms/Ms Determination of Antiretroviral Drugs in Influents and Effluents from Wastewater Treatment Plants in Kwazulu-Natal, South Africa, *Chemosphere,* 200**,** 660-670, https://doi.org/10.1016/j.chemosphere.2018.02.105.

Adekoya G.J., Sadiku E.R., Hamam Y., Mwakikunga B.W., and Ray S.S. (2023), DFT and MC Investigation of Edot on Honeycomb Borophene as Potential Energy Storage Material. AIP Conference Proceedings, AIP Publishing, https://doi.org/10.1063/5.0136110.

Adekoya O.C., Adekoya G.J., Sadiku R.E., Hamam Y., and Ray S.S., (2022), Density Functional Theory Interaction Study of a Polyethylene Glycol-Based Nanocomposite with Cephalexin Drug for the Elimination of Wound Infection, *ACS Omega*, 7, 33808-33820, https://doi.org/10.1021/acsomega.2c02347.

Adeola A.O., de Lange J., and Forbes P.B., (2021), Adsorption of Antiretroviral Drugs, Efavirenz and Nevirapine from Aqueous Solution by Graphene Wool: Kinetic, Equilibrium, Thermodynamic and Computational Studies, *Applied Surface Science Advances,* 6**,** 100157, https://doi.org/10.1016/j.apsadv.2021.100157.

Afonso, T. B., Bonifácio-Lopes, T., Costa, E. M., and Pintado, M. E., (2023), Phenolic Compounds from By-Products for Functional Textiles. *Materials*, *16*(22), 7248.

Afreen, G., and Upadhyayula, S., (2021), Alkylation of Phenol and Substituted Phenols with C1–C4 Alcohols/Olefins as an Upgrading Route for Bio-oil Oxygenates: A review. *Renewable and Sustainable Energy Reviews*, *147*, 111189.

Ahmadvand, S., Elahifard, M., Jabbarzadeh, M., Mirzanejad, A., Pflughoeft, K., Abbasi, B., and Abbasi, B., (2019), Bacteriostatic Effects of Apatite-Covered Ag/AgBr/TiO_2 Nanocomposite in the Dark: Anomaly in Bacterial Motility. *The Journal of Physical Chemistry B*, *123*(4), 787-791.

Ahmed, S., Khan, F.S.A., Mubarak, N.M., Khalid, M., Tan, Y.H., Mazari, S.A., Karri, R.R. and Abdullah, E.C., (2021), Emerging pollutants and their Removal using Visible-Light Responsive Photocatalysis–A Comprehensive Review, *Journal of Environmental Chemical Engineering*, *9*(6), p.106643. https://doi.org/doi.org/10.1016/j.jece.2021.106643.

Akawa, M. N., Dimpe, K. M., and Nomngongo, P. N., (2021), An adsorbent Composed of Alginate, Polyvinylpyrrolidone and Activated Carbon (AC@ PVP@ alginate) for Ultrasound-

Assisted Dispersive Micro-Solid Phase Extraction of Nevirapine and Zidovudine in Environmental Water Samples. *Environmental Nanotechnology, Monitoring & Management*, *16*, 100559.

Akenga P., Gachanja A., Fitzsimons M.F., Tappin A., and Comber S., (2021) , Uptake, Accumulation and Impact of Antiretroviral and Antiviral Pharmaceutical Compounds in Lettuce, Science of The Total Environment, 766, 144499, https://doi.org/10.1016/j.scitotenv.2020.144499.

Alexa, I., Popovici, R., Ignat, M., Popovici, E., and Voicu, V., (2011). Non-Toxic Nanocomposite Containing Captopril Intercalated Into Green Inorganic Carrier. *Digest Journal of Nanomaterials & Biostructures (DJNB)*, *6*(3).

Alimohammady, M., and Ghaemi, M., (2020), Adsorptive Removal of Hg^{2+} from Aqueous Solutions using Amino Phenyl-Pyrazole-Functionalized Graphene Oxide, *Carbon Letters*, *30*(5), 493–508, https://doi.org/10.1007/s42823-019-00119-8.

Alimohammady, M., Jahangiri, M., Kiani, F., and Tahermansouri, H., (2017), Highly Efficient Simultaneous Adsorption of Cd (II), Hg (II) and As (III) Ions from Aqueous Solutions by Modification of Graphene Oxide with 3-Aminopyrazole: Central Composite Design optimization, *New Journal of Chemistry*, *41*(17), 8905–8919, https://doi.org/10.1039/C7NJ01450C.

Amamra S., Djellouli B., Elkolli H., Benguerba Y., Erto A., Balsamo M., Ernst B., and Benachour D., (2021), Synthesis and Characterization of Layered Double Hydroxides Aimed at Encapsulation of Sodium Diclofenac: Theoretical and Experimental Study, *Journal of Molecular Liquids*, 338, 116677, https://doi.org/10.1016/j.molliq.2021.116677.

An, C., Wang, S., Sun, Y., Zhang, Q., Zhang, J., Wang, C., and Fang, J. (2016), Plasmonic Silver Incorporated Silver Halides for Efficient Photocatalysis. *Journal of Materials Chemistry A*, *4*(12), 4336-4352.

Antoniak-Jurak, K., Kowalik, P., Próchniak, W., Bicki, R., Michalska, K., and Słowik, G., (2021), Ecofriendly K-decorated ZnO/Zn (Al, La) 2O4 catalyst for Hydrogen Production–Effect of Heterostructure on Catalyst Activity at Steam-Lean Process Gas. *Fuel*, *302*, 121067.

Asghar, H., Maurino, V., and Iqbal, M. A, (2024), Development of Highly Photoactive Mixed Metal Oxide (MMO) Based on The Thermal Decomposition Of ZnAl-NO3-LDH. *Eng*, *5*(2), 589-599.

Asim, M., Saba, N., Jawaid, M., Nasir, M., Pervaiz, M. and Alothman, O.Y., (2018), A Review on Phenolic Resin and its Composites. *Current Analytical Chemistry*, *14*(3), pp.185-197.

Azu, O. O., (2012). Highly Active Antiretroviral Therapy (HAART) and Testicular Morphology: Current Status and a Case for a Stereologic Approach, *Journal of andrology*, *33*(6), 1130-1142.

Bahuguna, A., Singh, S., Bahuguna, A., Sharma, S. and Dadarwal, B. K., (2021), Physical Method of Wastewater treatment-A Review. *Journal of Research in Environmental and Earth Sciences,* 7**,** 2348-2532.

Bartolomeu, M., Neves, M., Faustino, M., and Almeida, A., (2018), Wastewater Chemical Contaminants: Remediation by Advanced Oxidation Processes. *Photochemical & Photobiological Sciences*, *17*(11), 1573-1598.

Belghit, A., Merouani, S., Hamdaoui, O., Bouhelassa, M., and Al-Zahrani, S., (2022), The Multiple Role of Inorganic and Organic Additives in the Degradation of Reactive Green 12 by UV/chlorine Advanced Oxidation Process. *Environmental Technology*, *43*(6), 835-847.

Belver, C., Bedia, J., Gómez-Avilés, A., Peñas-Garzón, M. and Rodriguez, J. J., (2019), Semiconductor Photocatalysis for Water Purification, *Nanoscale materials in water purification*, 581 - 651.

Binjhade R., Mondal R., and Mondal S., (2022), Continuous Photocatalytic Reactor: Critical Review on the Design and Performance, *Journal of Environmental Chemical Engineering,* 10**,** 107746.

Bodhankar, P. M., Sarawade, P. B., Singh, G., Vinu, A., and Dhawale, D. S., (2021), Recent advances in highly active nanostructured NiFe LDH catalyst for electrochemical water splitting. *Journal of Materials Chemistry A*, *9*(6), 3180-3208.

Boher, S., Ullah, R., Tuzen, M., and Saleh, T. A., (2023), Metal Doped Nanocomposites for Detection of Pesticides and Phenolic Compounds by Colorimetry: Trends and Challenges. *OpenNano*, 100168.

Brechtl, J. R., Breitbart, W., Galietta, M., Krivo, S., and Rosenfeld, B., (2001), The use of Highly Active Antiretroviral Therapy (HAART) in Patients with Advanced HIV infection: Impact on Medical, Palliative Care, and Quality of Life Outcomes. *Journal of pain and symptom management*, *21*(1), 41-51.

Broder, S. (2010), The Development of Antiretroviral Therapy and its Impact on the HIV-1/AIDS pandemic. *Antiviral research*, *85*(1), 1-18.

Bugosen, S., Mantilla, I. D., and Tarazona-Vasquez, F., (2020), Techno-Economic Analysis of Aniline Production *via* Amination of Phenol. *Heliyon*, *6*(12).

Cai, A., Wang, X., Guo, A., and Chang, Y., (2016), Mussel-inspired green synthesis of polydopamine-Ag-AgCl composites with efficient visible-light-driven photocatalytic activity. *Journal of Photochemistry and Photobiology B: Biology*, *162*, 486-492.

Caldas S.S., Escarrone A.L.V., and Primel E.G., (2017), Pharmaceuticals and Personal Care Products, *Chromatographic Analysis of the Environment,* CRC Press,

Camera-Roda G., Santarelli F., and Martin C.A., (2005), Design of Photocatalytic Reactors Made Easy by Considering the Photons as Immaterial Reactants, *Solar Energy,* 79**,** 343-352.

Capra L., Manolache M., Ion I., Stoica R., Stinga G., Doncea S.M., Alexandrescu E., Somoghi R., Calin M.R., and Radulescu I., (2018,) Adsorption of Sb (Iii) on Oxidized Exfoliated Graphite Nanoplatelets, *Nanomaterials,* 8**,** 992, https://doi.org/10.3390/nano8120992.

Carja, G., Dartu, L., Okada, K., and Fortunato, E., (2013), Nanoparticles of copper oxide on layered double hydroxides and the derived solid solutions as wide spectrum active nano-photocatalysts. *Chemical Engineering Journal*, *222*, 60-66.

Carja, G., Grosu, E. F., Mureseanu, M., & Lutic, D., (2017), A family of solar light responsive photocatalysts obtained using Zn^{2+} Me^{3+}(Me= Al/Ga) LDHs doped with Ga_2O_3 and In_2O_3 and their derived mixed oxides: a case study of phenol/4-nitrophenol decomposition. *Catalysis Science & Technology*, *7*(22), 5402-5412.

Chabi, N., Baghdadi M., Sani A.H., Golzary A., Hosseinzadeh M., (2020), Removal of Tetracycline with Aluminum Boride Carbide and Boehmite Particles Decorated Biochar Derived from Algae, *Bioresource Technology,* 316**,** 123950, https://doi.org/10.1016/j.biortech.2020.123950

Chakraborty, J., Sengupta, S., Dasgupta, S., Chakraborty, M., Ghosh, S., Mallik, S., Das, K. L., and Basu, D. (2012). Determination of trace level carbonate ion in Mg–Al layered double hydroxide: Its significance on the anion exchange behaviour. *Journal of Industrial and Engineering Chemistry*, *18*(6), 2211-2216.

Chan, S. S., Khoo, K. S., Chew, K. W., Ling, T. C. and Show, P. L., (2022), Recent Advances Biodegradation and Biosorption of Organic Compounds from Wastewater: Microalgae-Bacteria Consortium-A Review. *Bioresource Technology,* 344**,** 126159.

Chen C., Zeng H., Xiong J., Xu S. and An D., (2020a), Z-Scheme AgBr@ Ag/Coal Layered Double Hydroxide Heterojunction for Superior Photocatalytic Cr (VI) Reduction under Visible Light, *Applied Clay Science,* 192**,** 105627, https://doi.org/10.1016/j.clay.2020.105627.

Chen D., Cheng Y., Zhou N., Chen P., Wang Y., Li K., Huo S., Cheng P., Peng P. and Zhang R., (2020b), Photocatalytic Degradation of Organic Pollutants Using TiO_2-Based Photocatalysts: A Review, *Journal of Cleaner Production,* 268**,** 121725.

Chen, J., Yuan, D., and Wang, Y., (2023), Covalent Organic Frameworks Based Heterostructure in Solar-To-Fuel Conversion. *Advanced Functional Materials*, *33*(41), 2304071.

Cheng M., Zeng G., Huang D., Lai C., Xu P., Zhang C. and Liu Y., (2016), Hydroxyl Radicals Based Advanced Oxidation Processes (Aops) for Remediation of Soils Contaminated with Organic Compounds: A Review, *Chemical Engineering Journal,* 284**,** 582-598.

Chikhradze, N., Nadirashvili, M., Khomeriki, S., and Varshanidze, I., (2017), The synthesis of phenyl acetylene phenols for development of new explosives. IOP Conference Series: Earth and Environmental Science,

Chivu, V., Gilea, D., Cioatera, N., Carja, G., and Mureseanu, M., (2020), Heterostructures of Ce-Ti/layered double hydroxides and the derived MMOs for photoenergy applications. *Applied Surface Science*, *513*, 145853.

Chong, M.N., Jin, B., Chow, C.W., and Saint, C., (2010), Recent developments in photocatalytic water treatment technology: A review. Water research 44, 2997-3027. https://doi.org/10.1016/j.watres.2010.02.039.

Chuaicham, C., Karthikeyan, S., Song, J. T., Ishihara, T., Ohtani, B., & Sasaki, K., (2020), Importance of $ZnTiO_3$ phase in ZnTi-mixed metal oxide photocatalysts derived from layered double hydroxide. *ACS Applied Materials & Interfaces*, *12*(8), 9169-9180.

Clark I., Smith J., Gomes R.L. and Lester E., (2019), Continuous Synthesis of Zn_2Al-CO_3 Layered Double Hydroxides for the Adsorption of Reactive Dyes from Water, *Journal of Environmental Chemical Engineering*, 7, 103175, https://doi.org/10.1016/j.jece.2019.103175.

Colombo E. and Ashokkumar M., 2017, Comparison of the Photocatalytic Efficiencies of Continuous Stirred Tank Reactor (Cstr) and Batch Systems Using a Dispersed Micron Sized Photocatalyst, *RSC advances,* 7**,** 48222-48229.

Contreras-Ruiz, J., Martínez-Gallegos, S., García-Rivas, J., Illescas, J., González-Juárez, J., Macedo Miranda, G., and Ordonez Regil, E., (2019), Influence of the textural parameters of LDH-TiO 2 composites on phenol adsorption and photodegradation capacities. *International Journal of Photoenergy*, *2019*.

Cornejo, J., Celis, R., Pavlovic, I. and Ulibarri, M.A., (2008), Interactions of pesticides with clays and layered double hydroxides: a review. *Clay Minerals*, *43*(2), pp.155-175. https://doi.org/doi.org/10.1180/claymin.2008.043.2.01.

Crini, G. and Lichtfouse, E., (2019), Advantages and Disadvantages of Techniques used for Wastewater Treatment. *Environmental chemistry letters,* 17**,** 145-155.

Dai, B., Chen, X., Yang, X., Yang, G., Li, S., Zhang, L., Mu, F., Zhao, W. and Leung, D. Y., (2022), Designing S-scheme Au/g-C_3N_4/BiO1. 2I0. 6 Plasmonic Heterojunction for Efficient Visible-Light Photocatalysis, *Separation and Purification Technology*, 287, 120531.

Daud, M., Hai, A., Banat, F., Wazir, M. B., Habib, M., Bharath, G., and Al-Harthi, M. A., (2019), A review on the recent advances, challenges and future aspect of layered double hydroxides (LDH)–Containing hybrids as promising adsorbents for dyes removal. *Journal of Molecular Liquids*, *288*, 110989.

De Cock, K. M., and Weiss, H. A.,(2000). The global epidemiology of HIV/AIDS. *Tropical Medicine and International Health*, *5*(7), A3-A9.

Deng, P., Zhong, D., Yu, K., Zhang, Y., Wang, T., and Chen, X. (2013). Pharmacokinetics, metabolism, and excretion of the antiviral drug arbidol in humans. *Antimicrobial agents and chemotherapy*, *57*(4), 1743-1755.

Diffey, B. L. (2002). Sources and measurement of ultraviolet radiation. *Methods*, *28*(1), 4-13.

dos Santos R.M.M., Gonçalves R.G.L., Constantino V.R.L., Santilli C.V., Borges P.D., Tronto J., and Pinto F.G., (2017), Adsorption of Acid Yellow 42 Dye on Calcined Layered Double Hydroxide: effect of Time, Concentration, pH and Temperature, *Applied Clay Science,* 140**,** 132-139, https://doi.org/10.1016/j.clay.2017.02.005.

Eiby S., Tobler D., Nedel S., Bischoff A., Christiansen B., Hansen A., Kjaergaard H., and Stipp S., (2016), Competition between Chloride and Sulphate During the Reformation of Calcined Hydrotalcite, *Applied Clay Science*, 132, 650-659, https://doi.org/10.1016/j.clay.2016.08.017.

Elhachemi M., Chemat-Djenni Z., Chebli D., Bouguettoucha A., and Amrane A., (2022), Synthesis and Physicochemical Characterization of New Calcined Layered Double Hydroxide

Mg Zn Co Al-CO_3; Classical Modeling and Statistical Physics of Nitrate Adsorption, *Inorganic Chemistry Communications*, 145, 109549, https://doi.org/10.1016/j.inoche.2022.109549.

Elhalil, A., Elmoubarki, R., Machrouhi, A., Sadiq, M., Abdennouri, M., Qourzal, S., and Barka, N. (2017). Photocatalytic degradation of caffeine by ZnO-ZnAl2O4 nanoparticles derived from LDH structure. *Journal of environmental chemical engineering*, *5*(4), 3719-3726.

Emeji, I. C., Ama, O. M., Khoele, K., Osifo, P. O., and Ray, S. S., (2021), Electro-Fenton Degradation of Selected Antiretroviral Drugs Using a Low-cost iron-modified carbon-cloth electrode. *Electrocatalysis*, *12*, 327-339.

Epelle, E. I., Macfarlane, A., Cusack, M., Burns, A., Mackay, W. G., Rateb, M. E., and Yaseen, M., (2022), Application of ultraviolet-c radiation and gaseous ozone for microbial inactivation on different materials. *ACS omega*, *7*(47), 43006-43021.

Ezeh, C. I., Tomatis, M., Yang, X., He, J., and Sun, C., (2018), Ultrasonic and hydrothermal mediated synthesis routes for functionalized Mg-Al LDH: comparison study on surface morphology, basic site strength, cyclic sorption efficiency and effectiveness. *Ultrasonics sonochemistry*, *40*, 341-352.

Fan, H., Zhu, J., Sun, J., Zhang, S., and Ai, S., (2013), Ag/AgBr/Co–Ni–NO_3 layered double hydroxide nanocomposites with highly adsorptive and photocatalytic properties. *Chemistry–A European Journal*, *19*(7), 2523-2530.

Fan, Y., Han, D., Song, Z., Sun, Z., Dong, X., and Niu, L., (2018), Regulations of silver halide nanostructure and composites on photocatalysis. *Advanced Composites and Hybrid Materials*, *1*, 269-299.

Fang, H., Cao, X., Yu, J., Lv, X., Yang, N., Wang, T., and Jiang, W, (2019), Preparation of the all-solid-state Z-scheme WO3/Ag/AgCl film on glass accelerating the photodegradation of pollutants under visible light. *Journal of materials science*, *54*(1), 286-301.

Fang, H., Liang, D., Zhang, T., and Liu, Y., (2006), Anaerobic treatment of phenol in wastewater under thermophilic condition. *Water research*, *40*(3), 427-434.

Farrukh, M., Shahzadi, S., and Irfan, M., (2024), Drug Metabolism: Phase I and Phase II Metabolic Pathways. In *Drug Metabolism and Pharmacokinetics*. IntechOpen.

Feng, S., Chen, T., Liu, Z., Shi, J., Yue, X., and Li, Y., (2020), Z-scheme CdS/CQDs/g-C3N4 composites with visible-near-infrared light response for efficient photocatalytic organic pollutant degradation. *Science of The Total Environment*, *704*, 135404.

Fernández L.P., Brasca R., Repetti M.R., Attademo A.M., Peltzer P.M., Lajmanovich R.C., and Culzoni M.J., (2022), Bioaccumulation of Abacavir and Efavirenz in Rhinella Arenarum Tadpoles after Exposure to Environmentally Relevant Concentrations, *Chemosphere*, 301, 134361, https://doi.org/10.1016/j.chemosphere.2022.134631.

Forano, C., Costantino, U., Prévot, V., and Gueho, C. T., (2013), Layered double hydroxides (LDH). In *Developments in clay science* (Vol. 5, pp. 745-782). Elsevier.

Foruzin, L. J., Rezvani, Z., and Habibi, B., (2020), New ternary-component layered double hydroxide as a low-cost and efficient electrocatalyst for water oxidation: NiCaFe-LDH from eggshell bio-waste. *Applied clay science*, *188*, 105511.

Fu, Y.S., Li, J. and Li, J., (2019), Metal/Semiconductor Nanocomposites for Photocatalysis: Fundamentals, Structures, Applications and Properties, *Nanomaterials*, 9, 359.

Gao Y., Zhang Z., Wu J., Yi X., Zheng A., Umar A., O'Hare D., and Wang Q., (2013), Comprehensive Investigation of Co 2 Adsorption on Mg–Al–CO_3 LDH-Derived Mixed Metal Oxides, *Journal of Materials Chemistry A,* 1**,** 12782-12790, https://doi.org/10.1039/C3TA13039H.

Gevers B.R., Naseem S., Leuteritz A., and Labuschagné F.J., (2019), Comparison of Nano-Structured Transition Metal Modified Tri-Metal Mg-M-Al–LDHs (M= Fe, Zn, Cu, Ni, Co) Prepared Using Co-Precipitation, *RSC Advances*, 9, 28262-28275, https://doi.org/10.1039/C9RA05452A

Gevers, B.R., Roduner, E., and Labuschagné, F.J., (2022), Towards understanding photon absorption and emission in mgal layered double hydroxide. Mater. Adv. 3, 962-977. https://doi.org/10.1039/D1MA00893E.

Guo, C., Cao, Q., Chen, B., Yang, S. and Qian, Y., (2019), Development of Synergistic Extraction Process for Highly Efficient Removal of Phenols from Coal Gasification Wastewater, *Journal of Cleaner Production*, 211, 380-386.

Guo X. and Wang J., (2019), A General Kinetic Model for Adsorption: Theoretical Analysis and Modeling, *Journal of Molecular Liquids*, 288, 111100.

Gwenzi, W., Marumure, J., Makuvara, Z., Simbanegavi, T. T., Njomou-Ngounou, E. L., Nya, E. L., Kaetzl, K., Noubactep, C. and Rzymski, P. (2023). The Pit Latrine Paradox in Low-Income Settings: A Sanitation Technology of Choice or a Pollution Hotspot? *Science of The Total Environment,* 879**,** 163179.

Hadnađev, K. M. S., Vulić, T. J., Zorić, D. B., and Marinković, N. R. P., (2012). The influence of the UV irradiation intensity on photocatalytic activity of ZnAl layered double hydroxides and derived mixed oxides. *Chemical Industry and Chemical Engineering Quarterly/CICEQ*, *18*(2), 295-303.

Hanafi, M. F., and Sapawe, N. (2020). A review on the water problem associate with organic pollutants derived from phenol, methyl orange, and remazol brilliant blue dyes. *Materials Today: Proceedings*, *31*, A141-A150.

Hasan, S., Zeyad, M., Ahmed, S. M. and Anubhove, M. S. T., (2023), Optimization and Planning of Renewable Energy Sources Based Microgrid for a Residential Complex, *Environmental Progress and Sustainable Energy*, 42, e14124.

Hatleberg, C. I., Ryom, L., and Sabin, C. (2021). Cardiovascular risks associated with protease inhibitors for the treatment of HIV. *Expert Opinion on Drug Safety*, *20*(11), 1351-1366.

Hawkins, T. (2010). Understanding and managing the adverse effects of antiretroviral therapy. *Antiviral research*, *85*(1), 201-209.

Hayleeyesus, S. F. (2021). Electrochemical Processes for Degradation/Removal of Pollutants from Healthcare Wastewater.

Hequet, V., Raillard, C., Debono, O., Thévenet, F., Locoge, N. and Le Coq, L., 2018. Photocatalytic oxidation of VOCs at ppb level using a closed-loop reactor: the mixture effect. *Applied Catalysis B: Environmental*, *226*, pp.473-486. https://doi.org/10.1016/j.apcatb.2017.12.041.

Huang K., Li C., Zheng Y., Wang L., Wang W. ,Meng X., 2022, Recent Advances on Silver-Based Photocatalysis: Photocorrosion Inhibition, Visible-Light Responsivity Enhancement, and Charges Separation Acceleration, *Separation and Purification Technology,* 283**,** 120194, https://doi.org/10.1016/j.seppur.2021.120194.

Ibrahim, K. M. and Waziri, S. I., (2020), Improving ICT and Renewable Energy for Environmental Sustainability in Sub-Saharan Africa, *Journal of Research in Emerging Markets*, 2, 82.

Insani W.N., Qonita N.A., Jannah S.S., Nuraliyah N.M., Supadmi W., Gatera V.A., Alfian S.D., Abdulah R., 2020, Improper Disposal Practice of Unused and Expired Pharmaceutical Products in Indonesian Households, *Heliyon,* 6**,** e04551, https://doi.org/10.1016/j.heliyon.2020.e04551

Jain, M., Khan, S. A., Sharma, K., Jadhao, P. R., Pant, K. K., Ziora, Z. M. and Blaskovich, M. A. (2022). Current Perspective of Innovative Strategies for Bioremediation of Organic Pollutants from Wastewater. *Bioresource Technology,* 344**,** 126305.

Jandaghian, F., Pirbazari, A. E., Tavakoli, O., Asasian-Kolur, N., and Sharifian, S. (2023). Comparison of the performance of Ag-deposited ZnO and TiO2 nanoparticles in levofloxacin degradation under UV/visible radiation. *Journal of Hazardous Materials Advances*, *9*, 100240.

Jiang, Z., Yu, H., Liu, X., Zheng, Z., Shen, J., Zhang, H., and Bai, X. (2022). Scalable fabrication of LDH-based adsorbent for the removal of nitrate with enhanced performance. New Journal of Chemistry, 46(23), 11266-11276.

Jie Z., Yichen J., Ping L., Yang L., Huiyuan T., Xiuhong D., Zehua W., Xianying D., Chunguang L., Jiehu C., 2022, Rational Construction and Understanding the Effect of Metal Cation Substitution of Three Novel Ternary Zn-Co–Ni-LDHs from 2d to 3d and Its Enhanced Adsorption Properties for Mo, *Environmental Science and Pollution Research***,** 1-19.

Jinfeng, Z., and Tao, Z. (2013). Preparation and characterization of highly efficient and stable visible-light-responsive photocatalyst AgBr/Ag3PO4. *Journal of Nanomaterials*, *2013*, 6-6.

Johnson L.F.D., Rob E 2023. Modelling the Impact of Hivin South Africa's Provinces: 2023 Update. South Africa: University of Cape Town.

Johnson, L. F., Dorrington, R. E. and Moolla, H. (2017). Progress Towards the 2020 Targets for HIV Diagnosis and Antiretroviral Treatment in South Africa. *Southern African journal of HIV medicine,* 18**,** 1-8.

Joseph, J. K., Naiker, V., Sreeram, P., Mampulliyalil, F., Varghese, P. G., Dhawale, P. V., Sasidharan, S. P., Thakur, V. K. and Raghavan, P., (2024), Phenolic Resin: Preparation, Structure, Properties, and Applications, Handbook of Thermosetting Foams, Aerogels, and Hydrogels, 383 – 420.

Kashif, N., and Ouyang, F., (2009). Parameters effect on heterogeneous photocatalysed degradation of phenol in aqueous dispersion of TiO_2. J. Environ. Sci. **21**, 527-533. https://doi.org/10.1016/S1001-0742(08)62303-7.

Kazeem T.S., Zubair M., Daud M., Mu'azu N.D., Al-Harthi M.A., (2019), Graphene/Ternary Layered Double Hydroxide Composites: Efficient Removal of Anionic Dye from Aqueous Phase, *Korean Journal of Chemical Engineering,* 36**,** 1057-1068, https://doi.org/10.1007/s11814-019-0284-0

Kebede, T., Seroto, M., Chokwe, R., Dube, S., and Nindi, M. (2020). Adsorption of antiretroviral (ARVs) and related drugs from environmental wastewaters using nanofibers. *Journal of environmental chemical engineering*, *8*(5), 104049.

Khaki, M.R.D., Shafeeyan, M.S., Raman, A.A.A. and Daud, W.M.A.W., (2017). Application of doped photocatalysts for organic pollutant degradation-A review. *Journal of environmental management*, *198*, pp.78-94. https://doi.org/10.1016/j.jenvman.2017.04.099.

Khodam, F., Amani-Ghadim, H. R., Aber, S., Amani-Ghadim, A. R., and Ahadzadeh, I. (2018). Neodymium doped mixed metal oxide derived from CoAl-layered double hydroxide: Considerable enhancement in visible light photocatalytic activity. *Journal of Industrial and Engineering Chemistry*, *68*, 311-324.

Kim, S. Y., Kim, I. Y., Park, S.-H., Hwangbo, M., and Hwangbo, S., (2024), Novel ultrasonic technology for advanced oxidation processes of water treatment. *RSC advances*, *14*(17), 11939-11948.

Kim, S., Chen, J., Cheng, T., Gindulyte, A., He, J., He, S., Li, Q., Shoemaker, B.A., Thiessen, P.A., Yu, B. and Zaslavsky, L., (2021), PubChem in 2021: new data content and improved web interfaces. *Nucleic acids research*, *49*(D1), pp.D1388-D1395. https://doi.org/10.1093/nar/gkaa971.

Kim, S., Durand, P., André, E., and Carteret, C. (2017), Enhanced photocatalytic ability of Cu, Co doped ZnAl based mixed metal oxides derived from layered double hydroxides. *Colloids and Surfaces A: Physicochemical and Engineering Aspects*, *524*, 43-52.

Klen TJ, and Vodopivec B.M. (2012), DPPH solution (in)stability during kinetic UV/Vis spectrometry measurements of phenols antioxidant potential. Food Anal Methods 5: 781-783.

Kowlaser S., Barnhoorn I., Wagenaar I., (2022), Developmental Abnormalities and Growth Patterns in Juvenile Oreochromis Mossambicus Chronically Exposed to Efavirenz, *Emerging Contaminants*, 8, 83–89 , https://doi.org/10.1016/j.emcon.2022.02.001.

Krastanov, A., Alexieva, Z., and Yemendzhiev, H. (2013), Microbial degradation of phenol and phenolic derivatives. *Engineering in Life Sciences*, *13*(1), 76-87.

Lee, S. Y. and Stuckey, D. C. (2022). Separation and Biosynthesis of Value-Added Compounds from Food-Processing Wastewater: Towards Sustainable Wastewater Resource Recovery. *Journal of Cleaner Production,* 357**,** 131975.

Lei X., Jin M. and Williams G.R., (2014), Layered Double Hydroxides in the Remediation and Prevention of Water Pollution, *Energy and Environment Focus,* 3**,** 4-22, https://doi.org/10.1166/eef.2014.1086.

Leont'eva, N., Drozdov, V., Bel'skaya, O. and Cherepanova, S. (2020). Structural Analysis of Defects in Layered Double Hydroxides and Related Mixed Oxides. *Russian Journal of General Chemistry*, 90, 509-522.

Li B., Zhang Y., Zhou X., Liu Z., Liu Q., Li X., (2016), Different Dye Removal Mechanisms between Monodispersed and Uniform Hexagonal Thin Plate-Like MgAl–CO_3^{2-}-LDH and Its Calcined Product in Efficient Removal of Congo Red from Water, *Journal of Alloys and Compounds*, 673, 265-271, https://doi.org/10.1016/j.jallcom.2016.02.248.

Li S.S., Jiang M., Jiang T.J., Liu J.H., Guo Z., Huang X.J., (2017), Competitive Adsorption Behavior toward Metal Ions on Nano-Fe/Mg/Ni Ternary Layered Double Hydroxide Proved by Xps: Evidence of Selective and Sensitive Detection of Pb (II), *Journal of hazardous materials,* 338**,** 1-10, https://doi.org/10.1016/j.jhazmat.2017.05.017.

Li, B., Lai, C., Xu, P., Zeng, G., Huang, D., Qin, L., Yi, H., Cheng, M., Wang, L., Huang, F. and Liu, S., (2019), Facile synthesis of bismuth oxyhalogen-based Z-scheme photocatalyst for visible-light-driven pollutant removal: kinetics, degradation pathways and mechanism. *Journal of cleaner production*, *225*, pp.898-912. https://doi.org/10.1016/j.jclepro.2019.04.012.

Li, F., Li, X. and Hou, M., (2004). Photocatalytic Degradation of 2-Mercaptobenzothiazole in Aqueous La^{3+}–TiO2 Suspension for Odor Control. *Applied Catalysis B: Environmental,* 48**,** 185-194.

Liang, Q., Shi, Y., Ma, W., Li, Z., and Yang, X. (2013). Large-scale preparation and morphology-dependent photodegradation performances of monodispersed AgBr crystals. *Applied Catalysis A: General*, *455*, 199-205.

Liu, C., Sun, W., Zhuo, Y., Liu, C., and Chu, Y. (2013). PVP-assisted synthesis and visible light catalytic property of Ag/AgBr/TiO2 ternary nanostructures. Journal of Alloys and Compounds, 581, 115-120.

Liu, L., Li, S., An, Y., Sun, X., Wu, H., Li, J., Chen, X., and Li, H. (2019). Hybridization of nanodiamond and CuFe-LDH as heterogeneous photoactivator for visible-light driven photo-fenton reaction: Photocatalytic activity and mechanism. *Catalysts*, *9*(2), 118.

Luka, Y., Highina, B. K. and Zubairu, A. (2018). Bioremediation: A solution to Environmental Pollution-A review. *American Journal of Engineering Research and Review.* 7**,** 101-109.

Luo, B., Song, R., and Jing, D. (2017). ZnCr LDH nanosheets modified graphitic carbon nitride for enhanced photocatalytic hydrogen production. *International Journal of Hydrogen Energy*, *42*(37), 23427-23436.

Lupa, L., Cocheci, L., Pode, R., and Hulka, I., (2018), Phenol adsorption using aliquat 336 functionalized zn-al layered double hydroxide. Sep. Purif. Technol. 196, 82-95. https://doi.org/10.1016/j.seppur.2017.10.003.

Luttrell, T., Halpegamage, S., Tao, J., Kramer, A., Sutter, E. and Batzill, M., (2014), Why is Anatase a Better Photocatalyst than Rutile? Model Studies on Epitaxial TiO_2 Films, *Scientific Reports*, 4, 4043.

Madikizela L.M., Tavengwa N.T. ,Chimuka L., (2017), Status of Pharmaceuticals in African Water Bodies: Occurrence, Removal and Analytical Methods, *Journal of environmental management,* 193**,** 211-220.

Madikizela, L. M., Ncube, S., and Chimuka, L. (2020), Analysis, occurrence and removal of pharmaceuticals in African water resources: A current status. *Journal of environmental management*, *253*, 109741.

Madikizela, L. M., Rimayi, C., Khulu, S., Ncube, S., and Chimuka, L. (2022). Pharmaceuticals and personal care products. In *Emerging Freshwater Pollutants* (pp. 171-190). Elsevier.

Mahy, M. I., Sabin, K. M., Feizzadeh, A., and Wanyeki, I. (2021). Progress towards 2020 global HIV impact and treatment targets. *Journal of the International AIDS Society*, *24*, e25779.

Mantilla, A., Tzompantzi, F., Fernández, J., Góngora, J.D., and Gómez, R., (2010), Photodegradation of phenol and cresol in aqueous medium by using Zn/Al+ Fe mixed oxides obtained from layered double hydroxides materials. Catal. today. 150, 353-357. https://doi.org/10.1016/j.cattod.2009.11.006.

Mascolo G., Balest L., Cassano D., Laera G., Lopez A., Pollice A., Salerno C., (2010), Biodegradability of Pharmaceutical Industrial Wastewater and Formation of Recalcitrant Organic Compounds During Aerobic Biological Treatment, *Bioresource Technology,* 101**,** 2585-2591, https://doi.org/10.1016/j.biortech.2009.10.057.

Maurya, A. and Raj, A. (2020), Recent Advances in the Application of Biofilm in Bioremediation of Industrial Wastewater and Organic Pollutants. *Microorganisms for Sustainable Environment and Health*, 81-118.

Mhuka, V., Dube, S., and Nindi, M. M. (2020). Occurrence of pharmaceutical and personal care products (PPCPs) in wastewater and receiving waters in South Africa using LC-Orbitrap™ MS. *Emerging Contaminants*, *6*, 250-258.

Miao, Y.-E., Huang, Y., Zhang, C., and Liu, T. (2015). Hierarchically organized nanocomposites derived from low-dimensional nanomaterials for efficient removal of organic pollutants. *Current Organic Chemistry*, *19*(6), 498-511.

Mlunguza, N. Y., Ncube, S., Mahlambi, P. N., Chimuka, L., and Madikizela, L. M., (2020)., Determination of selected antiretroviral drugs in wastewater, surface water and aquatic plants using hollow fibre liquid phase microextraction and liquid chromatography-tandem mass spectrometry. *Journal of Hazardous Materials*, *382*, 121067.

Moja, M. M., Chirwa, E., and Tichapondwa, S. M., (2021), Visible light activated photocatalytic degradation of 2, 4-dichlorophenol using silver halide photocatalysts.

Moja, M. M., Mapossa, A. B., Chirwa, E. M. N. and Tichapondwa, S., (2024), Photocatalytic degradation of 2, 4-Dichlorophenol using Nanomaterials Silver Halide Catalysts. *Environmental Science and Pollution Research,* 31, 11857-11872.

Mourid E.H., Lakraimi M., Benaziz L., Elkhattabi E.H., Legrouri A., (2019), Wastewater Treatment Test by Removal of the Sulfamethoxazole Antibiotic by a Calcined Layered Double Hydroxide, *Applied Clay Science*, 168, 87-95, https://doi.org/10.1016/j.clay.2018.11.005.

Mtolo, S. P., Mahlambi, P. N., and Madikizela, L. M., (2019), Synthesis and application of a molecularly imprinted polymer in selective solid-phase extraction of efavirenz from water. *Water Science and Technology*, *79*(2), 356-365.

Naseem, S., Gevers, B., Boldt, R., Labuschagné, F. J. W., and Leuteritz, A., (2019), Comparison of transition metal (Fe, Co, Ni, Cu, and Zn) containing tri-metal layered double hydroxides (LDHs) prepared by urea hydrolysis. *RSC advances*, *9*(6), 3030-3040.

Natarajan S., Bajaj H.C. ,Tayade R.J., (2018), Recent Advances Based on the Synergetic Effect of Adsorption for Removal of Dyes from Waste Water Using Photocatalytic Process, *Journal of Environmental Sciences,* 65, 201-222.

Nayak, S., and Parida, K., (2018), Dynamics of charge-transfer behavior in a plasmon-induced quasi-type-II p–n/n–n dual heterojunction in Ag@ Ag_3PO_4/g-C_3N_4/NiFe LDH nanocomposites for photocatalytic Cr (VI) reduction and phenol oxidation. ACS omega, 3(7), 7324-7343.

Nazari, M., and Hosseini, S. A., (2021), Mixed oxides derived from layered double hydroxides of Ni and Co as photocatalysts for desulfurization of dibenzothiophene. *Journal of Chemical Sciences*, *133*, 1-11.

Ncube S., Madikizela L.M., Chimuka L., Nindi M.M., (2018), Environmental Fate and Ecotoxicological Effects of Antiretrovirals: A Current Global Status and Future Perspectives, *Water Research,* 145**,** 231-247, https://doi.org/10.1016/j.watres.2018.08.017.

Ncube, P., Zvinowanda, C., Belaid, M. and Ntuli, F., (2023). Heterogeneous Photocatalytic degradation of Nevirapine in wastewater using the UV/TiO_2/H_2O_2 process. *Environmental Processes*, *10*(1), p.1. https://doi.org/10.21203/rs.3.rs-1823748/v1.

Ng, S. F., Lau, M. Y. L., and Ong, W. J. (2021). Engineering layered double hydroxide–based photocatalysts toward artificial photosynthesis: state-of-the-art progress and prospects. *Solar Rrl*, *5*(6), 2000535.

Ngumba E., Gachanja A. ,Tuhkanen T., (2016), Occurrence of Selected Antibiotics and Antiretroviral Drugs in Nairobi River Basin, Kenya, *Science of the Total Environment,* 539**,** 206-213, https://doi.org/doi.org/10.1016/j.scitotenv.2015.08.139.

Ngumba, E., Gachanja, A., and Tuhkanen, T., (2020), Removal of selected antibiotics and antiretroviral drugs during post-treatment of municipal wastewater with UV, UV/chlorine and UV/hydrogen peroxide. *Water and Environment Journal*, *34*(4), 692-703.

Ngwenya P. ,Musee N., (2023), Modelling Ecological Risks of Antiretroviral Drugs in the Environment, *Environmental Chemistry and Ecotoxicology*.

Ojha, N., Karn, R., Abbas, S. and Bhugra, S., (2021), Bioremediation of Industrial Wastewater: A Review. IOP Conference Series: Earth and Environmental Science. IOP Publishing, 012012.

Okoro, H. K., Pandey, S., Ogunkunle, C. O., Ngila, C. J., Zvinowanda, C., Jimoh, I., Lawal, I. A., Orosun, M. M., and Adeniyi, A. G., (2022), Nanomaterial-based biosorbents: Adsorbent for efficient removal of selected organic pollutants from industrial wastewater. *Emerging Contaminants*, *8*, 46-58.

Olfs, H.-W., Torres-Dorante, L., Eckelt, R., and Kosslick, H., (2009), Comparison of different synthesis routes for Mg–Al layered double hydroxides (LDH): Characterization of the structural phases and anion exchange properties. *Applied clay science*, *43*(3-4), 459-464.

Oliveira E.L., Grande C.A., Rodrigues A.E., (2008), CO_2 Sorption on Hydrotalcite and Alkali-Modified (K and Cs) Hydrotalcites at High Temperatures, *Separation and Purification Technology,* 62**,** 137-147, https://doi.org/10.1016/j.seppur.2008.01.011.

Oshima, K., Fujii, H., Morita, K., Hosaka, M., Muroi, T., and Satokawa, S., (2020), Selective phenol recovery by catalytic cracking of thermal decomposition gas from epoxy-based carbon-fiber-reinforced plastic. *Industrial and engineering chemistry research*, *59*(30), 13460-13466.

Paillat, J.M., Robin, P., Hassouna, M. and Leterme, P., (2005), Predicting Ammonia and Carbon Dioxide Emissions from Carbon and Nitrogen Biodegradability during Animal Waste Composting. *Atmospheric environment,* 39**,** 6833-6842.

Palma V., Sannino D., Vaiano V., and Ciambelli P., (2010), Fluidized-Bed Reactor for the Intensification of Gas-Phase Photocatalytic Oxidative Dehydrogenation of Cyclohexane, *Industrial and engineering chemistry research,* 49**,** 10279-10286.

Pan, Q., Zheng, F., Deng, D., Chen, B., and Wang, Y., (2021), Interlayer spacing regulation of NiCo-LDH nanosheets with ultrahigh specific capacity for battery-type supercapacitors. *ACS Applied Materials and Interfaces*, *13*(47), 56692-56703.

Pandis P.K., Kalogirou C., Kanellou E., Vaitsis C., Savvidou M.G., Sourkouni G., Zorpas A.A., and Argirusis C., (2022), Key Points of Advanced Oxidation Processes (AOPs) for Wastewater, Organic Pollutants and Pharmaceutical Waste Treatment: A Mini Review, *ChemEngineering,* 6**,** 8.

Pang, Y., Song, L., Chen, C., and Ge, L., (2017), In situ synthesis of tetrahedron-shaped hollow porous Ag@ AgBr plasmonic photocatalysts with highly efficient visible-light performance by a template-assisted method. *Applied Surface Science*, *420*, 361-370.

Parolini M., Pedriali A., Binelli A., (2013), Application of a Biomarker Response Index for Ranking the Toxicity of Five Pharmaceutical and Personal Care Products (PPCPs) to the Bivalve Dreissena Polymorpha, *Archives of environmental contamination and toxicology,* 64**,** 439-447.

Parvizi, T., Parsa, J. B., and Farnood, R., (2022), Synergetic photocatalytic fuel cell and CuFe layered doubled hydroxide as photoactivator of persulfate for dramatically electricity

generation of organic pollutants degradation. Applied Catalysis B: Environmental, 319, 121894.

Patel, A. K., Singhania, R. R., Albarico, F. P. J. B., Pandey, A., Chen, C.-W. and Dong, C.D., (2022), Organic Wastes Bioremediation and its Changing Prospects. *Science of the Total Environment,* 824**,** 153889.

Patzkó, Á., Kun, R., Hornok, V., Dékány, I., Engelhardt, T., and Schall, N., (2005), ZnAl-layer double hydroxides as photocatalysts for oxidation of phenol in aqueous solution. Coll. Surf. A Physicochem. Eng. Asp. 265, 64-72. https://doi.org/10.1016/j.colsurfa.2005.01.039.

Paušová, Š., Krýsa, J., Jirkovský, J., Forano, C., Mailhot, G., and Prevot, V., (2015), Insight into the photocatalytic activity of ZnCr–CO3 LDH and derived mixed oxides. *Applied Catalysis B: Environmental*, *170*, 25-33.

Paut Kusturica M., Tomas A., Sabo A., (2016), Disposal of Unused Drugs: Knowledge and Behavior among People around the World, *Reviews of Environmental Contamination and Toxicology Volume 240***,** 71-104.

Peng, D., Jing, Q., Feng, Z., Niu, J., Cheng, X., Wu, X., Zheng, X., and Yuan, X., (2020), Facile preparation of AB-stacking graphene oxide/ZnAl-layered double hydroxide composites and enhanced visible-light photocatalytic performance of the calcined product. *Journal of Physics and Chemistry of Solids*, *136*, 109199.

Pica, M., (2019). Silver halide-based composite photocatalysts: An updated account. Rendiconti Lincei. Scienze Fisiche e Naturali 30, 453-467. https://doi.org/10.1007/s12210-019-00799-4.

Pieber B., Shalom M., Antonietti M., Seeberger P.H., and Gilmore K., (2018), Continuous Heterogeneous Photocatalysis in Serial Micro-Batch Reactors, *Angewandte Chemie International Edition,* 57**,** 9976-9979.

Piot, P., Bartos, M., Ghys, P. D., Walker, N., and Schwartländer, B. (2001), The global impact of HIV/AIDS. *Nature*, *410*(6831), 968-973.

Pourahmad, A., Sohrabnezhad, S., and Kashefian, E., (2010), AgBr/nanoAlMCM-41 visible light photocatalyst for degradation of methylene blue dye. *Spectrochimica Acta Part A: Molecular and Biomolecular Spectroscopy*, *77*(5), 1108-1114.

Prakruthi, K., Ujwal, M. P., Yashas, S. R., Mahesh, B., Kumara Swamy, N. and Shivaraju, H. P., (2022), Recent Advances in Photocatalytic Remediation of Emerging Organic Pollutants

using Semiconducting Metal Oxides: an Overview, *Environmental Science and Pollution Research*, 29, 4930-4957.

Prasse C., Schlüsener M.P., Schulz R., Ternes T.A., (2010), Antiviral Drugs in Wastewater and Surface Waters: A New Pharmaceutical Class of Environmental Relevance?, *Environmental science and technology,* 44**,** 1728-1735, https://doi.org/10.1021/es903216p.

Puga, F., Navío, J., and Hidalgo, M. (2021). Features of coupled AgBr/WO_3 materials as potential photocatalysts. *Journal of Alloys and Compounds*, *867*, 159191.

Richetta, M., Medaglia, P. G., Mattoccia, A., Varone, A., and Pizzoferrato, R. (2017). Layered double hydroxides: tailoring interlamellar nanospace for a vast field of applications. *J. Mater. Sci. Eng*, *6*(4), 2169-2222.

Rimayi, C., Odusanya, D., Weiss, J. M., de Boer, J., and Chimuka, L. (2018), Contaminants of emerging concern in the Hartbeespoort Dam catchment and the uMngeni River estuary 2016 pollution incident, South Africa. *Science of The Total Environment*, *627*, 1008-1017.

Rosenkranz, F., Cabrol, L., Carballa, M., Donoso-Bravo, A., Cruz, L., Ruiz-Filippi, G., Chamy, R., and Lema, J. (2013), Relationship between phenol degradation efficiency and microbial community structure in an anaerobic SBR. *Water research*, *47*(17), 6739-6749.

Ruan X., Huang S., Chen H., Qian G., (2013), Sorption of Aqueous Organic Contaminants onto Dodecyl Sulfate Intercalated Magnesium Iron Layered Double Hydroxide, *Applied Clay Science,* 72**,** 96-103, https://doi.org/10.1016/j.clay.2013.01.001.

Sabarinathan, P., Annamalai, V., Vishal, K., Nitin, M., Natrayan, L., Veeeman, D., and Mammo, W. D., (2022), Experimental study on removal of phenol formaldehyde resin coating from the abrasive disc and preparation of abrasive disc for polishing application. *Advances in Materials Science and Engineering*, *2022*, 1-8.

Saeed, M. U., Hussain, N., Sumrin, A., Shahbaz, A., Noor, S., Bilal, M., Aleya, L. and Iqbal, H. M., (2022), Microbial Bioremediation Strategies with Wastewater Treatment Potentialities–A Review. *Science of the total environment,* 818**,** 151754.

Saber, N. B., Mezni, A., Alrooqi, A. and Altalhi, T., (2020), A Review of Ternary Nanostructures based Noble Metal/Semiconductor for Environmental and Renewable Energy Applications, *Journal of Materials Research and Technology*, 9, 15233-15262.

Saleh, I. A., Zouari, N. and Al-Ghouti, M. A., (2020), Removal of Pesticides from Water and Wastewater: Chemical, Physical and Biological Treatment Approaches. *Environmental Technology and Innovation,* 19**,** 101026.

Samandari, M., Tagva Manesh, A., Hosseini, S. A. and Mansouri, S. (2021). Mg-Al LDH and Calcined LDH: Green Nanocatalysts for Wet Peroxide Oxidation of Phenol in Wastewater, *Journal of Water and Environmental Nanotechnology*, 6(1), 72-80.

Samuei, S., Rad, F. A., and Rezvani, Z., (2020), The influence of intercalated dye molecules shape and features on photostability and thermal stability between LDH layers. *Applied clay science*, *184*, 105388.

Sannino D., Vaiano V., Sacco O. ,Ciambelli P., (2013), Mathematical Modelling of Photocatalytic Degradation of Methylene Blue under Visible Light Irradiation, *Journal of Environmental Chemical Engineering,* 1**,** 56-60.

Schoeman, C., Dlamini, M., and Okonkwo, O., (2017), The impact of a Wastewater Treatment Works in Southern Gauteng, South Africa on efavirenz and nevirapine discharges into the aquatic environment. *Emerging Contaminants*, *3*(2), 95-106.

Schoeman, C., Mashiane, M., Dlamini, M., and Okonkwo, O., (2015), Quantification of selected antiretroviral drugs in a wastewater treatment works in South Africa using GC-TOFMS. *J. Chromatogr. Sep. Tech*, *6*(4), 1-10.

Seftel, E., Puscasu, M., Mertens, M., Cool, P., and Carja, G., (2014), Assemblies of nanoparticles of CeO2–ZnTi-LDHs and their derived mixed oxides as novel photocatalytic systems for phenol degradation. *Applied Catalysis B: Environmental*, *150*, 157-166.

Sharma S.K., Kushwaha P.K., Srivastava V.K., Bhatt S.D. ,Jasra R.V., (2007), Effect of Hydrothermal Conditions on Structural and Textural Properties of Synthetic Hydrotalcites of Varying Mg/Al Ratio, *Industrial and engineering chemistry research,* 46**,** 4856-4865, https://doi.org/10.1021/ie061438w.

Sharma, S., Dutta, V., Raizada, P., Hosseini-Bandegharaei, V., Thakur, A.V.K., Kalia, S., Nguyen, V.H., and Singh, P., (2021), Recent advances in silver bromide-based z-scheme photocatalytic systems for environmental and energy applications: A review. J. Environ. Chem. Eng. 9, 105157. https://doi.org/10.1016/j.jece.2021.105157.

Sherryna, A., and Tahir, M., (2022), Recent developments in layered double hydroxide structures with their role in promoting photocatalytic hydrogen production: A comprehensive review. *International Journal of Energy Research*, *46*(3), 2093-2140.

Shi, Y., Ma, J., Chen, Y., Qian, Y., Xu, B., Chu, W., and An, D.,(2022), Recent progress of silver-containing photocatalysts for water disinfection under visible light irradiation: A review. *Science of The Total Environment*, *804*, 150024.

Simelane, L., Mahlambi, P., Rochat, S., and Baker, B. (2024). Removal of antiretroviral drugs from wastewater using activated macadamia nutshells: Adsorption kinetics, adsorption isotherms, and thermodynamic studies. *Water Environment Research*, *96*(4), e11020.

Singh, A. K., Bilal, M., Iqbal, H. M., Meyer, A. S. and Raj, A., (2021), Bioremediation of Lignin Derivatives and Phenolics in Wastewater with Lignin Modifying Enzymes: Status, Opportunities and Challenges. *Science of the Total Environment,* 777**,** 145988.

Sipma, J., Osuna, M. B., Emanuelsson, M. A. and Castro, P. M., (2010). Biotreatment of industrial wastewaters under transient-state conditions: process stability with fluctuations of organic load, substrates, toxicants, and environmental parameters. *Critical Reviews in Environmental Science and Technology,* 40**,** 147-197.

Smalenskaite, A., Kaba, M. M., Grigoraviciute-Puroniene, I., Mikoliunaite, L., Zarkov, A., Ramanauskas, R., Morkan, I., and Kareiva, A., (2019). Sol–gel synthesis and characterization of coatings of Mg-Al layered double hydroxides. *Materials*, *12*(22), 3738.

Sohrabnezhad, S., and Rezaei, A., (2013). Plasmonic photocatalyst system using Ag/AgBr/mordenite nanocrystal under visible light. *Superlattices and Microstructures*, *55*, 168-179.

Soustelle M. 2011. An Introduction to Chemical Kinetics, John Wiley and Sons.

Späth, J., Arumugam, P., Lindberg, R. H., Abafe, O. A., Jansson, S., Fick, J., and Buckley, C. A. (2021). Biochar for the removal of detected micropollutants in South African domestic wastewater: a case study from a demonstration-scale decentralised wastewater treatment system in eThekwini. *Water SA*, *47*(4), 396–416-396–416.

Stats-SA 2022. Mid-Year Population Estimates. Pretoria: Department of Statistics South Africa.

Subramaniam, K., Ahmad, S. and Shaharuddin, N., (2020), Mini Review on Phenol Biodegradation in Antarctica using Native Microorganisms. *Asia Pac. J. Mol. Biol. Biotechnol,* 28**,** 77-89.

Sundar K.P., and Kanmani S., (2020), Progression of Photocatalytic Reactors and It's Comparison: A Review, *Chemical Engineering Research and Design,* 154**,** 135-150.

Svanstrom S., Jacobsson T.J., Boschloo G., Johansson E.M., Rensmo H. ,Cappel U.B., (2020), Degradation Mechanism of Silver Metal Deposited on Lead Halide Perovskites, *ACS applied materials and interfaces,* 12**,** 7212-7221, https://doi.org/10.1021/acsami.9b20315.

Svanstrom, S., Jacobsson, T. J., Boschloo, G., Johansson, E. M., Rensmo, H., and Cappel, U. B., (2020), Degradation mechanism of silver metal deposited on lead halide perovskites. *ACS Applied Materials and Interfaces*, *12*(6), 7212-7221.

Swanepoel, C., Bouwman, H., Pieters, R., and Bezuidenhout, C. (2015) Presence, Concentrations and Potential Implications of HIV-ARVs in Selected Water Sources in South Africa.

Tabana, L. S., (2021), Efficacy of Calcined Layered Double Hydroxide Clays in the Remediation of Phenol from Wastewater, University of Pretoria, South Africa.

Tabana L., Tichapondwa S., Labuschagne F. ,Chirwa E., (2020), Adsorption of Phenol from Wastewater Using Calcined Magnesium-Zinc-Aluminium Layered Double Hydroxide Clay, *Sustainability,* 12**,** 4273, https://doi.org/10.3390/su12104273.

Tafreshi, N., Sharifnia, S. and Dehaghi, S.M., (2019. Photocatalytic treatment of a multicomponent petrochemical wastewater by floatable ZnO/Oak charcoal composite: Optimization of operating parameters. *Journal of Environmental Chemical Engineering*, *7*(5), p.103397. https://doi.org/10.1016/j.jece.2019.103397.

Tambosi J.L., Yamanaka L.Y., José H.J., Moreira R.d.F.P.M., and Schröder H.F., (2010), Recent Research Data on the Removal of Pharmaceuticals from Sewage Treatment Plants (STP), *Química Nova,* 33**,** 411-420, https://doi.org/10.1590/S0100-40422010000200032.

Tang, H., Wang, Y., Zhang, D., Wu, K., and Huang, H., (2016). Shape-controllable synthesis and morphology-dependent photocatalytic properties of AgBr photocatalysts. *Journal of Materials Science: Materials in Electronics*, *27*, 6955-6963.

Tanvir, R. U., Zhang, J., Canter, T., Chen, D., Lu, J. and Hu, Z., (2021), Harnessing Solar Energy using Phototrophic Microorganisms: A Sustainable Pathway to Bioenergy,

Biomaterials, and Environmental Solutions, *Renewable and Sustainable Energy Reviews*, 146, 111181.

Tao, J., Wang, M., Zhang, X., Lu, L., Tang, H., Liu, Q., Lei, S., Qiao, G., and Liu, G. (2023). Construction of 0D/3D CdS/CoAl-LDH S-scheme heterojunction with boosted charge transfer and highly hydrophilic surface for enhanced photocatalytic hydrogen evolution and antibiotic degradation. *Fuel*, *338*, 127259.

Theiss, F. L., Ayoko, G. A., and Frost, R. L. (2016). Synthesis of layered double hydroxides containing Mg^{2+}, Zn^{2+}, Ca^{2+} and Al^{3+} layer cations by co-precipitation methods—A review. *Applied Surface Science*, *383*, 200-213.

Thiebault T., Guégan R., and Boussafir M., (2015), Adsorption Mechanisms of Emerging Micro-Pollutants with a Clay Mineral: Case of Tramadol and Doxepine Pharmaceutical Products, *Journal of Colloid and Interface Science*, 453, 1-8, https://doi.org/10.1016/j.jcis.2015.04.029.

Tsukanov, A., and Psakhie, S., (2016), Energy and structure of bonds in the interaction of organic anions with layered double hydroxide nanosheets: A molecular dynamics study. Sci. Rep. **6**, 1-8.

Valente, J. S., Tzompantzi, F., Prince, J., Cortez, J. G., and Gomez, R., (2009), Adsorption and photocatalytic degradation of phenol and 2, 4 dichlorophenoxiacetic acid by Mg–Zn–Al layered double hydroxides. *Applied Catalysis B: Environmental*, *90*(3-4), 330-338.

van Schalkwyk, C., Mahy, M., Johnson, L.F. and Imai-Eaton, J.W., (2024). Updated Data and Methods for the 2023 UNAIDS HIV Estimates. *JAIDS Journal of Acquired Immune Deficiency Syndromes*, *95*(1S), pp.e1-e4.

Verma, R., Belgamwar, R. and Polshettiwar, V., (2021), Plasmonic Photocatalysis for CO_2 Conversion to Chemicals and Fuels, *ACS Materials Letters*, 3, 574-598.

Wang, N., Xing, Y., Song, S., Liu, J., Xia, H., Tian, F., Xu, G., Ren, Z., and Chen, P., (2024), The synthesis of Ag/AgI with controllable size and silver content via a bola-type assisted protocol and their enhanced photocatalytic performance. *Applied Surface Science*, *654*, 159521.

Wang, L., Zhu, Z., Wang, F., Qi, Y., Zhang, W., and Wang, C., (2021), State-of-the-art and prospects of zn-containing layered double hydroxides (zn-ldh)-based materials for photocatalytic water remediation. Chemosphere 278, 130367.

Wang, P., Huang, B., Qin, X., Zhang, X., Dai, Y., and Whangbo, M.H., (2009), Ag/AgBr/WO_3·H2O: visible-light photocatalyst for bacteria destruction. Inorganic chemistry, 48(22), 10697-10702.

Wang X., Bi W., Zhai P., Wang X., Li H., Mailhot G. ,Dong W., (2016), Adsorption and Photocatalytic Degradation of Pharmaceuticals by Bioclxiy Nanospheres in Aqueous Solution, *Applied Surface Science,* 360**,** 240-251.

Wang, W., Huang, G., Jimmy, C. Y. and Wong, P. K., (2015), Advances in Photocatalytic Disinfection of Bacteria: Development of Photocatalysts and Mechanisms, *Journal of Environmental Sciences*, 34, 232-247.

Wang, H., Lang, X., Gao, J., Liu, W., Wu, D., Wu, Y., Guo, L., and Li, J., (2012), Polyhedral AgBr Microcrystals with an Increased Percentage of Exposed {111} Facets as a Highly Efficient Visible-Light Photocatalyst. *Chemistry–A European Journal*, *18*(15), 4620-4626.

Wang, Q., and O'Hare, D., (2012), Recent advances in the synthesis and application of layered double hydroxide (LDH) nanosheets. Chemical reviews, 112(7), 4124-4155.

Wang, Y., Nie, Z., and Wang, F., (2020), Modulation of photocarrier relaxation dynamics in two-dimensional semiconductors. *Light: Science and Applications*, *9*(1), 192.

Weber, M., and Weber, M. (2010)., Phenols. *Phenolic resins: a century of progress*, 9-23.

Weng B., Qi M.-Y., Han C., Tang Z.-R. ,Xu Y.J., (2019), Photocorrosion Inhibition of Semiconductor-Based Photocatalysts: Basic Principle, Current Development, and Future Perspective, *Acs Catalysis,* 9**,** 4642-4687.

Weng, B., Qi, M.-Y., Han, C., Tang, Z.-R., and Xu, Y.J., (2019), Photocorrosion inhibition of semiconductor-based photocatalysts: basic principle, current development, and future perspective. *Acs Catalysis*, *9*(5), 4642-4687.

World Health Organisation, (2015). *Guideline on When to Start Antiretroviral Therapy and on Pre-Exposure Prophylaxis for Hiv*, World Health Organization.

Wood, T. P., Duvenage, C. S., and Rohwer, E., (2015), The occurrence of anti-retroviral compounds used for HIV treatment in South African surface water. *Environmental Pollution*, *199*, 235-243.

Wooding M., Rohwer E.R., Naudé Y., (2017) Determination of Endocrine Disrupting Chemicals and Antiretroviral Compounds in Surface Water: A Disposable Sorptive Sampler

with Comprehensive Gas Chromatography–Time-of-Flight Mass Spectrometry and Large Volume Injection with Ultra-High Performance Liquid Chromatography–Tandem Mass Spectrometry, *Journal of Chromatography A,* 1496**,** 122-132, https://doi.org/10.1016/j.chroma.2017.03.057

Wooding, M., Rohwer, E. R., and Naudé, Y., (2017), Determination of endocrine disrupting chemicals and antiretroviral compounds in surface water: a disposable sorptive sampler with comprehensive gas chromatography–time-of-flight mass spectrometry and large volume injection with ultra-high performance liquid chromatography–tandem mass spectrometry. *Journal of Chromatography A*, *1496*, 122-132.

Wu, M., Wu, J., Zhang, J., Chen, H., Zhou, J., Qian, G., Xu, Z., Du, Z., and Rao, Q, (2018), A review on fabricating heterostructures from layered double hydroxides for enhanced photocatalytic activities. *Catalysis Science and Technology*, *8*(5), 1207-1228.

Xia, S., Fang, L., Meng, Y., Zhang, X., Zhang, L., Yang, C., and Ni, Z., (2020), Water-gas shift reaction catalyzed by layered double hydroxides supported Au-Ni/Cu/Pt bimetallic alloys. *Applied Catalysis B: Environmental*, *272*, 118949.

Xia, S., Shao, M., Zhou, X., Pan, G., and Ni, Z., (2015), Ti/ZnO–M x O y composites (M= Al, Cr, Fe, Ce): synthesis, characterization and application as highly efficient photocatalysts for hexachlorobenzene degradation. *Physical Chemistry Chemical Physics*, *17*(40), 26690-26702.

Xie, C., Lu, X. T., Tong, X. W., Zhang, Z. X., Liang, F. X., Liang, L., Luo, L. B., and Wu, Y. C. (2019). Recent progress in solar-blind deep-ultraviolet photodetectors based on inorganic ultrawide bandgap semiconductors. *Advanced Functional Materials*, *29*(9), 1806006.

Xolo, T., and Mahlambi, P., (2024), Molecularly imprinted polymers as solid-phase and dispersive solid-phase extraction sorbents in the extraction of antiretroviral drugs in water: adsorption, selectivity and reusability studies. *Journal of Analytical Science and Technology*, *15*(1), 11.

Xu, X., Liu, A., Hu, S., Ares, I., Martínez-Larrañaga, M.R., Wang, X., Martínez, M., Anadón, A. and Martínez, M.A., (2021). Synthetic Phenolic Antioxidants: Metabolism, hazards and mechanism of action. *Food Chemistry,* 353**,** 129488.

Xu, Y., Xu, H., Yan, J., Li, H., Huang, L., Zhang, Q., Huang, C. and Wan, H., (2013), A Novel Visible-Light-Response Plasmonic Photocatalyst CNT/Ag/AgBr and its Photocatalytic Properties. *Physical Chemistry Chemical Physics,* 15**,** 5821-5830.

Yang T., Peng J., Zheng Y., He X., Hou Y., Wu L. ,Fu X., (2018), Enhanced Photocatalytic Ozonation Degradation of Organic Pollutants by Zno Modified Tio2 Nanocomposites, *Applied Catalysis B: Environmental,* 221**,** 223-234.

Yang Z., Wang F., Zhang C., Zeng G., Tan X., Yu Z., Zhong Y., Wang H., Cui F., (2016), Utilization of LDH-Based Materials as Potential Adsorbents and Photocatalysts for the Decontamination of Dyes Wastewater: A Review, *RSC Advances,* 6**,** 79415-79436, https://doi.org/10.1039/C6RA12727D

Yang, M., and Rosentrater, K. A, (2020), Life cycle assessment of urea-formaldehyde adhesive and phenol-formaldehyde adhesives. *Environmental Processes*, *7*, 553-561.

Yang, Q., Wang, S., Chen, F., Luo, K., Sun, J., Gong, C., Yao, F., Wang, X., Wu, J., and Li, X., (2017), Enhanced visible-light-driven photocatalytic removal of refractory pollutants by Zn/Fe mixed metal oxide derived from layered double hydroxide. *Catalysis Communications*, *99*, 15-19.

Ye, H., Liu, S., Yu, D., Zhou, X., Qin, L., Lai, C., Qin, F., Zhang, M., Chen, W., and Chen, W., (2022), Regeneration mechanism, modification strategy, and environment application of layered double hydroxides: Insights based on memory effect. *Coordination Chemistry Reviews*, *450*, 214253.

Yen, C. F., Tsai, J. J., Lu, P. L., Chen, Y. H., Chen, T. C., Chen, P. P., and Chen, T. P., (2004), Quality of life and its correlates in HIV/AIDS male outpatients receiving highly active antiretroviral therapy in Taiwan. *Psychiatry and clinical neurosciences*, *58*(5), 501-506.

Yin N., Wang K., Wang L., Li Z., (2016), Amino-Functionalized Mofs Combining Ceramic Membrane Ultrafiltration for Pb (II) Removal, *Chemical Engineering Journal,* 306**,** 619-628, https://doi.org/10.1016/j.cej.2016.07.064.

You, J., Guo, Y., Guo, R., and Liu, X., (2019), A review of visible light-active photocatalysts for water disinfection: Features and prospects. *Chemical Engineering Journal*, *373*, 624-641.

Yu H., Huang J., Jiang L., Yuan X., Yi K., Zhang W., Zhang J. ,Chen H., (2021), Steering Photo-Excitons Towards Active Sites: Intensified Substrates Affinity and Spatial Charge Separation for Photocatalytic Molecular Oxygen Activation and Pollutant Removal, *Chemical Engineering Journal,* 408**,** 127334.

Žerjav, G., Žižek, K., Zavašnik, J. and Pintar, A., (2022), Brookite vs. Rutile vs. Anatase: Whats Behind their Various Photocatalytic Activities? *Journal of Environmental Chemical Engineering*, 10, 107722.

Zhang J., (2019), Physical Insights into Kinetic Models of Adsorption, *Separation and Purification Technology*, 229, 115832, https://doi.org/10.1016/j.seppur.2019.115832.

Zhang, M., Luo, Z., Zhou, M., Zhang, G., Alamry, K. A., Taib, L. A., Asiri, A. M., and Wang, X., (2017), Ni-Co layered double hydroxides cocatalyst for sustainable oxygen photosynthesis. *Applied Catalysis B: Environmental*, *210*, 454-461.

Zhang, P., Wu, P., Bao, S., Wang, Z., Tian, B., and Zhang, J., (2016), Synthesis of sandwich-structured AgBr@ Ag@ TiO_2 composite photocatalyst and study of its photocatalytic performance for the oxidation of benzyl alcohols to benzaldehydes. *Chemical Engineering Journal*, *306*, 1151-1161.

Zhang, S., Khan, I., Qin, X., Qi, K., Liu, Y., and Bai, S., (2020), Construction of 1D Ag-AgBr/AlOOH plasmonic photocatalyst for degradation of tetracycline hydrochloride. Frontiers in Chemistry, 8, 117.

Zhang, X., Zhou, Q., Zou, W., and Hu, X.,(2017), Molecular mechanisms of developmental toxicity induced by graphene oxide at predicted environmental concentrations. *Environmental science and technology*, *51*(14), 7861-7871.

Zheng, F., Wang, J., Xiao, R., Chai, W., Xing, D. and Lu, H., (2021), Dissolved organic nitrogen in wastewater treatment processes: Transformation, biosynthesis and ecological impacts. *Environmental Pollution,* 273**,** 116436.

Zheng, J., Tang, X., Fan, C., Deng, Y., Li, X., Yang, Q., Wang, D., Duan, A., Luo, J., and Chen, Z., (2022), Facile synthesis of Ag@ AgCl/ZnAl-LDH sesame balls nanocomposites with enhanced photocatalytic performance for the degradation of neonicotinoid pesticides. *Chemical Engineering Journal*, *446*, 136485.

Zheng, J., Tang, X., Fan, C., Deng, Y., Li, X., Yang, Q., Wang, D., Duan, A., Luo, J., Chen, Z. and Zhang, B., (2022), Facile synthesis of Ag@ AgCl/ZnAl-LDH sesame balls nanocomposites with enhanced photocatalytic performance for the degradation of neonicotinoid pesticides. *Chemical Engineering Journal*, *446*, p.136485.https://doi.org/10.1016/j.cej.2022.136485.

Zhou, X., Hu, C., Hu, X., and Peng, T., (2012), Enhanced electron transfer and silver-releasing suppression in Ag–AgBr/titanium-doped Al_2O_3 suspensions with visible-light irradiation. *Journal of Hazardous Materials*, *219*, 276-282.

Zhu, J., Zhu, Z., Zhang, H., Lu, H., Qiu, Y., Zhu, L., and Küppers, S. (2016). Enhanced photocatalytic activity of Ce-doped Zn-Al multi-metal oxide composites derived from layered double hydroxide precursors. *Journal of colloid and interface science*, *481*, 144-157.

Zhu, Y.-X., Song, G.-L., Wu, P.-P., Huang, J.-F., and Zheng, D.J. (2021). A protective superhydrophobic Mg–Zn–Al LDH film on surface-alloyed magnesium. Journal of Alloys and Compounds, 855, 157550.

Zitha A.B., Ncube S., Mketo N., Nyoni H. ,Madikizela L.M., (2022), Antiretroviral Drugs in Water: An African Challenge with Kenya and South Africa as Hotspots and Plausible Remediation Strategies, *Chemistry Africa,* 5**,** 1237-1253, https://doi.org/10.1007/s42250-022-00417-1

Zou, X., Shi, R., Zhang, Z., Fu, G., Li, L., Yu, L., Tian, Y., and Luo, F., (2021), Calcined ZnTi-Layered Double Hydroxide Intercalated with H3PW12O40 with Efficiently Photocatalytic and Adsorption Performances. *Chemistry–A European Journal*, *27*(67), 16670-16681.

3APPENDICES

Appendix A

Table A 1: Positions of the basal planes and crystallite parameters

Parameter	Sample ID	
	LDH	Ag-AgBr-LDH
2θ (003) (°)	13.39	12.96
2θ (006) (°)	26.64	26.31
2θ (009) (°)	40.36	40.37
2θ (110) (°)	71.28	71.11
$d_{(003)}$ (Å)	7.67	7.92
c (Å)	23.21	23.56
a (Å)	3.07	3.07
L (nm)	18.26	14.09

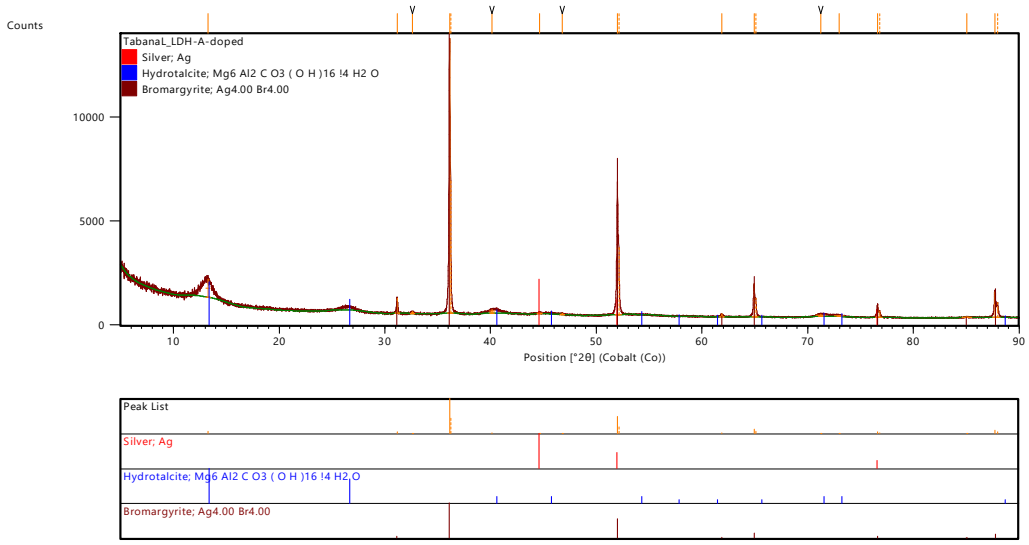

Figure A 1: XRD analysis for Ag-AgBr-LDH nanocomposite photocatalyst.

Appendix B

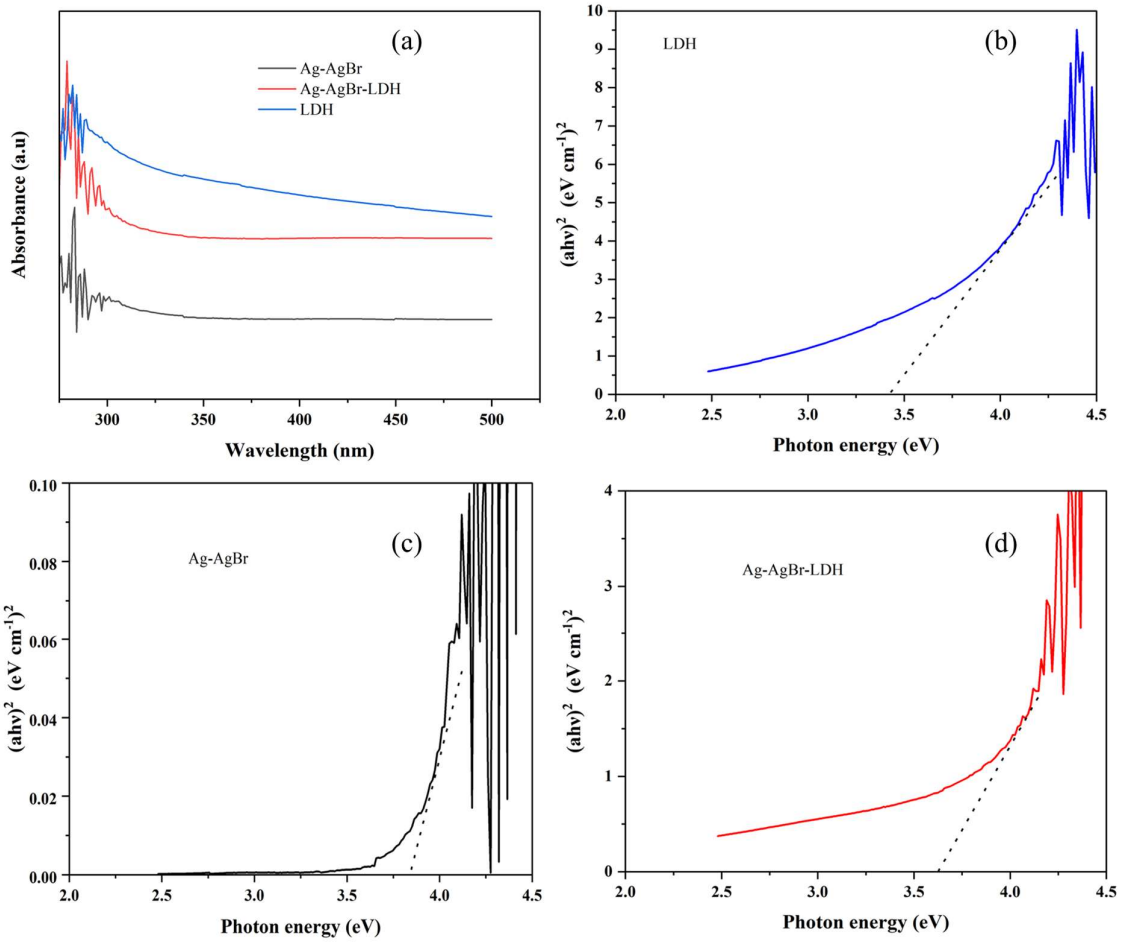

Figure B 1: (a) UV-vis absorption spectra for LDH-5, Ag-AgBr and LDH-doped 30, (b) Tauc plot for LDH-5, (c) Tauc plot for Ag-AgBr and (d) Tauc plot for LDH-doped 30

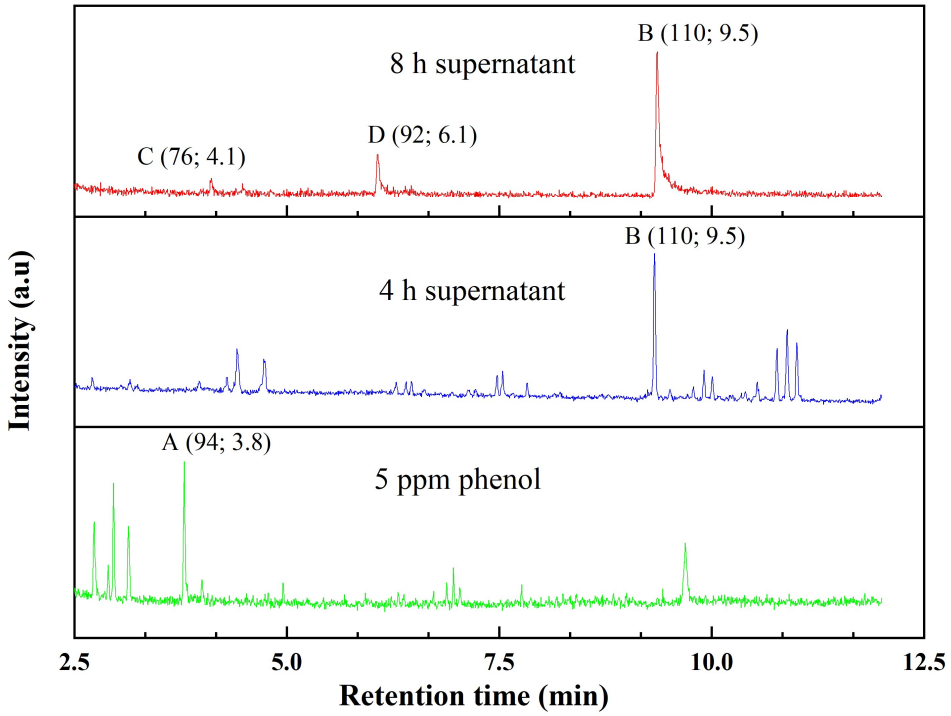

Figure B 2: GC-MS analysis for phenol after various irradiation times, (A) phenol, (B) Catechol, (C)hydroxy acetic acid and (D)glycerol.

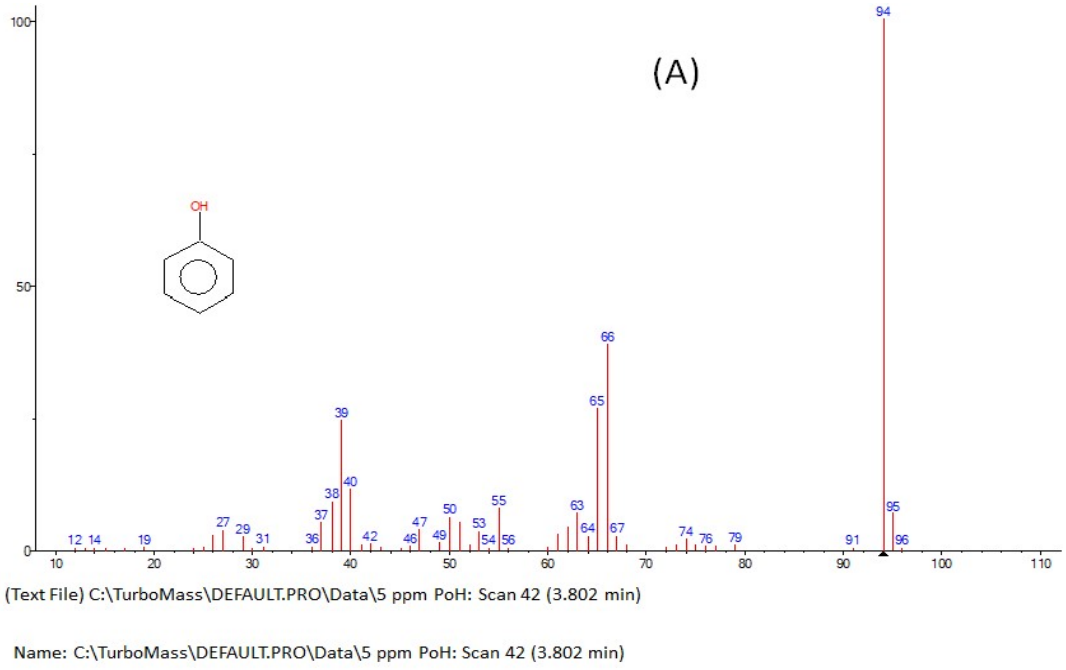

Figure B 3: Mass spectrum for Phenol.

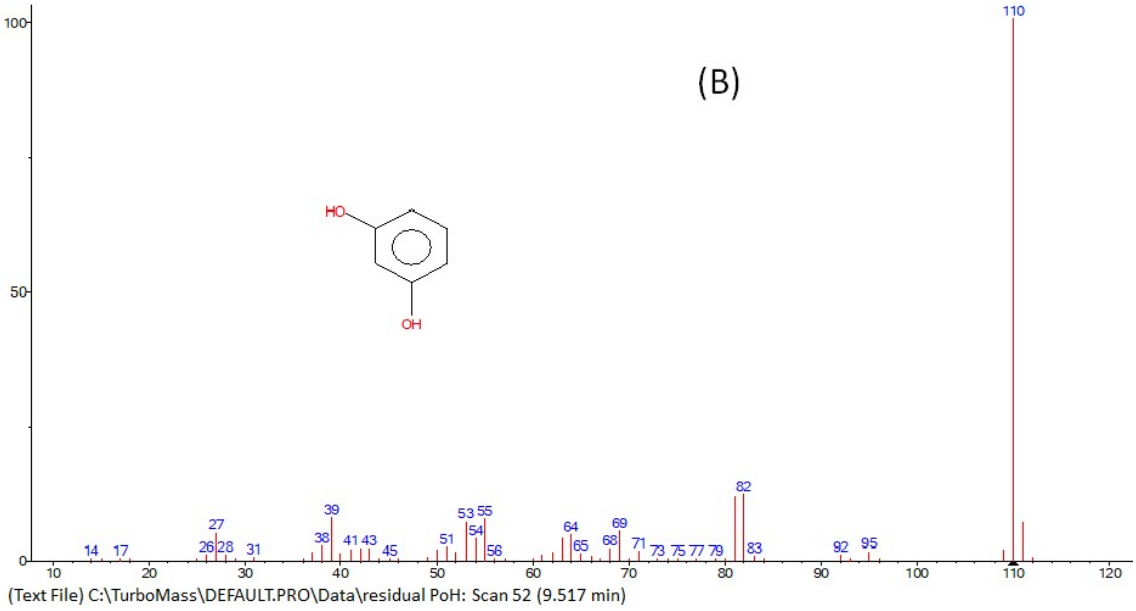

Figure B 4: Mass spectrum for catechol.

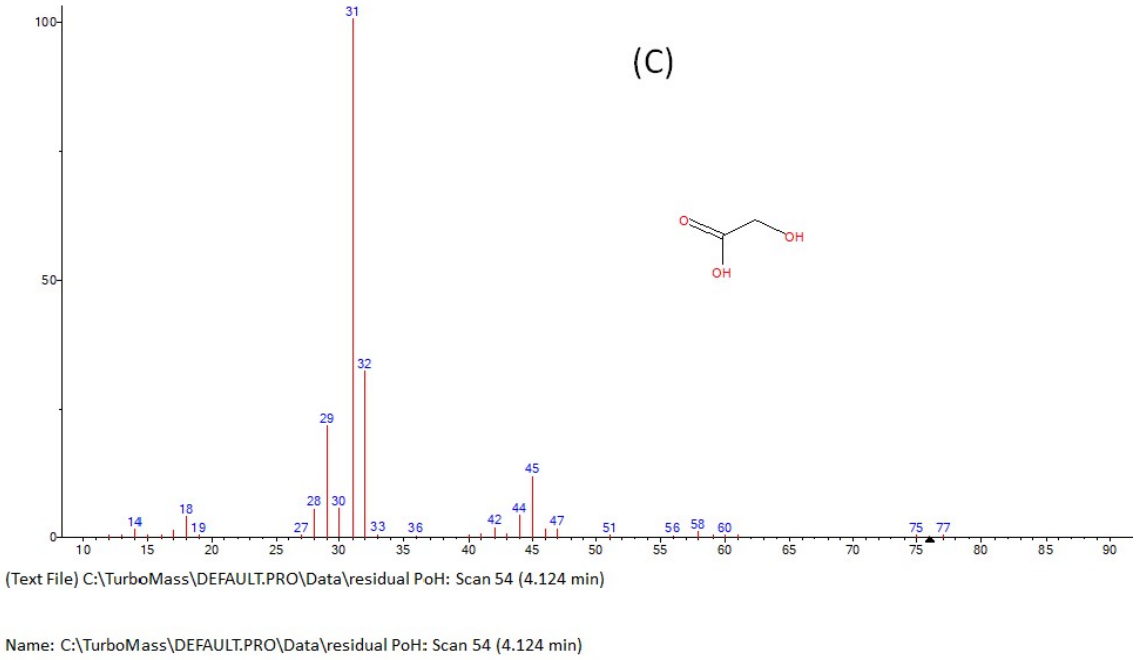

Figure B 5: Mass spectrum for hydroxy acetic acid.

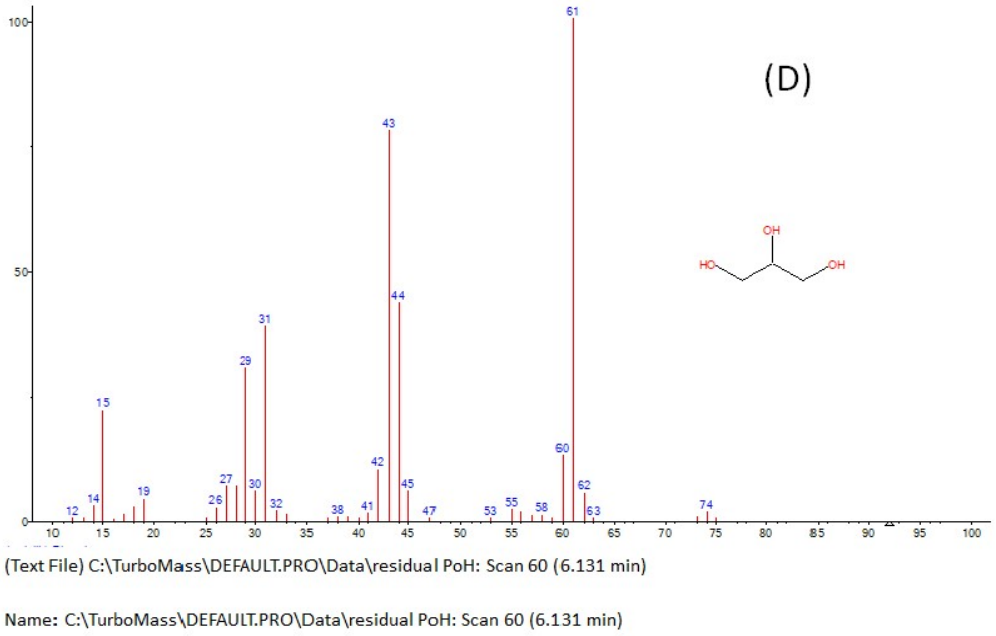

Figure B 6: Mass spectrum for glycerol.

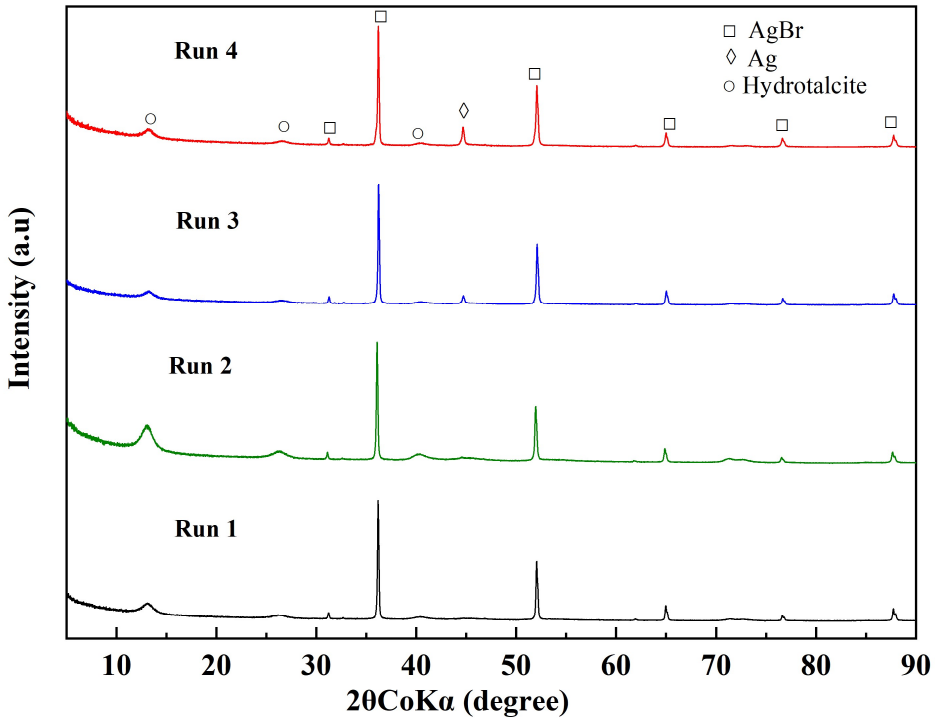

Figure B 7: X-ray diffraction spectra for feed catalyst into various photocatalytic degradation runs.

Appendix C

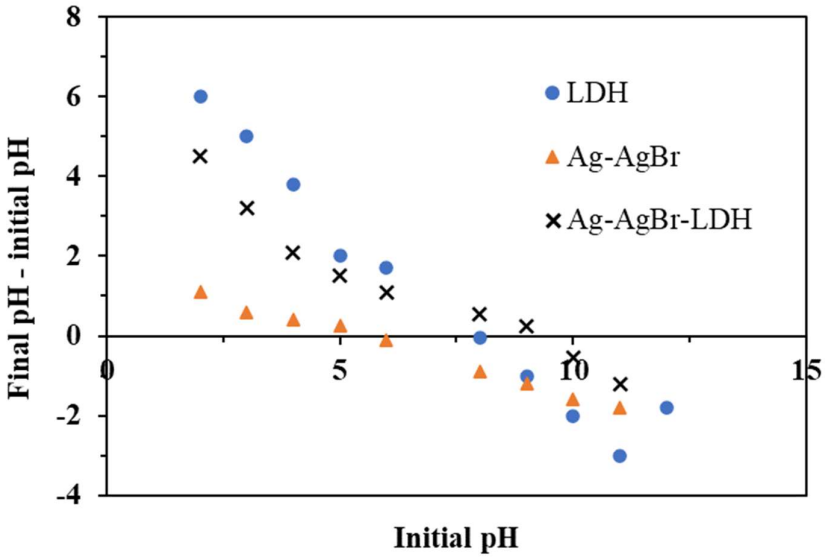

Figure C 1: Point of zero charge for various photocatalyst.

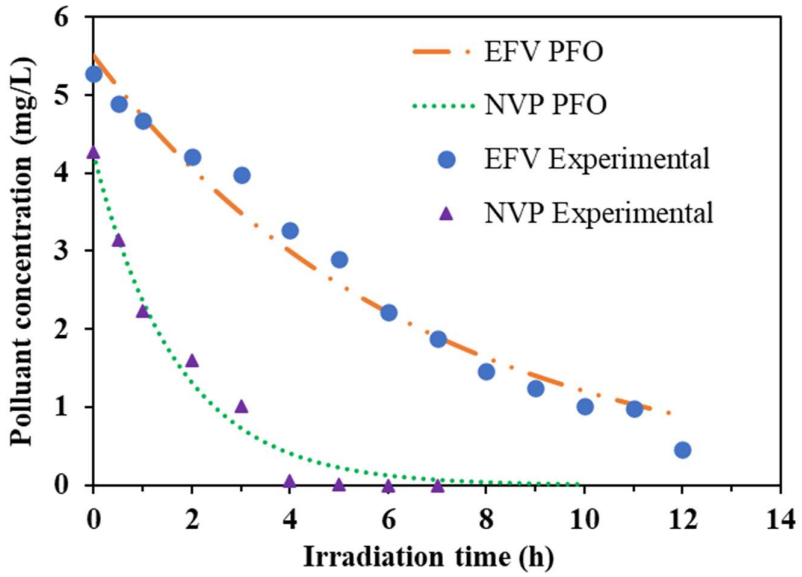

Figure C 2: PFO kinetics model fittings for efavirenz and nevirapine (5 mg/L).

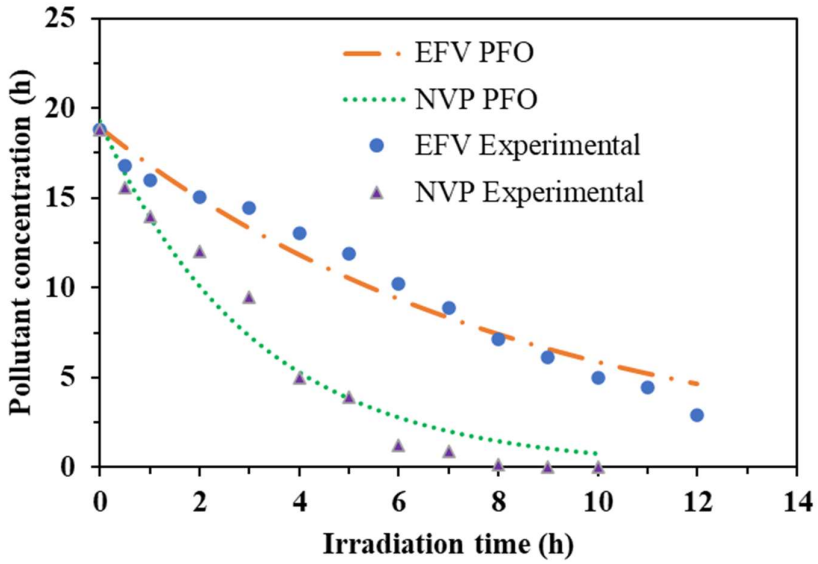

Figure C 3: PFO kinetics model fittings for efavirenz and nevirapine (20 mg/L).

Appendix D

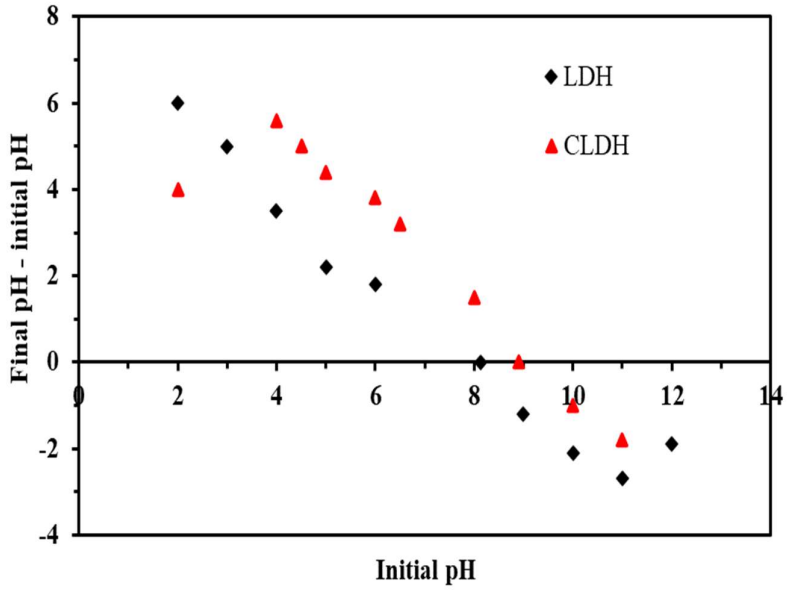

Figure D 1: Point of zero charge for LDH and CLDH

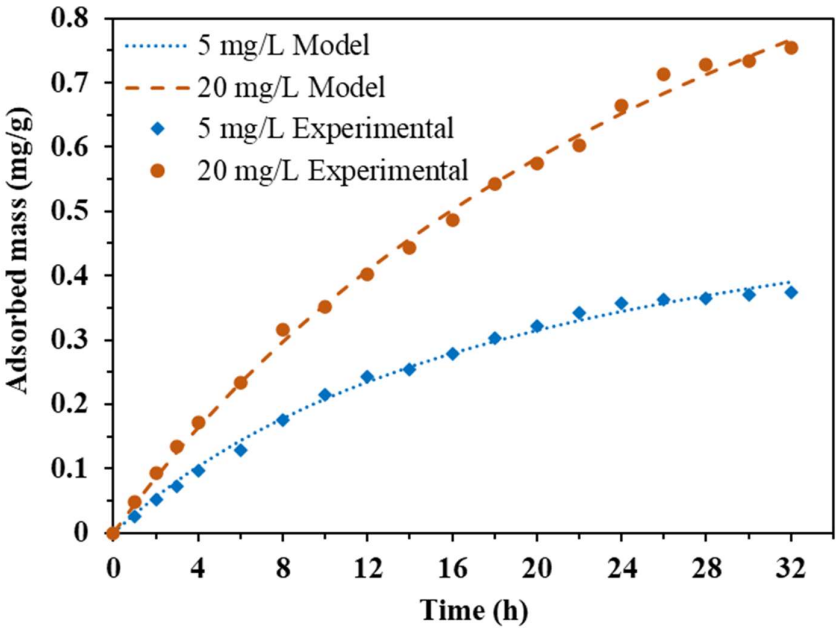

Figure D 2: PSO kinetics model for EFV at initial concentrations of 5 and 20 mg/L, pH 5, T=25 ℃ and a dosage of 10 g/L

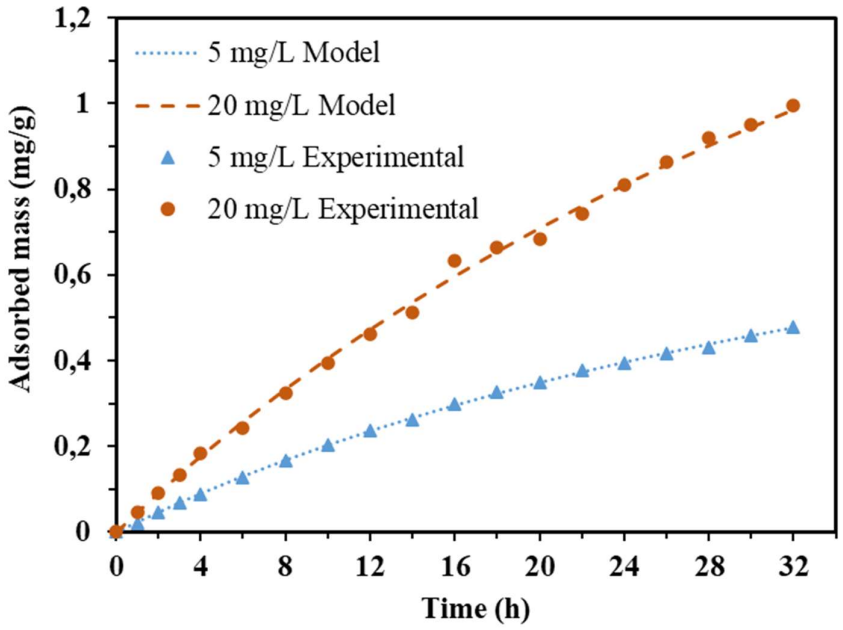

Figure D 3: PSO kinetics model for NVP at initial concentrations of 5 and 20 mg/L, pH 5, T=25°C and a dosage of 10 g/L

Table D 1: PFO kinetic models' parameters

Concentration	Parameter	Efavirenz	Nevirapine
5 mg/L	k_1 (h^{-1})	0.107	0.115
	q_e (calculated)(mg/g)	0.413	0.528
	q_e (experimental)(mg/g)	0.362	0.42
	R^2	0.92	0.90
10 mg/L	k_1 (h^{-1})	0.104	0.126
	q_e (calculated)(mg/g)	0.719	1
	q_e (experimental)(mg/g)	0.629	0.748
	R^2	0.93	0.95
20 mg/L	k_1 (h^{-1})	0.137	0.105
	q_e (calculated)(mg/g)	0.789	0.996
	q_e (experimental)(mg/g)	0.64	0.824
	R^2	0.95	0.93